



HAL
open science

Hollow Beta zeolites : synthesis and impact of the hollow morphology on diffusion and catalysis

Ana Rita Morgado Prates

► **To cite this version:**

Ana Rita Morgado Prates. Hollow Beta zeolites : synthesis and impact of the hollow morphology on diffusion and catalysis. Catalysis. Université de Lyon, 2019. English. NNT : 2019LYSE1155 . tel-02407012

HAL Id: tel-02407012

<https://theses.hal.science/tel-02407012>

Submitted on 12 Dec 2019

HAL is a multi-disciplinary open access archive for the deposit and dissemination of scientific research documents, whether they are published or not. The documents may come from teaching and research institutions in France or abroad, or from public or private research centers.

L'archive ouverte pluridisciplinaire **HAL**, est destinée au dépôt et à la diffusion de documents scientifiques de niveau recherche, publiés ou non, émanant des établissements d'enseignement et de recherche français ou étrangers, des laboratoires publics ou privés.



N°d'ordre NNT : 2019LYSE1155

THESE de DOCTORAT DE L'UNIVERSITE DE LYON

opérée au sein de
l'Université Claude Bernard Lyon 1

Ecole Doctorale N° 206
Ecole Doctorale de Chimie de Lyon

Spécialité de doctorat : Matériaux et Catalyse
Discipline : Chimie

Soutenue publiquement le 18/09/2019, par :
Ana Rita Morgado Prates

Hollow Beta zeolites: synthesis and impact of the hollow morphology on diffusion and catalysis

Devant le jury composé de :

Bianchi, Daniel	Professeur Émérite, Université Lyon 1, IRCELYON	Président
Massiani, Pascale	Directrice de Recherche, CNRS, Université Sorbonne, LRS	Rapporteure
Pouilloux, Yannick	Professeur, Université de Poitiers, IC2MP	Rapporteur
Roualdes, Stéphani	Maître de conférences, Université de Montpellier, I.E.M	Examinatrice
Simon-Masseron, Angélique	Professeure, Université de Haute Alsace, IS2M	Examinatrice
Tuel, Alain	Directeur de Recherche CNRS, IRCELYON	Directeur de thèse
Farrusseng, David	Directeur de Recherche CNRS, IRCELYON	Co-directeur
Dodin, Mathias	Ingénieur de Recherche, IFPEN	Invité
Martinez-Franco, Raquel	Ingénieure de Recherche, IFPEN	Invité

UNIVERSITE CLAUDE BERNARD - LYON 1

Président de l'Université

Président du Conseil Académique

Vice-président du Conseil d'Administration

Vice-président du Conseil Formation et Vie Universitaire

Vice-président de la Commission Recherche

Directrice Générale des Services

M. le Professeur Frédéric FLEURY

M. le Professeur Hamda BEN HADID

M. le Professeur Didier REVEL

M. le Professeur Philippe CHEVALIER

M. Fabrice VALLÉE

Mme Dominique MARCHAND

COMPOSANTES SANTE

Faculté de Médecine Lyon Est – Claude Bernard

Directeur : M. le Professeur G.RODE

Faculté de Médecine et de Maïeutique Lyon Sud – Charles Mérieux

Directeur : Mme la Professeure C. BURILLON

Faculté d'Odontologie

Directeur : M. le Professeur D. BOURGEOIS

Institut des Sciences Pharmaceutiques et Biologiques

Directeur : Mme la Professeure C. VINCIGUERRA

Institut des Sciences et Techniques de la Réadaptation

Directeur : M. X. PERROT

Département de formation et Centre de Recherche en Biologie Humaine

Directeur : Mme la Professeure A-M. SCHOTT

COMPOSANTES ET DEPARTEMENTS DE SCIENCES ET TECHNOLOGIE

Faculté des Sciences et Technologies

Directeur : M. F. DE MARCHI

Département Biologie

Directeur : M. le Professeur F. THEVENARD

Département Chimie Biochimie

Directeur : Mme C. FELIX

Département GEP

Directeur : M. Hassan HAMMOURI

Département Informatique

Directeur : M. le Professeur S. AKKOUCHE

Département Mathématiques

Directeur : M. le Professeur G. TOMANOV

Département Mécanique

Directeur : M. le Professeur H. BEN HADID

Département Physique

Directeur : M. le Professeur J-C PLENET

UFR Sciences et Techniques des Activités Physiques et Sportives

Directeur : M. Y.VANPOULLE

Observatoire des Sciences de l'Univers de Lyon

Directeur : M. B. GUIDERDONI

Polytech Lyon

Directeur : M. le Professeur E.PERRIN

Ecole Supérieure de Chimie Physique Electronique

Directeur : M. G. PIGNAULT

Institut Universitaire de Technologie de Lyon 1

Directeur : M. le Professeur C. VITON

Ecole Supérieure du Professorat et de l'Education

Directeur : M. le Professeur A. MOUGNIOTTE

Institut de Science Financière et d'Assurances

Directeur : M. N. LEBOISNE

Acknowledgements

I would like to express my appreciation to all people that, in one way or another, made this PhD possible. My thoughts:

I would like to give my deepest appreciations to my supervisors Alain Tuel and David Farrusseng. In very different ways, each one of you taught me a lot, and consequently I grew a lot professionally, scientifically and personally. It was a pleasure to work with such a high qualified and brilliant group. I'd like to give special thanks to David Farrusseng, who always believed in me and pushed me to continue when I had lost my confidence.

Nicolas Bats, former research engineer at IFPEN and former co-supervisor of this PhD, for all his support and discussions during my PhD, even after leaving IFPEN. Also, Mathias Dodin and Raquel Franco, who effectively took Nicolas' place, and embraced this project in the middle time, which is not an easy task. And finally Maria Manko, for providing valuable data in the synthesis of hollow Beta zeolite.

ING Team. Thank you for all the scientific discussions and the friendly companionship generally supported by croissants or after work beers. To Cecile Daniel, thank you for the BELMAX samples and formation, but most of all, thank you for your words and support. To Fred Meunier, for the hydrogenation reactions and scientific discussions. To Jean-Luc and Frank, for the daily good mood.

To the scientific services of IRCELYON, especially, the microscopy group. Laurence, merci pour les formations officielles et cachet de MEB et TEM. Merci pour les brunches, les discussions de couture et street art. Minoun, merci pour l'aide au microscope, pour l'amitié de ta part et ta famille. Thank you Lucian Roiban et Siddhardha Koneti, for the ETEM measurement that resulted in the 3D reconstructions of my zeolite crystals, which was extremely valuable for my work and my presentations.

To my "co-bureau" Céline Pagis, from whom I learned so much. I'm happy that I had you as my colleague and friend, during this 4 years of PhD.

My friends, colleagues and friends, that I had the pleasure to share so many good moments, and that encouraged me so many times: Diane, Gaby, Davide, Caroline, Aleksandra Lili, Natalia, David Laprune, Jeremy, Geraldine, Mathilde, Ranin. The flowery fun side, Alejandra, Lama! Thank you for all the talks, support and fun! My old mates Mafalda, Marisa, Sonia, Svetan, Ruben, Leonor, avec qui j'ai commencé cette nouvelle étape. Tarek, always optimist, that can always bring the best in me, and the best buddy to go out for drinks. My friends in Lisbon, Claudia, Catarina, Célios

Inês Bom, Simone, Débora, Pedro Lopes, Henrique, Daniel. To my good friends Rhiannon Thorpe and Richard Hardy, that managed to cheer me up countless times with cookies, coffee, apéros, delicious pizzas and so many laughs.

To Renaud Gakalla. Thank you for being my rock, my psychologist, and sometimes my punching bag so unfairly. Thank you for being there with the warmest hug.

Obrigada ao meu mano Rui Prates, Claudia, Mariana e Francisca. Perto na distancia, e sempre amigos.

Para os meus pais, Rui e Ana Paula, a quem dedico esta tese, a qual sem voces nao seria possivel. Embora sejam desconhecedores de toda a ciencia por detrás, foram voces que me deram os alicerces para aqui chegar, e me transmitiram os valores mais importantes de trabalho, persistencia e resistencia. Valores aos quais devo tudo aquilo que alcancei. Apesar da distancia, estiveram presentes todos os dias. Por isso, esta tese também é vossa. Obrigada por tudo aquilo que me proporcionaram, todo o empenho e paciencia durante os meus anos de escola e faculdade, mudanças, etc. Todo o apoio e carinho. Obrigada por serem a minha trincheira amiga. Sempre.

Résumé

De par leur morphologie, les cristaux creux de zéolithe permettent d'étudier les phénomènes de limitations diffusionnelles en catalyse et également d'encapsuler des particules métalliques ; les nano-réacteurs ainsi obtenus ont montré des activités catalytiques originales. Leur synthèse, qui nécessite des caractéristiques structurales particulières, a longtemps été limitée aux zéolithes de structure **MFI**. Le but de cette thèse était d'étudier différentes voies de synthèse pour préparer des cristaux creux de zéolithe Beta, une des zéolithes les plus utilisées dans l'industrie. Deux voies ont été suivies : l'utilisation d'un zincosilicate de même structure que la zéolithe Beta comme gabarit sacrificiel et une méthode plus classique de désilication sélective. L'encapsulation de nanoparticules de platine dans les cristaux obtenus selon la première voie a été confirmée par l'hydrogénation d'aromatiques substitués. L'influence de la morphologie sur la diffusion de différentes molécules a été étudiée par ZLC : le temps caractéristique de diffusion a été réduit de 34 à 78 % par rapport à des cristaux conventionnels. Malgré cela, la présence d'une cavité dans les cristaux de zéolithe Beta n'a pas d'effets sur l'activité catalytique dans les réactions d'hydro-isomérisation du n-C₁₆ et du craquage du cyclohexane. La thèse discute de la présence/absence de limitations diffusionnelles.

Mots clés : zéolite creuse, zéolithe Beta, diffusion, ZLC, catalyse, module de Thiele, encapsulation, platine

Abstract

Hollow zeolite single crystals have received particular interest in catalysis. The presence of a large cavity in these model zeolites enables the study of diffusional limitation in Catalysis. The cavity also enables the encapsulation of metal nanoparticles. However, their synthesis requires specific structural characteristics and it has been limited for long to zeolites with the **MFI** structure. The objective of this PhD work was to investigate the synthesis of hollow Beta zeolites (***BEA** framework type) and study the impact of the hollow morphology on molecular diffusion and catalysis. Two different strategies have been envisaged: a dissolution/recrystallization approach using CIT-6, a zincosilicate with the same ***BEA** topology and a selective desilication route. Pt nanoparticles encapsulated in hollow crystals obtained from CIT-6 showed remarkable size-selectivity in the hydrogenation of aromatics. The effect of the hollow morphology in molecular diffusion was studied using the ZLC technique; the characteristic diffusion time of the hollow morphology was reduced by 34 – 78 % compared to the corresponding bulk zeolite. Despite that, the hollow structure had no influence on the catalytic activities for the hydroisomerization of n-C₁₆ and for the cracking of cyclohexane. The presence/absence of diffusional limitation is discussed.

Key words: hollow zeolite, zeolite Beta, diffusion, ZLC, catalysis, Thiele modulus, encapsulation, platinum

Résumé

1. Introduction

Les zéolithes sont des aluminosilicates cristallisés dont la structure, formée de tétraèdres TO_4 ($T = Si$ ou Al) joints par un sommet oxygène, contient des cavités et/ou canaux de taille moléculaire comprise généralement entre 0,4 et 1nm. Les nombreuses manières d'agencer ces tétraèdres dans l'espace génèrent tout un ensemble de structures avec des canaux de taille et de forme différentes. Chaque atome d'aluminium en coordination tétraédrique confère une charge négative au réseau, qui est compensée par un cation, généralement un cation alcalin ou alcalinoterreux. Ces cations, localisés dans la porosité de la zéolithe, sont facilement échangeables en milieu aqueux ; la capacité d'échange dépend alors directement de la composition du réseau, en particulier de son rapport Si/Al . Lorsque ce cation est un proton, la zéolite possède alors des propriétés acides et peut être utilisée comme catalyseur dans de nombreuses réactions chimiques. Cette propriété, associée à une très forte surface spécifique et une bonne stabilité thermique fait que les zéolithes sont fortement utilisées en pétrochimie et raffinage.

La présence de pores de dimension nanométrique a cependant une forte influence sur les réactions catalytiques : outre le fait qu'ils jouent le rôle de tamis moléculaire en empêchant les « grosses » molécules de pénétrer dans le cristal, ils imposent une diffusion très lente des « petites » molécules. Ainsi, une molécule dont la taille est sensiblement la même que celle du pore peut diffuser si lentement qu'elle ne rencontrera jamais les sites catalytiques situés au centre du cristal ; seule la périphérie du cristal est alors « efficace » dans la réaction. L'effet des limitations diffusionnelles intra-cristallines peut être quantifié par le module de Thiele.

Différentes méthodes ont été développées ces dernières années pour tenter d'augmenter l'efficacité des zéolithes en conditions réactionnelles. L'une d'elles consiste à diminuer la longueur moyenne de diffusion « L » en utilisant de cristaux les plus petits possibles, par exemple de taille inférieure à 100 nm. D'autres proposent de modifier les cristaux existants en créant une

marco-, mésoporosité additionnelle (zéolithes hiérarchisées) qui permet aux réactifs et produits d'accéder plus rapidement aux sites catalytiques internes (Figure 1). Ces méthodes, bien qu'efficaces, modifient néanmoins les propriétés structurales du catalyseur (développement de la surface externe par exemple) et souvent également sa composition chimique (comme l'acidité).

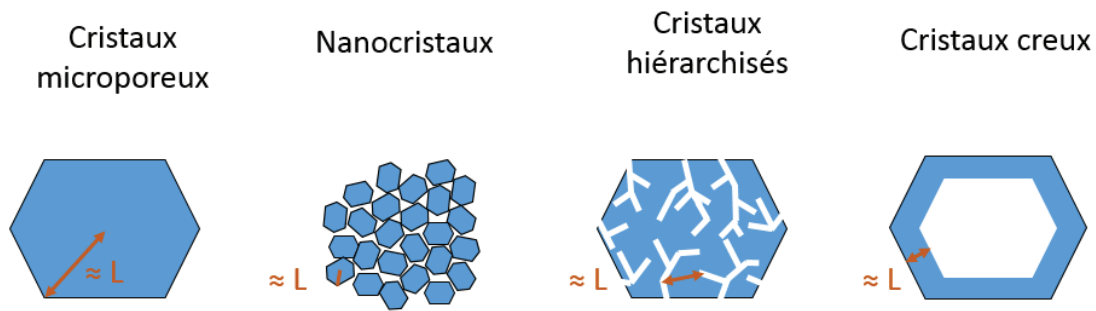


Figure 1 Différente stratégie de synthèse permettant de diminuer la longueur de diffusion moyenne L dans les cristaux zéolithiques

Plus récemment, le développement des cristaux creux ou « nanoboîtes » zéolithiques a permis de diminuer la longueur de diffusion (qui devient alors l'épaisseur des parois du cristal) sans modifier la surface externe. L'avantage de cette morphologie particulière a été montré dans l'hydrogénation du cyclohexène sur Pt déposé sur des nanoboîtes de zéolithe Y. D'autre part, ces cristaux creux peuvent également servir à emprisonner et stabiliser des particules métalliques ; les nano-réacteurs ainsi obtenus allient les propriétés de la particule à celle de la zéolithe.

Au commencement de ce travail, les seuls exemples de nanoboîtes rapportées dans la littérature concernaient les zéolithes de structure **MFI**, c'est-à-dire la ZSM-5 et la silicalite-1. Le but de la thèse est de préparer des nanoboîtes analogues avec des zéolithes de structure ***BEA**, une des 5 zéolithes les plus utilisées en industrie. Deux modes de synthèse différents ont été suivis : l'un utilisant un zincosilicate CIT-6 de même structure que la zéolithe Beta comme gabarit sacrificiel et l'autre consistant à dissoudre sélectivement le cœur de nanocristaux de zéolithe Beta. Les matériaux obtenus ont été caractérisés par différentes techniques, en particulier par des méthodes de microscopie électronique. L'étude de la diffusion du cyclohexane dans des cristaux creux par ZLC a permis de corrélérer la longueur de diffusion à la morphologie. Enfin, l'impact de la

morphologie sur l'activité catalytique a été étudié dans le craquage du cyclohexane et l'hydroisomérisation du n-C₁₆.

2. Synthèse de cristaux creux

La synthèse utilisant les cristaux sacrificiels de CIT-6 a permis d'obtenir des nanoboîtes de zéolithe Beta avec un rapport Si/Al d'environ 8 et des parois d'environ 150 nm d'épaisseur (Figure 2-a). L'incorporation de nanoparticules de platine dans la cavité du cristal ne se fait pas en une seule étape : les particules sont tout d'abord déposées sur la surface des cristaux de CIT-6 puis incorporées dans les cristaux creux lors de leur croissance. Malheureusement, ce mode desynthèse conduit à très faibles dispersions (Figure 2-b) et (dans quelques cas) également à la formation de particules à l'extérieur des cristaux qui peuvent nuire à la sélectivité du catalyseur (effet membrane de la paroi zéolithique). Afin de s'affranchir de la présence de particules extérieures, nous avons développé une méthode originale basée sur la dissolution du platine par un mélange bromure de tetraalkylammonium/Br₂ dans l'acétonitrile. La très grande dispersion et l'absence de nanoparticules sur la surface externe des cristaux creux a pu être confirmée par microscopie électronique en transmission (MET) et tomographie (Figure 2-b). Ces techniques ont montré que les particules sont en fait localisées à la fois sur la surface interne de la cavité et dans les murs de la zéolithe.

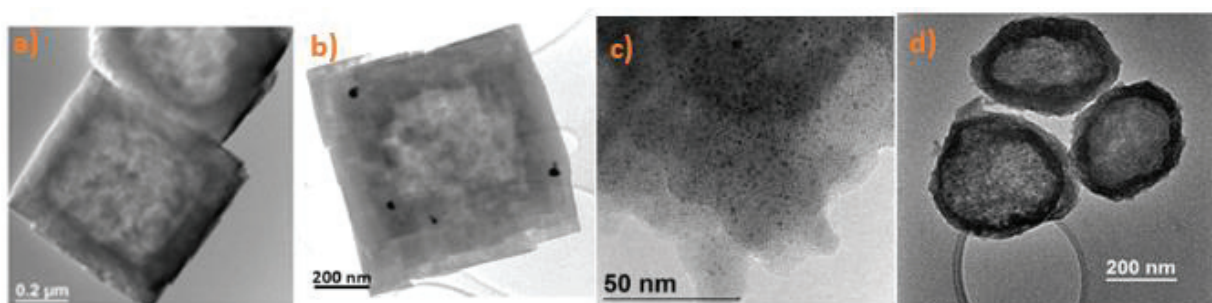


Figure 2 Cristaux creux de zéolithe Beta obtenus en utilisant des cristaux de CIT-6 comme gabarit sacrificiel (a), les mêmes cristaux avec des nanoparticules de Pt dans la cavité et dans les murs (b) les cristaux creux avec des nanoparticules de Pt dans les murs obtenus par traitement de bromure (c) et cristaux creux obtenus par dissolution sélective de nanocristaux en présence d'espèces aluminiques (d)

L'encapsulation des nanoparticules a également été vérifiée par l'hydrogénation de molécules aromatiques de taille croissante. Alors que le toluène, qui peut passer à travers la paroi zéolithique, est hydrogéné en méthylcyclohexane par les particules de platine, le mésitylène (ou 1,3,5-triméthylbenzène), plus volumineux, ne l'est pas.

L'autre voie de synthèse de nano-boîtes de *BEA qui consiste à dissoudre sélectivement le cœur de nanocristaux de zéolithe Beta se base sur les méthodes utilisées avec succès pour la ZSM-5. Cependant, si la ZSM-5 qui possède un gradient de composition permettant la dissolution préférentielle du cœur riche en silicium, ce n'est pas le cas de la zéolithe Beta. Les nanocristaux possèdent une composition plutôt homogène et leur structure s'effondre totalement lorsqu'ils sont soumis à un traitement alcalin à température modérée. Il est néanmoins possible d'obtenir des solides creux (Figure 2-d) en ajoutant des espèces aluminiques lors de la désilication. Ces espèces vont alors ré-aluminer la surface des cristaux et créer un gradient de composition artificiel similaire à celui de la ZSM-5. Les solides obtenus, même s'ils possèdent une morphologie intéressante (paroi homogène de quelques dizaines de nm d'épaisseur) ne sont malheureusement jamais purs et toujours contaminés par une phase amorphe. L'étude de nombreux paramètres de synthèse (température, alcalinité, agitation ...) a permis de mieux comprendre la formation ainsi que la nature des objets obtenus. En outre, l'ajout d'une molécule structurante comme le cation tétraéthylammonium dans la solution alcaline permet de minimiser la proportion de phase amorphe.

3. Impact de la morphologie sur la diffusion

Les cristaux creux obtenus à partir de CIT-6 ont été utilisés pour mesurer l'impact de la morphologie sur la diffusion du cyclohexane. Pour cela, les cristaux creux ont été comparés avec des cristaux pleins de zéolithe Beta, avec des propriétés structurales et des compositions assez similaires. Les temps caractéristique de diffusion $\tau = R^2/D_{\text{eff}}$ du cyclohexane ont été mesurés par la méthode dite ZLC (ou Zero Length Column) qui consiste à mesurer la désorption d'une molécule sonde en fonction du temps, où D_{eff} est le coefficient de diffusion apparent et R le rayon du cristal de zéolithe. La méthode a tout d'abord été optimisée sur des cristaux creux et pleins de silicalite-1 en utilisant le toluène comme molécule sonde. Ces cristaux possèdent en effet la même

composition et ne diffèrent entre eux que par leur longueur moyenne de diffusion. En admettant que D_{eff} est identique dans les cristaux pleins et creux (la structure de la zéolithe est identique dans les deux cas), alors le rapport des temps de diffusion τ_H/τ_B entre les cristaux creux et pleins permet de calculer le rapport R_H/R_B :

$$\frac{\tau_H}{\tau_B} = \frac{\frac{R_H^2}{D_{eff}}}{\frac{R_B^2}{D_{eff}}} = \left(\frac{R_H}{R_B}\right)^2$$

Pour les deux structures zéolithiques (**MFI** et ***BEA**), nous avons trouvé un bon accord entre le rapport R_H/R_B mesuré par ZLC et le rapport L_H/L_B estimé à partir des clichés de microscopie électronique. Ces études ont également permis de confirmer que le coefficient de diffusion apparent ne dépend que de la structure de la zéolithe, et peu de sa composition et de sa morphologie. Elles ont également montré que le temps caractéristique de diffusion τ est réduit d'environ 64-78% lorsque l'on passe d'une zéolithe Beta pleine à une zéolithe creuse (Figure 3).

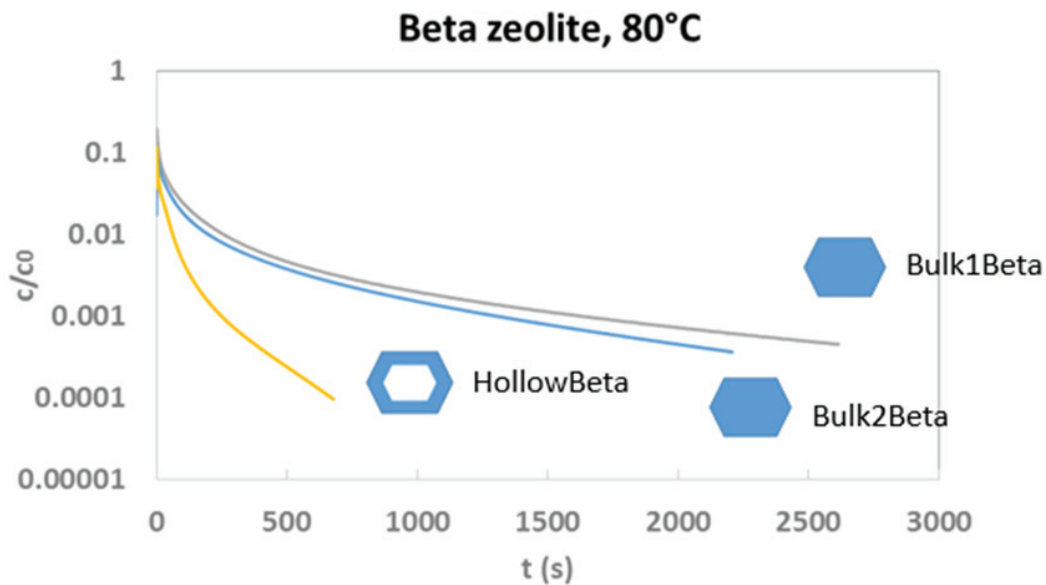


Figure 3 Courbe de désorption du cyclohexane pour des cristaux de zéolithe Beta conventionnels (Bulk1Beta et Bulk2Beta) et creux (HollowBeta)

4. Impact de la morphologie sur l'activité catalytique

L'impact de la morphologie a été évalué dans deux réactions catalytiques modèles : le craquage du cyclohexane et l'hydro-isomérisation du $n\text{-C}_{16}$. Pour ces deux réactions, la présence d'une cavité centrale dans les cristaux ne conduit pas à une augmentation de l'activité catalytique. La présence ou l'absence de limitation diffusionnelle est discutée en regard avec les résultats de la littérature, notamment avec ceux de la zéolithe Y. En se basant que l'estimation des constantes d'adsorption du $n\text{-C}_{16}$ à température de réaction, nous proposons l'absence de limitation diffusionnelle. Pour le craquage du cyclohexane, les modules du Thiele ont été estimés à partir des mesures catalytiques et les mesures de diffusion de ZLC. On propose également à l'absence de limitation diffusionnelle.

5. Conclusions

Lors de ce travail de thèse, des cristaux creux de zéolithe Beta ont pu être préparés selon deux voies très différentes. La voie de désilication sélective de nanocristaux a conduit à la morphologie attendue ; néanmoins les solides montrent une cristallinité et une porosité faibles, particulièrement après calcination. Ces travaux liminaires ont malgré tout permis de mieux comprendre les mécanismes de désilication sélective et de sélectionner les paramètres les plus pertinents. En revanche, l'approche qui utilise des cristaux de CIT-6 comme gabarit sacrificiel, a été totalement optimisée et maîtrisée. Les cristaux obtenus, riches en aluminium et qui possèdent des parois d'environ 150 nm d'épaisseur, ont pu être utilisés pour caractériser l'influence de la morphologie sur les propriétés catalytique et de diffusion.

L'étude ZLC a montré que le temps caractéristique de diffusion τ du cyclohexane à 80°C est réduit d'environ 64-78% pour une zéolithe Beta creuse par rapport à une zéolithe analogue pleine, en très bon accord avec les dimensions des cristaux.

Contrairement aux résultats en diffusion, l'activité catalytique pour les deux réactions modèles n'est pas augmentée pour les cristaux creux. Les estimations de modules de Thiele indiquent l'absence de limitation diffusionnelle.

En conclusion, ce travail exploratoire pose des bases pour l'élaboration de zéolites acides creuses ainsi que des éléments de discussions nouveaux pour établir la présence/absence de régime diffusionnel en catalyse acide.

Table of Contents

List of abbreviations and nomenclature	20
List of abbreviations	20
Nomenclature.....	21
Greek Symbols.....	23
List of Samples	24
Chapter III	24
“CIT-6 Dissolution – Recrystallization” approach	24
Encapsulation of Pt NP’s in hollow Beta single crystals	24
“Beta Zeolite Dissolution” approach	24
Chapter IV.....	25
Chapter V.....	25
n-C ₁₆ hydroisomerization reaction	25
Cyclohexane cracking reaction.....	25
Chapter I - Literature on Zeolites and their applications	27
1. Zeolites	27
1.1. History	27
1.2. Structure and active centers	28
1.3. Synthesis of zeolites	30
1.4. Synthesis mechanisms.....	34
1.5. Applications.....	36
1.6. Beta zeolite	40
2. Impact of crystal morphology on catalysis.....	43
2.1. Size selectivity vs diffusion limitations	43
2.2. Higher catalytic activity by the design of zeolite with appropriate morphology	44
3. Hollow zeolites	47
3.1. Hollow polycrystalline zeolites.....	49
3.2. Synthesis of hollow zeolite single crystals.....	51
4. Metal catalysts supported zeolite	59
4.1. Encapsulation of metal nanoparticles within zeolites.....	59
4.2. Encapsulation of NPs in in hollow zeolite single crystals	64

5.	Context and scope of the PhD thesis	65
6.	References.....	67
Chapter II – Experimental		77
1.	Material synthesis	77
1.1.	List of reactants	77
1.2.	“CIT-6 Dissolution-Recrystallization” approach	79
1.3.	Introduction of metal precursors into zeolite	80
1.4.	“Beta Zeolite Dissolution” approach	83
1.5.	Samples used for ZLC studies	85
1.6.	Samples used for n-C ₁₆ hydroisomerization reaction.....	86
2.	Characterization techniques.....	87
2.1.	Powder X-ray diffraction	87
2.2.	Electron microscopy	88
2.3.	Textural analysis	94
2.4.	Elementary analysis (ICP-OES).....	95
2.5.	Thermogravimetric analysis	96
2.6.	Solid-state nuclear magnetic resonance	96
2.7.	X-ray photoelectron spectroscopy	96
2.8.	Pyridine adsorption-desorption followed by IR spectroscopy	97
3.	Catalytic tests	97
3.1.	Hydrogenation catalytic tests.....	97
3.2.	Cyclohexane cracking	98
3.3.	n-C ₁₆ hydroisomerization.....	98
3.4.	Catalytic activities.....	99
4.	References.....	100
Chapter III – Synthesis of Hollow Beta Zeolite Single Crystals		103
1.	Introduction.....	103
2.	CIT-6 Dissolution-Recrystallization approach (Okubo et al.).....	105
2.1.	Assumptions on synthesis mechanisms from literature	105
2.2.	Optimization of the synthesis of CIT-6 crystals	106
2.3.	Optimization of the synthesis of hollow Beta single crystals	114
2.4.	Encapsulation of Pt NP’s in hollow Beta single crystals	132
2.5.	Summary on the “CIT-6 Dissolution-Recrystallization” approach.....	156

3.	Beta zeolite dissolution approach	158
3.1.	Description of the synthesis as indicated in the patent	159
3.2.	Assumptions on synthesis mechanisms	161
3.3.	Reproducing the patent/first results	162
3.4.	Effect of Al content.....	165
3.5.	Effect of pH.....	167
3.6.	Effect of TEA ⁺	169
3.7.	Summary on the “Beta Zeolite Dissolution” approach	172
4.	Conclusions.....	173
5.	References.....	175
Chapter V – Impact of the hollow morphology in catalysis.....		221
1.	Introduction.....	221
2.	Impact of diffusion in catalysis	221
3.	Hydroisomerization n-C ₁₆ – Bifunctional catalysis	224
3.1.	Synthesis and characterization of the zeolite phase	226
3.2.	Catalytic results	228
3.3.	Discussion	231
4.	Cyclohexane cracking – Acid catalysis.....	239
4.1.	Samples synthesis and characterization.....	239
4.2.	Catalytic results	240
4.3.	Effectiveness factor	241
5.	Conclusions.....	243
6.	References.....	244
Conclusions and Perspectives		247
Publications and Patents.....		251
Annexes - Chapter III		253
III.1.	“CIT-6 Dissolution-Recrystallization” approach.....	253
III.1.1.	CIT-6 crystals -effect of the “quality” of the reactant in CIT-6 synthesis	253
III.1.2.	CIT-6 crystals – effect of crystallization and temperature	255
III.1.3.	CIT-6 crystals - TGA analysis of as-made CIT-6 crystals.....	257
III.1.4.	Hollow Beta crystals - mercury intrusion over hollow Beta	257
III.1.5.	Hollow Beta crystals – effect of temperature and crystallization time.....	260

III.1.6. Hollow Beta crystals - XRD of samples TEAHollow β and ++TEAHollow β	262
III.1.7. XRD patterns.....	263
III.2. Encapsulation of Pt NP's in hollow Beta single crystals	263
III.2.1. Optimization of NaBH ₄ reduction over Pt/CIT-6	264
III.2.2. Pathway E – characterizations and catalytic data treatment.....	266
III.3. “Beta Zeolite Dissolution” approach	268
III.3.1. N ₂ isotherms of Hollow β	269
III.3.2. ²⁷ Al NMR of as-made and calcined parent Beta zeolite	270
III.3.3. Effect of TEA ⁺ - Increasing “crystallization time” – step3).....	271
Annexes – Chapter IV	272
IV.3. ZLC unit - sensitivity analysis.....	272
• Effect of the amount of sample.....	272
• Effect of granulometry	273
• Effect of sample preparation.....	274
• Influence of t ₀	275
• Baselining	276
• Effect of zeolite activation.....	278
Annexes – Chapter V	278
V.1. Characterization of the samples used for n-C ₁₆ hydroisomerization reaction.....	279
V.2. Pyridine adsorption	281
V.3. Cyclohexane cracking reaction.....	282
V.3.1. Determination of K _H at 600 °C.....	283
V.3.2. Determination of D _{eff} at 600 °C.....	283
V.3.3. Observed reaction rate	284
V.3.4. Observed reaction rate	285
References.....	286

List of abbreviations and nomenclature

List of abbreviations

BSE - backscattered electrons

CBU – composite building unit

EB - ethylbenzene

EDX – energy dispersive X-ray

EFAL – extra framework Al

ETEM – environmental transmission electron microscope

FCC – fluid catalytic cracking

FID - flame ionizer detector

I.E. – ionic exchange

IWI - incipient wetness impregnation

Mes – mesitylene

MIP – mercury intrusion porosimetry

n-C₁₆ – n-hexadecane

NMR – Nuclear magnetic resonance

NPs – nanoparticles

OSDA – Organic structure directing agent

PBU – primary building unit

Ppm – parts per million

XRD – X-ray diffraction

SDA – structure directing agent

SBU – secondary building unit

SE – secondary electrons
SEM – scanning electron microscope
 S_{ext} – external surface
TAA – tetraalkylammonium
TAP – temporal analysis of products
TEA⁺ - tetraethylammonium
TEM – transmission electron microscope
TGA - thermogravimetric analysis
Tol - toluene
TOF - Turnover Frequency (s^{-1})
TPA⁺ - tetrapropylammonium
 V_{mesp} – mesoporous volume ($\text{cm}^3/\text{g}_{\text{zeol}}$)
 V_{micro} – microporous volume ($\text{cm}^3/\text{g}_{\text{zeol}}$)
WHSV - weight hourly space velocity ($\text{g}_{\text{reactant}}/\text{g}_{\text{catalyst}}/\text{time}$)
XPS – X-ray photoelectron spectroscopy
ZLC – zero length column

Nomenclature

c – concentration of a given sorbate or reactant
 C_A – when used for Thiele modulus equation, it is attributed to the concentration of reactant adsorbed at the surface site ($\text{mol}/\text{m}^3_{\text{zeol}}$)
 c_0 – initial concentration of a given sorbate or reactant in the gas phase, for $t=0$
 D – intracrystalline diffusion coefficient or diffusivity (m^2/s)
 D_{eff} – effective or apparent intracrystalline diffusion coefficient, of a whole crystal particle (m^2/s)

D_{eff}/R^2 – parameter extracted from ZLC model, corresponding to the inverse of the characteristic transport time (s^{-1})

D_{metal} – metal dispersion i.e. ratio of surface atoms and the total atoms part of a metal nanoparticle

D_{meso} – diffusion coefficient associated with transport in mesoporous media (m^2/s)

D_{micro} – diffusion coefficient associated with transport in microporous media (m^2/s)

D_0 - pre-exponential factor of the Arrhenius form

E_d – diffusion energy, i.e. the energy required by a molecule to diffuse through the crystal (kJ/mol)

F – it is the inlet molecular flow of a given molecule or reactant (mol/s)

I - FID signal (dimensionless)

k – intrinsic constant rate, i.e. reaction without diffusion limitations (s^{-1})

K_H – Henry's constant (dimensionless)

L – Mean diffusion length or diffusional path length (m)

L_B – Mean diffusion length or diffusional path length for bulk zeolites (m)

L_H – Mean diffusion length or diffusional path length for hollow zeolites (m)

L_{ZLC} – ZLC parameter

m_{zeol} - the mass of zeolite (g)

m_{metal} - the mass of metal (g)

N_A = Flux of specie A ($\text{ml. s}^{-1}.\text{cm}^{-2}$)

N_s - the number of Bronsted sites per g of zeolite ($\text{mol/g}_{\text{zeol}}$)

q_0 - initial adsorbed phase concentration

R - Radius of the particle or radius of the equivalent volume sphere (m)

R_{gas} - the perfect gas constant

r_{obs} - observed reaction rate ($\text{mol/g}_{\text{zeol}}/\text{s}$)

V_g - is the fluid phase volume

V_s - is the adsorbent volume

X - the conversion fraction of a reactant

Greek Symbols

β_n – ZLC parameter

$-\Delta H$ – adsorption enthalpy (J/mol)

ΔS – adsorption entropy (J/mol/K)

η – effectiveness factor (dimensionless)

η' – modified effectiveness factor (dimensionless)

ρ – zeolite density ($\text{g}/\text{m}_{\text{zeol}}^3$)

τ – characteristic transport time or diffusion time through the crystal, obtained by ZLC and defined as R^2/D_{eff} (s)

ϕ – Thiele modulus (dimensionless)

ϕ_B – Thiele modulus for bulk zeolite (dimensionless)

ϕ_H – Thiele modulus for bulk zeolite (dimensionless)

ϕ' – modified Thiele modulus (dimensionless)

List of Samples

Herein we present the list of sample's names used in each chapter of this thesis.

Chapter III

“CIT-6 Dissolution – Recrystallization” approach

- 10%
- 25%
- TEAHollow β
- ++TEAHollow β

Encapsulation of Pt NP's in hollow Beta single crystals

- Pt@Hollow β
- Pt/CIT-6
- Pt/SiO₂
- TMA-Pt@Beta
- TEA-Pt@Beta
- TPA-Pt@Beta
- TBA-Pt@Beta

“Beta Zeolite Dissolution” approach

- Hollow β
- 25%Al- Hollow β
- 0%Al- Hollow β
- 13Hollow β
- 13.5Hollow β
- TEAHollow β

Chapter IV

- HollowSil1
- BulkSil1
- HollowBeta
- Bulk1Beta
- Bulk2Beta

Chapter V

n-C₁₆ hydroisomerization reaction

- 20Hollow
- 17Bulk
- 22Bulk
- REF

Cyclohexane cracking reaction

- HollowBeta'
- Bulk1Beta'

Chapter I - Literature on Zeolites and their applications

Zeolite crystals have been a matter of great interest in the scientific community due to their properties and major applications in industry. This chapter starts by a brief introduction to zeolite science including their synthesis mechanisms, main structural properties and major applications. The chapter continues with the different routes to synthesize particular zeolite morphologies. Different morphologies of zeolites are presented and discussed in the frame of accelerating the transport of substrates. Finally, ***hollow zeolites single crystals*** are presented as one of the particular morphologies recently developed. The synthesis of Pt nanoparticles encapsulated in zeolites is presented.

1. Zeolites

1.1. History

In 1756 a Swedish mineralogist A.F. Cronstedt found a mineral that released steam upon rapid heating, as if it was “boiling”. Cronstedt named this mineral zeolite, a combination of two Greek words *zeo* and *lithos*: “stone that boils”.¹ This boiling phenomenon was due to the desorption of water adsorbed by the zeolite pores.² For the next 200 years after Cronstedt recognized the first zeolite crystal, zeolites properties were not exploited to any particular application. Natural zeolite crystals could be found in Natural Museum mineral collections, but that was all. It is well known nowadays that zeolite crystals have high adsorption capacities due to their microporous crystalline structure. Later, in the XXth century, these properties were found useful in several industrial applications, which led to a big development of zeolite science.

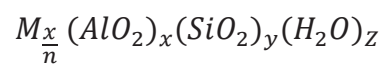
Zeolites can be found in nature, however, with the advent of synthetic zeolites these minerals started being used in several applications, such as adsorption catalysis and ionic exchange. Indeed, so **far already 237 framework types have been registered**,³ only around 40 of them can be found in nature.²

1.2. Structure and active centers

Zeolites are aluminosilicate crystals with a 3-dimensional structure built up from corner-sharing TO_4 tetrahedra (SiO_4 and AlO_4^- units), connected by oxygen atoms. This 3D construction results in microporous crystalline structures, with pores and cavities, whose dimension ranges from 0.3 nm to 1 nm (molecular sized pores).

When aluminum atom is tetrahedrally coordinated to oxygen atoms, the + 3 valence of aluminum results in a net formal charge of -1 , and the negatively charged framework (one charge per framework Al^{3+}) requires an extra-framework cation, for example Na^+ or K^+ , but also quaternary ammonium ions and protons.²

The general chemical formula of a zeolite unit cell is given as:²



Where:

n – is the charge of the cation

x – number of AlO_4^- tetrahedra per unit cell

y – number of SiO_4 tetrahedra per unit cell

M – Cation

Z – number of H_2O molecules adsorbed which depends on the zeolite hydrophobicity

The ratio of SiO_4 to AlO_4^- tetrahedra, (y/x) can be variable. While purely SiO_2 constructions can be synthesized, zeolites consisting of only AlO_4^- tetrahedra do not exist. The maximum amount of Al corresponds to $Si/Al \geq 1$, principle referred to as Loewenstein's rule.⁴ Besides Al and Si, other elements can be placed in tetrahedral position, such as divalent cations Be^{2+} and Zn^{2+} , other trivalent cations such as B^{3+} , Ga^{3+} , and Fe^{3+} , and tetravalent cations such as Ti^{4+} and Ge^{4+} .⁵ In some cases, the use of high concentration of certain elements gave rise to new structures, due to the different ionic radii in comparison to Al^{3+} or Si^{4+} .⁵

As mentioned before, so far already 237 framework topologies have been registered.³ Each observed framework topology is given a three letter code (e.g., **FAU** for faujasite, ***BEA** for Beta etc.). A star (*) symbol precedes the zeolite frameworks of partially disordered structures, which is the case for ***BEA** (this subject will be discussed later in this chapter). Each framework topology has a particular geometry and arrangement, and Al content can be variable, hence a zeolite with a certain framework type can have different Si/Al.⁵

Pore size can be quite variable depending on the framework topology. Generally, small pore zeolites have windows defined by 8 tetrahedra (8-membered rings or 8-MR), and pore sizes of approximately 4Å, medium pore zeolite by 10 tetrahedra (10-MR, pore sizes between 5 and 5.5Å) and large pore zeolites (12-MR, pore sizes between 7 and 8Å (which is the case of

Beta zeolite, for example)). More recently, extra-large-pore zeolites have been synthesized, having rings of 14 or 18 T-atoms for example.⁵

A given zeolite structure can be seen as a repetitive construction of different building units, all based on tetrahedral SiO_4 and AlO_4^- units. The SiO_4 and AlO_4^- tetrahedra are categorized into primary building units (**PBU**), which combine together by sharing oxygens to form a spatial arrangement of simple geometric forms (**SBU** – secondary building unit). 23 different types of SBUs are known to exist so far.⁶ These can be single rings, double rings, polyhedra and some more complex arrangements. SBUs are non-chiral and can contain up to 16 T-atoms. Eventually, SBU's are assembled, either on their own or in combination with others, to give composite building unit (**CBU**). Different combinations of CBU's with CBU's or SBU's are repeated periodically leading to different zeolite structures, as represented in Figure 1.⁵

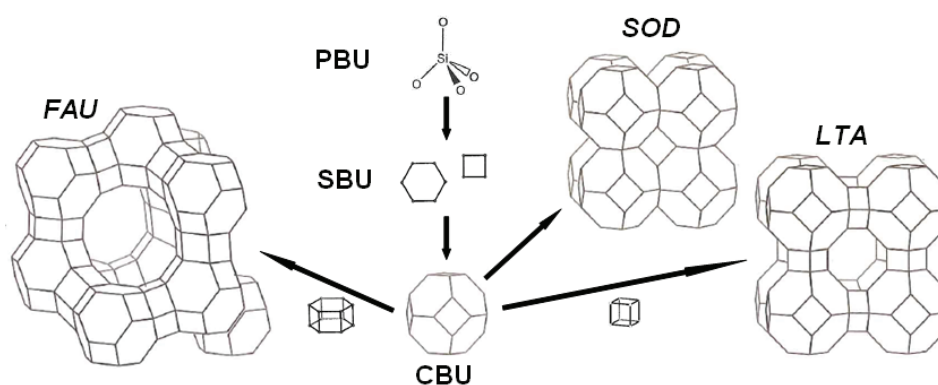


Figure 1 – Representation of primary building units PBU, two types of secondary building units SBU and a CBU that comes from the arrangement of the two SBU. Combining the CBU with itself gives the sodalite (SOD) structure while combination with a double 4-ring or a double 6-rings gives the **LTA** and **FAU** structures, respectively.. Reproduced from Dhainaut.⁷

1.2.1. Zeolites acidity

For each Al framework, an extra-framework cation is required to balance the negative charge. If this cation is a proton, the latter works as a **Brønsted acid site**, Figure 2. Indeed, zeolites can act like acid solids, and their acid properties are widely used in **acid catalysis**, which will be discussed later in this chapter. Therefore, the number of Brønsted sites is directly related to the number of Al in the zeolite framework.

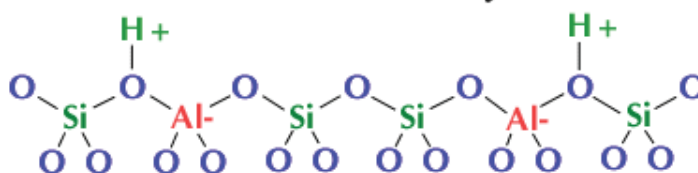


Figure 2 – Representation of Brønsted acid sites in zeolites

The acid strength of a Brønsted site depends of how weak is the bond between O and H, hence, this will depend on the environment around the Brønsted site. The angle of the T-O-T bond (T = Si or Al) has a great impact in the acid strength: the bigger it is, the stronger is the acid center, which explains why different zeolite framework types can have very different acid strengths.² The proximity to other Brønsted sites also decreases the acid strength. When the Brønsted site is isolated, the Si atom is more electronegative, which increases the bond between O and Si, and weakens the O-H bond. The presence of Lewis sites also has an impact on the strength of the Brønsted sites.² Brønsted sites can be generated by ionic exchange, generally by exchange with ammonium cations followed by calcination to decompose the ammonium cation, leaving a proton at its place.⁸

Zeolites can also have Lewis sites. These can be generated by dehydration of the zeolite framework and by dislodging Al atoms from the framework, when due to high temperatures or mild steaming. The nature of Lewis sites is generally related either to extra-framework Al (EFAL), and/or aluminic species partly linked to the framework. EFAL can occur in several oxide or hydroxide forms: $\text{Al}(\text{OH})_2^+$, $\text{Al}(\text{OH})_2^+$, AlO^+ , $[\text{Al}_2\text{O}_2\text{OH}]^+$, $(\text{Al}_2\text{O})^{4+}$, AlOOH or $\text{Al}(\text{OH})_3$.⁸ The presence of Lewis sites increases the acid strength and the catalytic activity of zeolites, because of the interaction of Lewis sites with Brønsted sites.^{2,8} Lewis sites can also act as acid catalysts, depending on the reaction.^{9,10}

1.3. Synthesis of zeolites

Zeolites are generally prepared by **hydrothermal synthesis (see Figure 3)**, many of them in basic media and in the presence of an organic template. Practically speaking, a classical zeolite synthesis could be described as follows:¹¹

- 1) An amorphous mixture is prepared, which is formed basically by a silica, an alumina and a cation source, usually in alkaline medium. This reaction mixture is often referred to as *primary amorphous phase*, and its nature can range from gel-like to colloidal in the so-called clear solution synthesis.
- 2) In some cases, the reaction mixture has an “aging” period under stirring or not (hours to few days)

- 3) The reaction mixture is introduced in a sealed autoclave that is heated (generally above 100 °C) for a certain time.
- 4) During heating, a “secondary amorphous phase” is created, being at equilibrium with a solution phase. It is called secondary amorphous phase because unlike the original amorphous mixture, this already has some small range structural order, but still amorphous though.
- 5) For some time no crystal is formed, which is denoted by the induction time.
- 6) After the induction time, where some nuclei are formed (more mechanistic details below), a crystalline zeolite product can be detected: crystallization starts, and the amorphous phase is converted into a crystalline phase.
- 7) The zeolite can be recovered from the gel by filtration, washing and drying

During hydrothermal reactions and due to the presence of a mineralizing agent, Si-O-Al bonds are created.

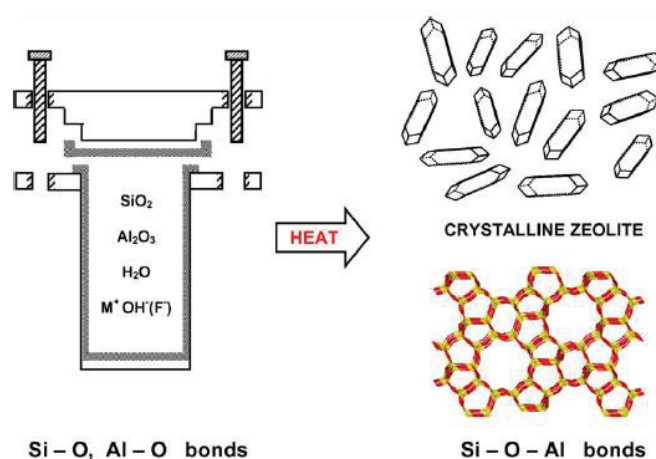


Figure 3 - Hydrothermal zeolite synthesis. The starting materials (Si-O and Al-O bonds) are converted by an aqueous mineralizing medium (OH⁻ and/or F⁻) into the crystalline product (Si-O-Al bonds) whose microporosity is defined by the crystal structure. Reproduced from¹¹

In more details, the synthesis gel is generally composed of:^{5,11,12}

- A solvent. Water is a common example, because of its ability to solubilize the components needed for zeolite synthesis;
- Aluminum and silicon sources;
- A mineralizing agent used to dissolve the different species in the synthesis gel. Typically these are OH⁻ or F⁻;
- Cations to neutralize the negative charge of the framework;
- In some cases, a structure directing agent: a soluble organic species (very commonly a quaternary ammonium ion) that assists the formation of the framework and directs the crystallization towards a given structure.

The crystallization parameters (time, temperature, mixing) have a big impact on the chemical/physical characteristics of the final product. But also, the synthesis can be sensitive to how the gel is prepared, namely the reagents type, the order of addition of each of the reagent, the mixing or lack of mixing, and the composition.¹²

As mentioned before, in the 80's, zeolites were conventionally prepared by hydrothermal synthesis, in basic media and in the presence of an organic template. However, different synthesis strategies have led to the discovery of new zeolite framework types, and zeolites with specific chemical and physical properties.

- **The structure directing agents (SDA)**

The so-called structure directing agent (SDA), or more commonly organic template plays an important role during nucleation, and directs the crystallization towards a given structure. Note that very often, the same organic molecule can be used to generate different products depending on the synthesis conditions.¹¹ The way that SDAs act during nucleation can be different depending on the molecule and the zeolite type. Davis et Lobo¹³ classify templates into three different types: i) "true" templates, when the framework adopts the geometry of the template molecule, (ii) structure-directing agents, when a specific structure is synthesized via a single organic species and (iii) space-filling species, in the case of hydrophobic high silica species. Before the use of SDA in zeolite synthesis, synthetic zeolites were made exclusively using inorganic reactants, and the variety of synthetic zeolites was limited to **CHA** (chabazite), **FAU** (Linde X) and **LTA** (Linde A). The use of organic SDA enabled the synthesis of several new zeolite structures and compositions, and notably high silica zeolites. Firstly, in 1961, Professor Barrer managed to synthesize high silica zeolite A ($\text{Si/Al} = 1.2$), a high silica version of Linde A.⁵ Most importantly, in 1967 Mobil Oil Company had created a new high silica zeolite structure, zeolite Beta ($5 < \text{Si/Al} < 100$), and in 1972, ZSM-5. These were the first synthetic zeolites with $\text{Si/Al} > 5$. Hence, this type of zeolites was more hydrophobic and with enhanced hydrocarbon adsorption capacities, which was particularly interesting for petroleum companies.¹⁴ Over the next two decades, a large number of new zeolite structures was synthesized thanks to the use of SDA.^{5,11}

- **Non-aqueous solvents**

Some other solvents have been used to synthesize zeolites, in some cases creating new zeolite structures. Bibby and Dale¹⁵ were the first to report a zeolite synthesis using a non-aqueous solvent, namely ethylene glycol. They were able to synthesize for the first time silica-sodalite. Using pyridine/HF and trimethylamine solvent systems, Kuperman *et al.*¹⁶ made "giant" crystals of **MTN**, **FER** and **MFI**. Later, ethylene glycol was found to be a useful solvent for the synthesis of zeotypes, such as AIPO (aluminophosphates) and Gallium phosphate materials.⁵

- **F⁻ as mineralizing agent**

Flanigen and Patton were the first to use fluoride in a zeolite synthesis, and they were able to prepare silicalite-1 (pure silica **MFI**).¹⁷ A number of other zeolites were synthesized using fluoride, such as Al,Si-**MFI** and Al,Si-***BEA**.^{18,19} Indeed, F⁻ is an effective mineralizing agent for the synthesis of pure silica zeolites, with low defect densities, and it even enabled the synthesis of new materials, such as the gallium phosphate Cloverite (**CLO**).²⁰ F⁻ catalyzes the formation of Si-O-Si bonds, and allows zeolite crystallization at neutral or mild acidic conditions. Fluoride ions have been proposed to work as a kind of inorganic SDA as it has been found in as made zeolites, namely within small rings and cages. It is thought that F⁻ strongly interacts with the zeolite framework, and it stabilizes these rings and cages.^{5,21} Upon calcination, F⁻ and the organic template are removed.

- **The use of seed crystals**

The addition of seed crystals into the synthesis gel is a very common practice that 1) reduces synthesis time regarding to a standard zeolite synthesis without seeds, 2) favors the synthesis of a certain type of zeolite (the zeolite correspondent to the seeds) and 3) enables controlling the crystal size distribution.¹¹ In a seed-free zeolite synthesis, crystal growth requires previous nucleation. During nucleation, time is needed for the TO₄ primary building units to organize themselves into clusters big enough to create a surface area on which the crystal can grow. In contrast, when seed crystals are added, nucleation step is not necessary, because the seeds surface is already available. The crystal grows over the crystal seed surface and crystallization will be sensitive to the stability of the seeds in the reaction media and to the available surface area of crystal seeds. If seed crystals are not stable in the reaction media, they will probably get dissolved before any crystal growth. Also if the quantity of crystal seeds is too small, there is not enough surface area to cause any difference in the reaction media for example.¹¹

- **Dry Gel Conversion Syntheses**

It consists of a crystallization process alternative to “classical” hydrothermal synthesis, in which the reaction gel is “dry” and it does not require an aqueous medium.²² This crystallization method can be performed by two different approaches: vapor-phase transport and steam-assisted conversion. In the vapor-phase transport approach, a dry aluminosilicate gel is crystallized by a vapor steam that includes a volatile structure-directing agent. It has the advantage of requiring smaller amounts of SDA than a classical hydrothermal synthesis; however, it requires a volatile SDA. For the steam-assisted conversion, the dry gel includes the SDA agent, which allows the use non-volatile SDA. This synthesis method has been widely applied for several zeolites, including Beta zeolite.

1.4. Synthesis mechanisms

In a classical hydrothermal synthesis, the main outline is that zeolite synthesis comes from the transformation of an amorphous, aqueous aluminosilicate gel under the action of heat into a crystalline zeolite product. Since the beginning of synthetic zeolite synthesis, several zeolite synthesis mechanisms have been proposed. There are several theories that try to explain this synthesis mechanism, these are described below:¹¹

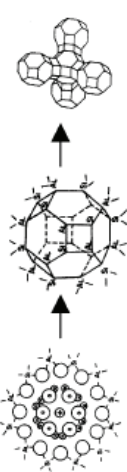
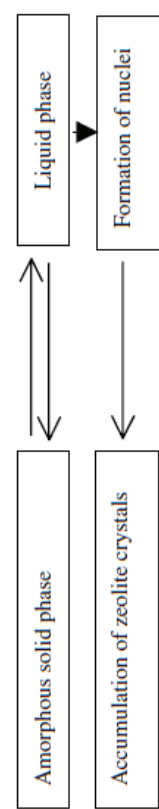
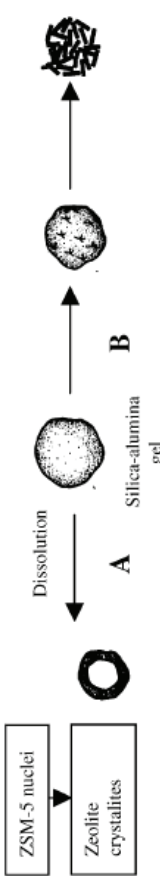
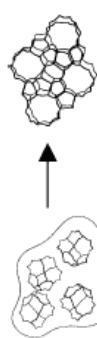
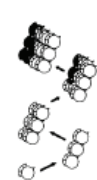
Barrer *et al.*²³ gave the first insights about zeolite synthesis mechanism, in 1959.¹¹ According to Barrer, zeolite synthesis and growth followed a solution mediated process, and this would probably result from the assembly of crystalline building units of several tetrahedra (such as rings of 3-6 tetrahedra, soluble 4 ring etc), rather than the systematic addition of single TO_4 units: “in the elaborate porous crystalline structures of zeolites, for instance, it would seem difficult for the lattice to persist in its very open pattern when rapidly adding such small units (TO_4) (...) “a plausible process would be the accretion in simple coordination of polygonal or polyhedral anions by condensation polymerization”.

In the 60's, Breck and Flanigen propose that crystal growth occurs mainly in the solid phase, suggesting the following phases: initial depolymerization of the gel structure by hydroxide ions, followed by the rearrangement of the TO_4 present in the gel assisted by the presence of the hydrated cation species. TO_4 would form polyhedral (24-hedra) units around hydrated sodium ions, that would link to each other, forming an ordered crystal structure.¹¹ Essentially, crystal growth would proceed by an OH^- catalyzed polymerization and depolymerization process, in the solid phase.

Zhdanov and Kerr proposed a solution oriented approach.^{11,24-26} The amorphous gel is in equilibrium with the liquid phase, and due to heat and temperature, amorphous gel would release species into solution, that would form nuclei (similarly to the building blocks proposed before) which would eventually grow to form crystals. In the 70's, the idea that crystal growth occurred on solution phase became popular, even though different studies would obtain different conclusions. The introduction of organic templates brought up different concepts of how these molecules would intervene in zeolites synthesis (not presented here).¹¹

Some of the main aqueous zeolite synthesis mechanisms available in the literature are summarized in Table 1.

Table 1 – Summary of the principal zeolite synthesis mechanisms proposed in the literature. Reproduced from Cundy and Cox.¹¹

Author(s)	Principal system studied	Main features of mechanism	Schematic summary
Barrer	Various low-silica phases	Condensation polymerisation of polygonal and polyhedral anions	
Flanigen and Breck	Na-A, Na-X	Linkage of polyhedra (formed by M ⁺ -assisted arrangement of anions): crystal growth mainly in the solid phase	
Kerr	Na-A	Crystal growth from solution species	Amorphous solid $\xrightleftharpoons{\text{fast}}$ soluble species(S) $\xrightarrow{\text{slow}}$ zeolite A 
Zhdanov	Na-A, Na-X	Solid \leftrightarrow liquid solubility equilibrium, nuclei from condensation reactions, crystal growth from solution	Amorphous solid phase \leftrightarrow Accumulation of zeolite crystals \leftrightarrow Liquid phase Formation of nuclei 
Derouane, Detremmerie, Giabelica and Blom	Na, TPA-ZSM-5	Synthesis "A": liquid phase ion transportation. Synthesis "B": solid hydrogel phase transformation	ZSM-5 nuclei \rightarrow Zeolite crystallites Dissolution \rightarrow Silica-alumina gel \rightarrow B A 
Chang and Bell	Na, TPA-Si-ZSM-5	Embryonic clathrate TPA-silicate units, ordered into nuclei through OH ⁻ -mediated Si-O-Si cleavage/recombination	
Burkett and Davis	TPA-Si-ZSM-5	Pre-organised inorganic-organic composites, nucleation through aggregation, crystal growth layer-by-layer	
Leuven Group	TPA-Si-ZSM-5	Oligomers \rightarrow precursor "trimer" (33 Si) \rightarrow $\times 12 \rightarrow$ "nanoslabs", growth by aggregation	

Nowadays it is commonly accepted that the most probable mechanistic pathways for zeolite formation include induction period, nucleation and crystal growth.

Nucleation is a very complex process where the initially amorphous structure is transformed into a crystalline framework. Starting from an inhomogeneous, non-equilibrated amorphous phase, atoms and molecules arrange themselves, and a “secondary amorphous phase” is formed, where structural order has increased, even though of very short range. It is accepted that this progressive ordering relies on a reversible mechanism of breaking and remaking chemical bonds, which is catalyzed by hydroxyl ions. Eventually, some “ordered areas” end up forming **nuclei**, molecular **clusters** large enough as to have the ability to grow irreversibly to a macroscopically larger size. The making and breaking of the T-O-T bonds is reversible.⁵

1.5. Applications

Few years after the first synthetic zeolites were developed (X,Y and A zeolites), they were found useful in three large areas of applications:²

- Adsorption: firstly for gas dryer and later for separation of n/iso-butane with zeolite A (1959)
- Catalysis, namely X and Y for isomerization (1959) and cracking (1962)
- Ionic exchange: use of zeolite A in detergent industry (1974)

The main consumption of natural and synthetic zeolites in 2004 are described in Table 2.²⁷ Natural zeolites are the most used, mainly for commodities of low value/large scale applications. Regarding synthetic zeolites, these represent a market value of 1.8 billion \$ in 2004. These are mostly applied to detergent industry. Catalysis industry constitutes 14.2% on a volume basis (95% used for de FCC process), but 27% on a monetized value basis.

Meanwhile, there is an increasing interest in using zeolites in other market niches such as process intensification, green chemistry, hybrid materials, medicine, animal food, optical and electrical based applications, multifunctional fabrics and nanotechnology.⁵

Table 2 – Zeolite market 2004.²⁷

Data from 2004	Consumption (kta)	Share % Volume	Share Value	Growth %
Synthetic zeolites consumption				
Detergent builder	1325	78.2	56	11.5
Catalysts	241	14.2	27	30.9
Adsorbents/desiccants	126	7.4	17	15.6
Natural Zeolites Consumption	>2500			-19.3

1.5.1. Ionic exchange

As mentioned before, the aluminosilicate framework of zeolites needs a cation to compensate the negative charge created by each framework Al atom. The weakly bonded extra-framework cations can be exchanged by washing with a solution containing another cation in excess. This ion exchange property has led to several applications, mainly in detergent industry. Indeed, the dominant commercial application of zeolites is detergent industry, where zeolites managed to replace sodium phosphates that were water pollutants.^{28,29} For example, Linde type A (Na-LTA) zeolite has been used to “capture” (exchange) calcium and magnesium ions present in water, working as water softeners but also avoiding soap powder deactivation.²⁹

Another large scale ion-exchange process involves the extraction of NH_4^+ from municipal and agricultural waste streams, using clinoptilolite (natural zeolite) for example.³⁰

Zeolites have been used for heavy metal removal in environmental cleaning processes; as an example, LTA is applied in water treatment to remove heavy metal ions.^{29,31} Zeolites have also been applied for the removal of radioactive fission products during the treatment of radioactive waste water²⁹ Clinoptilolite and mordenite containing rocks have shown to be particularly selective for cesium, barium and strontium elements, which is particularly interesting for washing radioactive waste solutions.³² The dispersion of metallic catalyst on zeolite supports can be also obtained by ionic exchange with a metal cation. This procedure has been applied for the studies presented in this thesis and it will be described in the following chapters.

1.5.2. Adsorption and separation

Nowadays, zeolites are used as adsorbents in several domains of applications. The capacity of a zeolite to adsorb a given sorbent depends on the physical/chemical characteristics of the zeolite, such as Si/Al ratio, the cation type, the presence of defects in the framework etc. When changing these properties, this will change the hydrophilic/hydrophobic properties of the zeolite.³¹ For example, dealumination post-treatments can increase the degree of hydrophobicity of a zeolite.³³ Therefore, zeolite affinity with a certain molecule can be tuned by changing its hydrophilic/hydrophobic character. Zeolites have been applied for the selective adsorption of organic pollutants for water treatment, namely dyes and humic substances (humic acid, fulvic acid or humin, that can be responsible for producing toxic chemicals).³¹ Zeolites have also been applied for air-purification, namely separation of CO₂ and H₂O,^{29,34} separation of O₂ and N₂, or even separation of azeotropic solutions in chemical industries and organics with close boiling points.²⁹

1.5.3. Catalysis

Nowadays approximately 90 % of chemical processes use heterogeneous catalysis. This represents a market estimated to 15-20 billion US\$, where half is directed to chemical industry, and the rest divided between environment and refinery applications. Zeolites have acid properties that makes them an extremely important class of catalysts in refinery applications². Fluid Catalytic Cracking (FCC) process is a good example of zeolite's success in industry. FCC is a process to produce gasoline fractions. The catalyst previously used (amorphous silica-alumina) deactivated very easily due to coke formation, and it needed to be regenerated frequently. The use of zeolites for the FCC process not only increased activity (zeolites are much more active than silica-alumina catalysts), but also increased selectivity towards gasoline fractions, and decreased coke formation.^{2,27} In 2005 FCC constituted more than **95% of the zeolite catalyst consumption**.²⁸

Besides FCC, several other chemical transformations have adopted zeolite based catalysts, in refining, petrochemical and base chemicals, Table 3.²⁷ Zeolites have been used for several other reactions and processes, such as hydroxylation (eg. phenol), alkylation (eg. ethylbenzene, cumene), oximation (eg. cyclohexanone oxime) and epoxidation (eg. propylene oxide). Another important zeolite based process is the deNO_x process, such as selective catalytic reduction (SCR). With the up-coming regulations on automotive NO_x emissions maximum values, there will be a need to continuously develop and optimize this process.²⁸

Table 3 - Types of commercial processes using zeolite-based catalysts. Reproduced from Vermeiren and Gilson.²⁷

Zeolite structure code	FAU	LTL	MOR	BEA	MWW	MCM-49	MTW	MFI	FER	AEL	RHO	EUO	Area
Zeolite name	Y, USY	L	Mordenite	Beta	MCM-22, MCM-49	ZSM-12	ZSM-12	ZSM-5, TS-1	Ferrierte	SAPO-11	Rho	EUO EU-1	
<i>Process</i>													
Naphtha isomerisation			B										Refining
Iso-dewaxing								B		B			
Dewaxing								M					
Hydro-cracking	B												
Hydro-dearomatization	B												
FCC	M							M					
Olefin oligomerisation					M								
Olefin isomerisation									M				
<i>Petrochemicals</i>													
Ethylbenzene					M								
Cumene	M		M	M	M								
C ₂ , C ₃ -transalkylation	M		M	M	M								
<i>p</i> -Ethyltoluene							M						
<i>p</i> -t-Butylethylbenzene													
Xylene isomerisation								M/B					
Ethylbenzene isomerisation			B									B	
Toluene disproportionation			B										
C ₉ + transalkylation			B										
Naphtha aromatisation		B											
LPG or olefin aromatisation												B	
Amination				M							M		Chemicals
Hydration													
Chlorination/isomerisation		M											
Beckmann rearrangement													
Oxidation													
Acylation	M			M									

M stands for monofunctional catalyst and B stands for bifunctional catalysts

1.6. Beta zeolite

1.6.1. History and structure

The synthesis of Beta zeolite appeared with the introduction of organic templates in zeolite synthesis, when in 1967, Wadlinger, Kerr and Rosinski reported for the first time the synthesis of a high silica zeolite, zeolite Beta ($5 < \text{Si}/\text{Al} < 100$).³⁵ It was the first zeolite synthesis using an organic template (TEA^+), and the first synthetic zeolite with $\text{Si}/\text{Al} > 5$.¹¹ Indeed, Beta is a silica rich zeolite, and nowadays it can be prepared in a broad range of compositions $5 < \text{Si}/\text{Al} < \infty$.^{36,37} The typical morphologies of zeolite Beta crystals are generally truncated bipyramids³⁶ or aggregates of more or less oriented nano crystallites, depending on the synthesis conditions. Even though Beta zeolite was first synthesized in 1967, its structure was only determined in 1988, due to its complexity.^{5,38}

Zeolite Beta has a 3D interconnected pore system. It is considered as a “large pore” zeolite, containing two straight 12-membered rings channels with an aperture of $6.6 \times 6.7 \text{ \AA}$ along [100] and [010] axes and one zigzag 12-membered rings channel of $5.6 \times 5.6 \text{ \AA}$ along the [001] axis,³⁸ as represented in Figure 4. However, Beta zeolite is highly disordered, made up of a random intergrowth of two different (but very similar) structure polymorphs A and B, Figure 5.³⁹ It has also been proposed four other polymorphs of zeolite Beta, based on the same building layers.⁴⁰ Moreover, Beta zeolite is known to have a large number of defect silanols. This has been explained by the fact that when two different stacking directions occur within the same layer, the frameworks of the two stacking variants is unable to connect at the boundary.

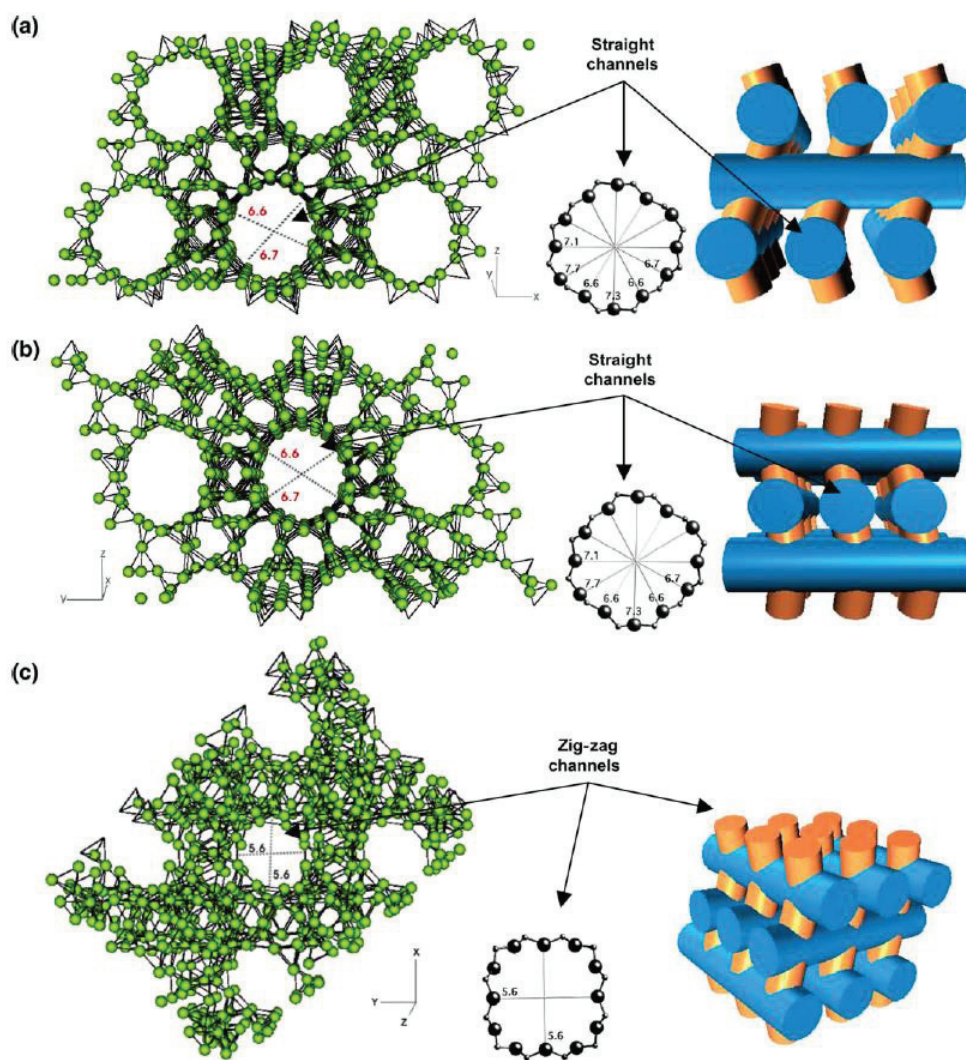


Figure 4 - Stereographic drawings and perspectives views of zeolite Beta viewed along axis (a) [100], (b) [010] and (c) [001]. The 12-membered ring free pore apertures of straight and zig-zag channels were also shown for a good visualization of its structure. In the stereographic drawings the spheres represent the oxygen atoms and the tetrahedron around which surround the tetrahedrally coordinated Si or Al T-atoms. The stereographic drawings were obtained from the World Wide Web under <http://www.iza-structure.org/databases/>. Perspective views show the pore network of zeolite Beta containing straight and zigzag channels. The cylinders represent the channels of the zeolite Beta; this representation facilitates the visualization of the intersections between the straight and zigzag channels. Reproduced from Barcia et al.³⁸

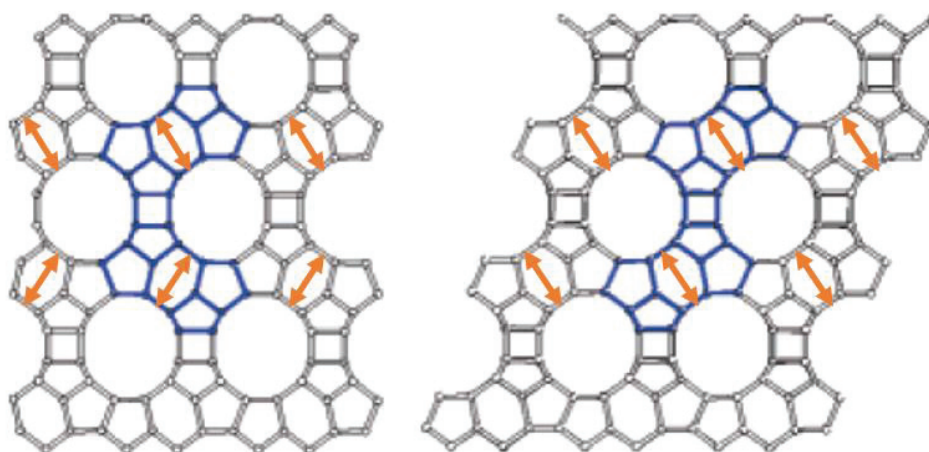


Figure 5 - Beta polytypes A (tetragonal, $P4122$, left) and B (monoclinic $C2/c$, right). Selected units in consecutively stacked layers are shown in blue with the orange arrows to indicate the different orientations. Reproduced from Wright *et al.*³⁹

1.6.2.Synthesis

Similarly to the first reported synthesis, Beta zeolite is frequently synthesized using tetraethylammonium cation (TEA^+) as SDA.⁴¹ So far, the synthesis of Beta zeolite without the presence of organic templates is only possible by adding Beta crystal seeds.^{41–43} Other types of SDA have been used to synthesize Beta zeolites with particular morphologies, such as the cationic polymer polydiallyldimethylammonium chloride (PDADMA) for the synthesis of hierarchical Beta zeolites⁴⁴ and another complex and bulky SDA, (called by the authors in short as “C22-6N”) for the synthesis of mesoporous Beta zeolite with nanosponge-like morphology.⁴⁵ Van der Waal *et al.* reported the synthesis of all-silica Beta (and also Ti-Beta) with dibenzyltrimethylammonium cation as the structure-directing agent.⁴⁶ High or pure silica zeolites can be easily crystallized when fluoride is used as mineralizing agent, using for example either HF ^{47,48} or $TEAF \cdot 2H_2O$.⁴⁹ The resulting crystals are larger in size (up to $20 \mu m$ ³⁶) and contain less framework defects.⁴⁹

1.6.3.Applications

Beta zeolite is widely used in several reactions in refining, petrochemical and fine chemical industries.⁴⁹⁵⁰ As an example, Beta zeolite has been used for acid catalyzed alkylation of benzene or toluene, to produce ethylbenzene (EB) and cumene, where Beta zeolite has exhibited excellent performance and higher activity and selectivity than Y zeolite.^{27,51,52} Chevron and Versalis (former Polimeri Europa and EniChem) have claimed and patented the use of Beta zeolite for EB production for example.⁵² We can also mention the oligomerization

of olefins,⁵³ and processes of hydro-cracking,⁵⁴ n-alkane hydroisomerization,⁵⁵ acylation of 2-methoxynaphthalene and isobutylbenzene.^{27,56}

2. Impact of crystal morphology on catalysis

2.1. Size selectivity vs diffusion limitations

In heterogeneous catalysis, a general catalytic cycle (see Figure 6) passes by: 1) diffusion of the reactant(s) into the boundary layer to the catalyst, 2) transport of the reactant to the active sites (where the reaction takes place), 3) interaction of the substrate with the catalyst (adsorption), 4) chemical reaction from which reaction products result, 5) desorption of the product, 6) diffusion of the product(s) out of the pores and finally, 7) diffusion of the product(s) through the boundary layer to the gas phase (or liquid phase, in the case of a liquid phase reaction).

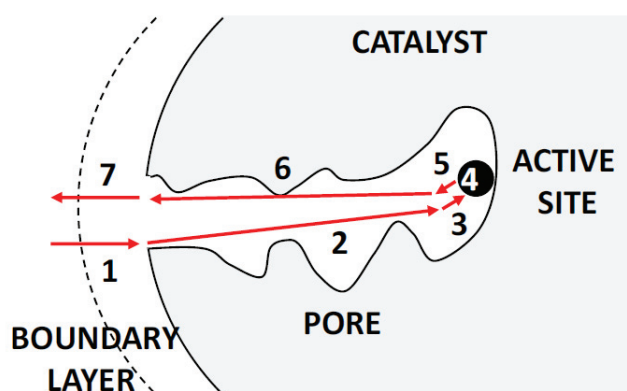


Figure 6 - Scheme of the different steps involved in a heterogeneous catalytic process.⁵⁷

In the case of a zeolite, the reaction is limited to reactants that are “small” enough to enter the pores and easily diffuse to the active site (Figure 7). Similarly, the pore and cavity sizes will condition the reaction products by their size (Products Shape Selectivity). The same can occur with the transition states in reactions.² As a consequence of this phenomena, zeolites can be extremely selective catalysts. Zeolites have been used as shape selective catalysts for major chemical and energy processes, such as disproportionation of toluene,⁵⁸ or the selective cracking of n-paraffins instead of branched paraffin, enhancing the octane number of gasoline (selectoforming).^{2,59}

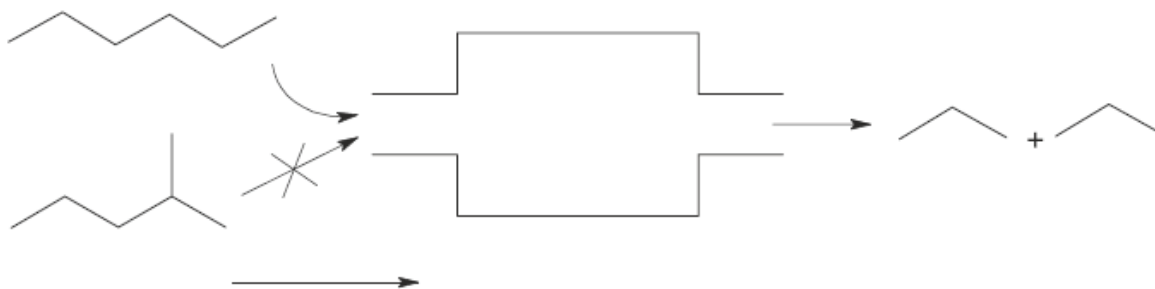


Figure 7 – Example of reactant shape selectivity: representation of the cracking reaction of *n*-hexane and *i*-hexane. Reproduced from.²

While molecular sized micropores are responsible for highly selective reactions, their molecular size yet impose severe mass-transfer constraints. Diffusion of substrates inside the microporous network is slow and may have an impact on the activity, selectivity, and also on catalyst deactivation, especially for large crystals. When the diffusion path length is long, most internal active sites cannot be reached by substrates, because the transport is too slow with respect to the reaction rate, and as consequence part of the catalyst does not participate in the catalytic reaction (low effectiveness).⁶⁰ In some extreme cases and for relatively bulky molecules, reaction happens mostly at the external surface of the crystal. Coke formation and deposition can be significant and might block part of the pore entry, hence blocking the access to internal active sites.²

Actually, **transport limitations** represent a major limitation in many refinery applications such as cracking, isomerization and alkylation.^{60,61}

2.2. Higher catalytic activity by the design of zeolite with appropriate morphology

In the objective to enhance catalytic activity, catalyst development has been directed towards materials with the highest degrees of utilization, which implies an easy and free access to all the active sites. This can be obtained:

- a) either by using zeolites with wide pores. Wider pores will facilitate molecular diffusion by increasing the diffusion coefficient D_{eff} .
- b) either by decreasing the size of the zeolite domains by playing on crystal morphologies, i.e. decreasing the diffusion path length, L , and facilitating access to the active sites.

Taking this into account, zeolite materials with improved transport characteristics have been categorized in four classes,⁶⁰ Figure 8:



Figure 8 - Classification of zeolite materials with enhanced transport characteristics. **Wide-pore** zeolites increase the catalyst effectiveness by attaining higher intracrystalline diffusivity (D_{eff}), while the **hierarchical pore** systems reduce the characteristic diffusion length (L). Both approaches reduce the Thiele modulus. The synthetic strategies leading to these architectures follow templating or non-templating routes, as detailed in the text. Reproduced from Pérez-Ramírez et al.⁶⁰

- “**Extra-large-pore zeolites** are defined by pore openings delimited by more than 14 T atoms. The UTD-1 was the first purely Si zeolite having pores delimited by 14 T atoms.⁶² However, for the stability of rings with more than 12T-atoms, it is necessary to use other T heteroatoms instead of Si, namely germanium, beryllium, bore, gallium etc.⁶³ Even though larger pores might effectively improve intracrystalline diffusion (D_{eff}) comparing to smaller sized pores, zeolites generally suffer from a low stability, low acidity (no Al atoms in the framework). Besides, so far, the chemical composition is relatively narrow, and the SDA used are generally expensive as compared to more “standard zeolites”.⁶⁰
- Another approach is to synthesize **nanosized zeolites**, with crystal sizes that can be smaller than 100 nm.⁶⁴ Nanocrystals synthesis has been achieved by mainly controlling nucleation and crystal growth processes.^{64–66} However, the synthesis of nanosized crystals is still a challenge.⁶¹ It must be noted that for nanosized zeolites diffusion path length is obviously smaller, while the external surface (per gram of zeolite) is bigger. Actually, for crystals smaller than 100 nm, external surface (that is different from the internal pore surface) consists of 25% of the total surface area.⁶⁴
- **Zeolite composites** consist of zeolites crystals supported on a material that is mesoporous and macroporous. The synthesis is obtained by controlled deposition of small zeolite crystals (generally nanosized zeolite crystals) onto a mesoporous supporting material, either on its surface, on the pores or embedded inside an essentially amorphous matrix.^{60,67}

This process can be performed either by impregnation and crystallization of a zeolite phase in amorphous ordered mesoporous material or by crystallization of a zeolite phase by introduction of seeds in the amorphous ordered mesoporous material.⁶⁷ For example, Wang *et al.*⁶⁸ reported the synthesis of a hierarchically structured composite (TUD-C) with ZSM-5 nanocrystals dispersed on the mesoporous matrix. The composite was obtained by steam induced crystallization on the matrix surface, from a ZSM-5 synthesis gel.

- **Mesoporous zeolites**, also denoted as “hierarchical zeolites”, exhibit at least two different levels of intracrystalline porosity, generally microporosity and mesoporosity. There are several synthesis strategies to create a second mesoporous network in a zeolite particle. The most popular ones are described below:

- 1- The two main approach that consists in **removing framework atoms** includes dealumination and desilication methods.⁶⁹ **Dealumination** is a common post-treatment for zeolite with small Si/Al. It was initially used to prepare faujasite type zeolites with high Si/Al ratios that were not feasible by direct synthesis. While extracting framework Al, dealumination creates vacancies in the framework, that can lead to a partial collapse of the zeolite structure with creation of mesopores, in the case of zeolites with low Si/Al. Dealumination can be obtained by acid leaching^{70,71} or steaming.⁷² The steaming approach is particularly used for stabilizing Y zeolite for FCC process. Basically the zeolite is submitted to a steam flow at 600-800 °C, which causes hydrolysis of the Al-O-Si bonds, dealumination and further formation of mesopores. However, these methods considerably change the acidic properties of the zeolite, and reduce the microporous volume. Depending on the synthesis conditions, the shape and size of the mesopores is not controllable, and their interconnectivity is scarce. **Desilication** is one of the most applied methods to create mesoporosity in zeolite crystals.⁶⁹ Basically it consists in an alkaline treatment, generally with NaOH that will preferentially remove silica from the framework. As a result, the Si/Al decreases, which also changes the acidic properties of the zeolite regarding the parent zeolite. Desilication as strategy to create controlled mesoporosity is more efficient on zeolites having the optimal window of $25 < \text{Si/Al} < 50$ which is a considerable drawback.⁶⁹ For low Si/Al, the high aluminum content prevents removal of silica; hence it is more difficult to create mesopores. For high Si/Al, silica is dissolved in excess, creating bigger mesopores, and lower mesoporous area.⁶⁹ Other treatment approaches have been trying to overcome this limitation.⁷³⁻⁷⁵
- 2- **Surfactant assisted** procedure uses big organic molecules, polymers, micelles etc. as template for the mesoporous phase, that after can be removed by calcination. Dual templating is a common procedure, where the synthesis includes the SDA for the synthesis of the zeolite structure and a surfactant template for the mesopore

formation.⁷⁶ However, this approach has failed in many situations (leading to the creation of segregated phases). The use of a single polymer as SDA can be responsible for the synthesis of the microporous zeolite with the mesopores included, which is the case of the synthesis of hierarchical Beta zeolite with the cationic polymer polydiallyldimethylammonium chloride (PDADMA).⁴⁴

- 3- **Hard template** methods include carbon made templates, hard polymers, CaCO₃ nanoparticles, mesoporous silica spheres, or even biological template such as natural sponge, wood tissue etc. These are added to the synthesis gel, crystallization occurs within and around the template. In this case, the shape and size of the mesopores can be controlled by the shape and size of the template. After zeolite synthesis, the template can be removed either by calcination, either by chemical treatment, which can also have an effect on the microporous properties of the zeolite, namely the creation of defects, internal silanols etc. Also, there have been difficulties for the respective scale-up.⁶⁹

Except to the “Extra-large pore” zeolites (where transport is enhanced due to wider pores), for zeolites with a secondary porous network, transport length scale **L** in the microporous zeolite structure is smaller. As consequence, zeolites with hierarchical porosities can benefit of enhanced effectiveness. However, the sole benefits of hierarchical pore networks on catalytic activity, selectivity and deactivation can be yet hardly quantified as other structural parameters are also modified along. For example, in the case of nanozeolites and hierarchical zeolites, **L** is smaller but it is accompanied by a major increase of the external surface. In addition, other structural modifications with respect to the corresponding classical zeolite can play a major role in catalysis, such as creations of possible EFAL with catalytic properties and modifications of Brønsted/Lewis sites.⁶⁵ Actually, many studies report that hierarchical zeolites show better catalytic performances, however the sole role of the secondary pore network is usually not obvious as other structural parameters are affected.⁷⁷

3. Hollow zeolites

Hollow zeolite single crystals (or nanoboxes) are a recent class of zeolite morphology consisting of a bulk zeolite containing a very large inner cavity. Contrary to nanozeolites or hierarchical zeolites, hollow zeolites single crystals have a reduced and well defined diffusion path length **L**, while the external surface remains the same, Figure 9.

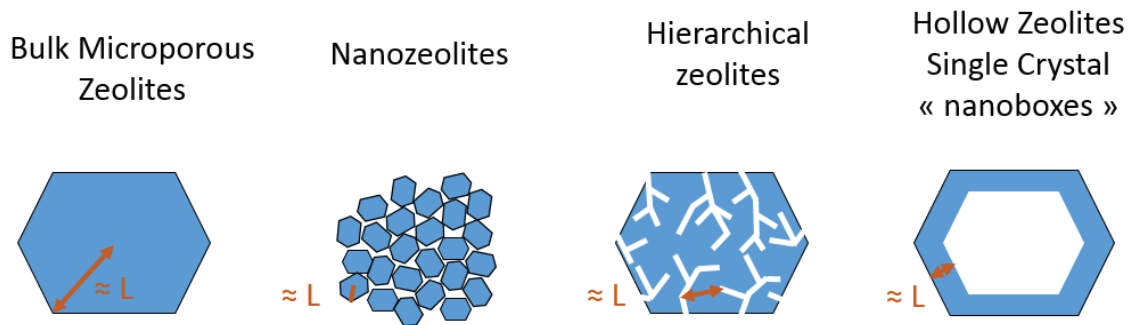


Figure 9 – Representation of different zeolite morphologies and their respective diffusion path lengths L .

In this thesis, we will use **Hollow Single *BEA zeolites**, as model catalysts in order to study the **impact of reduced diffusion path length L** on transport and acid catalysis.

There are two different types of hollow zeolites: polycrystalline shells and hollow zeolite single crystals. Generally in the literature, **hollow zeolites** are associated either to **hollow polycrystalline shells** or **hollow zeolite single crystals**. There is an extensive literature about hollow polycrystalline zeolites.⁶¹ More details can be found in our review.⁶¹

Hollow polycrystalline shells and hollow zeolite single crystals have in common the hollow structure, however these are very different from each other, Figure 10. **Hollow polycrystalline zeolites** possess a polycrystalline shell that therefore has a microporous and sometimes mesoporous nature (due to the inter-crystalline space). Generally, these structures are relatively “big”, in the order of tens of μm , and the shell thickness is the size of the polycrystalline layer. **Hollow zeolite single crystals** are synthesized from one single bulk crystal. These have the advantage to produce relatively small hollow particles with single crystal shells whose thickness can be easily controlled down to a few nanometers. In this case the zeolite wall is mainly microporous.

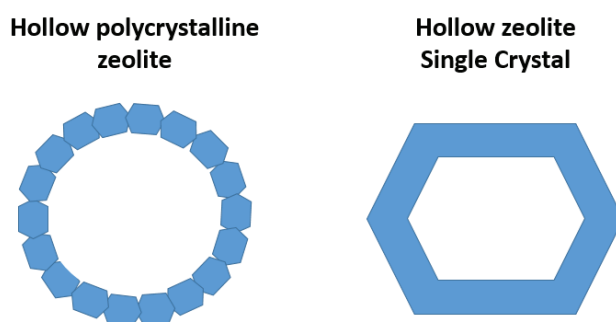


Figure 10 – Representation of a polycrystalline hollow crystal (left side) and a hollow zeolite single crystal (right side).

The approach used to synthesize hollow zeolites greatly influences the characteristics of the shell as well as the overall size of the particles, Figure 11. The synthesis of **hollow**

polycrystalline zeolites consists in a **bottom-up approach**, polycrystalline zeolite layers are formed in the presence of a template, which can be further eliminated by chemical or thermal treatments. For the synthesis of hollow zeolite single crystals, a **top-down approach** is generally used, which consists in creating hollow structures by preferential dissolution of the core of bulk zeolite crystals with zoning composition, usually with an Al-rich surface

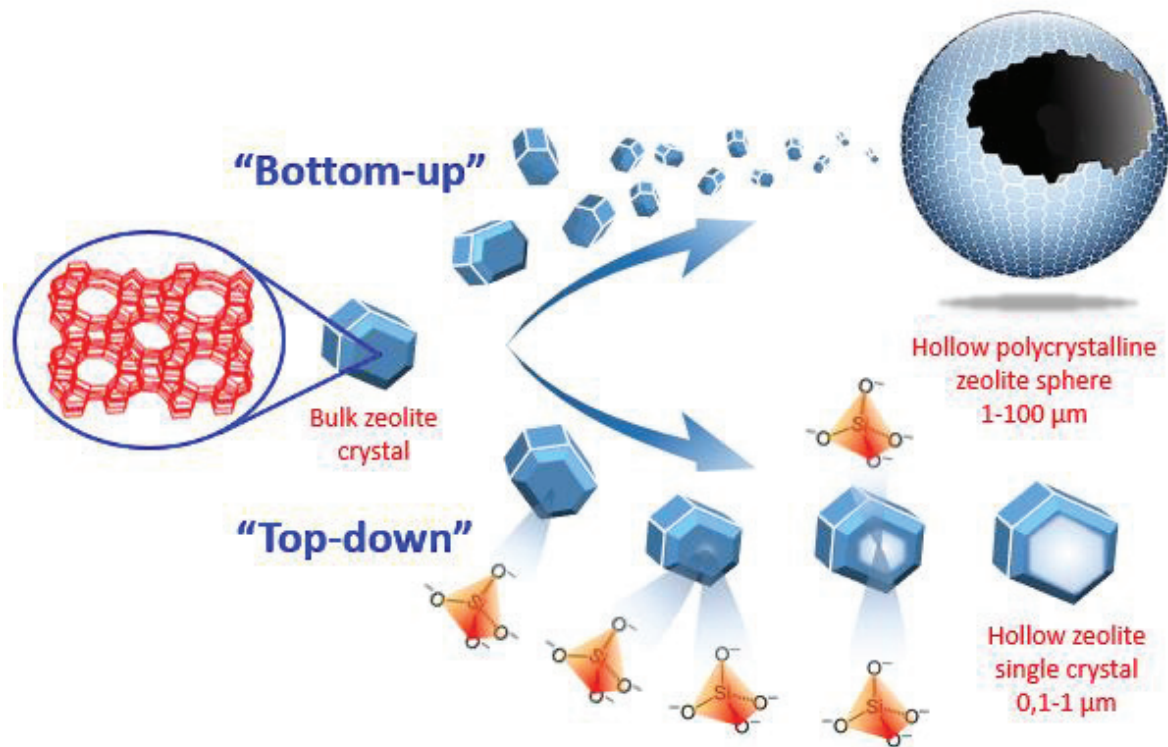


Figure 11 – Two different approaches for the synthesis of hollow zeolites : bottom-up approach, which leads to a polycrystalline hollow zeolite structure, and top-down approach, that leads to a hollow zeolite single crystal. Reported from.⁶¹

Note that in this thesis, **hollow zeolites single crystals can be also referred as hollow zeolites.**

3.1. Hollow polycrystalline zeolites

The growth of uniform zeolite layers on organic or inorganic templates was one of the first and most straightforward methods used to prepare hollow zeolites (Figure 12).

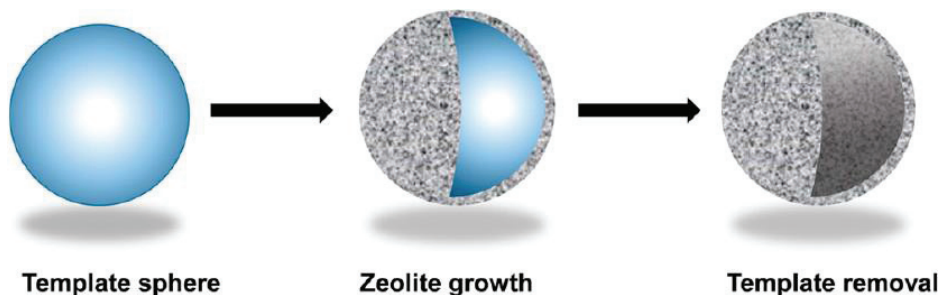


Figure 12 – Schematic Representation of the Formation of Hollow Polycrystalline Zeolite Capsules on the Surface of Hard Templates.

Crystallization of hollow zeolites **on soft templates** includes crystallization around spherical bubbles of emulsions of non-miscible liquids, such as oil and water. This technique was applied for **MFI** zeolites,⁷⁸ as well as A, X and L zeolites.⁷⁹ Cavitation bubbles formed under ultrasonic treatment have been also template for the synthesis of silicalite-1 hollow spheres.⁸⁰

Crystallization over **hard templates** has been obtained using carbon beads or polymer spheres. These are inert, insoluble in alkaline solution and can be removed after the synthesis. Synthesis of hollow zeolites can be obtained either by crystallization with a zeolite precursor gel, either by predeposition of zeolites nanocrystals on the template's surface. The deposition of zeolite crystals on the template surface is obtained by covering the beads with a polycation to adsorb electrostatically the nanocrystals in solution. The thickness of the polycrystalline shell can be enhanced repeating the previous procedure, as "layer-by-layer" deposition. This synthesis route has been used to prepare hollow **LTA**, **FAU**, **MFI** and ***BEA**.⁸¹ In the case of hollow Beta, up to 4 layers of 40 nm Beta zeolite crystals were deposited on 0.53 μm polystyrene spheres.⁸² Another strategy is that the nanocrystals covering the beads serve as seeds for zeolite growth and the core-shell structures are formed by hydrothermal secondary crystallization, a technique that generally leads to more compact and thick layers, made of highly intergrown individual crystals,⁸³ Figure 13.

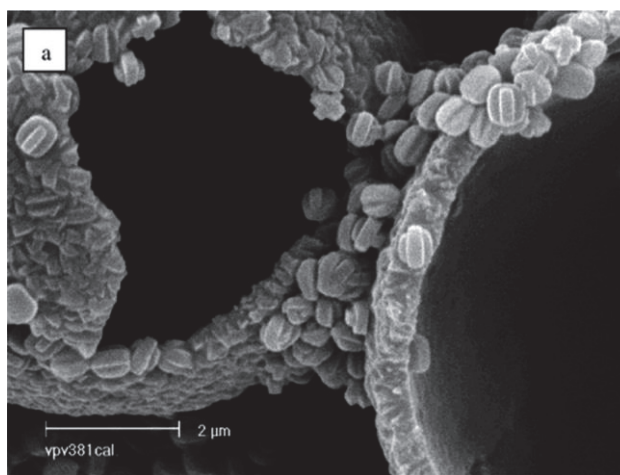


Figure 13 – TEM picture of hollow ZSM-5 spheres obtained by hydrothermal crystallization of pretreated polystyrene beads in zeolite precursor solutions. Reproduced from Valtchev.⁸³

3.2. Synthesis of hollow zeolite single crystals

In the synthesis methods of polycrystalline zeolite shells presented above, the hollow zeolite structure is constituted by an assembly of several zeolite crystals – **bottom-up method**. Consequently, the zeolite shell is polycrystalline and relatively thick (function of the size of the seed crystals or the amount of crystal layers). In contrast, hollow zeolite single crystals are created from a **single bulk crystal**, resulting in a hollow crystal/nanobox that possesses an inner cavity and **microporous shell**, Figure 11. The creation of the inner cavity results from the selective dissolution of the core of the crystal. This is possible when the crystal possesses spatial heterogeneity of composition, namely when the core has a different composition regarding the rest of the crystal. This heterogeneous composition can be found in **MFI** type zeolites, or it can be created artificially, which has been shown recently for ***BEA** and **FAU** zeolites.⁸⁴

Because the cavity is formed by removing matter from bulk crystals and not by depositing new crystals on an existing template, the overall size is approximately that of the original zeolite crystals and the wall thickness depends on how much matter is extracted, Figure 9.

3.2.1. Selective desilication

One of the first reports on **hollow ZSM-5** used the difference in solubility between Al-rich and Al-poor regions of Al-zoned crystals.⁸⁵ ZSM-5 crystals are generally not homogeneous, having an aluminum rich surface compared to the crystal core.^{83, 84} Under alkaline conditions, the Si-rich parts of the crystals are thus preferentially dissolved, whereas the Al-rich shell is preserved, leading to Al-rich hollow crystals. Irregular dissolution patterns were essentially obtained on large twinned ZSM-5 crystals with a size of 25 μm in which Al-zoning was particularly marked (Figure 14).

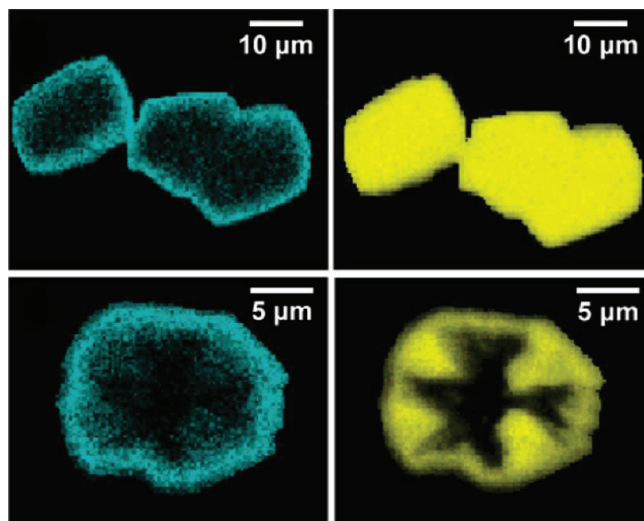


Figure 14 - SEM-EDX images of polished ZSM-5 large crystals before (top) and after (bottom) treatment in NaOH solutions. Blue and yellow colors represent aluminum and silicon, respectively. Reproduced from Groen et al.⁸⁵

For smaller crystals whose size was around 500 nm, the homogeneous Al distribution led to a uniform mesoporosity throughout the crystals. Though interesting, perspectives offered by the controlled desilication of ZSM-5 crystals were nonetheless limited by the size-dependence of the method and the impossibility to obtain hollow nanocrystals with a size below 1 μm . Moreover, walls of hollow crystals were still too thick to allow significant reduction of diffusion limitations in catalysis. More recently, the method was more or less successfully applied to ZSM-5 nanocrystals with a size of ca. 100 nm.⁸⁸ Irregular holes could be obtained upon desilication with NaOH, leading to hollow crystals with a 15 nm thick shell. However, batches were quite inhomogeneous with intact crystals coexisting with hollow ones, highlighting tiny structural differences between individual crystals.⁸⁹ Regular ZSM-5 nanoboxes with thin walls were obtained by mild alkaline treatments of bulk nanocrystals with Na_2CO_3 solutions.⁹⁰ Compared to NaOH, the use of sodium carbonate as a desilicating agent allowed a better control of the dissolution and avoided excessive destruction of the crystals. Very regular walls with a uniform thickness of 15–25 nm and a Si/Al molar ratio of 49 were obtained by treating a HZSM-5 with Si/Al = 72 for 36 h in a 0.6 M Na_2CO_3 solution^{61,90} (Figure 15).

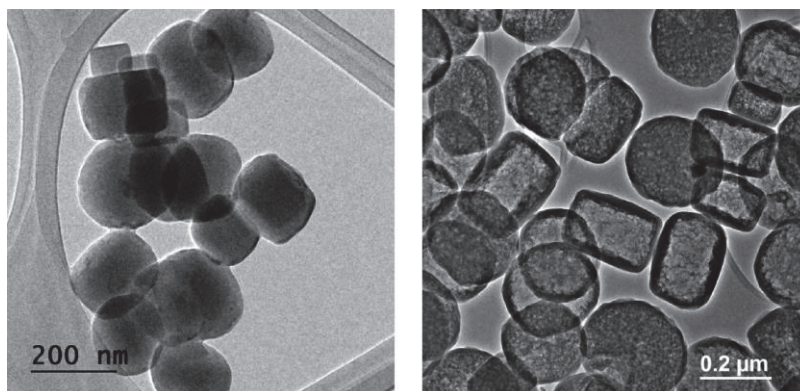


Figure 15 - TEM images of ZSM-5 nanocrystals before (left) and after (right) treatment with 0.8 M Na_2CO_3 solution at 80 °C following a recipe adapted from Mei *et al.*⁹⁰ Reported by.⁶¹

However, no information was reported on the influence of parameters such as the Al content in the zeolite, the temperature and the duration of the treatment or the sodium carbonate concentration on the morphology of the final hollow crystals. The formation of hollow structures by preferential dissolution of crystal cores is unfortunately limited to ZSM-5 in which the Al distribution is intrinsically heterogeneous.

In the case of **Beta zeolite**, a patent of Fan *et al.*⁹¹ reported the synthesis of Beta hollow structures by dissolution of calcined Beta nanocrystals at moderate temperature in the presence of alkaline aluminum species. The respective parent Beta corresponded to a known synthesis of Beta zeolite, reported in the literature by Cambor *et al.*⁹² The patent presented a very limited description/characterization of the final product hollow Beta. The final product is described as a crystalline Beta zeolite, and the document presents a XRD pattern corresponding to *BEA framework type diffraction peaks. According to the reference, the crystal has a hollow morphology, with a crystal particle diameter of 100-1500 nm and a particle wall thickness of 30-500 nm. There are only two TEM images available, presenting what seems to be a homogeneous population of hollow particles, with an average crystal size of 200-300 nm, Figure 16.

Dissolution of the core was carried out using an alkaline solution with sodium aluminate. We assume that the mechanism likely involved the enrichment of the outer surface of the crystals by Al species, creating **an artificial Al gradient**, followed by the preferential dissolution of the core. Indeed, as far as we know Beta zeolite does not have a heterogeneous composition such as Al zoning as it is for some ZSM-5 zeolites.

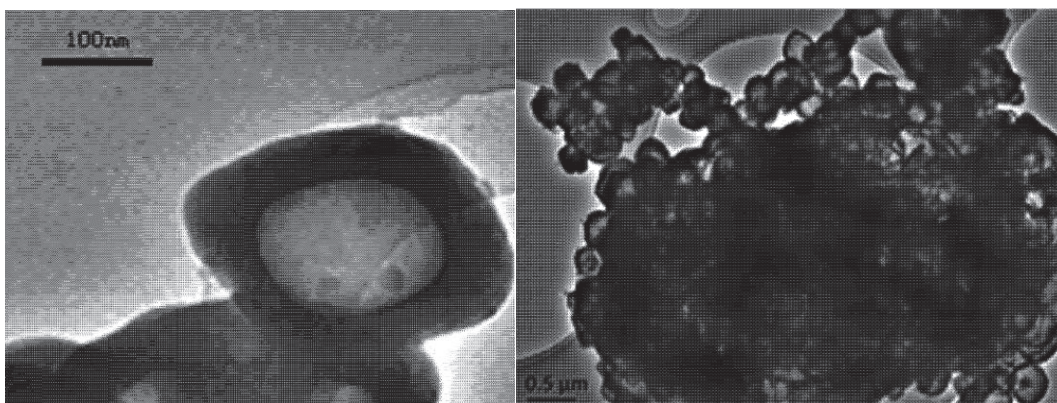


Figure 16 – TEM image of hollow Beta zeolite, reported by.⁹¹

3.2.2. Dissolution-Recrystallization

Hollow zeolite crystals are particularly interesting because of their small size as well as the facility to control many parameters, in particular the wall thickness. However, extracted species resulting from a controlled dissolution process are definitely lost, which can be an obstacle for large scale utilization, especially if the zeolite is expensive. When dissolution is performed in the presence of structure-directing molecules and under appropriate conditions, dissolved species can recrystallize on the outer surface of hollow crystals (Figure 17).

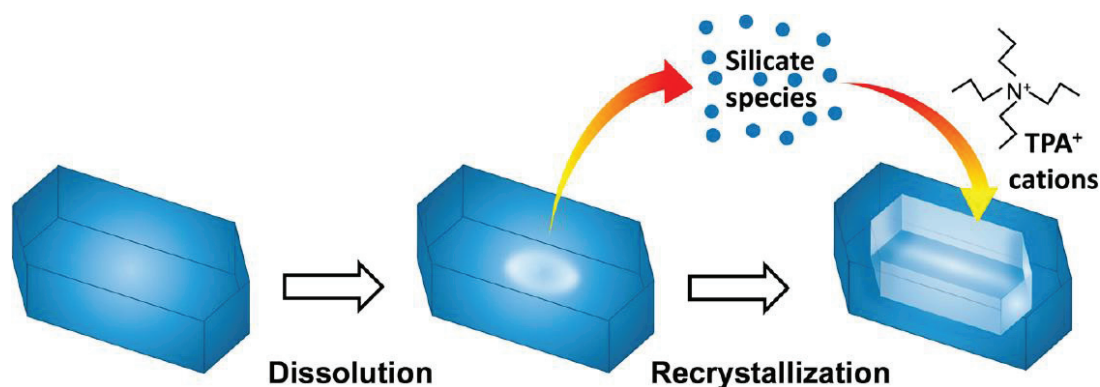


Figure 17 - Schematic Representation of the Formation of Hollow Zeolite Crystal by a Dissolution Recrystallization Method.

The first example of such a dissolution – recrystallization process was reported for TS-1, a titanium-containing silicalite-1.⁹³ Upon treating calcined TS-1 crystals in a concentrated tetrapropylammonium hydroxide (TPAOH) solution at 170 °C, zeolite cores were dissolved and species recrystallized in the presence of TPA⁺ cations (Figure 18). Because similar observations were made on pure silicalite-1 crystals, the preferential dissolution of the center of the crystals could not be explained by a heterogeneous chemical composition. It was attributed to a lower crystallinity in the middle of the crystals, resulting from a high concentration of defect sites at

the early stages of the crystallization.^{94,94} TPA⁺ cations being too large to enter the zeolite pores, crystallization occurred only on the outer surface, making possible the preparation of hollow crystals with gradients of composition. Indeed, addition of Al species in the TPAOH solution led to the formation of hollow ZSM-5 from silicalite-1 crystals, Al being essentially located on the outer part of the crystals.⁹⁵ External recrystallization of dissolved Si species could be directly demonstrated by following the location of Ag nanoparticles during the dissolution process. Initially deposited on the outer surface of bulk crystals, Ag nanoparticles were found inside the zeolite shell after treatment, confirming that they had been recovered by newly formed zeolite layers.⁹⁶ The nearly complete recrystallization of dissolved silica species makes that the characteristics of the final hollow structure depend only on the size and shape of original crystals. The dissolution – recrystallization process was also successfully used to prepare hollow ZSM-5 from bulk crystals with an Al-rich surface.^{97,98}

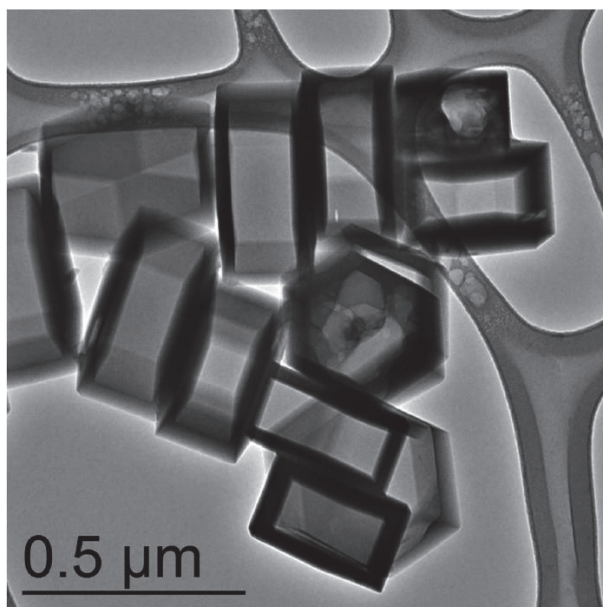


Figure 18 - TEM picture of hollow silicalite-1 crystals obtained by a dissolution – recrystallization process at 170 °C in the presence of TPAOH. Reported from.⁶¹

3.2.3. Creation of artificial composition zoning

Most of zeolites do not naturally present a heterogeneous distribution of Al species, such as Beta or Faujasite. Gradients of composition can, nonetheless, be obtained by changing the composition of the outer surface of the crystals by post-synthesis modifications.

ZSM-5

A convenient approach consists in the formation of core-shell materials in which a unique crystal, the core, is covered by a shell with the same zeolite structure. For example, silicalite-1@ZSM-5 composites prepared by secondary crystallization of a layer of ZSM-5 on silicalite-1 crystals can be regarded as heterogeneous single crystals with an abrupt change in Al concentration.⁹⁹ Such materials are prepared by dispersing as-made silicalite-1 seeds with a size between 100 and 700 nm (4% with respect to the total amount of silica) in an alkaline template-free synthesis gel containing sodium, alumina and silica with Si/Al = 50. After mixing at room temperature for 3 h and heating for a couple of hours at 210 °C, well-shaped crystals were obtained whose size largely exceeded that of initial seeds. When such crystals were treated with sodium carbonate solutions, the internal silicon-rich part of the crystals was selectively dissolved, leading to hollow nanocrystals with ZSM-5 shells. Moreover, the shell thickness could be easily controlled as it was found to be inversely proportional to the amount of seeds introduced in the synthesis gel.

Beta

In an attempt to synthesize SDA free Beta zeolite, Okubo *et al.*¹⁰⁰ used a seeded synthesis approach, using CIT-6 as crystals seeds instead of Beta seeds (CIT-6 crystals are zincosilicates with the *BEA framework type). Okubo managed to obtain Beta zeolite crystals with $5.5 < \text{Si/Al} < 10.5$ and very low Zn content. However, these Beta crystals had a hollow morphology, as proven by TEM images of the sliced crystals, Figure 19. Hollow Beta crystals present a truncated octahedral morphology typical from Beta zeolite crystals, with an average crystal size of 0.6-1 μm . TEM images of the sliced crystal show a inner cavity size of approximately 500 nm corresponding to the size of CIT-6 crystals, suggesting a full dissolution of the latter. Wall thickness is about 90-120 nm. The N₂ physisorption isotherm of the hollow Beta crystals at 77 K presents a type I adsorption branch at low pressure, indicating that the zeolite wall is purely microporous. The desorption branch possess a hysteresis that closes at $p/p^\circ = 0.53$, which the author associates to condensation phenomena in the inner cavity.

The synthesis consisted in a typical seed assisted synthesis, but without any organic template. Essentially, a certain amount of as-made CIT-6 crystals, corresponding to 10 wt. % relative to the silica source, was added to an organic-free aluminosilicate gel and the mixture was heated at 140–150 °C for different periods. According to the authors, during the hydrothermal treatment Beta zeolite starts to recrystallize on the CIT-6 surface, which afterwards is gradually dissolved, leading to hollow single crystals.

We can assume that there are three factors for the success of the synthesis of hollow Beta:

- One of the key factors in the preparation of hollow Beta zeolites was the use of **as-made** CIT-6 crystals as seeds. Under reaction conditions, seeds were less stable than Al-containing Beta zeolites but sufficiently stable to act as active surfaces for crystal growth. The relative stability was attributed to the presence of organic molecules in the pores, which prevented fast dissolution of the framework in alkaline media. In contrast, according to the authors calcined CIT-6 crystals were totally dissolved prior to Beta crystallization and Mordenite was the only zeolite formed after long hydrothermal periods.
- Beta zeolite crystals do not have any heterogeneous composition such as Al zoning that would lead to a selective dissolution of the core. However, when creating a “core-shell” of CIT-6 and Beta zeolite, an **artificial Al zoning** is created, where a zincosilicate core is less stable in alkaline media and dissolves itself.
- Another key factor for the synthesis is the fact that CIT-6 and Beta zeolite have the **same framework type *BEA**, which directs the synthesis into Beta zeolite instead of other zeolite framework types.

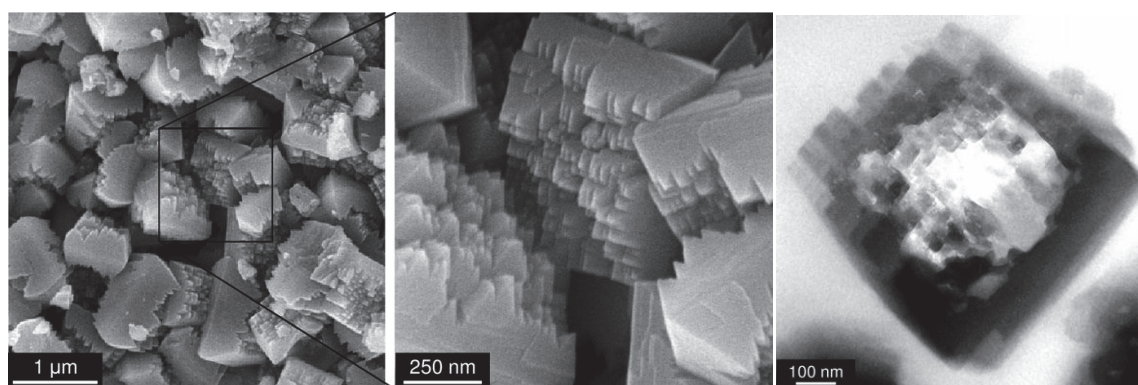


Figure 19 – SEM images (left) of hollow Beta and TEM image (right) of the sliced crystal. Reproduced from Okubo *et al.*¹⁰⁰

Another example in the literature reports the synthesis of hollow Beta.^{101,102} The synthesis is a multi-step procedure, Figure 20, that includes the creation of core – shell crystals in which the shell is an all-silica Beta zeolite and the core is an aluminosilicate Beta zeolite. Typically, Al-Beta crystals were synthesized in the presence of fluoride anions and further calcined to remove the organics. This Beta zeolite consisted of the aluminosilicate core zeolite. Cores were then dispersed in a gel containing silica, tetraethylammonium hydroxide (TEAOH) and hydrofluoric acid (HF), and the mixture was crystallized in order to form all-silica Beta shells on the surface of primary crystals, producing the core-shell zeolite with an Al rich core. Then, Al species were eliminated from cores by acid treatment leaving a defect rich and hydrophilic core. The selective removal of the core was obtained by firstly impregnating the hydrophilic core with sodium acetate solution, leaving the hydrophobic shell. Then, the zeolite

was exposed to dimethyl carbonate (DMC) vapor at 380 °C. DMC reacts with sodium acetate present in the core decomposing silica; hence the core is decomposed, leaving the all-Si Beta shell. The final hollow pure-silica Beta crystals (Si/Al = 495) possessed an external size of ca. 5 μm with a shell thickness around 1 μm , Figure 21. Compared to the synthesis proposed by Okubo *et al.*, these hollow Beta are much bigger, and they cannot be used in acid-catalyzed reactions because they are purely silicic. The synthesis route is complex, as it includes several different steps and reactions and therefore many different parameters to be mastered.

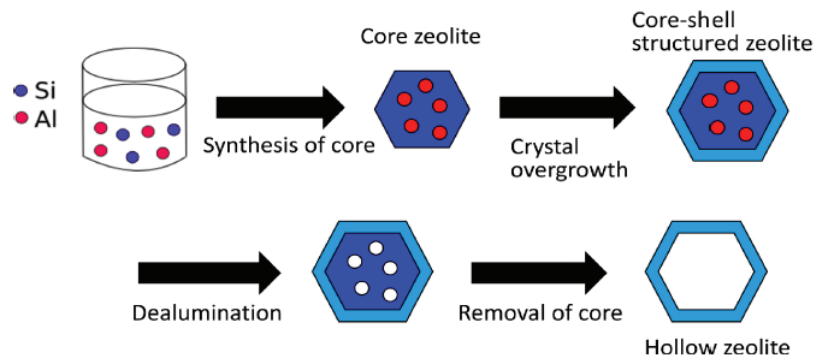


Figure 20 – Scheme for the synthesis of the hollow Beta zeolite, reproduced from.¹⁰²

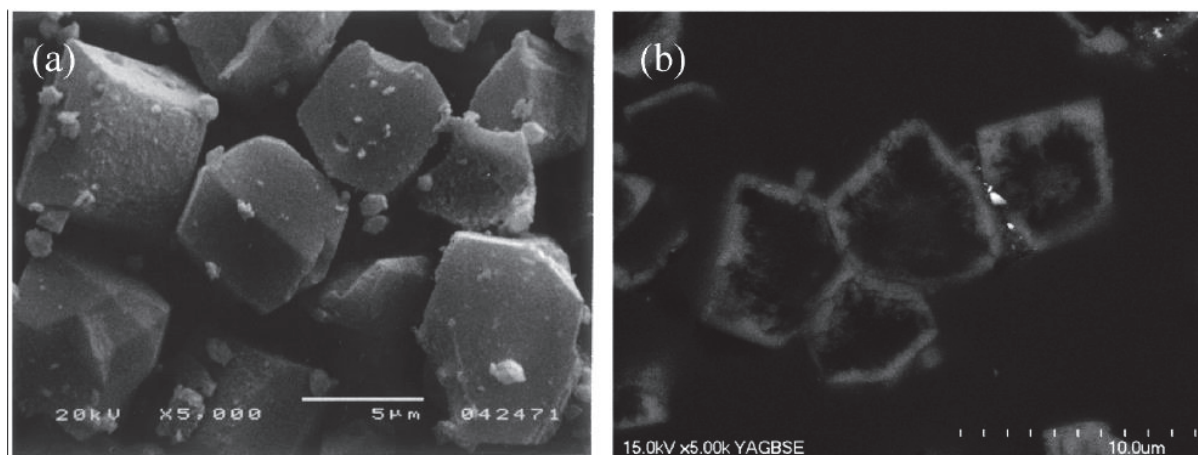


Figure 21 – SEM images of Hollow Beta a) crystals, and b) cross section of the same crystals.¹⁰²

Faujasite

Recently, we have obtained highly crystalline hollow Y zeolites from crystals with an artificial zoning obtained by post-synthesis modification of a conventional NaY.¹⁰³ The top-down transformation involves substantial dealumination of the zeolite framework by silicon tetrachloride (step 1) followed by acid leaching with HCl to remove extra-framework Al species

(step 2) and finally, selective dissolution of the crystal core in the presence of NaAlO_2 solutions (step 3), see Figure 22. The preferential desilication of the core of the crystals was attributed to a partial reincorporation of Al species into the external layers of the crystals under alkaline conditions.

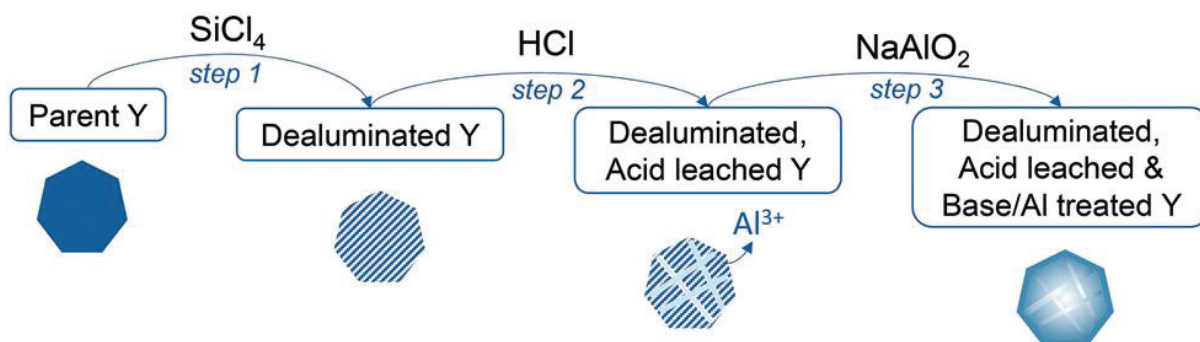


Figure 22 - Schematic illustration for the fabrication of hollow Y zeolite by a three-step process.¹⁰³

The formation of internal cavities depends on the extent of dealumination of the zeolite as well as on the efficiency to remove extra-framework Al species prior to realumination. Hollow Y zeolite crystals possess more or less regular internal cavities of ca. $0.8 \mu\text{m}$ diameter with external size and shape similar to those of the original NaY crystals.¹⁰³ Yuan *et al.*¹⁰⁴ used a similar method to obtain hollow Y zeolite single crystals. However, hollow zeolite shells are highly mesoporous.

4. Metal catalysts supported zeolite

4.1. Encapsulation of metal nanoparticles within zeolites

Metal nanoparticles supported in zeolites have proven to present high catalytic activity in many reactions such as hydrogenations, oxidations and reduction of NO_x with hydrocarbons. The higher the dispersion of NPs, the higher the surface sited and therefore, the higher the catalytic activity¹⁰⁵ However, small nanoparticles have low thermal stability. In harsh reaction conditions metal nanoparticles tend to sinter into larger particles, losing active surface and then catalytic activity.¹⁰⁶ Ostwald ripening and nanoparticle migration and coalescence have been proposed as main sintering mechanisms.¹⁰⁷ Anchoring nanoparticles in zeolite micropore is often applied to limit sintering¹⁰⁶.

The encapsulation of nanoparticles within zeolites is not always straightforward. Depending on the loading conditions, metal nanoparticles might get dispersed on the external surface of the crystals, and be subjected to sintering phenomena. Moreover, post-treatments

such as calcination and reduction can change the distribution of metal nanoparticles inside the porous media, or even force nanoparticle to migrate onto the external surface.

In the literature, there are several approaches to selectively encapsulate nanoparticles within the porous volume of zeolites. These can be divided into “post-synthesis” methods or “pre-incorporation methods”.

4.1.1. Post-synthesis methods

“**Post-synthesis**” methods or “direct loading” regards metal loading after the zeolite’s synthesis. For all loading methods, encapsulation is not always verified, and often there is a population of metal nanoparticles supported on the external surface of the zeolite.

4.1.1.1. The different loading methods

Supported metal zeolites are typically made by impregnation, ion-exchange followed by drying, calcination and reduction steps, Figure 23.

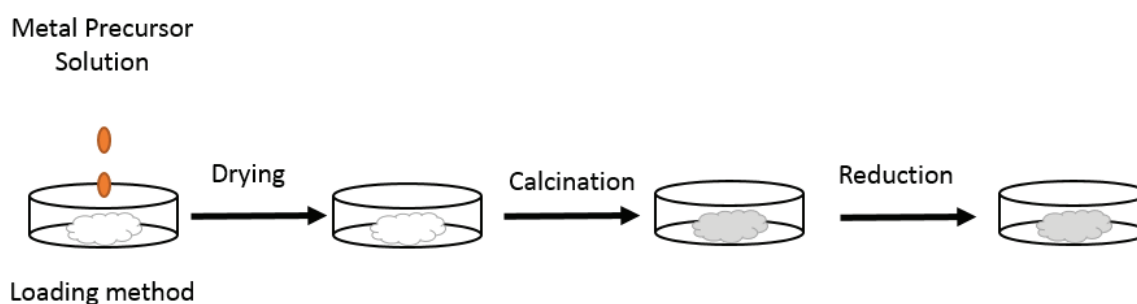


Figure 23 – Scheme of a traditional synthesis route for metal loading in zeolite supports. The first step includes getting the zeolite in touch with a liquid, which can be by impregnation, ion exchange etc.

Impregnation consists in filling the pores of the zeolites with a solution containing a metal precursor, where the volume of solution added is superior to the porous volume of the support. The solution is evaporated after mixing with the zeolite for a long time. **Incipient wetness impregnation (IWI)** consists of an impregnation with just enough metal solution to fill the microporous volume of the zeolite (volume of solution is \leq pore volume).¹⁰⁵ However, the max metal loading is limited by the solubility of the precursor in the pore filling solution.

Also, if the sorbate has weak interaction with the support, the evaporation of solution during the drying step can “carry” and redistribute the Pt precursor, leading to a heterogeneous distribution on the support.¹⁰⁸

In the case of **ion exchange (I.E.)**, generally the metals are introduced as cationic complexes, (e.g., $[\text{Pt}(\text{NH}_3)_4]^{2+}$) whose cations replace the extra-framework cations, Na^+ , K^+ etc. In this case, the amount of exchanged cations is directly dependent on the amount of framework Al, hence, this method cannot be applied to pure Si zeolites. **Competitive ion exchange** requires the addition of an excess of competitive cation, such as Na^+ or NH_4^+ . The cation competes with $[\text{Pt}(\text{NH}_3)_4]^{2+}$ for the cation positions on the micropore surface, hence forcing the $[\text{Pt}(\text{NH}_3)_4]^{2+}$ ions to travel deeper in pore network for the cation positions. This results in a more homogeneous distribution of metal particles throughout the zeolite. This case was only proven for zeolites Y, mordenite and ZSM-5, that performed ion exchange with a solution of $\text{Pt}(\text{NH}_3)_4\text{Cl}_2$ and an excess of NH_4^+ .^{109,110}

The chosen loading method has an effect on the size, dispersion and location of the metal particles. Moreover, the results can be different for different supports (different zeolites), and the results largely depend on other parameters such as the temperature, the calcination and reduction conditions, etc. Hence, it is difficult to generalize the results of ion exchange and impregnation method in terms of metal dispersion or location for zeolites in general. Philippaerts *et al.*¹⁰⁹ studied the loading method for Pt/ZSM-5, concluding that ion exchange and competitive ion exchange present higher dispersions than impregnation. Competitive ion exchange managed to obtain better Pt distribution inside the ZSM-5 crystal. Ryoo *et al.*¹¹¹ suggested that for zeolite Y supported Pt catalyst, **ion-exchange** results in most of **Pt NPs located inside** the microporous network, whereas with **impregnation** most of the **Pt are located on the external** surface of the crystals. For KL zeolite, it is generally accepted that better Pt dispersions are obtained by impregnation instead of ion-exchange.¹¹² Ostgard et al. compared IWI and ion exchange method for supporting Pt NPs on KL zeolite. **IWI** method led to **higher dispersions with Pt mainly encapsulated in the microporous** volume while **I.E.** led to smaller dispersions and part of **NPs on the external surface of the zeolite**.¹¹³

Generally, for small and medium sized pore zeolites, there are diffusion limitations of the precursors inside the pores, hence metal encapsulation is more difficult.^{114,115}

The loading method can also have an impact on the structural and chemical properties of the catalyst and/or support itself. As an example, studies showed that the loading method might have an impact on the zeolite acidity. Ion exchanged loaded Pt/Beta presented higher acidity than impregnated Pt/Beta, due to the formation of Brønsted sites during the reduction step of the ion-exchanged sample.¹¹³ Also, the pH of the metal solution can have an impact in the zeolite structure, leading to dealumination in the case of low pH values or even partially destruction of the framework.

4.1.1.2. Selective removal of metal from the external surface

As mentioned before, there are several examples in the literature where metal loading by impregnation^{116–120} and ion exchange¹²¹ led to encapsulated metal nanoparticles without nanoparticles on the external surface of the zeolite. However, the selective loading into the microporous structure is not straightforward and sometimes difficult to achieve by impregnation or ion exchange. Moreover, there might be migration of the NPs to the external surface of the zeolite during calcination or reduction.

Knapp *et al.*¹²² proposed a method to selectively remove metal nanoparticles anchored on the external surface of the zeolite, leaving the ones anchored in the micropores.

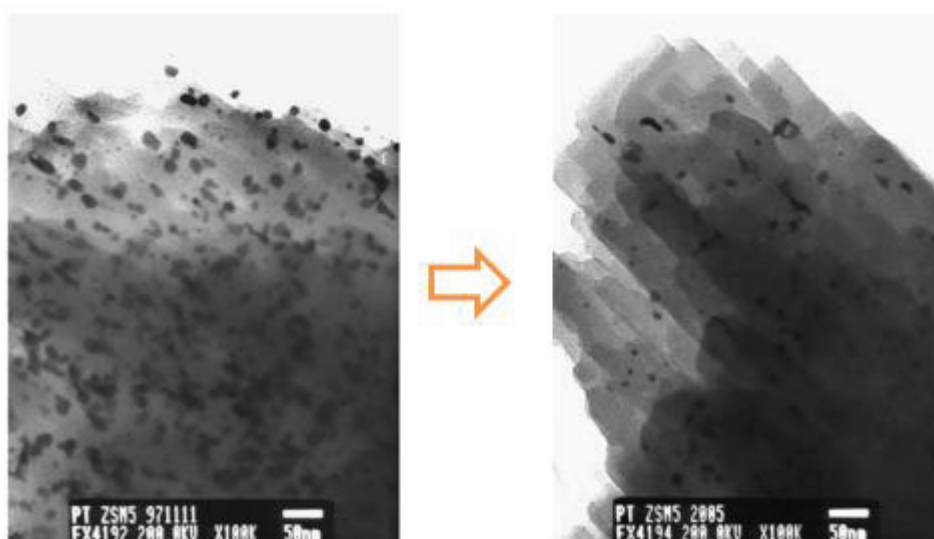


Figure 24 – Pt/ZSM-5 before (left side) and after treatment (right side).

The presented technique removes Pt NPs from the outer surface of ZSM-5 zeolite, based on a halogen-halide system for metal dissolution (see Figure 24).^{123,124} In the case of Knapp's study, the treatment was performed in an organic solvent containing a halogen and a tetraalkylammonium (TAA) halide. The highest dispersion measured after the treatment was obtained with Br₂ and tetraethylammonium bromide (TEABr) in acetonitrile. According to the literature¹²², the halide (TEABr) stabilizes the halogen (Br₂) in the form of a complex [TEA⁺Br₃⁻] which is too large to enter the zeolite pores. As a consequence, the halogen cannot react with internal particles and dissolves only those which are fully accessible on the surface of the crystals.

4.1.2. Pre-incorporation methods

Encapsulation of metal NPs can be also achieved by “**pre-incorporation**” methods, where the metal is present in the synthesis gel before the zeolite synthesis.^{125,126} Iglesia *et al.*¹²⁶ used this method to encapsulate different metals in small pore zeolites (**SOD**, **GIS** and **ANA**).

4.1.3. Pt nanoparticles supported on *BEA

In the literature, Beta supported Pt has been widely applied for several reactions such as hydrogenation, hydroisomerization, reforming and aromatization of hydrocarbons. Pt loading method was generally ion exchange^{55,112} and impregnation.^{112,116,118–120,127–134}

The characterization of Pt nanoparticles in terms of dispersion and location is not always detailed. Some impregnation studies presented very high dispersions in general (higher than 40%) and Pt particle size (<5nm).^{112,116–119,127–129,133,135} For some of the previous studies using impregnation, the Pt location was investigated by XPS or TEM analysis and Pt NPs were found encapsulated in the microporous volume.^{116–120} Studies using Pt loading though ion-exchange also led to extremely highly dispersed Pt NPs, and 100% encapsulation in the microporous volume.^{121,136} As mentioned before, it must be noted that, even for a same loading method and zeolite framework type, Pt dispersion and location will depend of the precursors used, the reduction and calcination conditions, the different Beta compositions, alkali cations present etc. (see Figure 25).

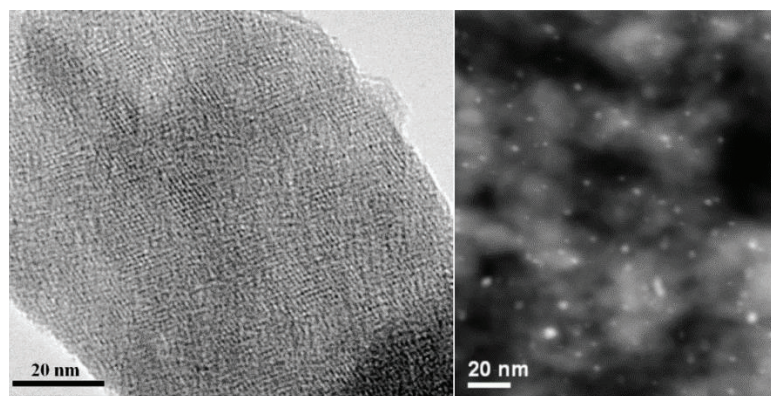


Figure 25 – Two examples of highly dispersed and encapsulated Pt nanoparticles within Beta zeolite, both obtained by impregnation. Left image from Chen *et al.*¹¹⁶ and right image from Lobo *et al.*¹¹⁸ Note in the left image that the absence of Pt nanoparticles on the external borders is an indicator of the absence of Pt nanoparticles on the external surface of the crystal.

4.2. Encapsulation of NPs in hollow zeolite single crystals

Encapsulating metal nanoparticles within a hollow zeolite single crystal (within the cavity and/or the zeolite walls), has gained particular interest due to their remarkable size-selectivity, sintering resistance, and also smaller diffusional path lengths, as described below.

Post-introduction of metals in the internal cavity of hollow zeolite crystals is difficult due to the very small pore opening. Attempts to introduce metals in hollow ZSM-5 crystals by ion exchange or incipient wetness impregnation were not conclusive. Particles were generally poly dispersed and quite large and they were found both inside the cavities and on the outer surface of the crystals.¹³⁷ It has been reported that metal nanoparticles could actually be formed in situ during the formation of the hollow structure provided that bulk crystals have been impregnated with the corresponding precursors prior to dissolution.^{138,139} This method generally led to a unique particle per hollow crystal, whose size could be controlled by simply changing the concentration of the impregnating precursor solution. In the case of silicalite-1, bulk crystals were impregnated with noble metal precursors (Au, Pt, Pd, ...) and transformed into hollow structures by recrystallization at high temperature in the presence of TPAOH. For each metal, the particle size could be controlled between ca. 2 and 10 nm, while keeping a relatively narrow particle size distribution. In all cases, metal particles were totally encapsulated into the cavity of hollow single crystals and their accessibility restricted to molecules capable of diffusing through the shell, i.e. through micropores of 0.55 nm diameter (Figure 26). In this case, the particle is too large to pass through the zeolite shell, and its size and location will remain the same even after calcination or reduction at high temperatures. The same method was successfully used to encapsulate transition metal nanoparticles in silicalite-1.⁹⁸ However, treatment with TPAOH did not directly lead to nanoparticles but to phyllosilicates, which could be further transformed into NPs by reduction at high temperature.

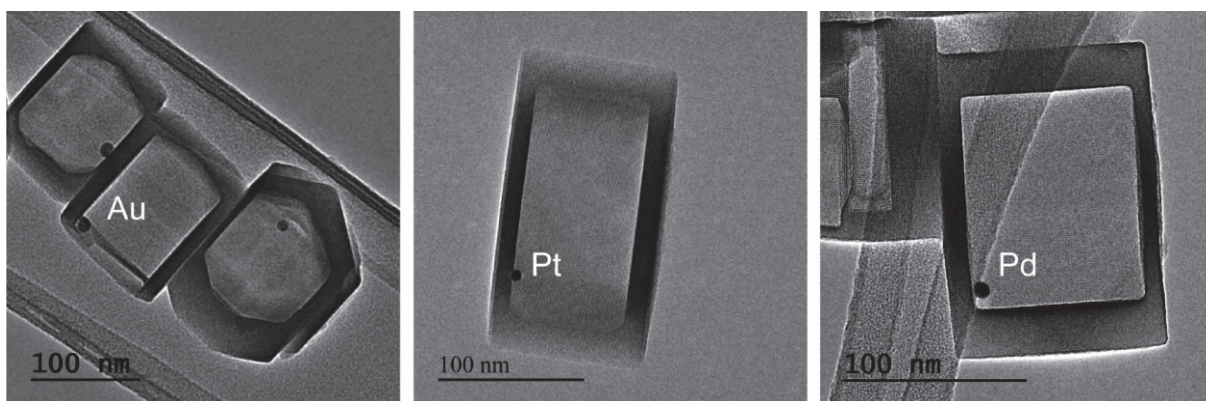


Figure 26 - TEM pictures of Au, Pt and Pd nanoparticles in hollow silicalite-1 single crystals.⁶¹

Pt NPs in silicalite-1 hollow crystals were compared with a standard Pt/SiO₂ catalyst in the hydrogenation of substituted aromatics. As expected, encapsulated Pt could hydrogenate

toluene but not the bulky mesitylene (1,3,5-trimethylbenzene), whereas a conventional Pt/SiO₂ catalyst was active for both substrates with quite similar reaction rates (Figure 27).¹³⁸ Similar observations were made over Ni nanoparticles in hollow silicalite-1.⁹⁸

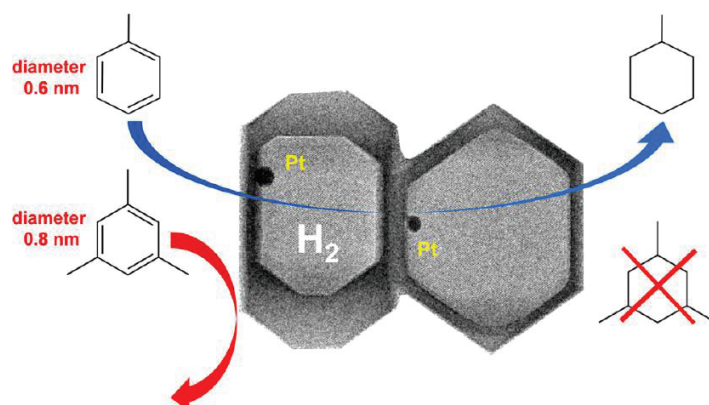


Figure 27 - Selective hydrogenation of mono-alkylbenzenes over Pt NPs encapsulated in hollow silicalite-1 crystals.^{61,138}

Recently, it has been reported high effectiveness factor of hollow single zeolites for the hydrogenation of cyclohexene, using hollow Y single crystals and bulk Y with encapsulated Pt NPs, in the micropores.¹⁴⁰ The impact of the hollow morphology vs bulk was evaluated in terms of Thiele modulus and effectiveness factor. In this case, it is assumed that the rate of transport of a sorbate inside the crystal, D_{eff} , is the same for hollow and bulk zeolites. Thiele modulus were determined taking into account the different diffusion path length (L) and as a result, hollow Y showed lower values of Thiele modulus and an effectiveness factor of 97% (against 63% of the bulk sample). This study has showed that the shortening of the diffusion length allow increasing catalytic activity, everything else being the same.

5. Context and scope of the PhD thesis

This PhD thesis started a few years ago at a moment where the synthesis of zeolite crystals with specific morphologies was particularly active in the scientist community. Indeed, the morphology of zeolite crystals not only affects its catalytic properties, it also offers the possibility to use zeolites in less conventional applications, for example as sensors, electronic devices or nanoreactors. Within the very large family of materials that have been reported all along the last decade, we had shown that conventional zeolite crystals could be converted into hollow architectures by selective dissolution of their inner part under appropriate conditions. These hollow crystals have been used to encapsulate metal nanoparticles and the corresponding nanoreactors found very interesting applications in size-selective hydrogenation reactions. However, the formation of hollow zeolites was not straightforward

and it has been limited for many years to silicalite-1 and ZSM-5, two zeolites with the **MFI** framework type. The main reason was that the selective dissolution of the core of the crystals necessitate that the latter are heterogeneous, with a core composition different from the surface. For zeolites with a homogeneous composition, in particular those with a random distribution of Al atoms in the crystals, the method could not be directly applied. This was the case of Y and Beta zeolites, two large pore zeolites widely used in industry and with pore openings significantly greater than those of ZSM-5.

Within this context, **the main objective** of this thesis was to explore the possibilities to synthesize hollow Beta zeolite single crystals following two different strategies:

1) “*CIT-6 Dissolution-Recrystallization*” approach

This method is based on the synthesis method presented by Okubo *et al.*¹⁰⁰ It is similar to the dissolution-recrystallization method used in the literature for **MFI**-type zeolites, where the parent zeolite is submitted to a second hydrothermal treatment, leading to hollow **MFI** crystals. In this case the parent crystal is not a Beta crystal but a CIT-6 zincosilicate that has the same ***BEA** framework type and is less stable in alkaline media than the corresponding aluminosilicate. Under appropriate conditions, Beta zeolite grows epitaxially on the external surface of CIT-6 seeds to form core-shell structures. Then CIT-6 cores gradually dissolve, leaving hollow structures with Beta zeolite composition.

2) “*Beta Zeolite Dissolution*” approach

This method is based on the synthesis method presented by In this case, a calcined Beta nanozeolite undergoes a post-treatment with an aqueous solution of NaOH and sodium aluminate. Hollow structures are formed by preferential desilication of crystal cores under alkaline conditions. The presence of sodium aluminates is essential to realuminate the external part of the crystals and prevents it from dissolution.

A **second objective** was to study the impact of the hollow morphology on molecular transport and catalysis, i.e. the impact of a reduced diffusional path length L as compared to bulk crystals. The founding hypothesis is that hollow and bulk present similar physical and chemical characteristics allowing the quantification of the effect diffusion path length, L , as sole parameter. Molecular transport was studied using the zero length column (ZLC) technique, which measures hydrocarbon diffusion through a fixed bed of zeolite crystals. From the desorption curves of the hydrocarbon, it was possible to have an estimation of the diffusion coefficient D_{eff} . The obtained hollow zeolites were evaluated using two acid catalyzed model reactions: the hydroisomerization of n-hexadecane (using Pt-loaded alumina binder) and the cracking of cyclohexane.

Considering the objectives presented above, this PhD thesis is organized in the following way:

- Chapter I includes a brief introduction about zeolite synthesis and applications, with special attention regarding Beta zeolite, the zeolite type studied during this thesis. The different synthesis methods of hollow zeolites single crystals are presented. Finally, different methods of introduction of metallic catalysts in zeolites (with special attention to Beta zeolite) and hollow zeolite single crystals are described.

- In chapter II we describe the preparation methods of all the materials, with the corresponding characterization techniques and catalytic reactions.

- Chapter III shows the two different approaches used to synthesize hollow Beta zeolite single crystals. It also includes all the studies regarding hollow Beta crystals as support for Pt nanoparticles. The encapsulation of Pt nanoparticles was supported by the catalytic hydrogenation of hydrocarbons with different molecular sizes.

- Chapter IV presents the impact of the hollow morphology on molecular diffusion and transport by the Zero Length Column (ZLC) technique. The technique was set-up and optimized in order to compare the diffusion of cyclohexane in hollow and bulk Beta crystal, but also the diffusion of toluene in hollow and bulk silicalite-1, previously obtained by colleagues at IRCE Lyon.

- In chapter V the catalytic performances of hollow and bulk Beta zeolites were compared for model reactions in bifunctional catalysis (hydroisomerization of n-C₁₆) and acid catalysis (cracking of cyclohexane).

6. References

- (1) Cronstedt, A. F. *Akad. Handl. Stockholm*. 1756, pp 120–130.
- (2) Guisnet, M.; Ramôa Ribeiro, F. *Les Zéolithes, Un Nanomonde Au Service De La Catalyse de Michel Guisnet Format Broché*; 2006.
- (3) History of the Database of Zeolite Structures <http://www.iza-structure.org/DatabaseHistory.htm> (accessed Mar 5, 2019).
- (4) Loewenstein, W. The Distribution of Aluminum in the Tetrahedra of Silicates and Aluminates. *Am. Miner.* **1954**, *39* (1–2), 92–96.
- (5) Cejka, J.; Corma, A.; Zones, S. *Zeolites and Catalysis: Synthesis, Reactions and Applications*; 2010.
- (6) Baerlocher, C.; McCusker, L. B.; Olson, D. H. *Atlas of Zeolite Framework Types*, 6th rev. ed.; Elsevier: Amsterdam, 2007.
- (7) JÉRÉMY DHAINAUT. VERS L'IDENTIFICATION D'INHIBITEURS DE CROISSANCE POUR LA SYNTHÈSE DE CRISTAUX DE ZÉOLITHES DE TAILLE NANOMÉTRIQUE, Université de Haute-Alsace, 2012.
- (8) Derouane, E. G.; Vedrine, J. C.; Ramos Pinto, R.; Borges, P. M.; Costa, L.; Lemos, M. a. N. D. A.; Lemos, F.; Ramoa Ribeiro, F. The Acidity of Zeolites: Concepts, Measurements and

- Relation to Catalysis: A Review on Experimental and Theoretical Methods for the Study of Zeolite Acidity. *Catal. Rev.-Sci. Eng.* **2013**, *55* (4), 454–515. <https://doi.org/10.1080/01614940.2013.822266>.
- (9) Dai, W.; Wang, C.; Tang, B.; Wu, G.; Guan, N.; Xie, Z.; Hunger, M.; Li, L. Lewis Acid Catalysis Confined in Zeolite Cages as a Strategy for Sustainable Heterogeneous Hydration of Epoxides. *ACS Catal.* **2016**, *6* (5), 2955–2964. <https://doi.org/10.1021/acscatal.5b02823>.
- (10) Abate, S.; Barbera, K.; Centi, G.; Lanzafame, P.; Perathoner, S. Disruptive Catalysis by Zeolites. *Catal. Sci. Technol.* **2016**, *6* (8), 2485–2501. <https://doi.org/10.1039/C5CY02184G>.
- (11) Cundy, C. S.; Cox, P. A. The Hydrothermal Synthesis of Zeolites: Precursors, Intermediates and Reaction Mechanism. *Microporous Mesoporous Mat.* **2005**, *82* (1–2), 1–78. <https://doi.org/10.1016/j.micromeso.2005.02.016>.
- (12) Helmkamp, M.; Davis, M. Synthesis of Porous Silicates. *Annu. Rev. Mater. Sci.* **1995**, *25*, 161–192.
- (13) Davis, M.; Lobo, R. Zeolite and Molecular-Sieve Synthesis. *Chem. Mat.* **1992**, *4* (4), 756–768. <https://doi.org/10.1021/cm00022a005>.
- (14) Masters, A. F.; Maschmeyer, T. Zeolites - From Curiosity to Cornerstone. *Microporous Mesoporous Mat.* **2011**, *142* (2–3), 423–438. <https://doi.org/10.1016/j.micromeso.2010.12.026>.
- (15) Bibby, D.; Dale, M. Synthesis of Silica-Sodalite from Non-Aqueous Systems. *Nature* **1985**, *317* (6033), 157–158. <https://doi.org/10.1038/317157a0>.
- (16) Kuperman, A.; Nadimi, S.; Oliver, S.; Ozin, G.; Garces, J.; Olken, M. Nonaqueous Synthesis of Giant Crystals of Zeolites and Molecular-Sieves. *Nature* **1993**, *365* (6443), 239–242. <https://doi.org/10.1038/365239a0>.
- (17) Flanigen, E. M.; Patton, R. I. US Patent 4073865, 1978.
- (18) Souldard, M.; Bilger, S.; Kessler, H.; Guth, J. Thermoanalytical Characterization of Mfi-Type Zeolites Prepared Either. *Zeolites* **1987**, *7* (5), 463–470. [https://doi.org/10.1016/0144-2449\(87\)90016-9](https://doi.org/10.1016/0144-2449(87)90016-9).
- (19) Cullet, P.; Hazm, J.; Guth, J.; Joly, J.; Lynch, J.; Raatz, F. Synthesis of Zeolite-Beta from Nonalkaline Fluoride Aqueous Aluminosilicate Gels. *Zeolites* **1992**, *12* (3), 240–250. [https://doi.org/10.1016/S0144-2449\(05\)80290-8](https://doi.org/10.1016/S0144-2449(05)80290-8).
- (20) Estermann, M.; Mccusker, L.; Baerlocher, C.; Merrouche, A.; Kessler, H. A Synthetic Gallophosphate Molecular-Sieve with a 20-Tetrahedral-Atom Pore Opening. *Nature* **1991**, *352* (6333), 320–323. <https://doi.org/10.1038/352320a0>.
- (21) Shayib, R. M.; George, N. C.; Seshadri, R.; Burton, A. W.; Zones, S. I.; Chmelka, B. F. Structure-Directing Roles and Interactions of Fluoride and Organocations with Siliceous Zeolite Frameworks. *J. Am. Chem. Soc.* **2011**, *133* (46), 18728–18741. <https://doi.org/10.1021/ja205164u>.
- (22) Rao, P.; Matsukata, M. Dry-Gel Conversion Technique for Synthesis of Zeolite BEA. *Chem. Commun.* **1996**, No. 12, 1441–1442. <https://doi.org/10.1039/cc9960001441>.
- (23) Barrer; Baynham; Bultitude; Meier. Hydrothermal Chemistry of the Silicates. Part VIII.* Low Temperature Crystal Growth of Aluminosilicates, and of Some Gallium and Germanium Analogues. 1959, pp 195–208.
- (24) Kerr, G. Chemistry of Crystalline Aluminosilicates .i. Factors Affecting Formation of Zeolite A. *J. Phys. Chem.* **1966**, *70* (4), 1047-. <https://doi.org/10.1021/j100876a015>.
- (25) Kerr, G. Crystallization of Sodium Zeolite-A. *Zeolites* **1989**, *9* (5), 451–451. [https://doi.org/10.1016/0144-2449\(89\)90104-8](https://doi.org/10.1016/0144-2449(89)90104-8).
- (26) Zhdanov, S. Some Problems of Zeolite Crystallization. *Advances in Chemistry Series* **1971**, No. 101, 20-.
- (27) Vermeiren, W.; Gilson, J.-P. Impact of Zeolites on the Petroleum and Petrochemical Industry. *Top. Catal.* **2009**, *52* (9), 1131–1161. <https://doi.org/10.1007/s11244-009-9271-8>.
- (28) Yilmaz, B.; Mueller, U. Catalytic Applications of Zeolites in Chemical Industry. *Top. Catal.* **2009**, *52* (6–7), 888–895. <https://doi.org/10.1007/s11244-009-9226-0>.

- (29) Ghobarkar, H.; Schaf, O.; Guth, U. Zeolites - from Kitchen to Space. *Prog. Solid State Chem.* **1999**, *27* (2–4), 29–73. [https://doi.org/10.1016/S0079-6786\(00\)00002-9](https://doi.org/10.1016/S0079-6786(00)00002-9).
- (30) Mumpton, F. A. La Roca Magica: Uses of Natural Zeolites in Agriculture and Industry. *Proc. Natl. Acad. Sci. U. S. A.* **1999**, *96* (7), 3463–3470. <https://doi.org/10.1073/pnas.96.7.3463>.
- (31) Wang, S.; Peng, Y. Natural Zeolites as Effective Adsorbents in Water and Wastewater Treatment. *Chem. Eng. J.* **2010**, *156* (1), 11–24. <https://doi.org/10.1016/j.cej.2009.10.029>.
- (32) Borai, E. H.; Harjula, R.; Malinen, L.; Paajanen, A. Efficient Removal of Cesium from Low-Level Radioactive Liquid Waste Using Natural and Impregnated Zeolite Minerals. *J. Hazard. Mater.* **2009**, *172* (1), 416–422. <https://doi.org/10.1016/j.jhazmat.2009.07.033>.
- (33) Bourgeat-Lami, E.; Fajula, F.; Anglerot, D.; Courieres, T. Single-Step Dealumination of Zeolite-Beta Precursors for the Preparation. *Microporous Mater.* **1993**, *1* (4), 237–245.
- (34) Wang, Y.; LeVan, M. D. Adsorption Equilibrium of Carbon Dioxide and Water Vapor on Zeolites 5A and 13X and Silica Gel: Pure Components. *J. Chem. Eng. Data* **2009**, *54* (10), 2839–2844. <https://doi.org/10.1021/je800900a>.
- (35) Wadlinger, R. L.; Kerr, G. T.; Rosinski, E. J. US Patent 3308069, 1967.
- (36) Larlus, O.; Valtchev, V. P. Control of the Morphology of All-Silica BEA-Type Zeolite Synthesized in Basic Media. *Chem. Mat.* **2005**, *17* (4), 881–886. <https://doi.org/10.1021/cm048799r>.
- (37) Camblor, M. A.; Corma, A.; Valencia, S. Characterization of Nanocrystalline Zeolite Beta. *Microporous Mesoporous Mat.* **1998**, *25* (1–3), 59–74. [https://doi.org/10.1016/S1387-1811\(98\)00172-3](https://doi.org/10.1016/S1387-1811(98)00172-3).
- (38) Barcia, P. S.; Silva, J. a. C.; Rodrigues, A. E. Adsorption Equilibrium and Kinetics of Branched Hexane Isomers in Pellets of BETA Zeolite. *Microporous Mesoporous Mat.* **2005**, *79* (1–3), 145–163. <https://doi.org/10.1016/j.micromeso.2004.10.037>.
- (39) Wright, P. A.; Zhou, W.; Pérez-Pariente, J.; Arranz, M. Direct Observation of Growth Defects in Zeolite Beta. *J. Am. Chem. Soc.* **2005**, *127* (2), 494–495. <https://doi.org/10.1021/ja043948s>.
- (40) Tong, M.; Zhang, D.; Fan, W.; Xu, J.; Zhu, L.; Guo, W.; Yan, W.; Yu, J.; Qiu, S.; Wang, J.; et al. Synthesis of Chiral Polymorph A-Enriched Zeolite Beta with an Extremely Concentrated Fluoride Route. *Sci Rep* **2015**, *5*, 11521. <https://doi.org/10.1038/srep11521>.
- (41) De Baerdemaeker, T.; Yilmaz, B.; Mueller, U.; Feyen, M.; Xiao, F.-S.; Zhang, W.; Tatsumi, T.; Gies, H.; Bao, X.; De Vos, D. Catalytic Applications of OSDA-Free Beta Zeolite. *J. Catal.* **2013**, *308*, 73–81. <https://doi.org/10.1016/j.jcat.2013.05.025>.
- (42) Majano, G.; Delmotte, L.; Valtchev, V.; Mintova, S. Al-Rich Zeolite Beta by Seeding in the Absence of Organic Template. *Chem. Mat.* **2009**, *21* (18), 4184–4191. <https://doi.org/10.1021/cm900462u>.
- (43) Kamimura, Y.; Chaikittisilp, W.; Itabashi, K.; Shimojima, A.; Okubo, T. Critical Factors in the Seed-Assisted Synthesis of Zeolite Beta and “Green Beta” from OSDA-Free Na+-Aluminosilicate Gels. *Chem.-Asian J.* **2010**, *5* (10), 2182–2191. <https://doi.org/10.1002/asia.201000234>.
- (44) Yuan, Y.; Tian, P.; Yang, M.; Fan, D.; Wang, L.; Xu, S.; Wang, C.; Wang, D.; Yang, Y.; Liu, Z. Synthesis of Hierarchical Beta Zeolite by Using a Bifunctional Cationic Polymer and the Improved Catalytic Performance. *RSC Adv.* **2015**, *5* (13), 9852–9860. <https://doi.org/10.1039/c4ra14295k>.
- (45) Kim, T.-W.; Kim, S.-Y.; Kim, J.-C.; Kim, Y.; Ryoo, R.; Kim, C.-U. Selective p-Xylene Production from Biomass-Derived Dimethylfuran and Ethylene over Zeolite Beta Nanosponge Catalysts. *Appl. Catal. B-Environ.* **2016**, *185*, 100–109. <https://doi.org/10.1016/j.apcatb.2015.11.046>.
- (46) Vanderwaal, J.; Rigutto, M.; Vanbekkum, H. Synthesis of All-Silica Zeolite-Beta. *J. Chem. Soc.-Chem. Commun.* **1994**, No. 10, 1241–1242. <https://doi.org/10.1039/c39940001241>.
- (47) Stelzer, J.; Paulus, M.; Hunger, M.; Weitkamp, J. Hydrophobic Properties of All-Silica Zeolite Beta. *Microporous Mesoporous Mat.* **1998**, *22* (1–3), 1–8. [https://doi.org/10.1016/S1387-1811\(98\)00071-7](https://doi.org/10.1016/S1387-1811(98)00071-7).

- (48) Camblor, M. A.; Corma, A.; Valencia, S. Synthesis in Fluoride Media and Characterisation of Aluminosilicate Zeolite Beta. *J. Mater. Chem.* **1998**, *8* (9), 2137–2145. <https://doi.org/10.1039/a804457k>.
- (49) Larlus, O.; Valtchev, V. Synthesis of All-Silica BEA-Type Material in Basic Media. *Microporous Mesoporous Mat.* **2006**, *93* (1–3), 55–61. <https://doi.org/10.1016/j.micromeso.2006.02.003>.
- (50) Bhat, R.; Kumar, R. Synthesis of Zeolite-Beta Using Silica-Gel as a Source of SiO₂. *J. Chem. Technol. Biotechnol.* **1990**, *48* (4), 453–466.
- (51) Bellussi, G.; Pazzuconi, G.; Perego, C.; Girotti, G.; Terzoni, G. Liquid-Phase Alkylation of Benzene with Light Olefins Catalyzed by Beta-Zeolites. *J. Catal.* **1995**, *157* (1), 227–234. <https://doi.org/10.1006/jcat.1995.1283>.
- (52) Perego, C.; Ingallina, P. Combining Alkylation and Transalkylation for Alkylaromatic Production. *Green Chem.* **2004**, *6* (6), 274–279. <https://doi.org/10.1039/b403277m>.
- (53) Yoon, J. W.; Chang, J.-S.; Lee, H.-D.; Kim, T.-J.; Jhung, S. H. Trimerization of Isobutene over a Zeolite Beta Catalyst. *J. Catal.* **2007**, *245* (1), 253–256. <https://doi.org/10.1016/j.jcat.2006.10.008>.
- (54) Hassan, A.; Ahmed, S.; Ali, M. A.; Hamid, H.; Inui, T. A Comparison between Beta- and USY-Zeolite-Based Hydrocracking Catalysts. *Appl. Catal. A-Gen.* **2001**, *220* (1–2), 59–68. [https://doi.org/10.1016/S0926-860X\(01\)00705-0](https://doi.org/10.1016/S0926-860X(01)00705-0).
- (55) Martins, A.; Silva, J. M.; Ribeiro, M. F. Influence of Rare Earth Elements on the Acid and Metal Sites of Pt/HBEA Catalyst for Short Chain n-Alkane Hydroisomerization. *Appl. Catal. A-Gen.* **2013**, *466*, 293–299. <https://doi.org/10.1016/j.apcata.2013.06.043>.
- (56) Andy, P.; Garcia-Martinez, J.; Lee, G.; Gonzalez, H.; Jones, C. W.; Davis, M. E. Acylation of 2-Methoxynaphthalene and Isobutylbenzene over Zeolite Beta. *J. Catal.* **2000**, *192* (1), 215–223. <https://doi.org/10.1006/jcat.2000.2855>.
- (57) Laprune, D. Application de Catalyseur Encapsulés à Base de Nickel Au Réformage d'un Gaz Modèle Issu de La Gazéification de La Biomasse, Université Claude Bernard Lyon 1, 2017.
- (58) Nishiyama, N.; Miyamoto, M.; Egashira, Y.; Ueyama, K. Zeolite Membrane on Catalyst Particles for Selective Formation of p-Xylene in the Disproportionation of Toluene. *Chem. Commun.* **2001**, No. 18, 1746–1747. <https://doi.org/10.1039/b105256j>.
- (59) Corma, A. State of the Art and Future Challenges of Zeolites as Catalysts. *J. Catal.* **2003**, *216* (1–2), 298–312. [https://doi.org/10.1016/S0021-9517\(02\)00132-X](https://doi.org/10.1016/S0021-9517(02)00132-X).
- (60) Perez-Ramirez, J.; Christensen, C. H.; Egeblad, K.; Christensen, C. H.; Groen, J. C. Hierarchical Zeolites: Enhanced Utilisation of Microporous Crystals in Catalysis by Advances in Materials Design. *Chem. Soc. Rev.* **2008**, *37* (11), 2530–2542. <https://doi.org/10.1039/b809030k>.
- (61) Pagis, C.; Morgado Prates, A. R.; Farrusseng, D.; Bats, N.; Tuel, A. Hollow Zeolite Structures: An Overview of Synthesis Methods. *Chemistry of Materials* **2016**, *28* (15), 5205–5223. <https://doi.org/10.1021/acs.chemmater.6b02172>.
- (62) Freyhardt, C. C.; Tsapatsis, M.; Lobo, R. F.; Balkus, K. J.; Davis, M. E. A High-Silica Zeolite with a 14-Tetrahedral-Atom Pore Opening. *Nature* **1996**, *381* (6580), 295–298. <https://doi.org/10.1038/381295a0>.
- (63) Jiang, J.; Yu, J.; Corma, A. Extra-Large-Pore Zeolites: Bridging the Gap between Micro and Mesoporous Structures. *Angew. Chem.-Int. Edit.* **2010**, *49* (18), 3120–3145. <https://doi.org/10.1002/anie.200904016>.
- (64) Larsen, S. C. Nanocrystalline Zeolites and Zeolite Structures: Synthesis, Characterization, and Applications. *J. Phys. Chem. C* **2007**, *111* (50), 18464–18474. <https://doi.org/10.1021/jp074980m>.
- (65) Teixeira, A. R.; Chang, C.-C.; Coogan, T.; Kendall, R.; Fan, W.; Dauenhauer, P. J. Dominance of Surface Barriers in Molecular Transport through Silicalite-1. *J. Phys. Chem. C* **2013**, *117* (48), 25545–25555. <https://doi.org/10.1021/jp4089595>.
- (66) Tosheva, L.; Valtchev, V. P. Nanozeolites: Synthesis, Crystallization Mechanism, and Applications. *Chem. Mat.* **2005**, *17* (10), 2494–2513. <https://doi.org/10.1021/cm047908z>.

- (67) Chal, R.; Gerardin, C.; Bulut, M.; van Donk, S. Overview and Industrial Assessment of Synthesis Strategies towards Zeolites with Mesopores. *ChemCatChem* **2011**, *3* (1), 67–81. <https://doi.org/10.1002/cctc.201000158>.
- (68) Wang, J.; Groen, J. C.; Yue, W.; Zhou, W.; Coppens, M.-O. Single-Template Synthesis of Zeolite ZSM-5 Composites with Tunable Mesoporosity. *Chem. Commun.* **2007**, No. 44, 4653–4655. <https://doi.org/10.1039/b708822a>.
- (69) Serrano, D. P.; Escola, J. M.; Pizarro, P. Synthesis Strategies in the Search for Hierarchical Zeolites. *Chem. Soc. Rev.* **2013**, *42* (9), 4004–4035. <https://doi.org/10.1039/c2cs35330j>.
- (70) Sulikowski, B. The Fractal Dimension in Molecular Sieves: Synthetic Faujasite and Related Solids. *J. Phys. Chem.* **1993**, *97* (7), 1420–1425. <https://doi.org/10.1021/j100109a028>.
- (71) Van Oers, C. J.; Stevens, W. J. J.; Bruijn, E.; Mertens, M.; Lebedev, O. I.; Van Tendeloo, G.; Meynen, V.; Cool, P. Formation of a Combined Micro- and Mesoporous Material Using Zeolite Beta Nanoparticles. *Microporous Mesoporous Mat.* **2009**, *120* (1–2), 29–34. <https://doi.org/10.1016/j.micromeso.2008.08.056>.
- (72) Szostak, R. Chapter 6 Secondary Synthesis Methods. In *Studies in Surface Science and Catalysis*; van Bekkum, H., Flanigen, E. M., Jacobs, P. A., Jansen, J. C., Eds.; Introduction to Zeolite Science and Practice; Elsevier, 2001; Vol. 137, pp 261–297. [https://doi.org/10.1016/S0167-2991\(01\)80248-2](https://doi.org/10.1016/S0167-2991(01)80248-2).
- (73) Caicedo-Realpe, R.; Perez-Ramirez, J. Mesoporous ZSM-5 Zeolites Prepared by a Two-Step Route Comprising Sodium Aluminate and Acid Treatments. *Microporous Mesoporous Mat.* **2010**, *128* (1–3), 91–100. <https://doi.org/10.1016/j.micromeso.2009.08.009>.
- (74) Verboekend, D.; Pérez-Ramírez, J. Desilication Mechanism Revisited: Highly Mesoporous All-Silica Zeolites Enabled Through Pore-Directing Agents. *Chemistry – A European Journal* **2011**, *17* (4), 1137–1147. <https://doi.org/10.1002/chem.201002589>.
- (75) Verboekend, D.; Mitchell, S.; Milina, M.; Groen, J. C.; Pérez-Ramírez, J. Full Compositional Flexibility in the Preparation of Mesoporous MFI Zeolites by Desilication. *J. Phys. Chem. C* **2011**, *115* (29), 14193–14203. <https://doi.org/10.1021/jp201671s>.
- (76) Xiao, F.-S.; Wang, L.; Yin, C.; Lin, K.; Di, Y.; Li, J.; Xu, R.; Su, D. S.; Schlögl, R.; Yokoi, T.; et al. Catalytic Properties of Hierarchical Mesoporous Zeolites Templated with a Mixture of Small Organic Ammonium Salts and Mesoscale Cationic Polymers. *Angewandte Chemie International Edition* **2006**, *45* (19), 3090–3093. <https://doi.org/10.1002/anie.200600241>.
- (77) Verboekend, D.; Perez-Ramirez, J. Design of Hierarchical Zeolite Catalysts by Desilication. *Catal. Sci. Technol.* **2011**, *1* (6), 879–890. <https://doi.org/10.1039/c1cy00150g>.
- (78) Cheng, J.; Pei, S.; Yue, B.; Qian, L.; He, C.; Zhou, Y.; He, H. Synthesis and Characterization of Hollow Zeolite Microspheres with a Mesoporous Shell by O/W/O Emulsion and Vapor-Phase Transport Method. *Microporous Mesoporous Mat.* **2008**, *115* (3), 383–388. <https://doi.org/10.1016/j.micromeso.2008.02.009>.
- (79) Kulak, A.; Lee, Y. J.; Park, Y. S.; Kim, H. S.; Lee, G. S.; Yoon, K. B. Anionic Surfactants as Nanotools for the Alignment of Non-Spherical Zeolite Nanocrystals. *Advanced Materials* **2002**, *14* (7), 526–529. [https://doi.org/10.1002/1521-4095\(20020404\)14:7<526::AID-ADMA526>3.0.CO;2-T](https://doi.org/10.1002/1521-4095(20020404)14:7<526::AID-ADMA526>3.0.CO;2-T).
- (80) Naik, S. P.; Chiang, A. S. T.; Thompson, R. W.; Huang, F. C. Formation of Silicalite-1 Hollow Spheres by the Self-Assembly of Nanocrystals. *Chem. Mat.* **2003**, *15* (3), 787–792. <https://doi.org/10.1021/cm020786v>.
- (81) Yang, W. L.; Wang, X. D.; Tang, Y.; Wang, Y. J.; Ke, C.; Fu, S. K. Layer-by-Layer Assembly of Nanozeolite Based on Polymeric Microsphere: Zeolite Coated Sphere and Hollow Zeolite Sphere. *J. Macromol. Sci.-Pure Appl. Chem.* **2002**, *39* (6), 509–526. <https://doi.org/10.1081/MA-120004244>.
- (82) Wang, X. D.; Yang, W. L.; Tang, Y.; Wang, Y. J.; Fu, S. K.; Gao, Z. Fabrication of Hollow Zeolite Spheres. *Chem. Commun.* **2000**, No. 21, 2161–2162. <https://doi.org/10.1039/b006539k>.
- (83) Valtchev, V. Silicalite-1 Hollow Spheres and Bodies with a Regular System of Macrocavities. *Chem. Mat.* **2002**, *14* (10), 4371–4377. <https://doi.org/10.1021/cm020579v>.

- (84) Tuel, A.; Farrusseng, D. Hollow Zeolite Single Crystals: Synthesis Routes and Functionalization Methods. *Small Methods* **2018**, *2* (12), 1800197. <https://doi.org/10.1002/smt.201800197>.
- (85) Groen, J. C.; Bach, T.; Ziese, U.; Donk, A.; de Jong, K. P.; Moulijn, J. A.; Perez-Ramirez, J. Creation of Hollow Zeolite Architectures by Controlled Desilication of Al-Zoned ZSM-5 Crystals. *J. Am. Chem. Soc.* **2005**, *127* (31), 10792–10793. <https://doi.org/10.1021/ja052592x>.
- (86) Ballmoos, R. von; Meier, W. M. Zoned Aluminium Distribution in Synthetic Zeolite ZSM-5. *Nature* **1981**, *289* (5800), 782. <https://doi.org/10.1038/289782a0>.
- (87) Derouane, E.; Detremmerie, S.; Gabelica, Z.; Blom, N. Synthesis and Characterization of Zsm-5 Type Zeolites .1. Physicochemical Properties of Precursors and Intermediates. *Applied Catalysis* **1981**, *1* (3–4), 201–224. [https://doi.org/10.1016/0166-9834\(81\)80007-3](https://doi.org/10.1016/0166-9834(81)80007-3).
- (88) Fodor, D.; Pacosova, L.; Krumeich, F.; van Bokhoven, J. A. Facile Synthesis of Nano-Sized Hollow Single Crystal Zeolites under Mild Conditions. *Chem. Commun.* **2014**, *50* (1), 76–78. <https://doi.org/10.1039/c3cc45336g>.
- (89) Fodor, D.; Krumeich, F.; Hauert, R.; van Bokhoven, J. A. Differences Between Individual ZSM-5 Crystals in Forming Hollow Single Crystals and Mesopores During Base Leaching. *Chem.-Eur. J.* **2015**, *21* (16), 6272–6277. <https://doi.org/10.1002/chem.201406182>.
- (90) Mei, C.; Liu, Z.; Wen, P.; Xie, Z.; Hua, W.; Gao, Z. Regular HZSM-5 Microboxes Prepared via a Mild Alkaline Treatment. *J. Mater. Chem.* **2008**, *18* (29), 3496–3500. <https://doi.org/10.1039/b805385e>.
- (91) Fan, F.; Ling, F.; Wang, S.; Zhang, H.; Chen, X.; Wang, C. One Kind of Hollow Beta Zeolite and Its Preparation Method. CN 104591220, 2013.
- (92) Camblor, M.; Mifsud, A.; Pérez -Pariente, J. Influence of the Synthesis Conditions on the Crystallization of Zeolite Beta. *Zeolites* **1991**, *11* (8), 792–797. [https://doi.org/10.1016/S0144-2449\(05\)80057-0](https://doi.org/10.1016/S0144-2449(05)80057-0).
- (93) Wang, Y.; Lin, M.; Tuel, A. Hollow TS-1 Crystals Formed via a Dissolution-Recrystallization Process. *Microporous Mesoporous Mat.* **2007**, *102* (1–3), 80–85. <https://doi.org/10.1016/j.micromeso.2006.12.019>.
- (94) Anderson, M. W.; Agger, J. R.; Hanif, N.; Terasaki, O. Growth Models in Microporous Materials. *Microporous Mesoporous Mat.* **2001**, *48* (1–3), 1–9. [https://doi.org/10.1016/S1387-1811\(01\)00324-9](https://doi.org/10.1016/S1387-1811(01)00324-9).
- (95) Wang, Y.; Tuel, A. Nanoporous Zeolite Single Crystals: ZSM-5 Nanoboxes with Uniform Intracrystalline Hollow Structures. *Microporous and Mesoporous Materials* **2008**, *113* (1–3), 286–295. <https://doi.org/10.1016/j.micromeso.2007.11.027>.
- (96) Dai, C.; Zhang, A.; Li, L.; Hou, K.; Ding, F.; Li, J.; Mu, D.; Song, C.; Liu, M.; Guo, X. Synthesis of Hollow Nanocubes and Macroporous Monoliths of Silicalite-1 by Alkaline Treatment. *Chem. Mat.* **2013**, *25* (21), 4197–4205. <https://doi.org/10.1021/cm401739e>.
- (97) Dai, C.; Zhang, A.; Liu, M.; Guo, X.; Song, C. Hollow ZSM-5 with Silicon-Rich Surface, Double Shells, and Functionalized Interior with Metallic Nanoparticles and Carbon Nanotubes. *Adv. Funct. Mater.* **2015**, *25* (48), 7479–7487. <https://doi.org/10.1002/adfm.201502980>.
- (98) Li, S.; Tuel, A.; Laprune, D.; Meunier, F.; Farrusseng, D. Transition-Metal Nanoparticles in Hollow Zeolite Single Crystals as Bifunctional and Size-Selective Hydrogenation Catalysts. *Chemistry of Materials* **2015**, *27* (1), 276–282. <https://doi.org/10.1021/cm503921f>.
- (99) Ren, N.; Yang, Z.-J.; Lv, X.-C.; Shi, J.; Zhang, Y.-H.; Tang, Y. A Seed Surface Crystallization Approach for Rapid Synthesis of Submicron ZSM-5 Zeolite with Controllable Crystal Size and Morphology. *Microporous Mesoporous Mat.* **2010**, *131* (1–3), 103–114. <https://doi.org/10.1016/j.micromeso.2009.12.009>.
- (100) Iyoki, K.; Itabashi, K.; Okubo, T. Seed-Assisted, One-Pot Synthesis of Hollow Zeolite Beta without Using Organic Structure-Directing Agents. *Chem. Asian J.* **2013**, *8* (7), 1419–1427. <https://doi.org/10.1002/asia.201300365>.
- (101) Okamoto; You; Iwasoto. Synthesis Methods and Hollowzeolite, and Drug Carrier Comprising the Hollow Zeolite. Japanese Patent JP 2009-269788, 2009.

- (102) Okamoto, M. Synthesis of Core-Shell Structured Porous Materials and Applications as Catalysts and Precursors for Hollow Porous Materials. *J. Jpn. Pet. Inst* **2013**, *56* (4), 198–205.
- (103) Pagis, C.; Prates, A. R. M.; Bats, N.; Tuel, A.; Farrusseng, D. High-Silica Hollow Y Zeolite by Selective Desilication of Dealuminated NaY Crystals in the Presence of Protective Al Species. *Crystengcomm* **2018**, *20* (11), 1564–1572. <https://doi.org/10.1039/c8ce00121a>.
- (104) Yuan, D.; Kang, C.; Wang, W.; Li, H.; Zhu, X.; Wang, Y.; Gao, X.; Wang, B.; Zhao, H.; Liu, C.; et al. Creation of Mesoporous Hollow Y Zeolite by Selective Demetallation of an Artificial Heterogeneous Al Distributed Zeolite Crystal. *Catal. Sci. Technol.* **2016**, *6* (23), 8364–8374. <https://doi.org/10.1039/c6cy01841f>.
- (105) Gates, B. Supported Metal-Clusters - Synthesis, Structure, and Catalysis. *Chem. Rev.* **1995**, *95* (3), 511–522. <https://doi.org/10.1021/cr00035a003>.
- (106) Farrusseng, D.; Tuel, A. Perspectives on Zeolite-Encapsulated Metal Nanoparticles and Their Applications in Catalysis. *New J. Chem.* **2016**, *40* (5), 3933–3949. <https://doi.org/10.1039/C5NJ02608C>.
- (107) Hansen, T. W.; Delariva, A. T.; Challa, S. R.; Datye, A. K. Sintering of Catalytic Nanoparticles: Particle Migration or Ostwald Ripening? *Accounts Chem. Res.* **2013**, *46* (8), 1720–1730. <https://doi.org/10.1021/ar3002427>.
- (108) Schwarz, J.; Contescu, C.; Contescu, A. Methods for Preparation of Catalytic Materials. *Chem. Rev.* **1995**, *95* (3), 477–510. <https://doi.org/10.1021/cr00035a002>.
- (109) Philippaerts, A.; Paulussen, S.; Turner, S.; Lebedev, O. I.; Van Tendeloo, G.; Poelman, H.; Bulut, M.; De Clippel, F.; Smeets, P.; Sels, B.; et al. Selectivity in Sorption and Hydrogenation of Methyl Oleate and Elaidate on MFI Zeolites. *J. Catal.* **2010**, *270* (1), 172–184. <https://doi.org/10.1016/j.jcat.2009.12.022>.
- (110) Ribeiro, F.; Marcilly, C.; Thomas, G. Dépôt Homogène de Platine Sur Zéolithe Par Échange Cationique Avec Compétition. *C. R. Acad. Sc. Paris* **1978**.
- (111) Yang, O.; Woo, S.; Ryoo, R. Xe-129 Nmr Proof for the Distribution of Platinum Species During Pt/NaY Preparation by H₂ptcl₆ Impregnation and Pt(Nh-3)4(2+) Cation-Exchange Methods. *J. Catal.* **1990**, *123* (2), 375–382. [https://doi.org/10.1016/0021-9517\(90\)90136-8](https://doi.org/10.1016/0021-9517(90)90136-8).
- (112) Maldonado-Hodar, F. J.; Ribeiro, M. F.; Silva, J. M.; Antunes, A. P.; Ribeiro, F. R. Aromatization of N-Heptane on Pt/Alkali or Alkali-Earth Exchanged Beta Zeolite Catalysts: Catalyst Deactivation and Regeneration. *J. Catal.* **1998**, *178* (1), 1–13. <https://doi.org/10.1006/jcat.1998.2154>.
- (113) Ostgard, D.; Kustov, L.; Poepelmeier, K.; Sachtler, W. Comparison of Pt/KI Catalysts Prepared by Ion-Exchange or Incipient Wetness Impregnation. *J. Catal.* **1992**, *133* (2), 342–357. [https://doi.org/10.1016/0021-9517\(92\)90245-D](https://doi.org/10.1016/0021-9517(92)90245-D).
- (114) Gucci, L.; Kiricsi, I. Zeolite Supported Mono- and Bimetallic Systems: Structure and Performance as CO Hydrogenation Catalysts. *Appl. Catal. A-Gen.* **1999**, *186* (1–2), 375–394. [https://doi.org/10.1016/S0926-860X\(99\)00156-8](https://doi.org/10.1016/S0926-860X(99)00156-8).
- (115) Tahri, Z.; Luchez, F.; Yordanov, I.; Poizat, O.; Moissette, A.; Valtchev, V.; Mintova, S.; Mostafavi, M.; Waele, V. D. Nanosecond Probing of the Early Nucleation Steps of Silver Atoms in Colloidal Zeolite by Pulse Radiolysis and Flash Photolysis Techniques. *Res. Chem. Intermed.* **2009**, *35* (4), 379–388. <https://doi.org/10.1007/s11164-009-0049-1>.
- (116) Chen, C.; Zhu, J.; Chen, F.; Meng, X.; Zheng, X.; Gao, X.; Xiao, F.-S. Enhanced Performance in Catalytic Combustion of Toluene over Mesoporous Beta Zeolite-Supported Platinum Catalyst. *Appl. Catal. B-Environ.* **2013**, *140*, 199–205. <https://doi.org/10.1016/j.apcatb.2013.03.050>.
- (117) Chen, C.; Wu, Q.; Chen, F.; Zhang, L.; Pan, S.; Bian, C.; Zheng, X.; Meng, X.; Xiao, F.-S. Aluminium-Rich Beta Zeolite-Supported Platinum Nanoparticles for the Low-Temperature Catalytic Removal of Toluene. *J. Mater. Chem. A* **2015**, *3* (10), 5556–5562. <https://doi.org/10.1039/c4ta06407k>.
- (118) Martínez-Iñesta, M. M.; Lobo, R. F. Investigation of the Structure of Platinum Clusters Supported in Zeolite Beta Using the Pair Distribution Function. *J. Phys. Chem. C* **2007**, *111* (24), 8573–8579. <https://doi.org/10.1021/jp061728q>.

- (119) Arribas, M. A.; Marquez, F.; Martinez, A. Activity, Selectivity, and Sulfur Resistance of Pt/WO_x-ZrO₂ and Pt/Beta Catalysts for the Simultaneous Hydroisomerization of n-Heptane and Hydrogenation of Benzene. *J. Catal.* **2000**, *190* (2), 309–319. <https://doi.org/10.1006/jcat.2000.2768>.
- (120) Kumar, M. S.; Holmen, A.; Chen, D. The Influence of Pore Geometry of Pt Containing ZSM-5, Beta and SBA-15 Catalysts on Dehydrogenation of Propane. *Microporous Mesoporous Mat.* **2009**, *126* (1–2), 152–158. <https://doi.org/10.1016/j.micromeso.2009.05.031>.
- (121) Gallezot, P.; Blanc, B.; Barthomeuf, D.; Dasilva, M. *Selective Hydrogenation of Cinnamaldehyde Controlled by Host-Guest Interactions in Beta-Zeolite*; Weitkamp, J., Karge, H. G., Pfeifer, H., Holderich, W., Eds.; Elsevier Science Publ B V: Amsterdam, 1994; Vol. 84.
- (122) Knapp, C.; Obuchi, A.; Uchisawa, J. O.; Kushiya, S.; Avila, P. Method for Selective Removal of Supported Platinum Particles from External Zeolite Surfaces: Characterisation of and Application to a Catalyst for the Selective Reduction of Nitrogen Oxide by Hydrocarbons. *Microporous Mesoporous Mat.* **1999**, *31* (1–2), 23–31. [https://doi.org/10.1016/S1387-1811\(99\)00054-2](https://doi.org/10.1016/S1387-1811(99)00054-2).
- (123) Nakao, Y. Dissolution of Noble-Metals in Halogen Halide Polar Organic-Solvent Systems. *J. Chem. Soc.-Chem. Commun.* **1992**, No. 5, 426–427. <https://doi.org/10.1039/c39920000426>.
- (124) Nakao, Y.; Sone, K. Reversible Dissolution/Deposition of Gold in Iodine-Iodide-Acetonitrile Systems. *Chem. Commun.* **1996**, No. 8, 897–898. <https://doi.org/10.1039/cc9960000897>.
- (125) Wu, Z.; Goel, S.; Choi, M.; Iglesia, E. Hydrothermal Synthesis of LTA-Encapsulated Metal Clusters and Consequences for Catalyst Stability, Reactivity, and Selectivity. *J. Catal.* **2014**, *311*, 458–468. <https://doi.org/10.1016/j.jcat.2013.12.021>.
- (126) Goel, S.; Wu, Z.; Zones, S. I.; Iglesia, E. Synthesis and Catalytic Properties of Metal Clusters Encapsulated within Small-Pore (SOD, GIS, ANA) Zeolites. *J. Am. Chem. Soc.* **2012**, *134* (42), 17688–17695. <https://doi.org/10.1021/ja307370z>.
- (127) de Lucas, A.; Ramos, M. J.; Dorado, F.; Sanchez, P.; Valverde, J. L. Influence of the Si/Al Ratio in the Hydroisomerization of n-Octane over Platinum and Palladium Beta Zeolite-Based Catalysts with or without Binder. *Appl. Catal. A-Gen.* **2005**, *289* (2), 205–213. <https://doi.org/10.1016/j.apcata.2005.05.001>.
- (128) Zheng, J.; Dong, J.; Xu, Q.; Liu, Y.; Yan, A. Comparison Between Beta-Zeolites and L-Zeolites Supported Platinum for N-Hexane Aromatization. *Appl. Catal. A-Gen.* **1995**, *126* (1), 141–152. [https://doi.org/10.1016/0926-860X\(95\)80149-9](https://doi.org/10.1016/0926-860X(95)80149-9).
- (129) Ping, L.; Yue, Y.; Xingguang, Z.; Jun, W. Rare Earth Metals Ion-Exchanged Beta-Zeolites as Supports of Platinum Catalysts for Hydroisomerization of n-Heptane. *Chin. J. Chem. Eng.* **2011**, *19* (2), 278–284. [https://doi.org/10.1016/S1004-9541\(11\)60166-3](https://doi.org/10.1016/S1004-9541(11)60166-3).
- (130) Kumar, N.; Masloboisichikova, O. V.; Kustov, L. M.; Heikkila, T.; Salmi, T.; Murzin, D. Y. Synthesis of Pt Modified ZSM-5 and Beta Zeolite Catalysts: Influence of Ultrasonic Irradiation and Preparation Methods on Physico-Chemical and Catalytic Properties in Pentane Isomerization. *Ultrason. Sonochem.* **2007**, *14* (2), 122–130. <https://doi.org/10.1016/j.ultsonch.2006.05.001>.
- (131) Smirniotis, P.; Ruckenstein, E. Platinum Impregnated Zeolite-Beta as a Reforming Catalyst. *Catal. Lett.* **1993**, *17* (3–4), 341–347. <https://doi.org/10.1007/BF00766157>.
- (132) Ho, L. W.; Hwang, C. P.; Lee, J. F.; Wang, I.; Yeh, C. T. Reduction of Platinum Dispersed on Dealuminated Beta Zeolite. *J. Mol. Catal. A-Chem.* **1998**, *136* (3), 293–299. [https://doi.org/10.1016/S1381-1169\(98\)00081-8](https://doi.org/10.1016/S1381-1169(98)00081-8).
- (133) Lee, J. K.; Rhee, H. K. Sulfur Tolerance of Zeolite Beta-Supported Pd-Pt Catalysts for the Isomerization of n-Hexane. *J. Catal.* **1998**, *177* (2), 208–216. <https://doi.org/10.1006/jcat.1998.2100>.
- (134) Tsai, K.-Y.; Wang, I.; Tsai, T.-C. Zeolite Supported Platinum Catalysts for Benzene Hydrogenation and Naphthene Isomerization. *Catal. Today* **2011**, *166* (1), 73–78. <https://doi.org/10.1016/j.cattod.2010.06.009>.

- (135) Martinez-Inesta, M. A. M.; Lobo, R. F. Investigation of the Structure of Platinum Clusters Supported in Zeolite Beta Using the Pair Distribution Function. *J. Phys. Chem. C* **2007**, *111* (24), 8573–8579. <https://doi.org/10.1021/jp061728q>.
- (136) Goel, S.; Zones, S. I.; Iglesia, E. Encapsulation of Metal Clusters within MFI via Interzeolite Transformations and Direct Hydrothermal Syntheses and Catalytic Consequences of Their Confinement. *J. Am. Chem. Soc.* **2014**, *136* (43), 15280–15290. <https://doi.org/10.1021/ja507956m>.
- (137) Fodor, D.; Ishikawa, T.; Krumeich, F.; van Bokhoven, J. A. Synthesis of Single Crystal Nanoreactor Materials with Multiple Catalytic Functions by Incipient Wetness Impregnation and Ion Exchange. *Adv. Mater.* **2015**, *27* (11), 1919-+.
<https://doi.org/10.1002/adma.201404628>.
- (138) Li, S.; Boucheron, T.; Tuel, A.; Farrusseng, D.; Meunier, F. Size-Selective Hydrogenation at the Subnanometer Scale over Platinum Nanoparticles Encapsulated in Silicalite-1 Single Crystal Hollow Shells. *Chemical Communications* **2014**, *50* (15), 1824.
<https://doi.org/10.1039/c3cc48648f>.
- (139) Li, S.; Burel, L.; Aquino, C.; Tuel, A.; Morfin, F.; Rousset, J.-L.; Farrusseng, D. Ultimate Size Control of Encapsulated Gold Nanoparticles. *Chemical Communications* **2013**, *49* (76), 8507.
<https://doi.org/10.1039/c3cc44843f>.
- (140) Pagis, C.; Meunier, F.; Schuurman, Y.; Tuel, A.; Dodin, M.; Martinez-Franco, R.; Farrusseng, D. Demonstration of Improved Effectiveness Factor of Catalysts Based on Hollow Single Crystal Zeolites. *ChemCatChem* **2018**, *10* (10), 4525– 4529.

Chapter II – Experimental

1. Material synthesis

In this experimental part we will describe in detail the different syntheses carried out during this thesis. The synthesis procedures are presented according to the “*CIT-6 Dissolution-Recrystallization*” method, then the different metal introduction studies and finally, the synthesis performed for the “*Beta Zeolite Dissolution*” approach.

1.1. List of reactants

Table 1 shows the list of reactants used for the synthesis of materials presented in this thesis.

Table 1 - Characteristics of the main reactants used for this thesis.

Type	Reactants	Composition	Phase	Supplier
Si source	Ludox® HS-40 (SiO ₂)	40 wt. % suspension in H ₂ O Na ₂ O : 0,4 wt. %	Colloidal	Sigma Aldrich
Si source	Ludox® HS-30 (SiO ₂)	30 wt. % suspension in H ₂ O Na ₂ O : 0,4 wt. %	Colloidal	Sigma Aldrich
Si source	Aerosil® 200 (SiO ₂)	> 98,9 wt. %	Solid	Evonik Industries
Al source	Sodium aluminate (NaAlO ₂)	Al ₂ O ₃ : 50–56 (53 wt. %) Na ₂ O : 40–45 (42 wt. %) H ₂ O : > 5 wt. %	Solid	Honeywell Riedel-de Haën

Type	Reactants	Composition	Phase	Supplier
Al source	Aluminium powder (Al)	> 99 wt. %	Solid	Sigma Aldrich
Zn source	Zinc acetate dihydrate (Zn(CH ₃ CO ₂) ₂ ·2H ₂ O)	> 98 wt. %	Solid	Sigma Aldrich
Base	Sodium hydroxide (NaOH)	≥ 97,0 wt. %	Solid	Carlo Erba
Base	Sodium carbonate (Na ₂ CO ₃)	≥ 99,5 wt. %	Solid	Fluka
Base	Ammonium hydroxide (NH ₄ OH)	25 wt. % NH ₃ in H ₂ O	Liquid	Sigma Aldrich
Base	Lithium hydroxide (LiOH)	> 98 wt. %	Solid	Sigma Aldrich
Acid	Nitric acid (HNO ₃)	~ 70 wt. % in H ₂ O	Liquid	Sigma Aldrich
Salt	Sodium chloride (NaCl)	≥ 99,5 wt. %	Solid	Fluka
Salt	Potassium chloride (KCl)	≥ 99 wt. %	Solid	Sigma Aldrich
SDA	Tetraethylammonium hydroxide (TEAOH)	35 wt. % in H ₂ O	Liquid	Sigma Aldrich
SDA	Tetramethylammonium bromide (TMABr)	> 98 wt. %	Solid	Sigma Aldrich
SDA	Tetraethylammonium bromide (TEABr)	> 98 wt. %	Solid	Sigma Aldrich
SDA	Tetrapropylammonium bromide (TPABr)	> 98 wt. %	Solid	Sigma Aldrich
SDA	Tetrabutylammonium bromide (TBABr)	> 98 wt. %	Solid	Sigma Aldrich
Salt	Ammonium nitrate (NH ₄ NO ₃)	≥ 95 wt. %	Solid	Merck
Pt source	Tetraamine platinum (II) nitrate (Pt(NH ₃) ₄ (NO ₃) ₂)	> 99 wt. %	Solid	Strem chemicals

Type	Reactants	Composition	Phase	Supplier
Pt source	Chloroplatinic acid ($H_2(PtCl_6)$)	25 wt. % Pt	Liquid	Johnson Matthey
Reducing agent	Sodium borohydride ($NaBH_4$)	≥ 96 wt. %	Solid	Sigma Aldrich
Solvent	Distilled water	-----	Liquid	Lab
Solvent	Acetonitrile (C_2H_3N)	> 99.8 wt. %	Liquid	Sigma Aldrich
Halogen	Bromine (Br_2)	> 99 wt. %	Liquid	Sigma Aldrich

1.2. “CIT-6 Dissolution-Recrystallization” approach

This synthesis is a double step process which includes the synthesis of CIT-6 crystals and hydrothermal treatment of these to yield hollow Beta zeolite crystals, Figure 1.

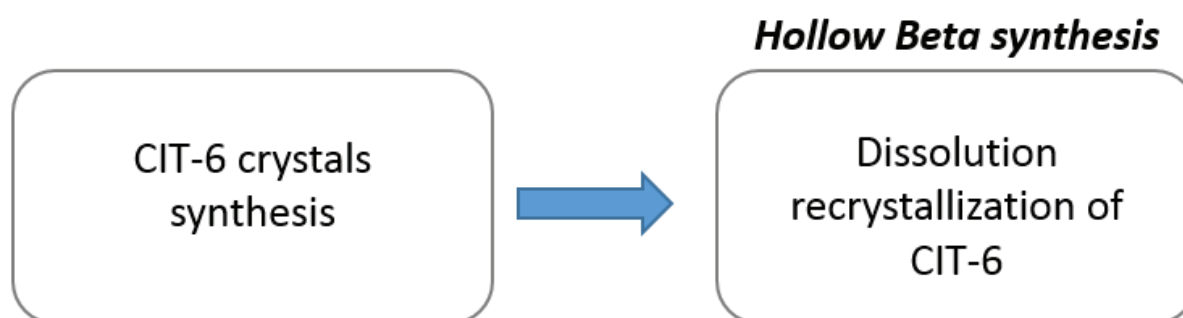


Figure 1 – Diagram of the two step process for the synthesis of hollow Beta using the “CIT-6 Dissolution-Recrystallization” approach.

1.2.1. CIT-6 crystals

CIT-6 crystals were synthesized by hydrothermal treatment of zincosilicate gels and TEAOH with the following molar composition: $SiO_2 : 0.05 LiOH : 0.65 TEA : 0.03 Zn(CH_3CO_2)_2 : 30 H_2O$. Initially, 0.24 g of LiOH and 53.5 ml of TEAOH (35 wt. %) were dissolved in 54.0 ml of distilled water, followed by the addition of 1.33 g of zinc acetate dihydrate ($Zn(CH_3CO_2)_2 \cdot 2H_2O$). Ludox HS-40 (30.00 g) was added dropwise, and the resulting mixture was stirred for 1 h at 40 °C to

yield a clear solution. The final gel was divided into four equal portions, each of them being crystallized in a 48 ml Teflon-lined stainless-steel autoclave. Crystallizations were performed by thermal treatment under static conditions, between 140-150 °C, for 68 h to 9 days. The product was washed with distilled water, separated by centrifugation, and dried overnight at 80 °C. Calcination was carried out in air at 550 °C for 10 hours with a heating rate of 87.5 °C/h.

1.2.2. Hollow Beta by “CIT-6 Dissolution-Recrystallization” approach

The seed-assisted synthesis of hollow Beta was performed by adding **as-made** CIT-6 crystals to a SDA-free aluminosilicate gel with the following molar composition: SiO₂ : 0.01 Al₂O₃ : 0.3 NaOH : 20 H₂O. CIT-6 seeds, which represented 10 wt. % of the total silica source, were synthesized as described just above, hydrothermal synthesis carried out at 145 °C for 4 days. First, 3.054 g of NaOH was added to 48.0 g of distilled water and stirred until dissolution (400 rpm), followed by 0.256 g of NaAlO₂. Then, 0.8 g of CIT-6 crystals was added to the solution, which was gently stirred (200 rpm) until the dispersion became homogeneous. Finally, 7.2 g of Aerosil 200 were added as the silica source, with vigorous stirring (300 rpm) during 10 min, until a homogeneous thick gel was obtained. The gel was transferred to two 48 ml Teflon-lined autoclaves and subjected to hydrothermal treatment at 150 °C for 22 h under dynamic conditions. After hydrothermal treatment, the product was washed abundantly with distilled water heated at 80 °C, and separated by filtration. The resulting hollow Beta crystals were dried overnight at 80 °C. They were then calcined in air at 550 °C for 10 hours with a heating rate of 87.5 °C/h.

1.3. Introduction of metal precursors into zeolite

The introduction of Pt NPs in hollow Beta zeolites is a multi-step process. The introduction of metal can be done either by impregnation or ionic-exchange. It can be done directly on the calcined hollow Beta crystal, or it can be introduced directly on the CIT-6 crystals before the hollow Beta zeolite synthesis. The type of precursor, the type of introduction method, and the fact that the metal is introduced directly on the hollow Beta crystals or before on the CIT-6 crystals, has consequences on the location and dispersion of the Pt NPs, as explained in chapter III.

1.3.1. Impregnation over hollow Beta crystals

The calcined hollow Beta crystals were impregnated with an aqueous solution of the corresponding metal salts, with a volume of solution superior to the porous volume of the crystal itself. The zeolite is first heated at 400 °C in a closed oven for 3h. After cooling down to 100 °C, the zeolite is then impregnated with the aqueous solution.

Pt(NH₃)₄(NO₃)₂

For impregnation with Pt(NH₃)₄(NO₃)₂, zeolite was dispersed in a 0.3M solution. The volume of solution depended on the amount of Pt wt. % wanted. Since the solution was highly concentrated in Pt(NH₃)₄(NO₃)₂, for small Pt wt. % (up to approx. 5 wt. % of Pt) the volume of solution was very small comparing to the zeolite volume, creating a “sticky paste” instead of a liquid dispersion. The mixture (the so-called paste) was manually stirred with a spatula for at least 5 min. The “wet” zeolite was then left for maturation in a closed flask for at least 12 h at room temperature and finally dried in an oven at 80 °C. Reduction by H₂ flow was followed as described in “Reduction with H₂” in this chapter.

H₂PtCl₆

For impregnations with H₂PtCl₆ solution, 185 mg Pt/L, the zeolite was added to the solution under stirring and left in oil bath at 50 °C until evaporation. The final powder was dried in an oven at 80 °C. Reduction by H₂ flow was followed as described in “Reduction with H₂” in this chapter.

1.3.2. Competitive ionic-exchange over hollow Beta crystals

The calcined hollow Beta zeolite was exchanged twice with NH₄⁺ using the following conditions: 10 ml NH₄NO₃ (1 M) g⁻¹ zeolite, 353 K, 8 h stirring, pH 7–8. After each ion exchange, the product was recovered by centrifugation and washed several times with distilled water, followed by drying at 80 °C. Platinum was loaded into the support materials by ion exchange, using Pt(NH₃)₄(NO₃)₂ as precursor, 1600 ppm (mg/L), 0.01 g_{zeol}/ml. The exchange was carried out for 23 h at 80 °C and under stirring, followed by centrifugation with distilled water, and drying at 80 °C. The ionic exchange was done in presence of NH₄⁺ ions (NH₄NO₃), using a NH₄/Pt

atomic ratio of 1. Reduction by H₂ flow was followed as described in “Reduction with H₂” in this chapter.

1.3.3. Impregnation over CIT-6 crystals

As-made CIT-6 crystals were heated at 100 °C in an oven for 2 h. Impregnation was carried out either by Pt(NH₃)₄(NO₃)₂ solution, either by H₂PtCl₆ solution.

Pt(NH₃)₄(NO₃)₂

Pt was introduced by impregnation of a 0.3 M Pt(NH₃)₄(NO₃)₂ solution, 2 wt. % Pt, onto as-made CIT-6 crystals, that were previously heated up to 100 °C. For example, for 0.270 g of CIT-6, 0.091 ml of solution was added with adjustable volume pipettes, and stirred with a spatula for at least 5 min, until homogenization. The “wet” crystals were left for maturation overnight at room temperature in a closed glass flask. Then the wet zeolite was dried in the oven at 80 °C.

H₂PtCl₆

Pt was introduced by impregnation of an H₂PtCl₆ aqueous solution, 185 mg Pt/L. The volume of solution depended on the amount of Pt wt. % wanted. The support was added to the solution under stirring, left in an oil bath at 50 °C until evaporation. The final powder was dried in the oven at 80 °C.

1.3.4. Reduction with H₂

All metal containing crystals are further reduced under hydrogen flow to get metallic particles. The general conditions are H₂ flow of 75 cc/min, reduction temperature of 300 °C for 3h, with temperature ramp of 5 °C/min. When reduction was performed over Pt/CIT-6 crystals, this was performed at 150 °C.

1.3.5. Reduction of Pt/CIT-6 with NaBH₄

Freshly made NaBH₄ solution (exactly 1 min old), was added dropwise in the Pt/CIT-6 containing glass flak, and stirred for 1 h (0.05 g_{zeol}/ml, NaBH₄/Pt=20). Finally, the crystals were washed and separated by centrifugation. The resulting Pt/CIT-6 was then dried overnight at 80 °C.

1.3.6. Br₂ treatment

Hollow Beta crystals with supported Pt NPs were treated with four different halogen-halide-organic solvent systems, in which the halogen and organic solvent were always Br₂ and acetonitrile, respectively. The halides used were tetramethyl- (TMABr), tetraethyl- (TEABr), tetrapropyl- (TPABr) and tetrabutyl- (TBABr) ammonium bromides (procedure details in supporting information). These four systems were used under the same conditions: 10 mg_{zeol}/ml_{sol}, %V_{Br₂}/V_{sol} = 0.2 %, molar ratio of [Halide-Br]/[Br₂]= 2. For each treatment, Pt/Beta was refluxed for 7 h at 80 °C. After cooling down, the zeolite was recovered by centrifugation and washed with acetonitrile at room temperature, refluxed twice with acetonitrile at 80 °C for 30 min and finally dried overnight at 80 °C.

1.4. “Beta Zeolite Dissolution” approach

This approach includes the synthesis of zeolite Beta crystals and the subsequent post-treatments:

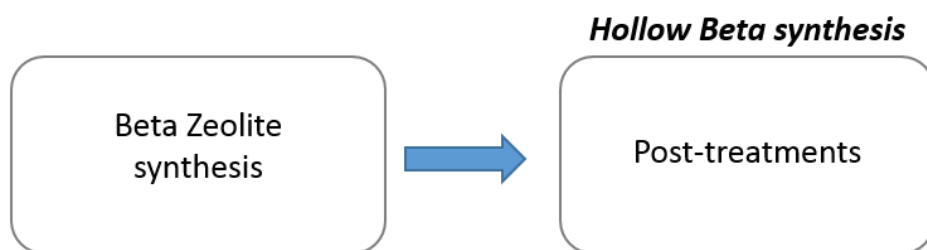


Figure 2 - Diagram of the two step process for the synthesis of hollow Beta using the "Beta Zeolite Dissolution" approach.

1.4.1. Zeolite Beta synthesis

Beta zeolites were synthesized following the recipe reported by Cambor *et al.*^{1,2} In a typical preparation, 68.27 g of TEOH (35 wt. % aqueous solution), 0.353 g of NaCl, 0.96 g of KCl and 31 g of H₂O were mixed together. Then, 19.69 g of SiO₂ (Aerosil 200) were slowly added by portions and the obtained gel was vigorously stirred until complete homogenization. Finally, a solution containing 0.22 g of NaOH and 1.193 g of NaAlO₂ in 13.3 g of H₂O was added and stirring was maintained for 15 min. The thick gel, with the following composition: 1.97 Na₂O: 1.00 K₂O: 12.5 (TEA)₂O: 1.00 Al₂O₃: 50 SiO₂: 750 H₂O: 2.9 HCl was then transferred into 2 x 100 mL autoclaves and heated under dynamic conditions (60 rpm) at 135 °C for 20 h. After crystallization, autoclaves were quenched in cold water; the solid recovered by centrifugation, washed with deionized water and dried at 110 °C overnight. Calcination was performed in static air at 550 °C for 10 hours with a heating rate of 87.5 °C/h.

1.4.2. Post-synthesis treatments

In a standard treatment,³ 1.12 g of NaOH and 0.35 g of NaAlO₂ were dissolved in 50 mL of H₂O. Then, 1 g of calcined Beta zeolite was added and the suspension was stirred at room temperature for 30 min. It was then transferred into a 100 mL Teflon-lined, stainless-steel autoclave and heated at 90 °C for 5 h under static conditions. After treatment, the zeolite was recovered by centrifugation, washed with distilled water and dried at 80 °C overnight.

During this thesis different treatments were also performed, by changing:

- 1) the amount of aluminum (0.085g and 0g of NaAlO₂ for samples denoted 25%Al-Hollowβ and 0%Al-Hollowβ, respectively)
- 2) the pH value, by adjusting the amount of NaOH: 0.107 g for pH=13 and 0.230g for pH=13.5.
- 3) partially NaOH by TEOH - sample TEA-Hollowβ: in this case 0.463 g of NaOH and 0.35 g NaAlO₂ were dissolved in 49 mL of distilled water. Then, 8.82 ml of TEOH were added and the solution was stirred for 10 min. Then, 1 g of calcined Beta zeolite was added and the suspension was stirred at room temperature for 30 min. It was then transferred into a 100 mL

Teflon-lined, stainless-steel autoclave and heated at 135 °C for 5 h under static conditions. After treatment, the zeolite was recovered by centrifugation, washed with distilled water and dried at 80 °C overnight.

1.5. Samples used for ZLC studies

There were synthesized three Beta samples for the ZLC studies presented in chapter IV: one hollow samples denoted as **HollowBeta** and two bulk samples denoted as **Bulk1Beta**, **Bulk2Beta**. The synthesis routes are represented in Figure 3 and described below.

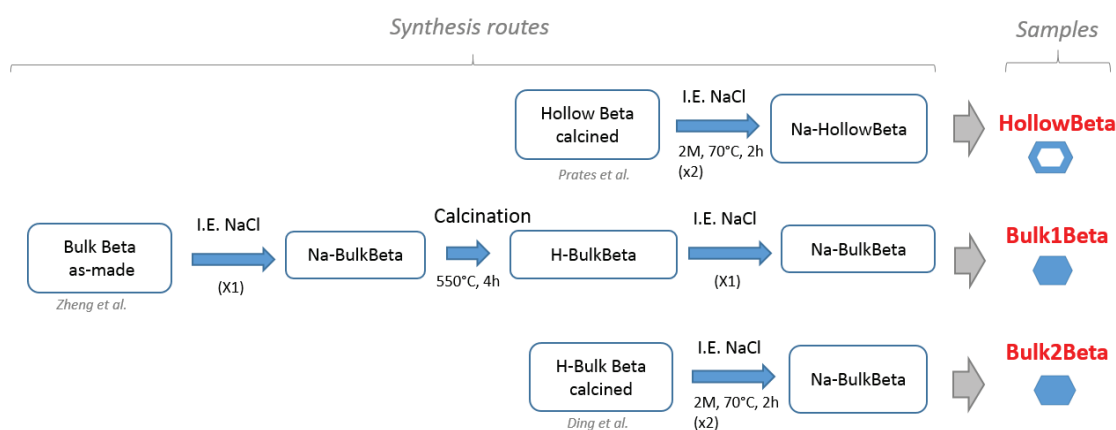


Figure 3 – Synthesis scheme of the Beta samples used for ZLC tests in chapter IV: **HollowBeta**, **Bulk1Beta** and **Bulk2Beta**.

HollowBeta was first prepared as the hollow Beta crystals prepared by the “*CIT-6 Dissolution-Recrystallization*” approach described earlier in this chapter. The calcined crystals were exchanged twice with a 2M NaCl solution, 0.1 g_{zeol}/ml, in order to ensure the greatest elimination of protons. The ion exchange process was carried out at 70 °C for 2h, under vigorous stirring. The dispersion was centrifuged and the solid washed and dried overnight at 80 °C.

Bulk1Beta was first prepared similarly as reported by Zheng et al.⁴ A gel of Beta zeolite was first prepared with molar composition of the gel: 2.2 Na₂O : 20 SiO₂ : Al₂O₃ : 4.6 (TEA)₂O : 2.3 (NH₄)₂O : 401 H₂O. Initially, 0.64 g of NaOH, 18.07 g of TEABr and 1.76 g of NaAlO₂ were dissolved in 36.7 g of distilled water, followed by the addition of 5.63 ml of NH₄OH. Ludox HS-30 (36.70 g) was added slowly with vigorous stirring. The mixture was stirred at room temperature for 2 h, then transferred into a 100 mL autoclave and kept at 140 °C for 10 days without stirring. The obtained zeolite was filtered, washed with distilled water and dried at 80

°C. The as-made crystals were exchanged with a 2M NaCl solution, 0.1 g_{zeol}/ml, similarly to HollowBeta sample. Then, calcination was carried out in air at 550 °C for 4h hours with a heating rate of 87.5 °C/h followed by another ion-exchange with NaCl in similar conditions.

Bulk2Beta was first prepared similarly as reported by Ding et al.⁵ A gel of Beta zeolite was first prepared with molar composition of the gel: 10.5 TEAOH : 50 SiO₂ : Al₂O₃ : 750 H₂O. Initially, 9.6 ml of TEAOH 35% were mixed with 23.6 ml of distilled water. After stirring, the solution is split into solution A and solution B (10 ml of solution). Then, 6.67 g of Aerosil 200 was slowly added to solution A with vigorous stirring. Then, Al powder (0.12 g) were dissolved in solution B, with vigorous stirring for 10 min. Finally, solution A and B are mixed and stirred at room temperature for 4 h. Then the gel was transferred into two 48 mL autoclave and kept at 140 °C for 7 days while stirring. The obtained zeolite was centrifuged, washed with distilled water and dried at 80 °C. Calcination step and ion-exchange step were carried out similarly to HollowBeta sample.

1.6. Samples used for n-C₁₆ hydroisomerization reaction

There were synthesized three beta samples for the n-C₁₆ hydroisomerization reaction presented in chapter V: one hollow sample denoted as **20Hollow** and two bulk samples denoted as **17Bulk** and **22Bulk**. The synthesis routes are represented in Figure 4 and described below.

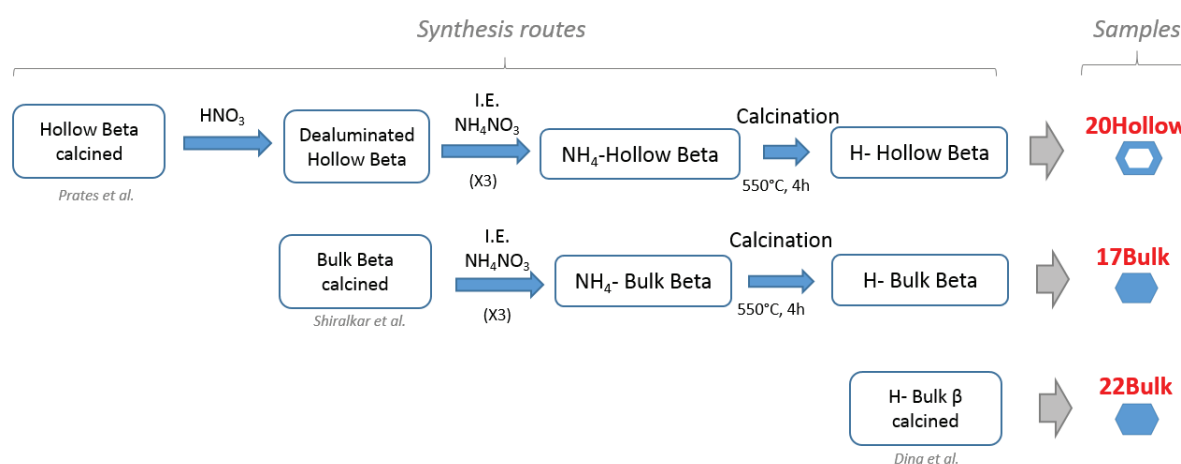


Figure 4 - Synthesis scheme of the Beta samples used for the n-C₁₆ hydroisomerization reaction in chapter V: 20Hollow, 17Bulk and 22Bulk.

20Hollow sample was first prepared as the hollow Beta crystals prepared by the “CIT-6 Dissolution-Recrystallization” approach described earlier in this chapter. The dealumination

step was carried out by a single step treatment with HNO_3 , as described by Lami et al.⁶ The zeolite was dealuminated by dispersing the calcined hollow Beta crystals in a solution of nitric acid, 0.0875M, 10.0 $\text{g}_{\text{zeol}}/\text{ml}$. The suspension was heated to 80 °C with stirring and maintained at this temperature for 4h30min. The crystals were recovered by filtration, washed with distilled water and dried overnight at 80 °C. This material was exchanged 3 times with a NH_4NO_3 solution, 1 M and 10ml/ g_{zeol} , in order to get the NH_4 form of the zeolite. After recovering by centrifugation, washing, and drying overnight at 80 °C, the samples were calcined at 550 °C for 4h hours with, a heating rate of 87.5 °C/h, in order to get into the protonic form.

17Bulk sample was first prepared similarly to Shiralkar et al.⁷ The molar composition of the gel was: 47 SiO_2 : 3.1 Na_2 : 15 $(\text{NH}_4)\text{O}$: 6.7 $(\text{TEA})_2\text{O}$: Al_2O_3 : 656 H_2O . For this synthesis, two solutions were prepared simultaneously. For solution A, 31.1 ml of TEAOH were mixed with 15 ml of distilled water under vigorous stirring. Then 25.7 ml of NH_4OH were added and solution is left under vigorous stirring for 15 min. For Solution B, 0.78 g of NaOH and 1.06 g of $\text{Na}_2\text{Al}_2\text{O}_4$ were dissolved in 12.3 ml of distilled water, and left under vigorous stirring during 1-15 min. Then, solution A and B were slowly mixed under vigorous stirring. Finally, Ludox HS-30 (51.73 g) was added slowly with vigorous stirring. The mixture was stirred at room temperature for 1 h, then transferred into four 23 mL autoclave and kept at 140 °C for 10 days without stirring. The obtained zeolite was filtered, washed with distilled water and dried at 80 °C. Calcination was carried out in air at 550 °C for 10 hours with a heating rate of 87.5 °C/h. This material was exchanged 3 times with a NH_4NO_3 solution, 1 M and 10ml/ g_{zeol} , in order to get the NH_4 form of the zeolite. After recovering by centrifugation, washing, and drying overnight at 80 °C, the samples were calcined at 550 °C for 4h hours with, a heating rate of 87.5 °C/h, in order to get into the protonic form.

22Bulk was firstly prepared as the BVeta zeolite for **Bulk2Beta** described earlier in this chapter. However, for 22Bulk there were no exchanges with NaCl, in order to keep the sample in the protonic form.

2. Characterization techniques

2.1. Powder X-ray diffraction

Powder X-ray diffraction (PXRD) patterns of the solid are recorded on a Bruker (Siemens) D5005 diffractometer using $\text{CuK}\alpha$ radiation. Diffractogrammes are collected between 4 and

80° (2 θ) with steps of 0.02° and 1 s per step. This technique is used to verify the crystallinity of zeolite related materials and estimate the metal particle size when possible.

In this thesis, PXRD patterns (in this thesis referred as XRD) were used to:

- Identify the crystalline phases and their purity
- Evaluate the crystallinity of the sample, by comparing the area of certain peaks with the area of the peaks of a reference sample.
- Estimate the Pt metallic crystallite sizes for high metal content samples.

2.2. Electron microscopy

SEM and TEM were used for the characterization of the zeolite samples used in this thesis. These were essential to get information about the morphology of the zeolite crystals, the crystal size and the homogeneity of the samples. The dispersion, homogeneity and location of metallic nanoparticles were also studied. Most importantly, electronic microscopy images are the main characterization technique that can provide **evidence for the presence of an internal cavity**, i.e. **the main tool to recognize hollow structures**.

2.2.1. Scanning electron microscopy

The electron gun, placed at the top of the microscope emits the electron beam in vacuum. All along the microscope, electromagnetic lenses condense the electron beam to properly focus it on the sample. When the electron beam hits the surface of the sample, several phenomena take place: some of the electrons are absorbed by the sample, others are reflected from the sample (backscattered electrons BSE), also, the electron beam can excite the atoms of the sample that will release the secondary electrons (SE) etc., see Figure 5. Each type of electron can be detected by a specific electron detector, which converts the information into an image. Typically, SEM images are created from the detector of secondary electrons (SE).

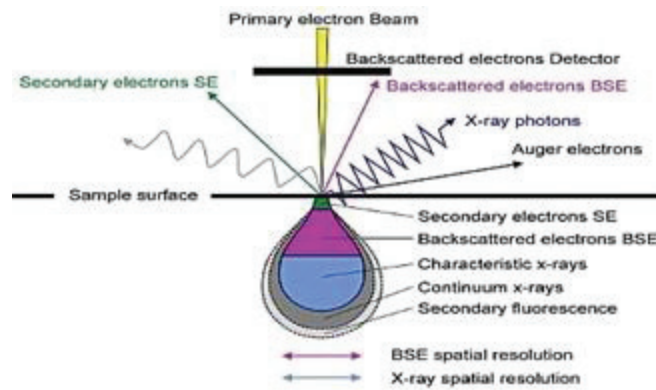


Figure 5 - Scanning Electron Microscopy Scheme. The scheme illustrates the different types of electrons that are released when the electron beam hits the surface of the sample: secondary electron, (SE), backscattered electrons (BSE), etc. The bulb shape illustrates the relative deepness from each type of electrons. Reproduced from.⁸

It is called a “scanning” electronic microscope because the beam “travels” (scans) through the area of interest of the sample, and one can reconstitute the surface topography. The position of the electron beam on the sample is controlled by scan coils situated above the objective lens. These coils allow the beam to be scanned over the surface of the sample.

- **SEM apparatus**

The SEM used for this thesis is a FEI ESEM-XL30 (Philips), with a field emission gun (FEG), see Figure 6.



Figure 6 – Picture of SEM from CLYM, used for this thesis.

- **Sample preparation – specifications adapted for this thesis**

Generally, a SEM sample requires the deposition of a thin metallic layer on the surface of the sample, usually by Au coating, to assure a good conduction of electrons and avoid overcharge. The corresponding image is a reconstitution of the surface topography of the sample.

For this thesis though, SEM samples were prepared similarly to TEM samples (see further on in this chapter), and most importantly, **without Au coating on the surface**. This type of preparation, coupled with a high voltage (~20kV), allows a deeper penetration of the electron beam in the sample. As a consequence, the contrast obtained is function of the density of the crystal. The image does not only provide good resolution from the surface of the sample, but also provides information about the density of the sample. Therefore, hollow crystals can be identified.

- **The use of SEM for this thesis**

In this thesis, most of the images were obtained using the SE detector. Essentially, this type of observation allowed to:

- Study the crystal size and morphology and homogeneity of the sample, especially for crystals bigger than 500 nm;
- Obtain the average crystal size distribution, by counting around 200-300 crystals, using Image J software;
- Recognize a hollow crystal from a bulk crystal: while a bulk crystal presents a homogeneous contrast (bright) due to a homogeneous density, in a hollow crystal the cavity area has lower density, therefore the contrast is poorer than the external surface of the crystal.

The BSE detector has also been used to study the dispersion of supported metallic Pt NPs. In the case of backscattered electrons, atoms with bigger atomic numbers z can reflect more electrons, producing a more intense signal. Hence, the image gives information about the chemical nature of the sample, where the better contrast (most intense signal) is associated with heavier atoms. The dispersion of Pt NPs can be easily spotted on an aluminosilicate or zirconosilicate crystal, see Figure 7. These types of images did not have enough resolution to measure the average particle size, but it is a fast and easy way to evaluate the homogeneity of the Pt dispersion over a big population of crystals.

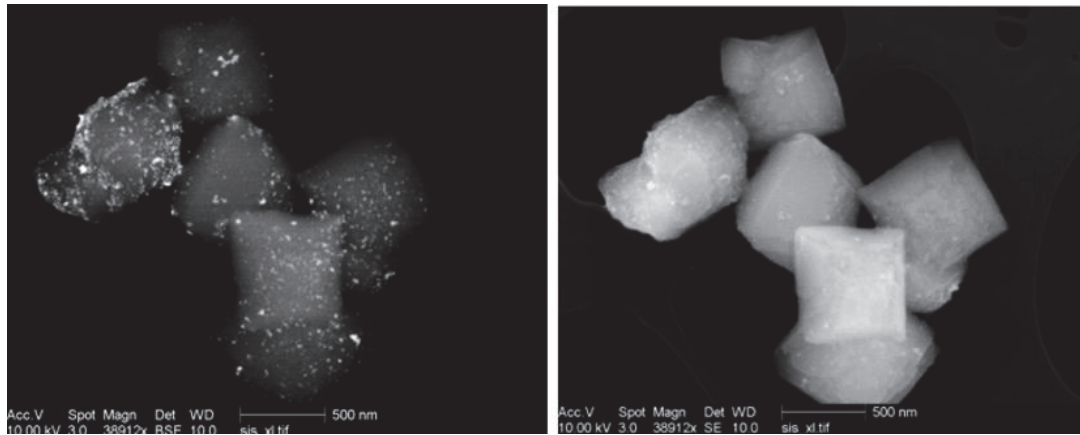


Figure 7 - Example of a SEM image using the BSE detector (left side) and the SE detector (right side). The sample consisted in a Pt supported zincosilicate crystal (CIT-6). In the left image, the bright dot corresponds to Pt NPs, with a higher atomic number than the rest of the crystal.

2.2.2. Transmission electron microscopy

Similarly to the SEM technique, a transmission electron microscope includes an electron emission source, electromagnetic lenses and an electron detector. The electron beam is emitted from the top of the microscope by an electron gun containing an emission source connected to a high voltage source under vacuum. Different electromagnetic lenses converge and focus the beam on the sample (the tunnel should be in vacuum, so there are no interferences, and the electron beam passes fast). TEM operates at much higher voltage than SEM (about 200 kV). Hence, the correspondent wavelength is smaller, which allows higher resolution than SEM. Unlike SEM, TEM images are created from the electrons that are transmitted bellow the sample.

- **TEM apparatus**

For this thesis, TEM images are obtained on a JEOL 2010 microscope operating at 200 kV, (resolution of 0.19 nm in Jeol 2010), Figure 8. The electron beam is generated by a heated LaB_6 crystal, connected to a high voltage source (200 kV in JEOL 2010) under vacuum.

The images are projected either on a fluorescent screen, either by a CCD camera controlled by Digital Micrograph software, from which we obtain the TEM images presented in this thesis.



Figure 8 - Picture of JEOL 2010 TEM apparatus.

- **Sample preparation for TEM observation**

Sample preparation involves grinding of a catalyst in ethanol in a mortar and deposition of a drop of the suspension on a Cu TEM holey carbon grid. This procedure allows for a very thin layer of the sample to deposit on the grid, avoiding overlap between catalyst particles and making it easier to image the metal particles in thin hollow zeolite or on the support.

- **The use of TEM for this thesis**

In this work, TEM has been used for:

- Studying the crystal size, morphology, and homogeneity of the sample, for crystals smaller than 500 nm;
- Identifying hollow structures, i.e the presence of inner large cavities by lighter color than the rest of the crystal, due to lower density;

- Obtaining the average crystal size distribution, by measuring around 200-300 crystals, using Image J software;
- Recognizing metallic nanoparticles and revealing their location (external surface, inside the microporous framework etc), measuring the nanoparticle size distribution and determining nanoparticle (NPs) dispersion values;
- Estimating chemical composition by Energy Dispersive X-Ray Spectroscopy (EDX) measurements.

For the analysis of metallic NPs size distribution in metal-containing samples at least 400 particles are measured using Image J software. Each distribution is modeled using a normal law centered on the number weighted mean diameter d_{10} (defined as $\sum n_i d_i / \sum n_i$ where n_i is the number of particles with diameter d_i) and broadened by the experimental standard deviation. The surface weighted mean diameter d_{32} (defined as $n_i d_i^3 / \sum n_i d_i^2$) is estimated from the size distribution which represents the size of a particle that has the same surface/volume ratio as the entire distribution.

The dispersion (D_{metal}) of a metal is estimated from d_{32} using a cuboctahedral model and a calculation method according to Van Hardeveld and Hartog.⁹ Essentially, the model allows to calculate the number of Pt atoms on the surface of a nanoparticle with a given diameter.

The JEOL 2010 microscope is equipped with an EDX Link ISIS analyzer (Oxford Instruments). It is possible to identify the elements present in a certain region of the crystal. When the electron beam passes through the sample, X-rays are generated and emitted from the sample. X-rays escaping from the sample can be detected and measured from the characteristic spectrum of each element. In addition, the number of photons emitted is proportional to the mass concentration of this species. Hence, EDX can provide precise composition of a part of the sample at the nanometer scale. In this thesis, EDX measurements were used to confirm the presence of Pt NPs (especially in the case where NPs were smaller than 3 nm or not clearly visible on the images) and also to obtain local Si/Al ratios in zeolite crystals.

2.2.3. Environmental transmission electron microscopy

In this work, single-tilt tomography has been performed on Pt NPs encapsulated in hollow Beta sample (the sample Pt@Hollow β from chapter III more precisely), to make a 3D reconstruction of a single crystal. This 3D reconstruction confirmed the presence of the inner cavity in the hollow Beta samples, and also gave information on the location of the Pt NPs, namely the confirmation of the encapsulation of the NPs on the cavity and zeolite wall.

High-angle annular dark-field scanning transmission electron microscopy (HAADF-STEM) analysis was performed on an FEI Titan ETEM operating at 300 V. HAADF images show little or no diffraction effects, this imaging technique is particularly adapted to tomography reconstruction as it generates strong contrast between heavy metal particles and inorganic supports.

The sample was dispersed in ethanol, and then ultrasonicated for 10 min to sufficiently separate the crystals, and then a droplet was placed on a microscopy grid and dried. The recording of tilted images was performed using a Fischione high-tilt holder from -68° to $+68^\circ$ with an angular step of 2° and the tomography plug-in implemented in TIA software. Next, the images were aligned using IMOD software,¹⁰ and then the volume reconstruction was performed using 15 iterations of the ordered-subset simultaneous algebraic reconstruction technique (OS-SART) implemented in the Tomoj¹¹ plug-in of Image J software. Volume visualization and segmentation was performed using Image J and 3DSlicer.¹²

2.3. Textural analysis

2.3.1. N₂ adsorption isotherms

N₂ physisorption isotherms are measured at 77 K on a BELSORP-mini (BEL Japan) sorption apparatus. Approximately 100 mg of sample is degassed in a cell at 300 °C for 12 h prior to adsorption. Then the cell is weighed, so we can know the real mass of the sample without any adsorbed substances. When the cell is introduced in the BELSORP-mini apparatus it is put in vacuum and a small dose of N₂ is introduced in the cell. While the N₂ is adsorbed by the sample, the cell pressure decreases until it reaches equilibrium. When the pressure is constant its value is measured by the sorption apparatus and another N₂ dose is introduced. The adsorption isotherm is constructed point-by-point by admission of successive charges of gas to the sample.

Nitrogen adsorption is an important tool for the characterization of porous materials, in what concerns pore size distributions and micro-mesoporous volumes. The shape of the isotherms can give important information about the porous structure of the sample.¹³

In this thesis, apparent surface area is calculated using the BET method in the relative pressure range of $0 < p/p_0 < 0.1$ ^[8] Generally, the t-plot method is a well-known technique that allows determining the micro- and/or mesoporous volumes, however the method is not adequate for mainly microporous materials such as microporous zeolites, for which microporous volume can be significantly underestimated.¹⁴ For this reason, we decided to not use the t-plot method to determine V_{micro} , V_{meso} , once the zeolite samples synthesized in this thesis are mainly microporous. The microporous volume is determined as the volume of N₂ adsorbed for very low partial pressures, more precisely when the slope of the adsorption branch becomes lower than $10^3 \text{ cm}^3(\text{STP}) \text{ g}^{-1}$. The total pore volume is estimated from the N₂ uptake at $P/P_0 = 0.9$ on the desorption branch. The mesoporous volume has been estimated by the difference between the V_{total} and V_{micro} .

2.3.2. Mercury intrusion porosimetry

Mercury intrusion porosimetry (MIP) is a common technique to estimate the mesopore and macropore, pore size volume and distribution. Essentially, a progressive increase in hydrostatic pressure has to be applied to enable the mercury to enter pores in decreasing order of width. This equipment can determine pore sizes in the range of 3.5 to 500 μm . The technique is based on the Washburn equation, that relates the pressure difference, surface tension of mercury and the pore size, considering a cylindrical pore.¹⁵

MIP experiments were performed on Autopore IV, Micrometrics, which operates in the pressure ranges from vacuum to 400 MPa (3.6 nm to 140 μm). Prior to the intrusion experiments the samples were degassed at 250 °C for 12 h. The pore size distribution was determined from the Washburn equation, using a surface tension of mercury of 485 dynes/cm and a contact angle of 140°.

2.3.3. Hydrocarbon adsorption isotherms

The adsorption of toluene, mesitylene and cyclohexane over different zeolite samples was measured over a BelSorp Max apparatus (Bel Japan) at different temperatures. The sample preparation and the adsorption measurement procedure were similar to the one for the N₂ adsorption isotherms.

In this thesis, the adsorption isotherms of hydrocarbons were particularly appropriate in order to investigate 1) if a given hydrocarbon can enter the *BEA pores 2) to compare the adsorption behavior between different samples.

In the case of cyclohexane adsorption isotherms, Henry's constant was obtained from the slopes of the adsorption isotherm at very low pressures.

Moreover, adsorption isotherms of toluene and mesitylene were carried out in order to investigate whether molecular sieving could occur for these sorbates over Pt@Hollow β .

2.4. Elementary analysis (ICP-OES)

Elementary analysis is carried out by Inductively-Coupled Plasma-Optical Emission Spectroscopy (HORIBA Jobin Yvon Activa ICP-OES). The reduced samples are first dissolved in an acid solution of HF, H₂SO₄ and aqua regia (a mixture of nitric acid and hydrochloric acid in

a molar ratio of 1:3). The solution is then introduced into the spectrometer. Excited atoms and ions produced from each element emit a characteristic radiation whose intensity is measured. This intensity is then correlated to the amount of each element. In this thesis, the ICP technique is used to determine the Pt metal contents, Si/Al and Na/Al ratios in the different zeolites. Note that the Al detected includes all the Al present in the sample, as part of the crystalline framework or extra-framework aluminum species.

2.5. Thermogravimetric analysis

Thermogravimetric analyses (TGA) were performed on a TGA/DSC MX1 microbalance (Mettler Toledo). Typically 5 mg of catalyst is placed in an Al₂O₃ sample holder and heated under air flow (30 mL min⁻¹) up to 750 °C at a heating rate of 10 °C min⁻¹. This technique is used for quantifying the water and amount of carbon-based compounds in solids.

2.6. Solid-state nuclear magnetic resonance

Solid-state NMR spectra are obtained on a Bruker DSX 400 spectrometer equipped with a double-bearing probe-head. Samples are spun at 10 kHz in 4 mm zirconia rotors. ²⁷Al NMR spectra are recorded with a pulse length of 0.6 μs ($\pi/12$) and a recycle delay of 500 ms. Chemical shifts are referred to as Al(H₂O)₆³⁺. NMR provides information about the environment of the Al species, in particular, the presence of framework and non-framework Al in the zeolite crystals. Framework Al, or tetrahedrally coordinated Al (Al(OSi)₄), present a peak between 52 and 60 ppm, while generally octahedral Al species presents a peak at 0 ppm. Taking into account the relative area for each peak, one can have an idea of the percentage of the Al in the framework and as extra-framework Al.^{16,17}

2.7. X-ray photoelectron spectroscopy

X-ray photoelectron spectroscopy (Spectrometer AXIS Ultra DLD (KRATOS Analytical), X-ray source: polychromatic Al) was used for measuring the relative Pt contents around the external surface of the Pt-supporting zeolites. The measured peak intensities of Pt 4d/6 (binding energy: 305 to 325 eV) and Si 2p_{3/2} (101 to 102 eV) were used to estimate the atomic Pt to Si ratios on the surface of Pt/Hollowβ, before and after treatment with Br₂.

2.8. Pyridine adsorption-desorption followed by IR spectroscopy

Infrared spectra were recorded with a Nicolet Magna 550 spectrometer (resolution 2 cm^{-1}), using a DTGS detector. Spectra have a resolution of 2 cm^{-1} , using 128 scans. Before pyridine adsorption, the samples were activated under vacuum at $450\text{ }^{\circ}\text{C}$ for 12 h. Pyridine adsorption is performed at $150\text{ }^{\circ}\text{C}$. Spectra were recorded after evacuation for 2 h at $150\text{ }^{\circ}\text{C}$, and then 1h AT $250\text{ }^{\circ}\text{C}$, $350\text{ }^{\circ}\text{C}$ and $450\text{ }^{\circ}\text{C}$.

The structure band region ($1750\text{-}1350\text{ cm}^{-1}$) was investigated using self-supporting thin wafers of the zeolites (with a diameter of 14mm). The concentrations of the Brønsted and Lewis acid sites were calculated from the integrated area of the bands 1545 and 1456 cm^{-1} correspondent to the species adsorbed on Brønsted and Lewis sites respectively. The molar extinction coefficients of these bands: $\epsilon_B=1.67\text{cm}/\mu\text{mol}$ for Brønsted and $\epsilon_L=2.22\text{cm}/\mu\text{mol}$ for Lewis sites.¹⁸

In this thesis, this technique was used to evaluate the number and strength of Brønsted and Lewis sites of the zeolites used for the catalytic tests.

3. Catalytic tests

3.1. Hydrogenation catalytic tests

Toluene and mesitylene hydrogenation reactions were carried out to evidence the presence or absence of metallic nanoparticles on the external surface of the hollow Beta zeolite samples.

Toluene and mesitylene hydrogenations were carried out using a tubular quartz plug flow reactor placed in a tubular furnace at atmospheric pressure. A mass of $10 \pm 0.1\text{ mg}$ of catalyst, held between quartz wool plugs, was used. Each substrate was fed separately using a saturator maintained at $0\text{ }^{\circ}\text{C}$ for toluene and $17\text{ }^{\circ}\text{C}$ for mesitylene, leading to partial pressures of 0.91 kPa and 0.20 kPa , respectively. The reactor effluent was analyzed in a 10 cm path length gas cell fitted in a Bruker Tensor 27 FT-IR spectrophotometer. Reactant conversion was

determined through integration of the 3200-3000 cm^{-1} spectral region corresponding only to the C-H stretching bands of the arene. Only the corresponding fully saturated cycloalkanes were obtained in each case.

3.2. Cyclohexane cracking

Cyclohexane cracking reaction was carried out over bulk and hollow Beta zeolites, in order to evaluate the impact of the hollow morphology, in comparison to an equivalent bulk zeolite.

Catalytic cracking of cyclohexane was performed in a fixed-bed reactor connected to a MicroGC Agilent 3000. A mass of 100mg of the catalyst was sieved in the range 200-500 μm , loaded in a quartz tube and supported over glass wool. Cyclohexane was filled in a 100ml tank, pressurized under 4 bar of N_2 . Reactant was fed to the reactor by a Coriolis Mass Flowmeter at a rate of 2.9g/h. An evaporator in a hot box at 170 $^\circ\text{C}$ vaporized the cyclohexane. Nitrogen was used as a carrier gas with a rate of 100mL/min. The weight hourly space velocity (WHSV) was between 29 h^{-1} ($\text{g}_{\text{cyclohexane}}/\text{g}_{\text{cat}}$).

Typically, reactions were sequentially performed at 400 $^\circ\text{C}$, 450 $^\circ\text{C}$, 500 $^\circ\text{C}$, 550 $^\circ\text{C}$ and 600 $^\circ\text{C}$. Between each reaction the catalyst was kept under N_2 flow (50mL/min). When the reactor reached the required temperature, the 4-way valve was switched to feed cyclohexane to the reactor for 20 min. During this time, gas was injected every 4 min to the MicroGC.

3.3. n-C₁₆ hydroisomerization

The hydroisomerization of n-hexadecane (Thermo-Fischer, 99% purity) took place at IFPEN, in an automated high-throughput catalytic fixed bed unit (Flowrence™) with sixteen inox reactor tubes. The catalytic test was fully automated, with the operating conditions of the catalytic bed of each reaction being monitored individually. Products were analyzed on-line by flame ionization detector using a GC chromatograph equipped with low polarity capillary columns.

Operating conditions:

-activation/reduction: reactor with catalyst is heated at 150 $^\circ\text{C}$ for 30 min over nitrogen flow, 10 ml/min. Then, reduction is performed using a H_2 flow, 21 ml/min, reduction temperature of 450 $^\circ\text{C}$ for 2 h, with temperature ramp of 5 $^\circ\text{C}/\text{min}$.

- catalyst: the catalysts powder (320mg) was shaped in 200–300 μm pellets. Note that 90 wt. % of the catalyst powder is γ -alumina as binder and 10 wt. % is the respective zeolite crystals.

- Inlet ratio: 10 mol H_2 + 1 mol n-C₁₆ (thermo-Fisher, 99%)

- Reactor: inox, 4mm diameter
- Pressure: 11 bar
- Temperature: 180-350 °C
- WHSV: 2 g n-C₁₆/(h.g_{catalyst})

Conversions were recorded by increasing the reaction temperature from 180 to 360 °C range. Each measure was duplicated after approximately 20min of interval.

For each sample, different assay were made in with different % wt. of Pt in order to verify which amount of Pt was enough to equilibrate the acid phase, i.e. when the catalytic activity is not depending on the Pt wt. %, and therefore the acid phase is the limiting phase. The results shown are for the samples with enough Pt wt. % to equilibrate the respective acid phase.

3.4. Catalytic activities

The conversion fraction (X) is the molar fraction of a molecule that has reacted; for a given reactant, it is thus calculated by:

$$X = \frac{n_0 - n_t}{n_0}$$

where n_0 and n_t are the number of moles of the reactant at the beginning and after a certain time (t) of reaction, respectively.

In the case of metallic catalysis, the reaction rate expressed in $\text{mol}\cdot\text{s}^{-1}\cdot\text{g}(\text{metal})^{-1}$ is calculated by:

$$r = \frac{X \cdot F}{m_{\text{metal}}}$$

where m_{metal} is the active mass of element in the catalyst and f is the flow of reactant in mol/s in the gas phase. The TOF (s^{-1}) is expressed as the number of molecules of reactant converted per second per surface catalyst atoms, which is calculated by the equation

$$TOF = \frac{r \cdot M_{\text{metal}}}{D_{\text{metal}}}$$

Where r is the reaction rate, M_{metal} is the molecular weight of the metallic catalyst and D_{metal} is the dispersion of the metal particles.

In the case of acid catalysis for cyclohexane cracking, reaction rate r is expressed in $\text{mol}\cdot\text{s}^{-1}\cdot\text{g}_{(\text{cat})}^{-1}$ is calculated by:

$$r = \frac{X F}{m_{\text{cat}}}$$

where m_{cat} is the mass of catalyst (zeolite).

For a n^{th} order irreversible reaction, Thiele modulus is given by¹⁹

$$\phi = L \sqrt{\frac{n+1}{2} \frac{kC^{n-1}}{D_{\text{eff}}}}$$

where n is the reaction order, k the intrinsic reaction rate constant, C the reactant concentration at the particle surface, L the diffusion path length, and the D_{eff} the effective diffusion constant within the catalyst.

For generalized geometries, effectiveness factor η can be given by¹⁹

$$\eta = \frac{\tanh(\phi)}{\phi}$$

4. References

- (1) Camblor, M.; Mifsud, A.; Pérez -Pariente, J. Influence of the Synthesis Conditions on the Crystallization of Zeolite Beta. *Zeolites* **1991**, *11* (8), 792–797. [https://doi.org/10.1016/S0144-2449\(05\)80057-0](https://doi.org/10.1016/S0144-2449(05)80057-0).
- (2) Camblor, M.; Pérez -Pariente, J. Crystallization of Zeolite Beta - Effect of Na and K-Ions. *Zeolites* **1991**, *11* (3), 202–210. [https://doi.org/10.1016/S0144-2449\(05\)80220-9](https://doi.org/10.1016/S0144-2449(05)80220-9).
- (3) Fan, F.; Ling, F.; Wang, S.; Zhang, H.; Chen, X.; Wang, C. One Kind of Hollow Beta Zeolite and Its Preparation Method. CN 104591220, 2013.
- (4) Zheng, J.; Zeng, Q.; Zhang, Y.; Wang, Y.; Ma, J.; Zhang, X.; Sun, W.; Li, R. Hierarchical Porous Zeolite Composite with a Core–Shell Structure Fabricated Using β -Zeolite Crystals as Nutrients as Well as Cores. *Chem. Mater.* **2010**, *22* (22), 6065–6074. <https://doi.org/10.1021/cm101418z>.
- (5) Ding, L.; Zheng, Y.; Zhang, Z.; Ring, Z.; Chen, J. Effect of Agitation on the Synthesis of Zeolite Beta and Its Synthesis Mechanism in Absence of Alkali Cations. *Microporous Mesoporous Mater.* **2006**, *94* (1–3), 1–8. <https://doi.org/10.1016/j.micromeso.2006.03.010>.

- (6) Bourgeat-Lami, E.; Fajula, F.; Anglerot, D.; Courieres, T. Single-Step Dealumination of Zeolite-Beta Precursors for the Preparation. *Microporous Mater.* **1993**, *1* (4), 237–245.
- (7) Eapen, M.; Reddy, K.; Shiralkar, V. Hydrothermal Crystallization of Zeolite-Beta Using Tetraethylammonium Bromide. *Zeolites* **1994**, *14* (4), 295–302.
[https://doi.org/10.1016/0144-2449\(94\)90099-X](https://doi.org/10.1016/0144-2449(94)90099-X).
- (8) How Scanning Electron Microscopes Work
<https://www.azom.com/article.aspx?ArticleID=14791> (accessed Apr 21, 2019).
- (9) Van Hardeveld, R.; Hartog, F. The Statistics of Surface Atoms and Surface Sites on Metal Crystals. *Surf. Sci.* **1969**, *15* (2), 189–230. [https://doi.org/10.1016/0039-6028\(69\)90148-4](https://doi.org/10.1016/0039-6028(69)90148-4).
- (10) Kremer, J. R.; Mastronarde, D. N.; McIntosh, J. R. Computer Visualization of Three-Dimensional Image Data Using IMOD. *J. Struct. Biol.* **1996**, *116* (1), 71–76.
<https://doi.org/10.1006/jsbi.1996.0013>.
- (11) Messaoudil, C.; Boudier, T.; Sorzano, C. O. S.; Marco, S. TomoJ: Tomography Software for Three-Dimensional Reconstruction in Transmission Electron Microscopy. *BMC Bioinformatics* **2007**, *8* (1), 288. <https://doi.org/10.1186/1471-2105-8-288>.
- (12) Fedorov, A.; Beichel, R.; Kalpathy-Cramer, J.; Finet, J.; Fillion-Robin, J.-C.; Pujol, S.; Bauer, C.; Jennings, D.; Fennessy, F.; Sonka, M.; et al. 3D Slicer as an Image Computing Platform for the Quantitative Imaging Network. *Magn Reson Imaging* **2012**, *30* (9), 1323–1341. <https://doi.org/10.1016/j.mri.2012.05.001>.
- (13) Thommes, M.; Kaneko, K.; Neimark, A. V.; Olivier, J. P.; Rodriguez-Reinoso, F.; Rouquerol, J.; Sing, K. S. W. Physisorption of Gases, with Special Reference to the Evaluation of Surface Area and Pore Size Distribution (IUPAC Technical Report). *Pure Appl. Chem.* **2015**, *87* (9–10), 1051–1069. <https://doi.org/10.1515/pac-2014-1117>.
- (14) Galarneau, A.; Villemot, F.; Rodriguez, J.; Fajula, F.; Coasne, B. Validity of the T-Plot Method to Assess Microporosity in Hierarchical Micro/Mesoporous Materials. *Langmuir* **2014**, *30* (44), 13266–13274. <https://doi.org/10.1021/la5026679>.
- (15) Giesche, H. Mercury Porosimetry: A General (Practical) Overview. *Part. Part. Syst. Char.* **2006**, *23* (1), 9–19. <https://doi.org/10.1002/ppsc.200601009>.
- (16) Muller, M.; Harvey, G.; Prins, R. Quantitative Multinuclear MAS NMR Studies of Zeolites. *Microporous Mesoporous Mater.* **2000**, *34* (3), 281–290.
[https://doi.org/10.1016/S1387-1811\(99\)00180-8](https://doi.org/10.1016/S1387-1811(99)00180-8).
- (17) Muller, M.; Harvey, G.; Prins, R. Comparison of the Dealumination of Zeolites Beta, Mordenite, ZSM-5 and Ferrierite by Thermal Treatment, Leaching with Oxalic Acid and Treatment with SiCl₄ by H-1, Si-29 and Al-27 MAS NMR. *Microporous Mesoporous Mater.* **2000**, *34* (2), 135–147. [https://doi.org/10.1016/S1387-1811\(99\)00167-5](https://doi.org/10.1016/S1387-1811(99)00167-5).
- (18) Emeis, C. Determination of Integrated Molar Extinction Coefficients for Infrared-Absorption Bands of Pyridine Adsorbed on Solid Acid Catalysts. *J. Catal.* **1993**, *141* (2), 347–354. <https://doi.org/10.1006/jcat.1993.1145>.
- (19) Hartmann, M.; Machoke, A. G.; Schwieger, W. Catalytic Test Reactions for the Evaluation of Hierarchical Zeolites. *Chem. Soc. Rev.* **2016**, *45* (12), 3313–3330.
<https://doi.org/10.1039/C5CS00935A>.

Chapter III – Synthesis of Hollow Beta Zeolite Single Crystals

1. Introduction

As described in Chapter I, two synthesis approaches of hollow Beta zeolite have been reported in the literature with more or less success and very often limited characterization. They are referred to here as 1) “CIT-6 Dissolution-Recrystallization”¹ and 2) “Beta Zeolite Dissolution”², Figure 1.

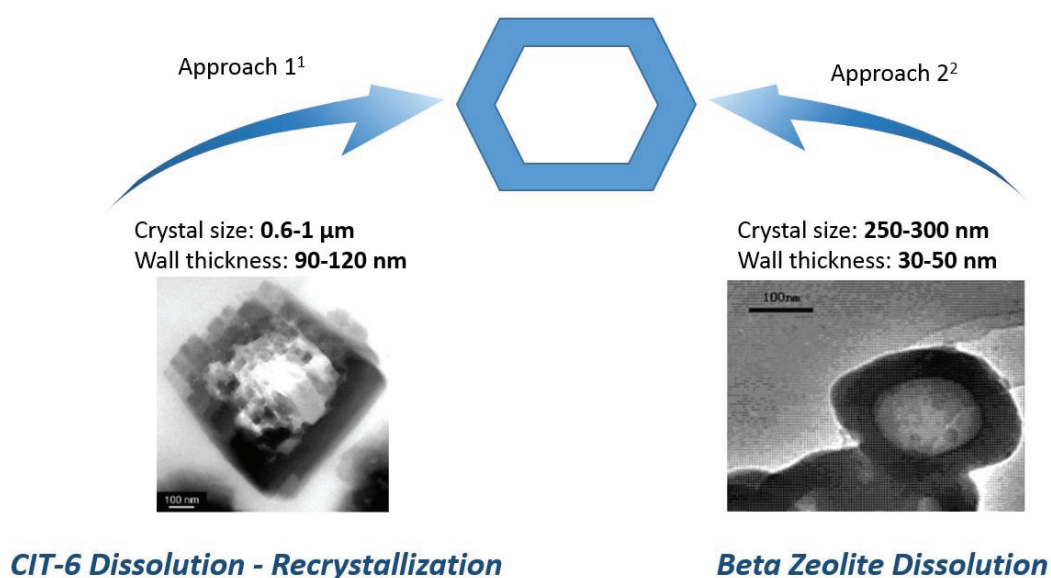


Figure 1 – The two different approaches used for the synthesis of hollow Beta zeolite.

In both approaches, the synthesis of hollow Beta crystals is obtained by post-synthesis treatments of a parent zeolite, CIT-6 crystals and Beta crystals respectively. It consists in a selective dissolution of the center of a parent zeolite in basic media, originated by a core particularly less stable than the rest of the crystal (see Chapter I). Each approach has yet distinct synthesis pathways and mechanisms, and therefore the resulting hollow Beta crystals are different: different crystal sizes, wall sizes, morphologies, compositions etc.

The “*CIT-6 Dissolution-Recrystallization*” approach (approach 1) was introduced by Okubo *et al.*¹ The hollow Beta crystals obtained were characterized by XRD, electron microscopy, N₂ adsorption isotherms (77 K) and chemical analysis, revealing a highly crystalline microporous Beta crystal. The presence of the inner cavity was confirmed by the TEM images of cross section of the crystals, confirming the hollow morphology of these Beta crystals. **The establishment of a reproducible synthesis method of hollow Beta crystals by “*CIT-6 Dissolution - Recrystallization*” and a more detailed characterization was a first task of this work.**

In the objective to investigate the impact of the reduction of the diffusion length on the transport and catalytic effectiveness, we have compared catalytic activities of hollow Beta crystals and bulk Beta zeolites (Chapter IV and V). In order to determine quantitatively the impact of the transport in catalysis, the composition of hollow Beta had to be well characterized in what concerns 1) the porous system, the presence or not of internal mesopores can have an important impact in transport and catalysis, and 2) chemical compositions, like the amount of residual Zn²⁺ (which could act as a catalytic species and eventually bias the comparison study) but also whether a gradient of Si/Al would exist. In order to allow testing a series of hollow Beta, we have investigated the synthesis of hollow Beta with different Si/Al ratio and with different shell thicknesses (which would allow studying different diffusion path lengths).

Having hollow Beta crystals in hands, we have investigated different synthesis approaches to encapsulate Pt nanoparticles in the shell. We have then put in place a catalytic test, hydrogenation of aromatics, as model reactions in order to quantify the respective amount of encapsulated particles and those which are located on the surface crystals, i.e. directly accessible from the outside of crystals.

Regarding the approach 2 (see Figure 1), the only report is the patent of Fan *et al.*² which describes the synthesis of Beta hollow structures by dissolution of calcined Beta nanocrystals at moderate temperature in the presence of sodium aluminate. To the best of our knowledge, the results were not published elsewhere. The patent presented a very limited description/characterization of the final product hollow Beta, and did not present any insights about the synthesis mechanism. There are only two TEM images available, showing what seems to be a homogeneous sample of hollow particles, with an average crystal size of 200-300 nm, Figure 48. As far as we know Beta zeolite does not have a heterogeneous composition such as Al zoning as it is for some ZSM-5 zeolites. We have assumed that the mechanism likely involved the enrichment of the outer surface of the crystals by Al species, creating **an artificial Al gradient**, followed by the preferential dissolution of the core. **The objective here was to reproduce the synthesis, characterize in detail the porous structure, understand the mechanism of selective dissolution and further optimize the synthesis to purposes.**

2. CIT-6 Dissolution-Recrystallization approach (Okubo et al.)

2.1. Assumptions on synthesis mechanisms from literature

As mentioned before, the synthesis of Hollow Beta single crystals is inspired by a seed-assisted synthesis approach described by Okubo *et al.*¹ which used CIT-6 crystals as seeds (see Figure 2). CIT-6 is a microporous zincosilicate with the same ***BEA** framework topology as Beta zeolite. Hollow Beta is obtained by hydrothermal treatment of the as-made CIT-6 in the presence of an organic-free aluminosilicate gel. During the hydrothermal treatment, Beta zeolite starts to recrystallize on the CIT-6 surface, which afterwards is dissolved, leading to hollow single crystals.

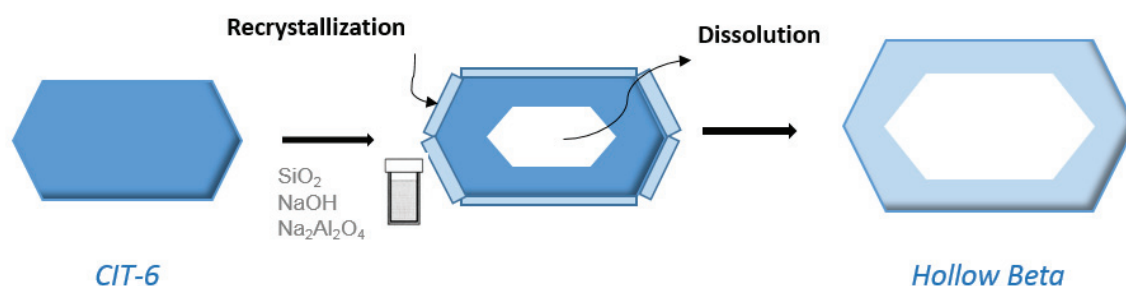


Figure 2 – The synthesis pathway proposed by Okubo *et al.*¹

According to Okubo¹ there are a few key factors for the success of this synthesis:

- the ***BEA** structure type of CIT-6 crystals favors the crystallization of Beta zeolite (also ***BEA** structure type) instead of other framework structure types,¹ similarly to a seed-assisted synthesis.

- CIT-6 zincosilicate is less stable in alkaline media than the correspondent aluminosilicate Beta which is the key factor for the formation of the hollow structure.¹ Indeed, during the synthesis there is crystallization of Beta zeolite over CIT-6 surface, but eventually the CIT-6 crystal is dissolved which creates the hollow structure,¹ see Figure 2. The same would not happen if we used Beta seeds instead of CIT-6. As far as we know, Beta zeolite is globally homogeneous concerning Al or defect concentration, and therefore there is no natural

preferential dissolution of the core in alkaline solution. Indeed, when performing the same synthesis scheme (Figure 2) using Al containing Beta zeolite seeds (instead of CIT-6), the final product consists in a bulk **microporous** Beta zeolite, with no evidence for hollow structure.³

- Also, it is crucial for the synthesis that the CIT-6 crystals are “as-made”, i.e. the organic template tetraethylammonium (TEA⁺) is still trapped inside the pores. When performing the same synthesis using calcined (TEA⁺ free) CIT-6 crystals, these were completely dissolved before any Beta growth on the surface.¹ Whereas using as made CIT-6 crystals, the remaining TEA⁺ cations are able to stabilize CIT-6 in alkaline solution,⁴ hence, CIT-6 crystals work as an active surface for Beta growth before they dissolve themselves.¹ It must be noted though, that these TEA⁺ cations do not seem to have a major contribution for the Beta crystal growth itself. Thermogravimetric analysis (TGA) revealed that the content of TEA⁺ in the final product hollow Beta is about 3%.¹

2.2. Optimization of the synthesis of CIT-6 crystals

2.2.1. Characterization of the optimal CIT-6 crystals

The synthesis of CIT-6 was first reported in 1999 by Davis' group^{5,6} as a new zincosilicate molecular sieve that possesses the ***BEA** topology.

Since then, all the synthesis reports of CIT-6^{1,7,8} recall the same synthesis procedure, suggesting how the synthesis conditions are very limited, namely due to the formation of other crystalline phases such as VPI-8 (**VET** framework type⁹), needle-shaped crystals that nucleate on the surface of CIT-6 crystals.¹⁰ All the synthesis methods present Si/Zn_(gel) of approximately 33, with the exception of Okubo's group¹⁰ that recently has developed a co-precipitation method that used Si/Zn_(gel) between 10 and 20. For the previous publications, the Si/Zn of the as-made crystal remained between 10-20 and exceptionally 32 for Takewaki *et al.*⁵

The synthesis of CIT-6 followed for this study was based on the classical synthesis of Davis' group,^{1,5} and it is described in detail in chapter II. After several studies (including some studies performed at IFPEN by Maria Manko not shown in here), the final conditions chosen for the hydrothermal synthesis were fixed at 145 °C for 4 days. The gel composition corresponds to the same used by Davis.⁷

X-ray diffraction (XRD) results show that CIT-6 is highly crystalline, presenting a ***BEA** framework type with no other crystalline or amorphous phases, see Figure 3.

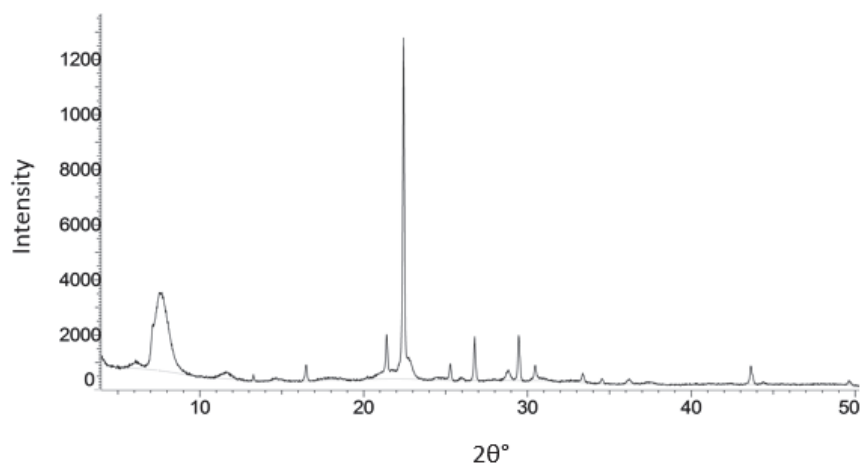


Figure 3 – XRD patterns of CIT-6 crystals, hydrothermal synthesis carried out at 145 °C for 4 days.

Nitrogen adsorption/desorption (77 K) performed on the calcined CIT-6 solid presents a type I isotherm typical of a purely microporous crystal (see Figure 4) with a V_{micro} of approximately $0.09 \text{ cm}^3/\text{g}$ and BET surface of $308 \text{ m}^2/\text{g}$ (Table 1). According to the literature,^{1,7} N_2 isotherms over CIT-6 crystals equally presented a type I isotherm, however with higher BET surface and V_{micro} between $400\text{-}632 \text{ m}^2/\text{g}$ and $0.15\text{-}0.22 \text{ cm}^3/\text{g}$ respectively. This difference might be due to different synthesis conditions and/or calcination procedures. It must be noted that during calcination, some Zn is removed from the framework, forming ZnO and partially filling the pores.^{5,6,11} Therefore, small differences in the synthesis conditions and/or the calcination procedures might have a big impact on the V_{micro} and also in the amount of zinc removed from the framework and filling the pores. Indeed, literature has shown how CIT-6 displays smaller V_{micro} than that of the correspondent aluminosilicate Beta for example, due to micropore filling.⁵

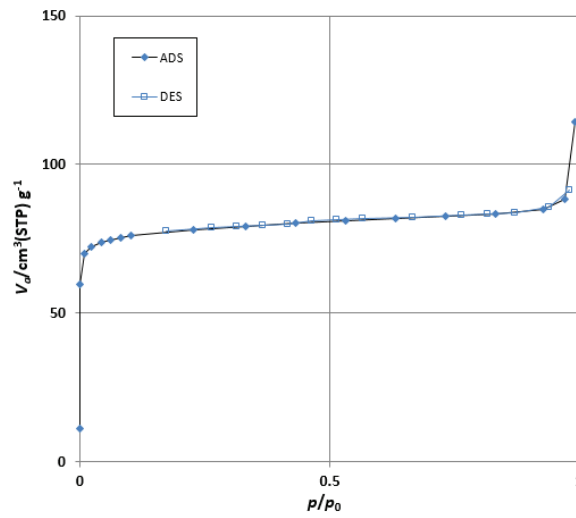


Figure 4 – N_2 adsorption/desorption isotherms of CIT-6 obtained at 145 °C for 4 days.

Table 1 – Textural properties of CIT-6 obtained at 145 °C for 4 days.

	CIT-6
S_{BET} [m ² /g]	308
V_{total} [cm ³ /g]	0.13
V_{micro} [cm ³ /g]	0.09

SEM images exhibit homogeneous crystals, with a crystal size distribution in the 0.6-1.1 μm range, see Figure 5. The observed crystals show a truncated octahedral morphology, pine tree shaped on each sides, which is typical for Beta zeolite crystal morphology^{12,13} and also corresponds to the typical morphology and size of CIT-6 crystals.

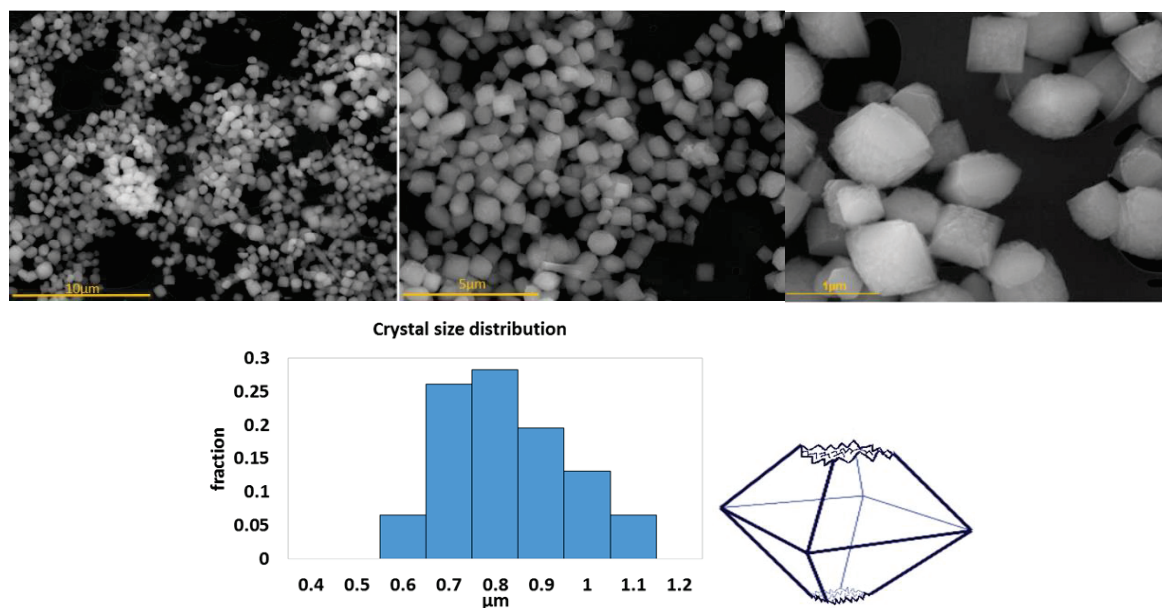


Figure 5 – SEM images of CIT-6 obtained at 145 °C for 4 days, corresponding crystal size distribution and scheme of the truncated octahedral morphology of the crystal.

Chemical analysis of the CIT-6 crystals gives Li/Zn and Si/Zn molar ratios of 0.7 and 17, respectively, which is also in accordance with the literature, whose Si/Zn are in order of 10 to 20^{1,6,10,11} and 32⁵ (no data available about Li/Zn).

The synthesis parameters for CIT-6 crystals are very “limited”, and also very vulnerable to yield other crystalline phases like VPI-8. Having as starting point the CIT-6 synthesis proposed by Okubo’s group,¹ a few studies were performed in order to find the optimal synthesis conditions, that gave the final product described above. The effects of crystallization time, temperature etc. on the preparation of CIT-6 were investigated.

2.2.2. Effect of crystallization time

The hydrothermal syntheses were carried out at 140 °C for 6, 7, 8 and 9 days, similarly to the literature.⁷

After heating at 140 °C for 6 days, the crystalline CIT-6 with *BEA framework type pattern is favored with respect to the VPI-8 phase, see Figure 6. However, a big “hump” is visible in the low angle region of the XRD pattern ($2\theta \sim 6^\circ$), that can be associated with some amorphous phase.⁷ As the crystallization time increases, the intensity of this “hump” decreases, suggesting that the remaining amorphous phase starts disappearing. However, after 8 days of crystallization VPI-8 begins to appear (VPI-8 XRD pattern available on the annexes), and the respective peaks increase after 9 days, resulting in a mixture of CIT-6 and

VPI-8 (Figure 6). The same behavior was previously found in the literature regarding VPI-8 crystallization: as crystallization time increases, the yield of VPI-8 increases.^{7,10} Serrano *et al.*⁷ showed how for longer crystallization times, VPI-8 yield increases up to a point where no more CIT-6 crystals can be found (supported by SEM and XRD). The authors suggest that VPI-8 nucleation occurs on CIT-6 surface and that the yield of VPI-8 increases while CIT-6 yield decreases.

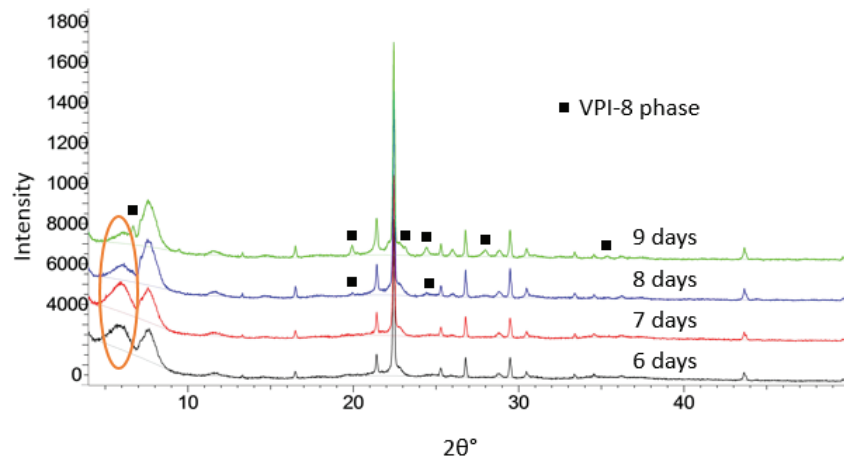


Figure 6 – XRD patterns of CIT-6, synthesized at 140 °C for 6, 7, 8 and 9 days, the peaks attributed to VPI-8 phase are noted as ■ . The orange circle points out a peak associated to amorphous phase.

SEM images support the behavior observed from XRD patterns, see Figure 7. Crystals obtained after 6 and 7 days (see Figure 7) present CIT-6 crystals with homogeneous size, no VPI-8 crystals are observed, but also an extra phase (maybe amorphous) that can be associated to the initial “hump” of the XRD patterns. At longer synthesis times as 9 days, SEM images clearly reveal the coexistence of CIT-6 crystals and other needle-shape phase, corresponding to VPI-8.

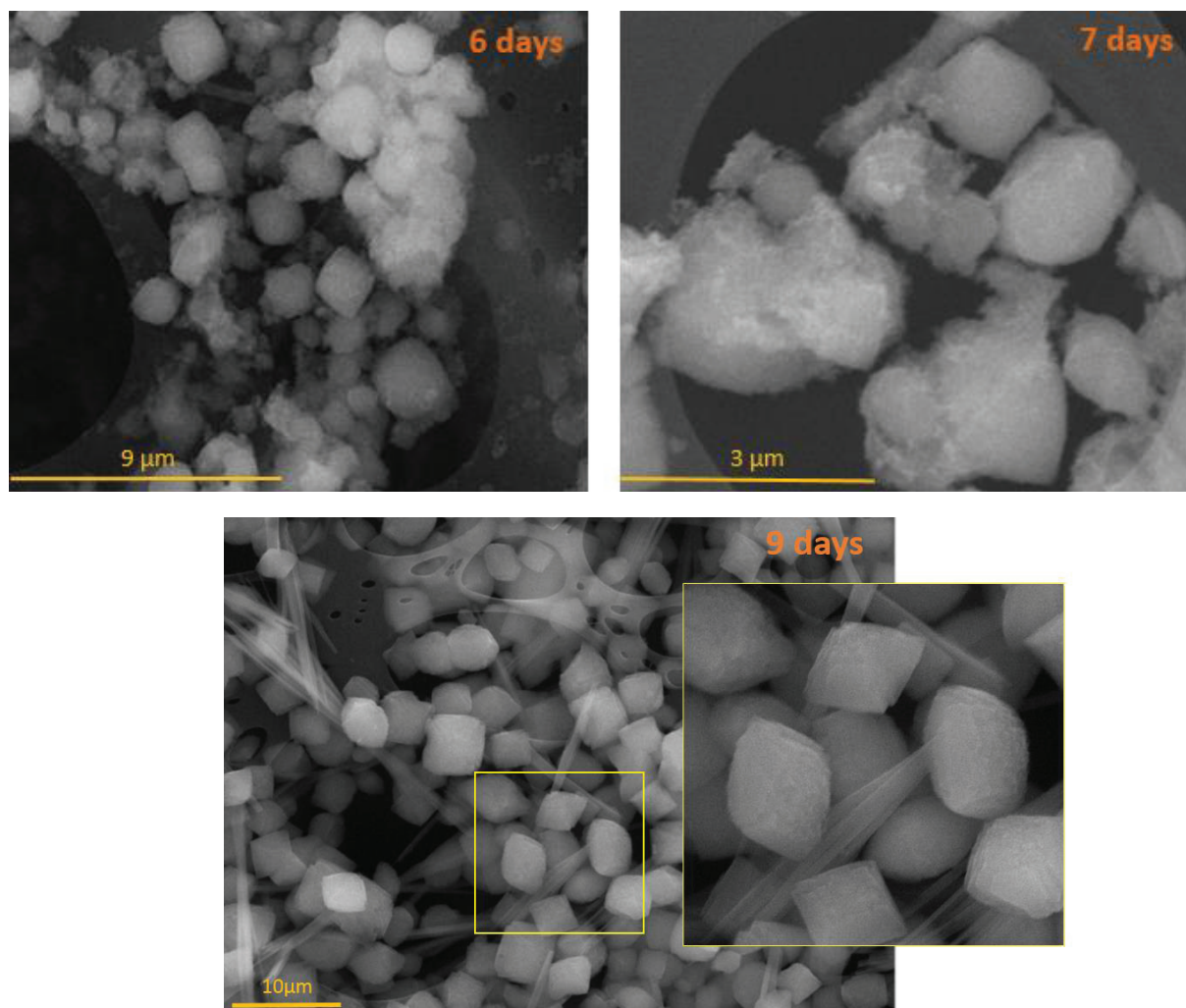


Figure 7 – SEM images of CIT-6 after hydrothermal treatment at 140 °C for 6 days, 7 days and 9 days.

The presence of these amorphous phase and VPI-8 phase is already described in the literature.⁷ As the crystallization progresses, CIT-6 crystals arise from the initial amorphous phase. These crystals exhibit the ***BEA** topology. As crystallization goes on, CIT-6 yield increases and amorphous yield decreases until eventually there are only CIT-6 crystals. Subsequently, the nucleation and the initial crystal growth of a VPI-8 needle-shaped phase occurs on the ***BEA** particles. At longer synthesis times, VPI-8 yield increases. This behavior was also found when the hydrothermal synthesis was carried out at 150 °C, which is reported below.

In the long term, we have realized that the amount of amorphous phase decreased significantly when using a new bottle of silica source (Ludox HS-40), (more details in Annexes Chapter III), and that similar issues were also found at IFPEN during the work carried out by Maria Manko. Nevertheless, the same tendency was still verified using fresh reactant: amorphous phase decreased with increasing crystallization time. The following studies were

therefore obtained using the fresh reactant, which decreased considerably the amount of amorphous phase.

2.2.3. Effect of crystallization temperature

According to the literature for CIT-6 synthesis, as the temperature increases, the crystallization kinetics is accelerated, with faster reorganization of amorphous phase to CIT-6, and also faster transformation of CIT-6 into VPI-8.⁷

Therefore, in an attempt to find the best and faster synthesis conditions, the hydrothermal treatment was carried out at several temperatures (140, 145 and 150 °C) and synthesis times, see Table 2. The XRD patterns and SEM images can be found on the Annexes – Chapter III.

Table 2 – Summary of the results (crystalline phases and Yield% of solid phase regarding SiO₂, Y%) at various hydrothermal synthesis conditions. Each colored square corresponds to a phase: yellow for amorphous phase, green for CIT-6 and red for VPI-8.

T (°C)	68h	3 days	4 days	6 days	7 days	8 days	9 days
140	----	----	----	(traces) Y% =50	 Y% =58	(traces) Y% =60	 Y% =65
145	----	(traces) Y% =39	 Y% =65	----	----	----	----
150	(traces) Y% =66	 Y% =70	 Y% =89				

As expected, as the crystallization temperature increases, CIT-6 crystallization is faster, however, the yield of VPI-8 is higher as there is faster transformation of CIT-6 into VPI-8,⁷ (SEM images and XRD patterns show well the increasing presence of VPI-8).

Regarding the previous results, performing the hydrothermal treatment at 145 °C for 4 days seemed to be a good compromise between short crystallization times, no impurities and high yields of pure CIT-6 crystals. At 150 °C crystallization kinetics are very high and therefore it would be difficult to find the optimal synthesis time in order to obtain pure CIT-6 (with no VPI-8 and no amorphous phase left). For these reasons, 150 °C was the maximum

crystallization temperature studied, and it is also the maximum temperature of crystallization found in the literature.^{5-7,11}

2.2.4. Effect of reactor size

Considering that the synthesis conditions of CIT-6 seemed to be very restricted, and that crystallization kinetics appeared to be highly sensitive, we decided to check the impact of using different reactors for the hydrothermal treatment. In the previous cases, the hydrothermal treatment was carried out using a 48 ml Teflon-lined stainless-steel autoclave. In this case the hydrothermal synthesis was performed at 150 °C for 3 days. The synthesis mixture was charged into Teflon-lined, stainless steel autoclaves of two autoclaves of 23 ml and one of 48 ml. The occupied volume ratio of the autoclave, as well as the temperature and crystallization time conditions were similar in both reactors. XRD patterns show that the crystals synthesized in smaller autoclaves of 23 ml have more prominent peaks associated to VPI-8 crystal, see Figure 8, suggesting a higher yield of VPI-8 when two 23 ml autoclaves are used instead of one of 48 ml.

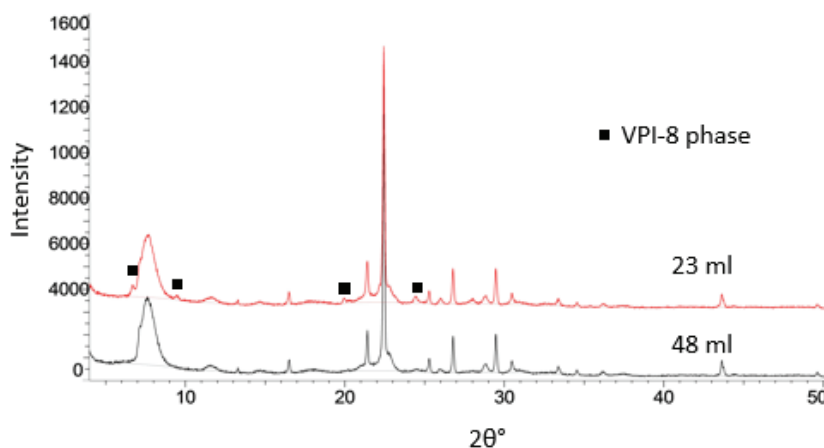


Figure 8 - XRD patterns of CIT-6 after hydrothermal treatment performed in a 23 ml and 48 ml stainless steel autoclaves. Hydrothermal synthesis carried out at 150 °C for 3 days. The black squares indicate the peaks attributed to VPI-8 phase.

Moreover, SEM images show indeed a higher concentration of VPI-8 crystals for the synthesis that used a smaller autoclave, see Figure 9, which is in agreement with the XRD patterns results.

-

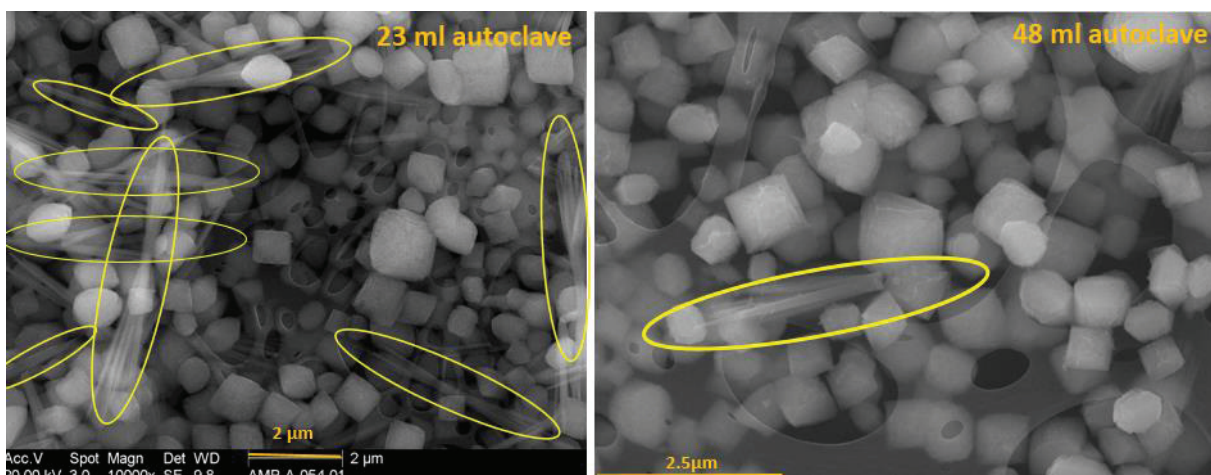


Figure 9- SEM images of CIT-6 after hydrothermal treatment performed in a 23 ml and 48 ml stainless steel autoclave. Yellow circles point out the VPI-8 crystals, needle shaped.

These results suggest how the type of reactor, or the *external surface/total gel volume*, has a big influence on the final yield of VPI-8, even though the occupied volume ratio remained the same for both reactors. When the synthesis is carried out in two 23 ml autoclaves, the *external surface/total gel volume* ratio is higher than for the same synthesis carried out in one 48 ml volume. This external surface is the first in contact with the heat surface, and therefore the heating rate is higher than the rest of the synthesis gel, which might yield CIT-6 and subsequently VPI-8 before the rest of the synthesis gel. Consequently, the total amount of VPI-8 is bigger. We must point out that this synthesis is performed in static conditions, which might create some significant temperature and composition heterogeneities inside the reactor.

It suggests once more how the synthesis conditions are relatively limited and VPI-8 yield is difficult to control.

2.3. Optimization of the synthesis of hollow Beta single crystals

Herein we present a complete characterization of the hollow Beta obtained and optimized during this doctoral thesis, based on dissolution - recrystallization approach.¹

Preliminary studies performed beforehand provided us an insight of formation mechanism of the samples. These preliminary studies report the influence of several synthesis parameters on crystallization rate, crystal size etc., that are reported below. The optimal synthesis conditions found were at 150 °C, during 22h, and experimental parameters as

described in chapter II. This hollow Beta was used *a posteriori* for diffusion and catalytic tests presented in this thesis, chapters IV and V.

2.3.1. Characterization of the optimal hollow Beta

As revealed by XRD patterns, after hydrothermal treatment a highly crystalline ***BEA** framework type is obtained (see Figure 10), without any other crystalline phases. CIT-6 presents a peak at approximately 16.5° that is not present in the hollow Beta sample. This peak is probably due to the presence of the organic template in the pores of CIT-6⁶ (about 14% by TG analysis), while as-prepared hollow Beta has only around 3 wt. %.¹ XRD patterns for hollow Beta show a peak shift regarding CIT-6 that might be attributed to the Al content in the framework, which changes the position of the main diffraction peak.¹⁴

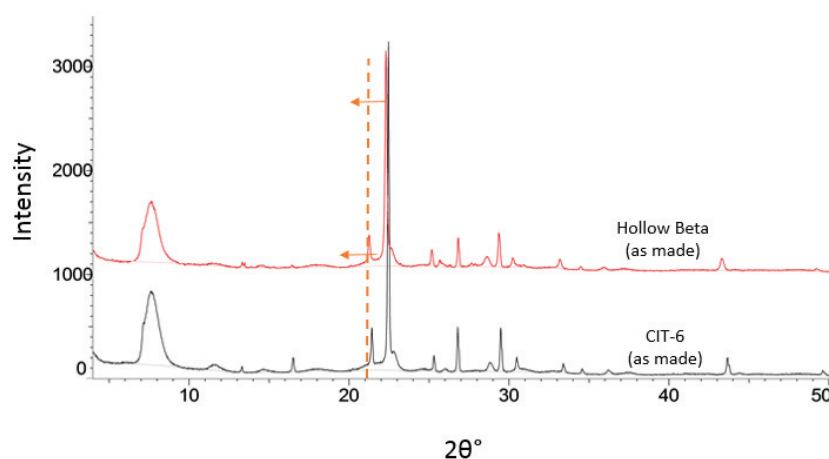


Figure 10 - XRD patterns of as-made CIT-6 and hollow Beta.

The observed crystal shape is a truncated tetragonal bipyramid, pine tree shaped on each sides, similar to the parent CIT-6 crystal, and also typical for Beta zeolite crystal morphology¹² (see Figure 11 and Figure 12). It presents a crystal size distribution between 0.8 μm and 2.2 μm , Figure 12. The hollow morphology is evidenced by the color contrast between the exterior and the center of the crystals, either by TEM or SEM. The size of the cavity corresponds approximately to that of the dissolved CIT-6 crystal, leaving an average shell thickness of 100–200 nm.

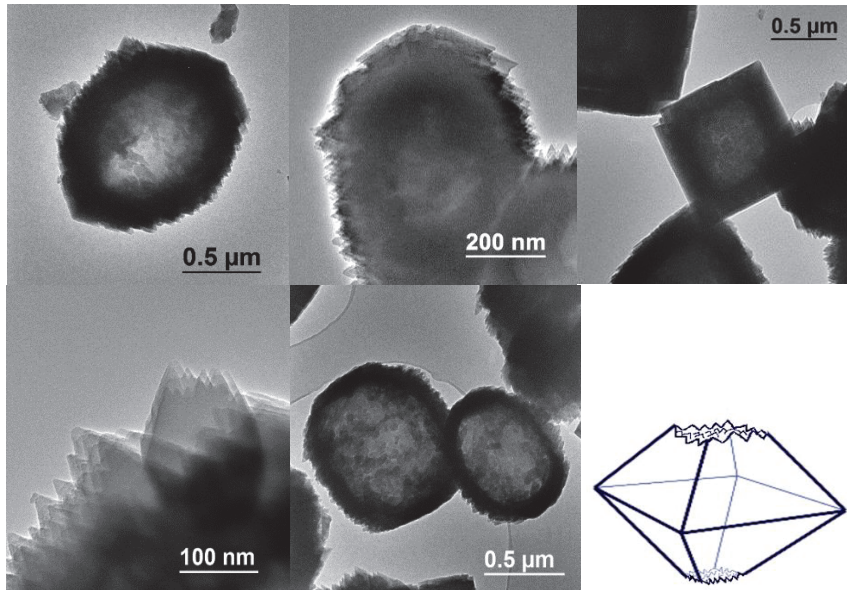


Figure 11 – TEM images of hollow Beta crystals and a representation of the external morphology of the crystal (on the bottom right).

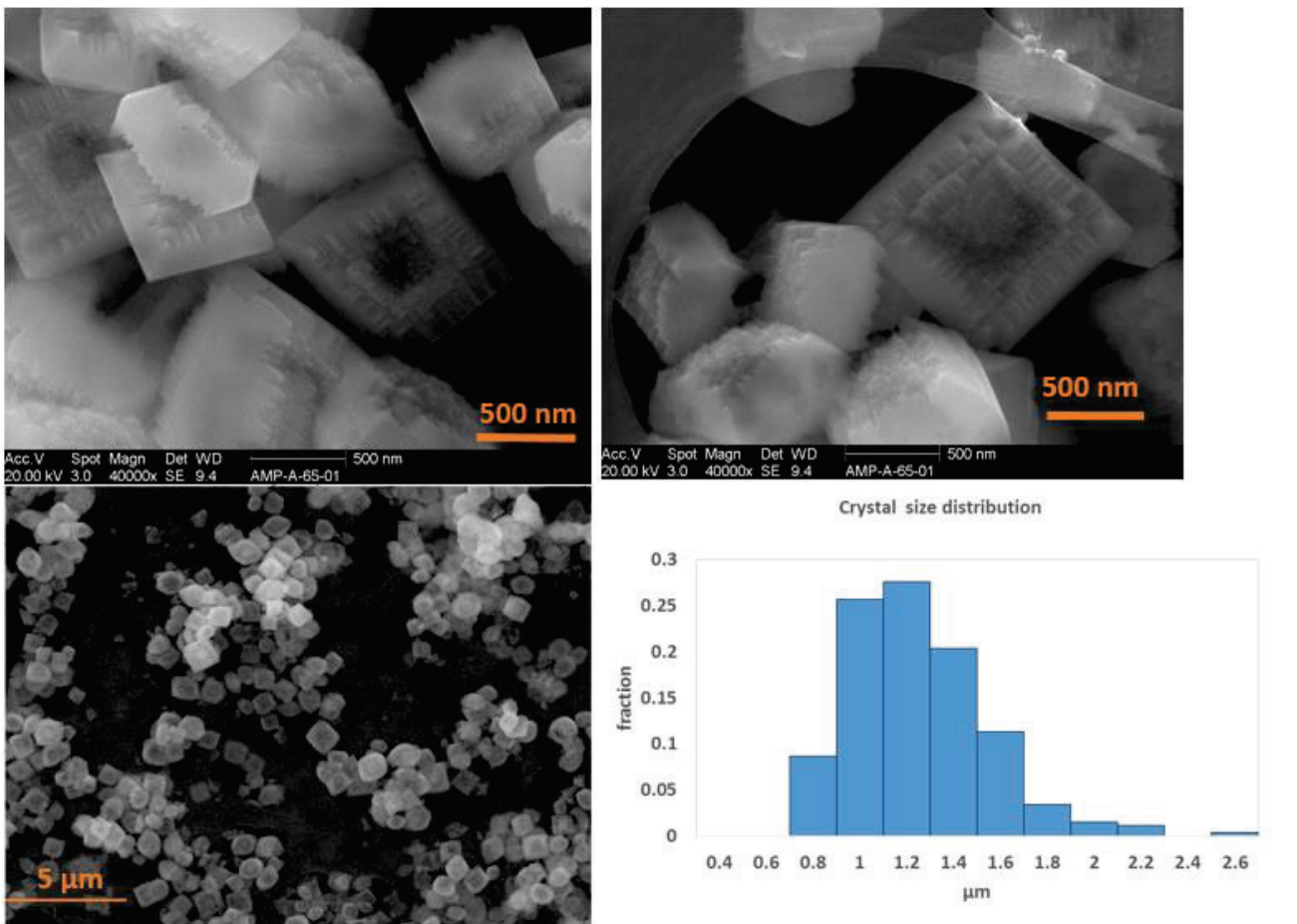


Figure 12 - SEM images of hollow Beta and corresponding crystal size distribution

Chemical analysis of the hollow Beta crystals gives Si/Al and Si/Zn molar ratios of 8 and 40, respectively. However, after ionic exchange with for example NH_4NO_3 , Si/Zn increases to 138, indicating that most of the Zn species present are extra-framework species that can be easily removed after ionic exchange. Such high Al content and low Zn content are a strong evidence that the final product is indeed an aluminosilicate instead of a zincosilicate, and therefore a Beta zeolite. The remaining Zn concentration is very low, clearly indicating that the dissolution of CIT-6 during the hydrothermal treatment is almost complete. The remaining fraction of Zn could result from Zn species reincorporated either in the hollow Beta framework or in the pores as extra-framework species.

Energy dispersive X-Ray spectroscopy analysis (EDX) and high resolution measurements were carried out on a cross-section of a resin embedded hollow Beta. The EDX analyses were performed on different zones of the zeolite wall, namely from the external surface throughout the internal cavity. EDX measurements showed that most of the crystals presented a low Si/Al ratio on the external surface, and that this ratio increases with depth, as it can be shown in Figure 13. Note that the sample used in Figure 13 has Si/Al = 9.5 instead of 7. The synthesis of the hollow Beta used in Figure 13 is the same as the hollow Beta presented above, however this batch used 4x less reactant (this sample was obtained before the scale-up) which has an impact on the final Si/Al. In any case, it is reasonable to assume that the mechanism of formation would be the same for both samples, and that there would be an Al gradient in both cases.

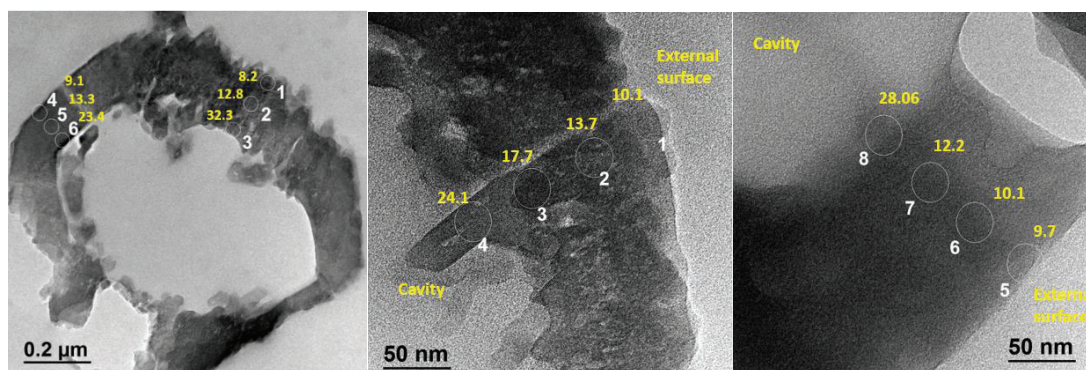


Figure 13 – TEM image of a 70 nm thick cross-section of a resin embedded hollow Beta. Each circle (and circle number 1-8) represents the different zones where EDX was performed. The respective Si/Al is written in yellow.

These results might suggest that hollow Beta has a natural Al zoning, where the external part of the crystal is richer in Al. This Al zoning suggests that the incorporation of Al in the framework increases during the recrystallization process.

As one of the objectives of this thesis is to study the impact of transport on catalytic activity, it is important to characterize the porosity of the hollow Beta crystals. The presence of mesopores, and the pore connectivity might have an impact on molecular diffusion and

catalysis, namely the presence of mesopores that connect the external surface and the internal surface.

HRTEM and STEM images of sliced hollow Beta crystals clearly show the presence of mesopores in the internal part of the microporous wall, Figure 14.

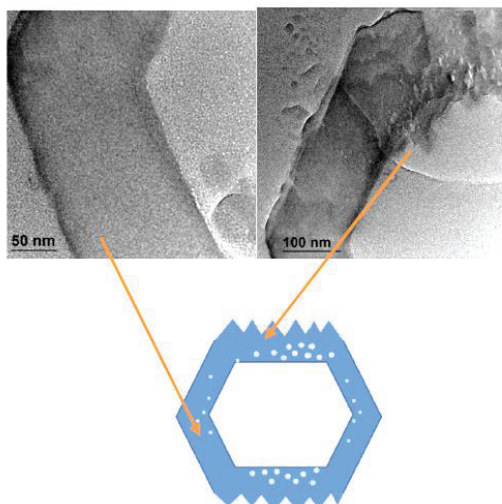


Figure 14 – HRTEM image of a sliced hollow Beta crystal and a simplistic illustration of the hollow Beta crystal and the mesopores (represented as white circles).

The N_2 adsorption/desorption isotherm of hollow Beta at 77 K, see Figure 15, shows a characteristic “type I” adsorption branch at low pressure, which is typical of a microporous material. However, the adsorption plateau of hollow Beta is not completely horizontal, which may be explained by the presence of mesopores.¹⁵ In fact, hollow Beta has a slightly higher V_{meso} than microporous CIT-6. It must be noted that, as mentioned before, the V_{micro} of hollow Beta is very superior to that of CIT-6 ($V_{\text{micro}} = 0.19$ and $0.09 \text{ cm}^3/\text{g}$ respectively), because after calcination of CIT-6, part of the Zn is removed from the framework and partially fills the pores as extra-framework Zn.^{5,5,6,11}

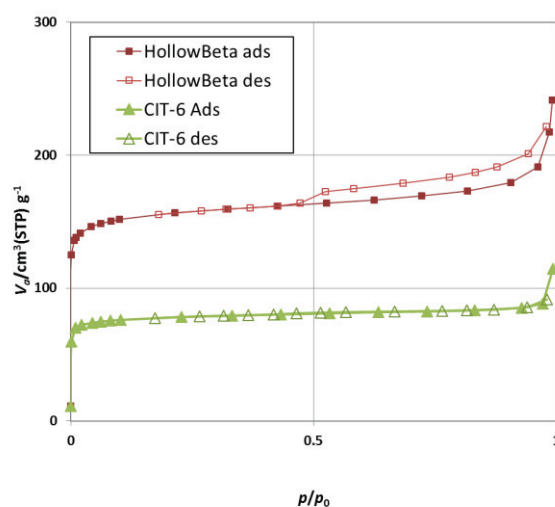


Figure 15 - N_2 adsorption/desorption isotherms of CIT-6 and hollow Beta.

Table 3 - Microporous and mesoporous characteristics of CIT-6 crystals and hollow Beta.

	CIT-6	Hollow Beta
S_{BET} [m^2/g]	308	610
V_{total} [cm^3/g]	0.13	0.28
V_{micro} [cm^3/g]	0.09	0.19
V_{meso} [cm^3/g]	0.04	0.08

Regarding the desorption branch, there is a hysteresis loop from which we can obtain some information about the shape, size and connectivity of the internal mesopores:^{15,16}

- a) In general, the hysteresis loop is an evidence of pore condensation phenomena, that happens when the pore exceeds a critical width of 4nm.¹⁵
- b) The type of hysteresis can be classified as H2 hysteresis, characterized by steep desorption branch and smoothly increasing adsorption branch.^{15,17} H2 hysteresis are characteristic of ink-bottle shape pores,¹⁸ Figure 16, and/or complex structures where network effects are important.¹⁵

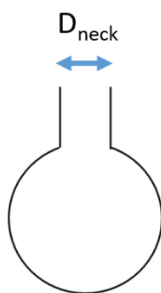


Figure 16 – Schematic illustration of ink-bottle type pores.

- c) In the case of ink-bottle shape pores, the closure point of the hysteresis loop gives evidence of the type of the desorption mechanism, from which we can obtain information about the neck size, D_{neck} . If the desorption mechanism is cavitation, $D_{\text{neck}} < 5\text{nm}$. If it is pore blocking, $D_{\text{neck}} > 5\text{nm}$. Thommes and Cychosz¹⁸ have noted that the closure point of the hysteresis is defined by the pressure at which the desorption branch meets the adsorption branch. The closure point depends not only on the adsorbate and the temperature, but also on the pore geometry.^{19,20} For N_2 at 77K, it is known that cavitation phenomena occur when the closure point is between 0.42-0.5,^{1,19,20} which is our case, indicating that these are ink-bottle pores with $D_{\text{neck}} < 5\text{nm}$.

Mercury-intrusion porosimetry (MIP) is another technique to study mesopore and specially macropore size distribution, between 3,5 nm and 500 μm .²¹ If the zeolite shell is purely microporous, Hg shall not be able to penetrate into the zeolite, whereas if there are mesopores accessible from the external surface, Hg will be able to penetrate. MIP experiments were performed over hollow Beta and an equivalent bulk Beta zeolite, i.e. with the same morphology and approximately the same crystal size, for the sake of comparison.

Regarding the bulk sample, the sample shows almost no V_{meso} , which was expected considering a microporous crystals, see Annexes. However hollow Beta presents some Hg volume centered on 10 nm, which increases abruptly for higher pressures, suggesting the presence of mesopores available from the external surface with a width of approximately 10 nm. These results are in accordance with the mesopore volume and hysteresis obtained from N_2 isotherms (77K), Figure 15, Table 3 and HRTEM images regarding the bottle neck pores, Figure 14. In this case, these pores could be accessible from the external surface.

However we assumed that the measured mesopore volume observed for the hollow Beta sample accounts for Hg penetration into the intercrystallites space in the pine shaped part of the crystal, Figure 17. It is interesting to note that bulk Beta, (that is purely microporous and also presents the same pine shaped surface), also possess a small peak centered on 10 nm. This coincidence supports the hypothesis of Hg penetration between the intercrystallites space.

Moreover, for the hollow Beta sample the volume of Hg continues to increase significantly below for higher pressures, which indicates that Hg either started filling the inner cavity reaching from the mesopores, either the nanoboxes broke with the high pressure, leaving the cavity volume available.

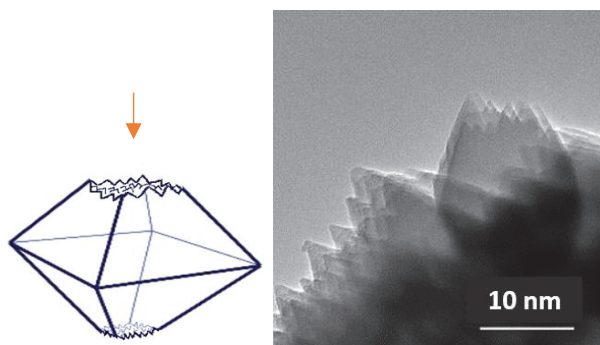


Figure 17 – Representation of the external morphology of the bulk and hollow Beta crystals. TEM image of the pin shaped side.

As summary, there is evidence of mesopores, namely bottleneck mesopores, not only by the hysteresis loop in the N_2 adsorption isotherms, but also the from the HRTEM images of the sliced crystal. The mesoporous volume is **28% of the** total pore volume (according to the N_2 isotherms) which is still minor fraction of the total porous volume regarding standard bulk Beta zeolites. The mesopore size may have a critical width superior to 4 nm, and in the case of bottle neck mesopores, $D_{neck} < 5$ nm. Although there is no clear evidence of the pore network connectivity, it seems reasonable to assume that the mesopores are not interconnected and are mainly present on the side of the internal part of the zeolite wall, not connecting with the external part of the crystal.

2.3.2. Effect of temperature and crystallization time

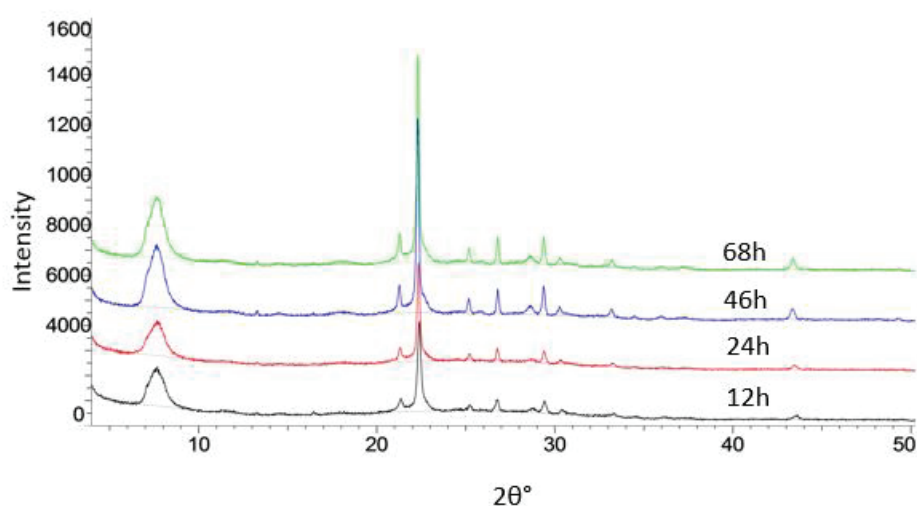
Okubo *et al.*¹ used synthesis gels with Si/Al and Na_2/Si between 15-125 and 0.22-0.35 respectively, and hydrothermal conditions between 140 and 150 °C, with 20 to 74h of crystallization time. Different synthesis conditions resulted in hollow Beta zeolites with different yields, Si/Al between 5.5 and 10.5, Si/Zn between 48 and 324, different V_{micro} and V_{meso} , different cavity sizes, and the presence or not of another crystalline zeolite phase such as mordenite (**MOR**). **MOR** is a crystalline phase generally found during hydrothermal treatment of the organic-free aluminosilicate gel and Beta or CIT-6 seeds.³

As a starting point we have established to reproduce the synthesis conditions that would represent a good compromise between high yield, pure crystalline Beta with no impurities and high V_{micro} and V_{cavity} . Regarding Okubo's results, the sample denoted as ref. 5

seemed to be a good compromise between all the criteria established.¹ (Note that the synthesis of “optimized” hollow Beta presented in III 2.3.1., uses the same gel composition as ref 5, but different crystallization time and temperature).

The hydrothermal synthesis corresponding to ref 5 in ¹ was carried out at different crystallization times and temperatures: at 140 °C for 12h, 24h, 46h, and 68h, and at 150 °C for 22h and 48h. The influence of the crystallization time was analyzed regarding crystallinity of the sample, morphology and porous structure, namely V_{micro} and V_{meso} .

Regarding the synthesis performed at 140 °C, XRD patterns of the products show how crystallization increases as crystallization time increases, namely the increase of intensity of the peak at 22.5°, see Figure 18. The sample obtained after 46h was 100% crystalline, as the intensity of the peak remained constant to 68h. When the hydrothermal treatment at 150 °C goes for 22h the product exhibits a highly crystalline pure Beta zeolite pattern, suggesting how the increase of temperature has increased the kinetics of crystallization. At 48h, XRD patterns show the presence of Mordenite (**MOR**) as a minor phase. The nucleation of **MOR** in this type of synthesis was already reported by Okubo’s group when performing the synthesis with CIT-6 or Beta seeds,¹ especially after prolonged crystallization times. As a matter of fact, Okubo *et al.* showed that **MOR** is obtained from the aluminosilicate gel without seeds.^{1,3} These studies suggest that **MOR** is a thermodynamically more stable phase in the present Na⁺-aluminosilicate system, while Beta phase was kinetically favored in the presence of Beta seeds. These results suggest the importance of parameters such as crystallization time, but also homogenization of the synthesis gel, in order to obtain pure Beta zeolite. If the CIT-6 seeds are not well dispersed in the synthesis gel, these might induce the spontaneous nucleation of Mordenite instead of Beta.



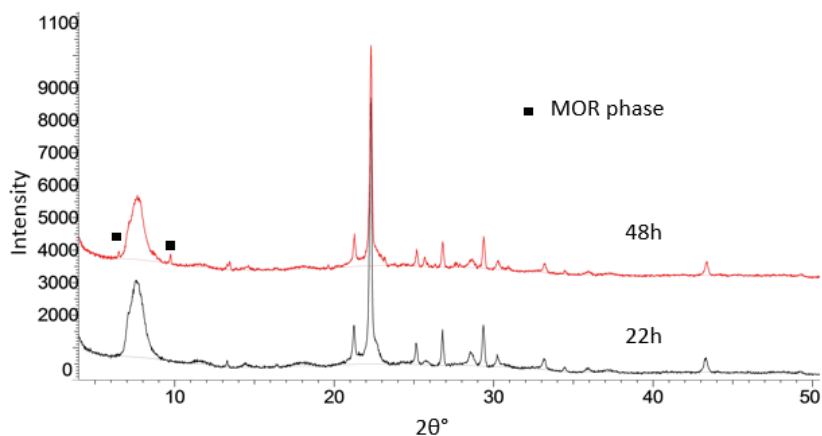


Figure 18 - XRD patterns of hollow Beta, hydrothermal synthesis at 140 °C for 12h, 24h, 46h, 68h (top) and hydrothermal synthesis at 150 °C, for 22h and 48h (bottom). Black squares are pointing out the peaks correspondent to the MOR phase.

Figure 19 shows the N₂ isotherms performed over the samples synthesized at 140 °C. All samples present a type I adsorption isotherm, characteristic of microporous materials, and the V_{micro} increases with increasing crystallization times, Table 4. As expected, the isotherms present a hysteresis loop on the desorption branch. In this case, the size of the hysteresis is different for each sample, which is an evidence of different mesopore volume and size (bottleneck type probably) depending on the crystallization time. At lower crystallization times, 24h, the hysteresis is bigger, i.e., the difference of V_{adsorbed} between the desorption branch and the adsorption branch is very important. This means that there is more N₂ volume that undergoes capillary condensation, suggesting that the mesoporous volume is bigger (bigger bottle neck pores and/or more bottle neck pores) than the samples 46 h or 68 h. For longer crystallization times than 24h, these mesopores decrease in size (or amount), indicating that there was crystallization growth toward the inside of the mesopores. Similarly to Okubo's work, the hysteresis changed with different crystallization times. However, Okubo *et al.*¹ claim that the hysteresis is due to pore condensation inside the cavity, and therefore, different hysteresis correspond to different cavity volumes.

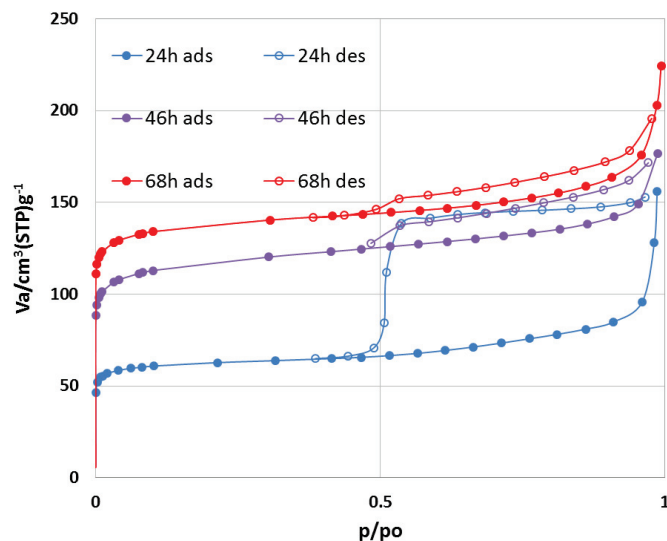


Figure 19 - N_2 adsorption/desorption isotherms of hollow Beta, synthesis performed at 140 °C for 24h, 46h and 68h.

Table 4 - Textural properties of Hollow β , hydrothermal treatment performed at 140 °C for 24 h, 46 h and 68 h.

	Hollow Beta 24 h	Hollow Beta 46 h	Hollow Beta 68 h
S_{BET} [m^2/g]	222	454	542
V_{total} [cm^3/g]	0.12	0.22	0.25
V_{micro} [cm^3/g]	0.07	0.15	0.16
V_{meso} [cm^3/g]	0.04	0.07	0.09

In the case of the synthesis performed at 150 °C, see Figure 20 and Table 5, there are no main differences between the two samples. If we attribute the hysteresis to pore condensation inside the mesopores, this means that the porous structure remains approximately the same between the two samples.

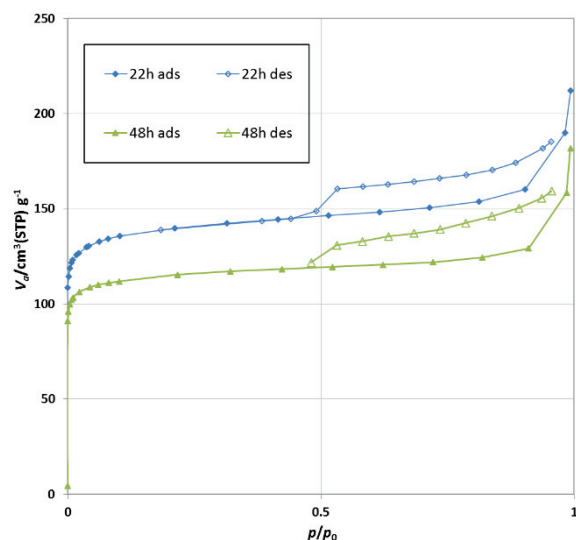


Figure 20 - N_2 adsorption/desorption isotherms of hollow Beta, hydrothermal synthesis performed at 150 °C for 22h and 48h.

Table 5 – Textural properties of hollow Beta, hydrothermal synthesis performed at 150 °C for 22h and 48h.

	Hollow Beta 22h	Hollow Beta 48h
S_{BET} [m^2/g]	546	455
V_{total} [cm^3/g]	0.25	0.20
V_{micro} [cm^3/g]	0.17	0.15
V_{meso} [cm^3/g]	0.08	0.05

SEM images show no apparent differences between the different syntheses, (images shown in the Annexes). The crystals have the same size and morphology as the hollow Beta reported previously, a truncated tetragonal pyramidal morphology, pine tree shaped on each sides. For all samples, the contrast of the center of the crystal is less bright than the external part of the crystal, suggesting once more the hollow structure. It must be noted that the sample prepared at 140 °C for 12h, presents always a round white mass inside the cavity area, which suggest that there is matter inside the cavity (probably CIT-6). This is in agreement with the formation mechanism of hollow Beta proposed by Okubo *et al.*: firstly crystallization of Beta zeolite starts on CIT-6 crystals surface, then (or during) CIT-6 starts dissolving itself. As crystallization continues, CIT-6 dissolves itself completely, leaving an empty inner cavity.

Table 6 illustrates the influence of crystallization time on Zn, Li and Na content, namely for the samples 150 °C at 22h and 48h. The Zn content decreases for higher crystallization times. Note that these values include framework and extra-framework Zn. We did not measure the Zn framework percentage for each sample. For this, one should wash the hollow Beta crystals with NH_4NO_3 or NaCl solution to remove any extra-framework species, and then

do the chemical analysis. If the amount of Zn corresponds to framework Zn, these results indicate that for higher crystallization times, more CIT-6 is dissolved. If the Zn content is associated to extra-framework Zn species, these can be located in the aluminosilicate volume and diffuse into the solution phase during crystallization time. The amount of Li is very small for both samples and the eventual differences of wt. % cannot be detectable by ICP analysis. Na contents are similar, suggesting that the amount of CIT-6 is similar for both samples, or that there is no CIT-6 left. In this case, the difference of Zn content between the two samples is associated to extra-framework Zn.

Table 6 – Effect of crystallization time on Zn, Li and Na concentration, when hydrothermal synthesis is performed at 150 °C.

	Zn (wt. %)	Li (wt. %)	Na (wt. %)
22h	1.25	< 0.02	2.33
48h	0.84	< 0.02	2.42

2.3.3. Effect of the amount of CIT-6

This dissolution - recrystallization scheme is based on the idea that zeolite will grow on the active surface of the CIT-6 seeds as a single crystal, while the aluminosilicate gel and CIT-6 itself is the Al and Si source (only Si for CIT-6).

Changing the amount of active surface (CIT-6) or the amount of available TO₄ building units for Beta crystallization (the amount of gel), should have an impact in the amount of zeolite crystallized (bigger or smaller zeolite walls). Okubo's group³ also studied the effect of different amount of seeds, but when using Beta seed-assisted synthesis of zeolite Beta. They concluded that when using fewer seed crystals (less active surface), crystallization of Beta phase was slower, but the final crystals were larger. However, no other characterization is available to give any information about porosity, composition, wall thickness etc. Applying the same logic to the synthesis of hollow Beta, we hoped to obtain different wall thicknesses using different wt. % of CIT-6.

Taking into account that we wanted to study the impact of wall size in diffusion and catalysis, it would be useful to be able to synthesize hollow Beta with different and precise wall sizes. In particular, very thin wall thickness would decrease the diffusion path length, which could be an advantage regarding reactions leading with diffusion limitations. In an attempt to decrease the wall thickness, hollow Beta was synthesized using 25 wt. % CIT-6 instead of 10 wt. %. Hydrothermal synthesis was performed at 150 °C for 22h, static conditions, for both samples. The samples are denoted **25%** and **10%**.

The powder XRD patterns of 10% and 25% as-made samples exhibit significantly higher peaks for 25%, Figure 21, which suggest that either 10% sample was not 100% crystalline, either 25% is denser.

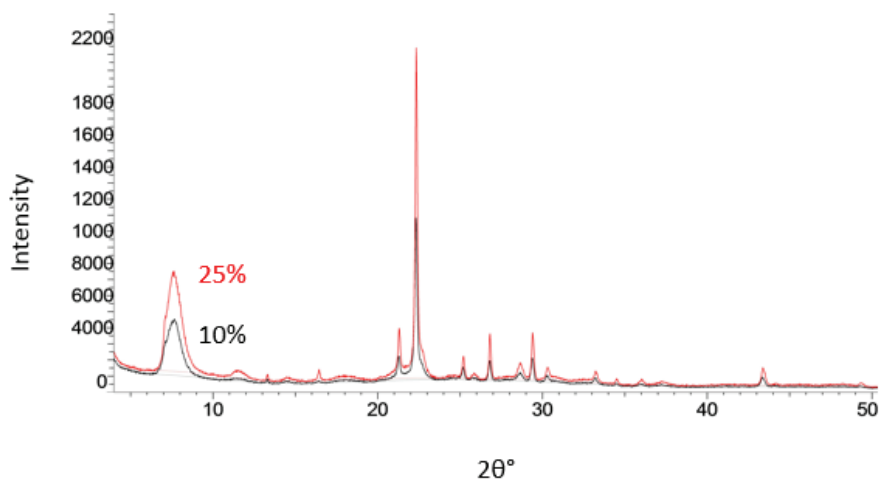


Figure 21 - XRD patterns of hollow Beta, hydrothermal synthesis at 150 °C using 10 wt. % (black) and 25 wt. % (red) of CIT-6.

SEM images show that both morphologies and crystal size are essentially the same, see Figure 22, even though 25% presents slightly smaller crystal size than 10%. This suggests that for 25% there was less the amount of recrystallized Beta, leading to a smaller crystal size, hence smaller wall thickness. Moreover, it must be noted that for the case of 25wt. % CIT-6, the cavity appears to not be completely empty.

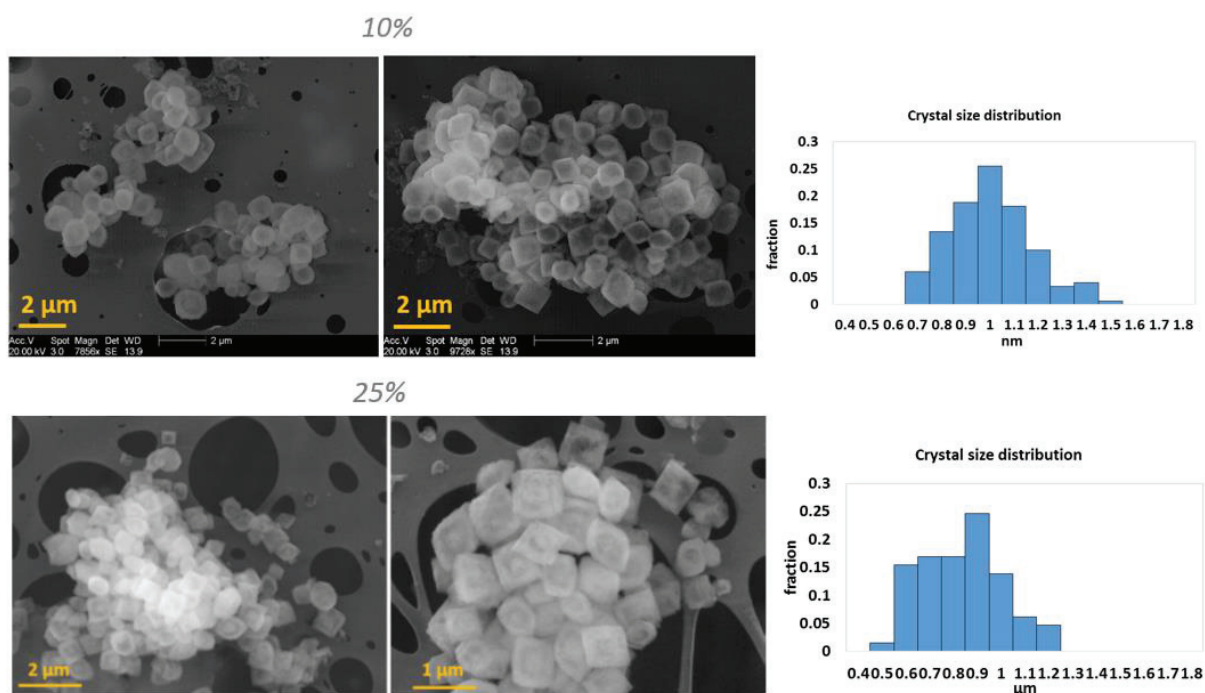


Figure 22 - SEM images of hollow Beta, hydrothermal synthesis at 150 °C using 10wt. % and 25wt. % of CIT-6, and corresponding crystal size distribution.

TEM images show more clearly the size and morphology of the crystals (see Figure 23). Again, the different of contrast between the center and the external part of the crystal are indicators of the hollow morphology for both samples. However, the inner cavity of 25% crystals does not seem to be completely empty as in for 10% crystals (see orange circles in Figure 23). The presence of this “matter” in the center of the crystal might be due to an incomplete dissolution of CIT-6, which is in agreement with the XRD shown above (see Fig 20): 25% sample presents higher peaks due to a higher crystal density (Beta and CIT-6), and therefore, smaller void volume of the inner cavity.

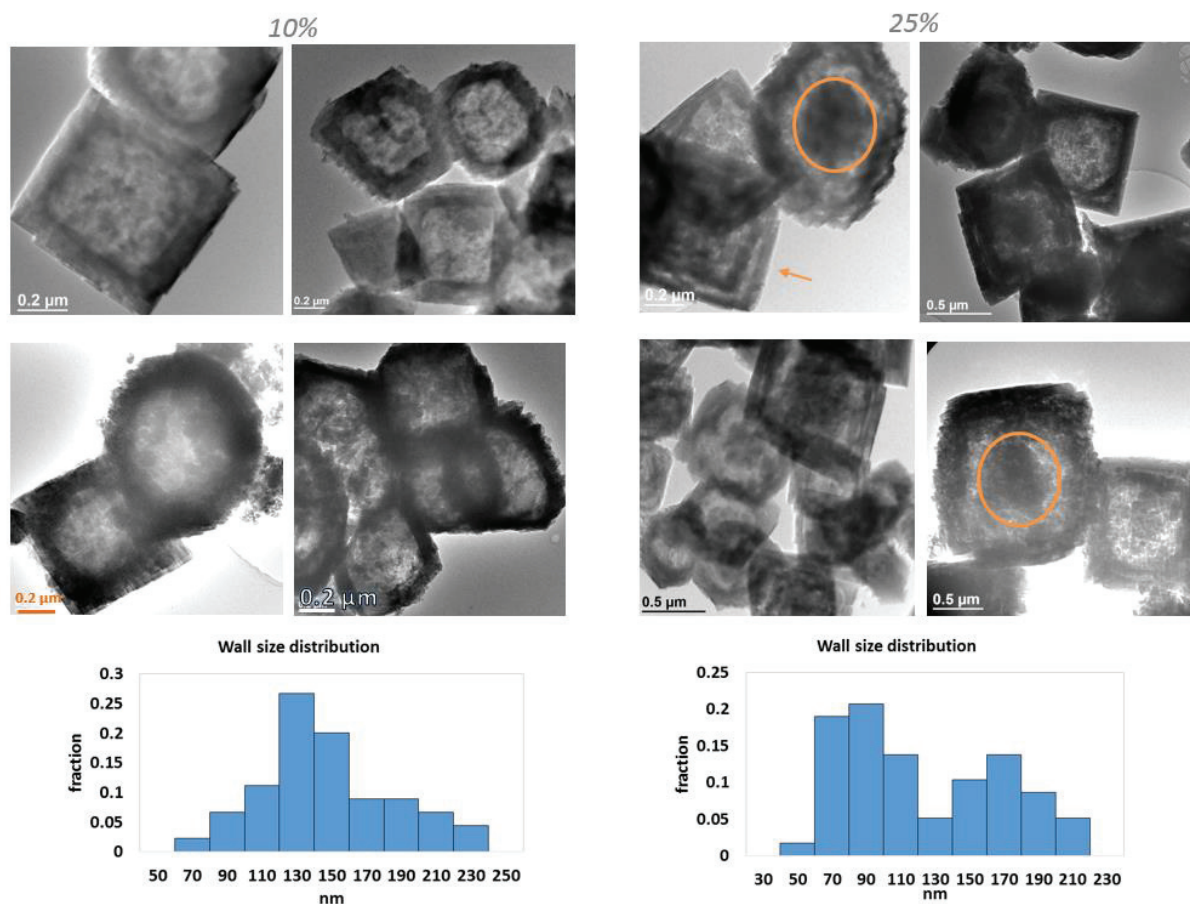


Figure 23 - TEM images of hollow Beta, hydrothermal synthesis at 150 °C using a) 10wt. % and b) 25wt. % of CIT-6, and corresponding wall size distribution. Orange arrows indicate the crystals that appear to have two zeolite walls. Orange circles indicate the area of the inner cavity with less contrast.

The wall thickness appears to be approximately the same, between 70 nm and 210 nm. However, we must take into account that measuring the size of the wall in TEM images, will depend of the crystal position, but also on the focus adjustments of the microscope. Moreover, there were found “double walls” in the case of 25% CIT-6, see Figure 23 the orange arrow. One might wonder if these are artifacts of the technique. If not, these particular crystals might present a different morphology than the hollow Beta synthesized with 10wt. % CIT-6. TEM images are extremely sensitive to several adjustments like contrast, focus, astigmatism etc. In the case of the present crystals, different adjustments would have an impact in the “apparent” thickness of the zeolite wall. Hence, the wall thickness that we can measure from the TEM images has a significant error (~10% from the point of view of the microscope operator). This is not sensitive to differences in the order of dozens nm. TEM images of a cross section of the sample, such the one in Figure 13, would eventually give more accurate insights about the morphology inside the cavity, and the wall thickness.

N₂ isotherms of both samples are very similar, even though that for the sample 25% the V_{meso} found was higher, see Figure 24 and Table 7. The hysteresis size is also different, suggesting different sizes and/or shapes of mesopores.

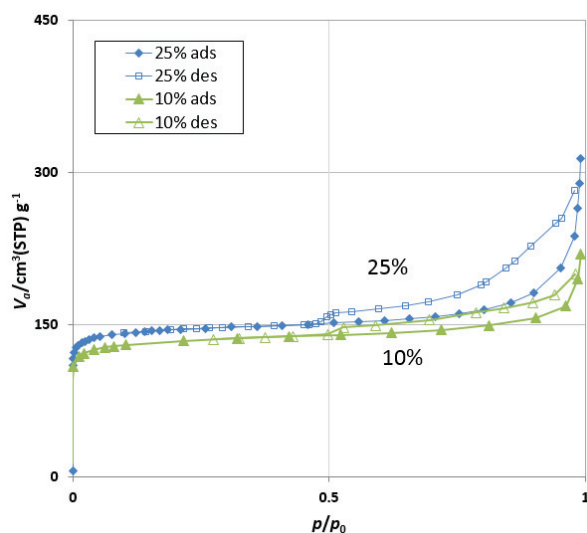


Figure 24 - N₂ adsorption/desorption isotherms of samples 10% and 25%, hydrothermal synthesis performed at 150 °C for 22h, static conditions.

Table 7 - Textural properties of samples 10% and 25%, hydrothermal synthesis performed at 150 °C for 22h, static conditions.

Sample	10%	25%
V _{micro} [cm ³ /g]	0.10	0.10
V _{meso} [cm ³ /g]	0.04	0.07

ICP analysis shows that Zn content is approximately the same for both samples (Zn/Si~0.03) and the Al is slightly lower for 25% CIT-6, suggesting that Al yield is lower than Si, for early stages of crystallization (Si/Al=8.1 for 10 wt. % CIT-6 sample and Si/Al=9.5 for 25 wt. % CIT-6 sample).

2.3.4. Effect of TEA⁺ – using calcined CIT-6 crystals

CIT-6 has to be stable enough in alkaline media to allow Beta recrystallization on its surface. However, we wondered if it is possible to obtain that stability using calcined CIT-6, and how. One idea to increase stability was to use calcined CIT-6 seeds, and to add the respective amount of organic molecules to the synthesis gel. Zeolites contain many Si-OH groups on their surfaces that lose H⁺ in alkaline medium. TEA⁺ ions get attached on Si-O⁻ via electrostatic interaction, reducing the dissolution of the zeolite external surface,²² hence, allowing Beta crystallization before complete dissolution.

We have performed the same hollow Beta synthesis, but using calcined CIT-6 and adding TEA⁺ into the aluminosilicate gel. Two samples were synthesized using different amounts of TEAOH. After TGA analysis of as-made CIT-6 crystals, we have noticed a 14 wt. % of organic template, (see Annexes-Chapter III). Therefore, we have performed the hollow Beta synthesis using an amount of TEAOH equivalent to 14 wt. % of the CIT-6 used, and another synthesis using 10 times more. The samples are denoted as **TEAHollow β** and **++TEAHollow β** .

In both cases, the final product obtained is a ***BEA** type structure with some amorphous phase (see Annexes-Chapter III) where the sample with more TEA⁺ content appears to be more crystalline. However, SEM images do not show the expected pyramidal nanoboxes or CIT-6 crystals shape, but rather agglomerates of small crystals with no particular shape, Figure 25.

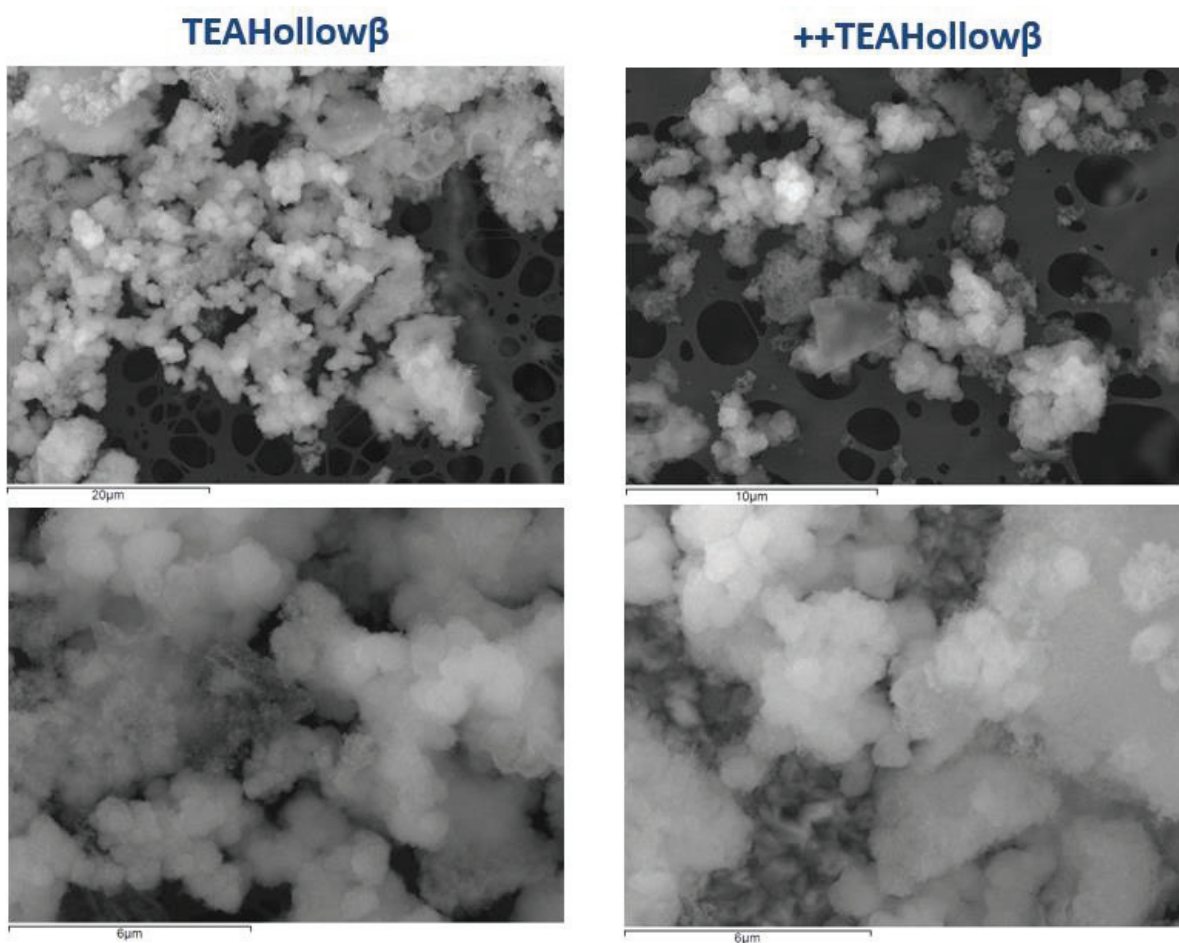


Figure 25 - SEM images of hollow Beta, hydrothermal synthesis using calcined CIT-6 crystal seeds and different quantities of TEAOH in the synthesis gel.

These results suggest that the presence of TEA^+ in the aluminosilicate gel was not able to protect CIT-6 crystals from dissolution, and there was crystallization of Beta zeolite elsewhere, probably because there were conditions for the natural nucleation of Beta zeolite, without the CIT-6 surface. Therefore, this approach was not further studied.

2.4. Encapsulation of Pt NP's in hollow Beta single crystals

Herein, we present different synthesis methods to introduce Pt NPs in the hollow Beta. We managed to selectively introduce Pt NPs either inside the cavity, inside the zeolite wall or on the external surface, depending on the synthesis method applied. Hollow Beta sample as a support for Pt NPs will be denoted as **Pt@Hollowβ**, independently of the different synthesis method.

2.4.1. Post-impregnation

We studied the introduction of Pt NPs on hollow Beta by different methods, such as competitive ion exchange and impregnation, and using different precursors, $\text{Pt}(\text{NH}_3)_4(\text{NO}_3)_2$ and H_2PtCl_6 . In each synthesis, the NPs were dispersed on the external surface and inside the porous network near the surface. We were not able to obtain any samples with NPs exclusively within the zeolite micropores.

For competitive ion exchange, TEM images showed that Pt NPs were distributed mainly on the external surface of the zeolite.

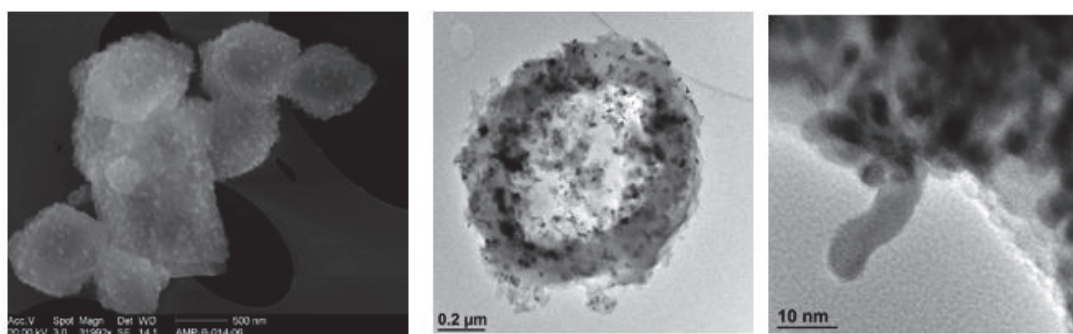


Figure 26 – SEM (left) and TEM images (2 right side images) of Pt@Hollow β obtained by ion exchange with Pt solution $\text{Pt}(\text{NH}_3)_4(\text{NO}_3)_2$, 1600ppm, 0.01 g_{zeol}/ml and reduction under H_2 flow.

The impregnation method was able to introduce NPs not only on the external surface, but also (very possibly) inside the zeolite framework – see Figure 27. It must be stressed out that from standard TEM pictures, it is not easy to determine the location of NPs. They can appear to be within the zeolite micropores but actually be on the outer surface.

Several synthesis parameters can have a huge impact on the dispersion and localization of the NP's, namely the preparation of the sample, the metal precursor, the drying step, calcination step prior to reduction,^{23,24} reduction method²⁵ etc. However, selective encapsulation by post-synthesis methods is not easy, probably because of diffusion limitations of the precursors through the pores for example.²⁶ The diffusion process of metal cations through the pores is a critical parameter that will influence the formation of the cluster inside the zeolite.²⁷ Indeed, none of the syntheses performed earlier resulted in nearly total encapsulation. Therefore, the post-impregnation method was not further studied.

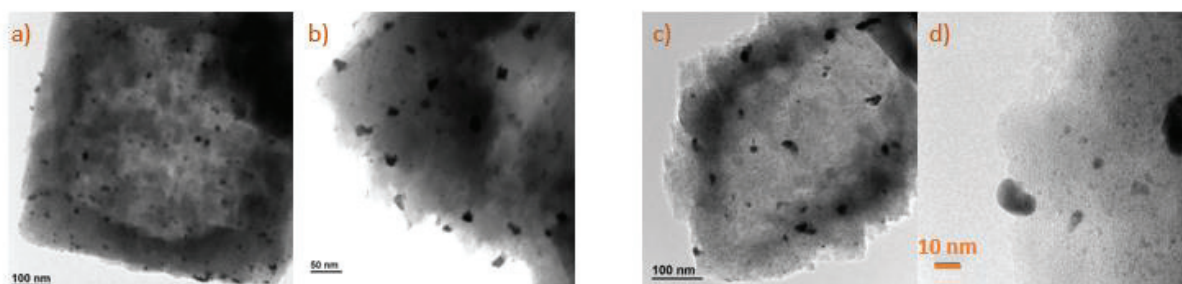


Figure 27 - TEM images of Pt@Hollow β obtained by impregnation with Pt solution $Pt(NH_3)_4(NO_3)_2$, 0.5 wt. % Pt, images a) and b), and 8.4 wt. % Pt images c) and d). Both samples were reduced under H_2 flow.

2.4.2. Pre-impregnation

Dai *et al.*²² showed the result of dissolution - recrystallization method over the Ag/silicalite-1, where the final product consists of hollow silicalite-1 single crystals with Ag NPs. After analyzing TEM images taken at several different tilting angles (from different perspectives), they conclude that the Ag NPs are located inside the zeolite micropores, not on the external surface of the crystal. Dai *et al.*²² showed how during hydrothermal synthesis, there is recrystallization on the surface of the crystal, encapsulating the Ag NPs within the zeolite wall.

Indeed, the prior literature of hollow zeolite single crystals with encapsulated NPs starts by the pre-impregnation on the parent zeolite, followed by the dissolution recrystallization method.^{22,28-30}

Similarly to the literature of hollow zeolites single crystals with encapsulated NPs, we have impregnated the parent crystals of CIT-6, prior to the dissolution-recrystallization step, denoted **Pt/CIT-6**. In the case of the current synthesis, CIT-6 crystals were not calcined. Taking this “pre-impregnation approach”, we decided to study different parameters that would (or not) have an effect in the dispersion, and location of the Pt NPs in the crystal:

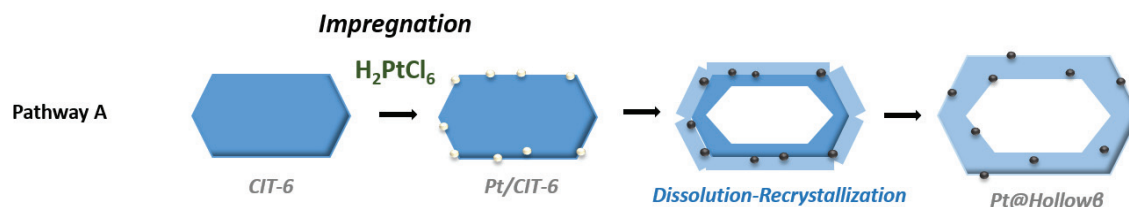
- Type of precursor, namely $Pt(NH_3)_4(NO_3)_2$ or H_2PtCl_6 solution
- Reduction step, either over the Pt/CIT-6, either only over the final Pt@Hollow β
- Type of reduction over Pt/CIT-6, namely $NaBH_4$ solution or H_2

In total, 5 different synthesis pathways were studied, denoted as pathway A, B, C, D and E.

All the impregnations, reductions etc. that were performed over the as-made CIT-6, did not overpass 150 °C, to avoid TEA^+ decomposition (as studies reported that the thermal decomposition of TEA^+ on zeolite Beta occurs after 150 °C³¹).

The results in terms of Pt NPs location were investigated by TEM and are presented below.

2.4.2.1. Pathway A



As-made CIT-6 was impregnated with a solution of H_2PtCl_6 , 2 wt. % Pt. The respective Pt/CIT-6, as-made was used for the synthesis of the respective Pt@Hollow β . Figure 28 shows TEM images of Pt@Hollow β . Pt NPs are clearly visible in the whole crystal image. It seems that Pt particles are mainly located inside the zeolite shell, but every crystal presented at least a few NP's undoubtedly located on the external surface.

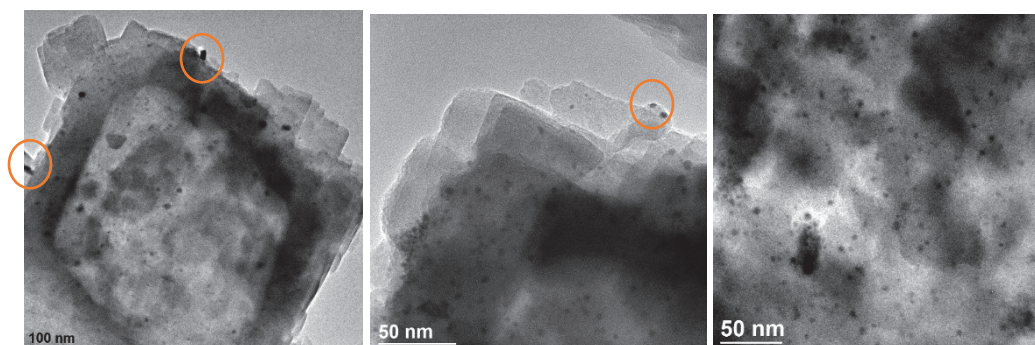
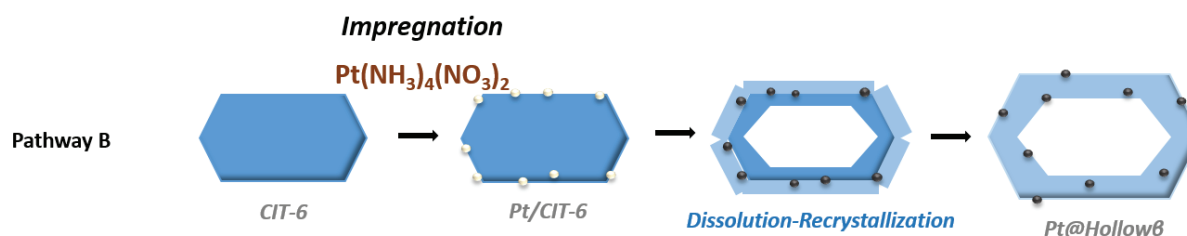


Figure 28 – TEM images of Pt@Hollow β by pathway A. Orange circles are pointing out the presence of Pt NPs on the external surface.

2.4.2.2. Pathway B



Similarly to the previous synthesis, as-made CIT-6 was impregnated with a $\text{Pt}(\text{NH}_3)_4(\text{NO}_3)_2$ solution, 0.3 M, 2 wt. % Pt. The respective Pt/CIT-6, as-made was used for the

synthesis of the respective Pt@Hollow β . As shown in Figure 29, there is a rather homogeneous dispersion of Pt NPs almost in the whole 2D image of the crystal. Contrary to all the impregnation syntheses shown before, there are very few (almost none) NP's found on the external border of the crystal, even if a few NPs were found clearly on the external surface, as the image on the right, see Figure 29. However, the detailed observations of the NP's location included 10 different crystals, which is a very small sample to have a solid conclusion. Also, as we mentioned before, when analyzing TEM images we cannot be sure if a certain NP is inside the porous network or on the external surface.

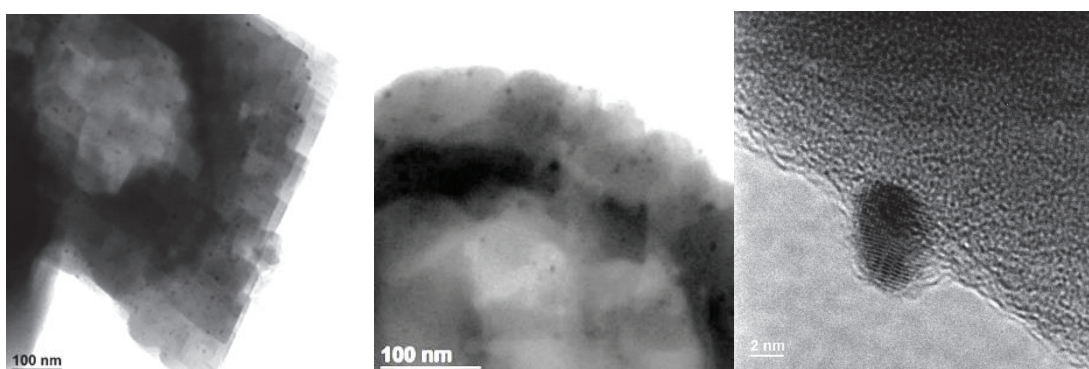


Figure 29 - TEM images of Pt@Hollow β prepared by Pathway B.

This same sample was calcined at 700 °C for 10h. At this temperature, NPs would naturally sinter/coalesce together, specially if they are located on the external surface of the crystal.

Figure 30 shows TEM images of the sample after calcination. Most of the crystals had almost no Pt NPs. The few NPs present were quite bigger than the original ones observed in Figure 29, and they were located mostly on the external surface. These results suggest that either most of the NP were located outside, and/or the encapsulated NPs managed to migrate to the external surface, specially if these were initially located near the surface. Even if this synthesis pathway did sucessfully encapsulate a big percentage of the Pt, this encapsulation is not stable, since dispersion and location of this NPs changed significantly after calcination.

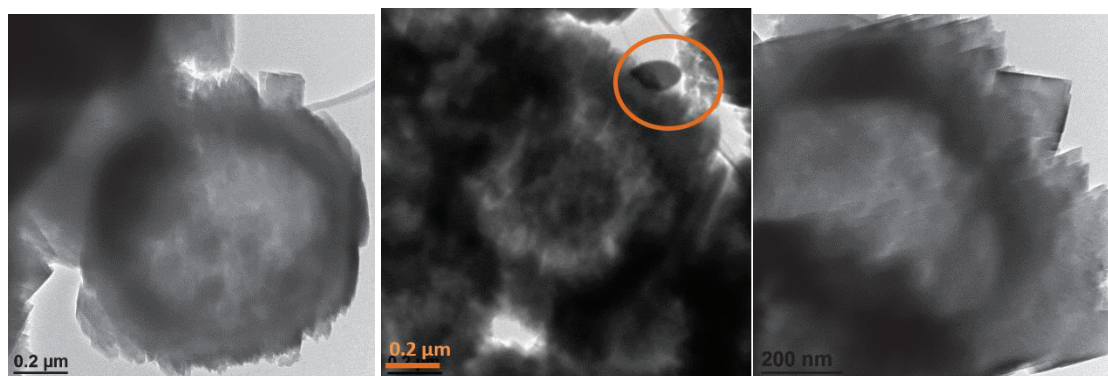
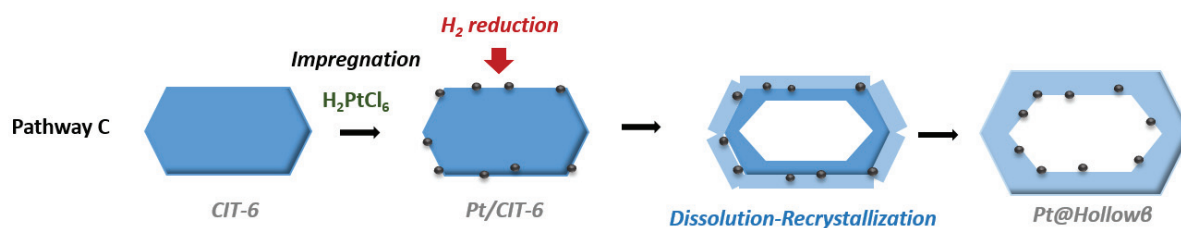


Figure 30 – TEM images of Pt@Hollowβ prepared by Pathway B, after calcination at 700 °C for 10h. Orange circle points out the presence of a Pt nano cluster.

2.4.2.3. Pathway C



Contrary to the literature, pre-impregnation methods like “Pathway A” and “Pathway B”, did not guarantee the encapsulation of Pt NPs inside the zeolite wall or the cavity. When such methods are applied to Pt impregnated hollow Beta crystals, the resulting Pt@Hollowβ crystals undoubtedly presented NPs on the external surface, and possibly some NPs encapsulated inside the zeolite micropores, mesopores and defects. Note that the metallic clusters were bigger than 1-2 nm, which is bigger than the pore diameter of the Beta zeolite. One must take into account that, contrary to the literature, the impregnation is carried out over an as-made CIT-6 (instead of calcined), that can result in a very different interaction regarding a silicalite-1 crystal. Also, there is the possibility of a natural migration of NPs during the synthesis, or during H₂ reduction. Also, it seems probable that the Pt ion can get solvated in solution during hydrothermal synthesis, and therefore Pt NPs can be anywhere where recrystallization occurs.

One possibility to avoid NPs on the external surface of the hollow Beta crystal, would be to encapsulate directly the Pt NP's on the CIT-6 pore system, and improve the impregnation process by previously increasing the desorption temperature of the CIT-6 for example. However, TEA⁺ must be kept inside the pore system, which limits the temperature range of the desorption step before impregnation. The presence of TEA⁺ within the CIT-6 pore system might also block the access of the metal precursor through the micropores.

We decided to reduce the Pt/CIT-6 before the “Dissolution-Recrystallization” procedure, as an attempt to create Pt NPs with low mobility, so they would not migrate during dissolution-recrystallization procedure. Therefore, the following studies show the synthesis of Pt@Hollow β using reduced Pt/CIT-6 crystals.

Traditionally, H₂ flow at relatively high temperature is the common reducing method for metal catalysts in zeolites. However, high temperatures can be responsible for the calcination of the TEA⁺ molecule, which is fundamental for the synthesis of the hollow Beta, as we have seen in the literature and in previous studies.¹

As mentioned before, studies have reported that the thermal decomposition of TEA⁺ on zeolite Beta only occurs after 150 °C³¹. Therefore, reduction was performed under H₂ at 150 °C, to avoid TEA⁺ decomposition.

For this study, as-made CIT-6 crystals were impregnated with a solution of H₂PtCl₆, 2 wt. % Pt. The Pt/CIT-6 crystals were reduced under H₂ at 150 °C. Figure 31 shows the SEM images (BSE mode) of the Pt/CIT-6 after reduction, where the Pt NPs correspond to the bright spots. It is clear that this reduction method was able to reduce the metal present in the CIT-6, which resulted in a homogeneous distribution of Pt NPs.

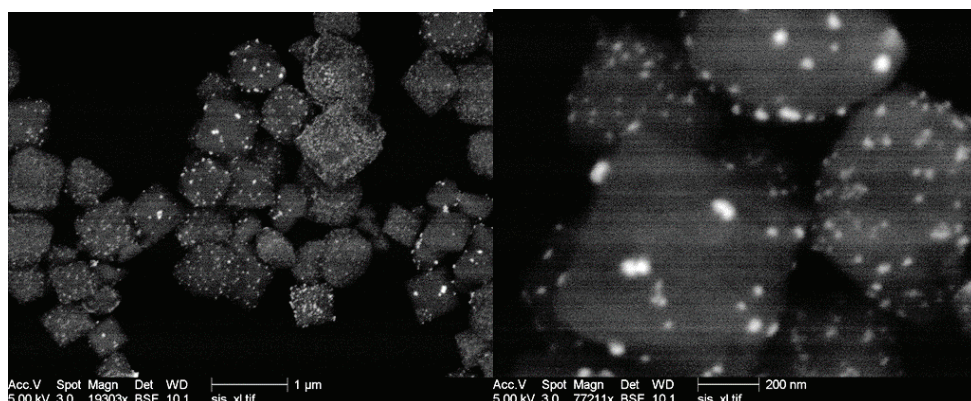


Figure 31 - SEM images (BSE mode) of Pt/CIT-6 after reduction by H₂ flow.

The resulting Pt@Hollow β crystals are shown in Figure 32. Pt NPs are almost nonexistent and very badly dispersed, consisting in a few agglomerations or a few isolated NPs. Moreover, the crystals appeared to have several internal mesopores and macropores instead of a hollow morphology.

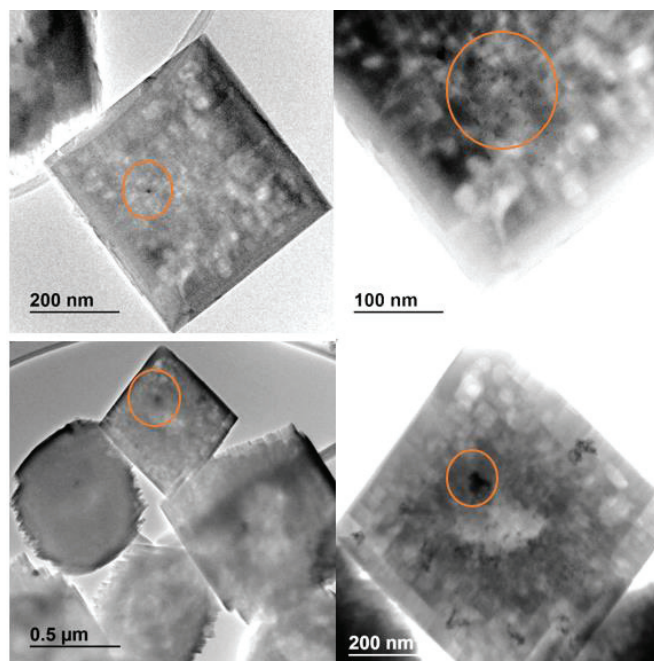
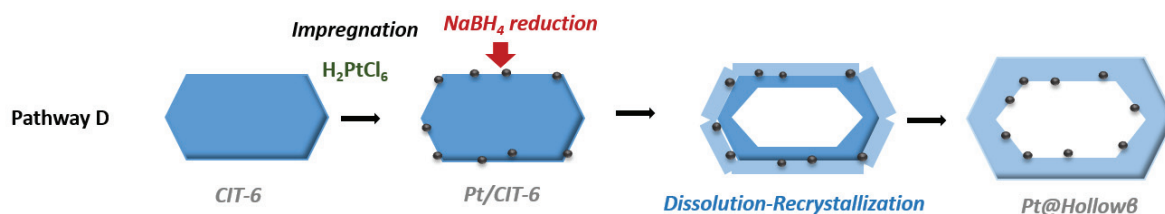


Figure 32 - TEM images of Pt@Hollow β by method pathway C.

We did not perform any further characterizations or optimizations in order to understand how and why the synthesis resulted in these mesoporous crystals. We did not study either the size or connectivity of this mesopore/macropore system, by N_2 isotherms for example. We can speculate about the effect of the H_2 reduction over the crystal. One hypothesis was that the TEA^+ partially decomposed after reduction, and therefore influenced dissolution-recrystallization process. In any case, this method was not further studied.

2.4.2.4. Pathway D



An alternative to the classical H_2 flow reduction method, can be a chemical reduction method with $NaBH_4$ solution for example.²⁵ In this case, reduction is performed in $NaBH_4$ solution at room temperature, avoiding any TEA^+ decomposition due to high temperatures.

NaBH_4 is soluble in water and reacts with water to produce H_2 .³² Also, the reduction reaction with NaBH_4 is extremely fast. Several parameters were studied regarding this reduction process, namely the concentration of NaBH_4 , the life time of the NaBH_4 solution as reducing agent (the reduction capacity of NaBH_4 solution with time), etc, (see Annexes Chapter III). These parameters showed to have a big impact on the dispersion of Pt NPs. The results presented below were made following the NaBH_4 reduction procedure considered to be the best, i.e. minimum loss of Pt and high dispersions.

CIT-6 crystals were impregnated with a H_2PtCl_6 solution, 2 wt. % of Pt and afterwards reduced by NaBH_4 , Figure 33, (synthesis details on Chapter 2).

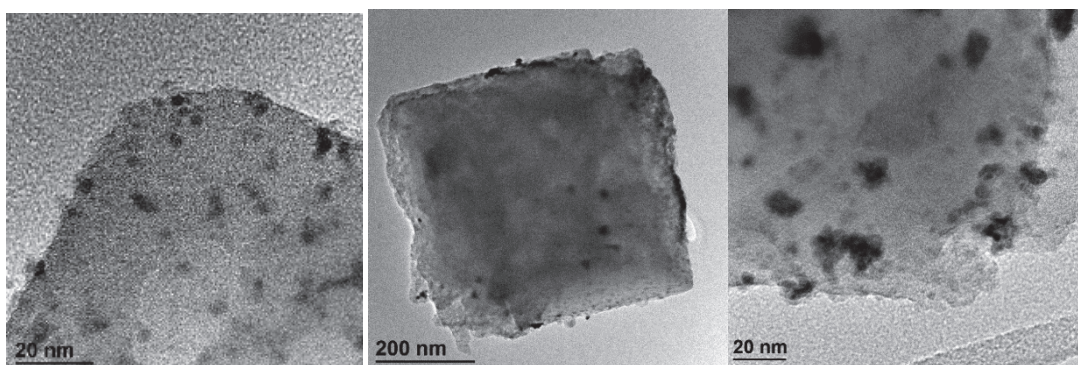


Figure 33 - TEM images of Pt/CIT-6 after reduction by NaBH_4 solution.

The previous Pt/CIT-6 crystals were used for the synthesis of the respective Pt@Hollow β . Figure 34 shows some SEM (BSE mode) images of Pt@Hollow β . In general, the Pt NP's are distributed in a relatively homogenous way, but the location of these NPs is not clear. However, there were found several NPs agglomerations on the external part of the crystals that are also represented in Figure 35.



Figure 34 – SEM BSE images of Pt@Hollow β prepared following pathway D.

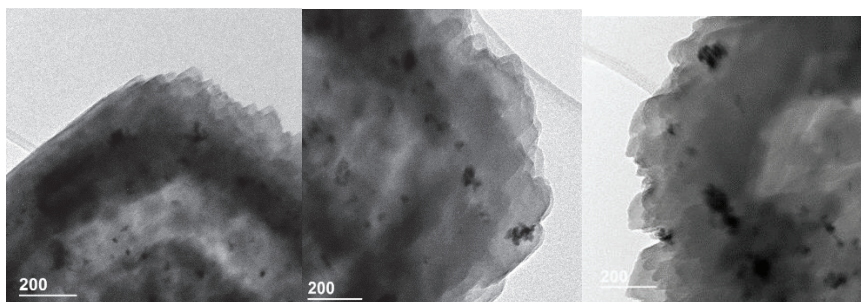
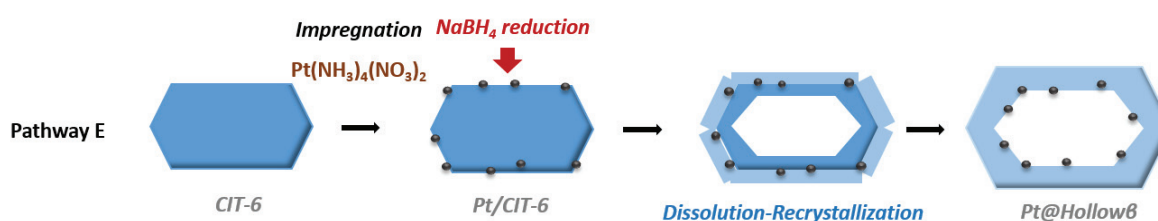


Figure 35 - TEM images of Pt@Hollowβ prepared following pathway D.

2.4.2.5. Pathway E



Similarly to the previous synthesis, CIT-6 crystals were impregnated with a Pt $(\text{NH}_3)_4(\text{NO}_3)_2$ solution, 2 wt. % of Pt, and afterwards reduced by NaBH_4 solution, (synthesis details in Chapter 2).

ICP analysis reveals a final Pt content of Pt/CIT-6 was 2.6 wt. %, which suggests that there was no Pt loss during NaBH_4 reduction. The location and size of platinum nanoparticles impregnated on the surface of CIT-6 were investigated by TEM (see Figure 36), which shows that the platinum nanoparticles (particle size between ~ 10 -20 nm) are successfully anchored on the external surface of the crystals.

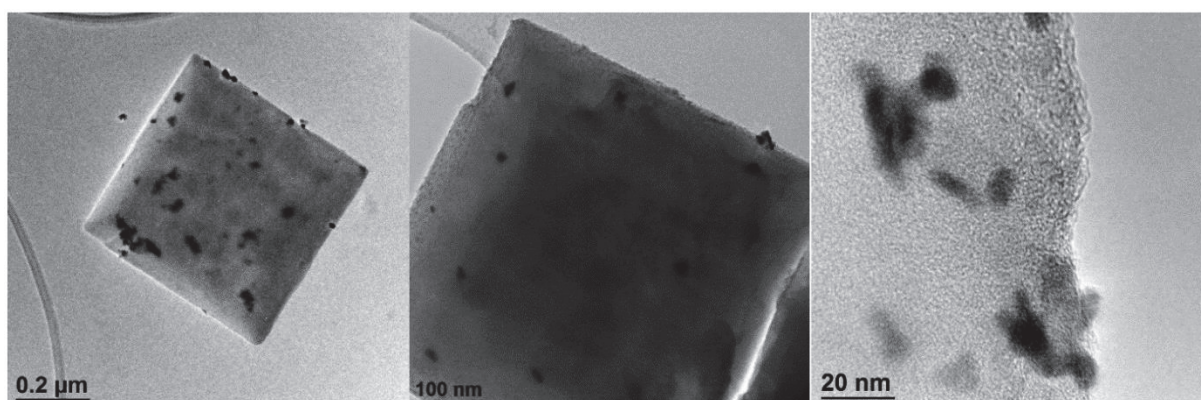


Figure 36 - TEM images of Pt/CIT-6 after reduction by NaBH_4 solution.

Figure 37 shows the TEM images corresponding to the Pt@Hollow β synthesized from the previous Pt/CIT-6. After hydrothermal treatment a highly crystalline Pt@Hollow β crystals is obtained, in which the Pt NPs are apparently encapsulated inside the cavity and/or in the zeolite shell, as no NPs are found on the external surface of the crystals (contrary to the previous examples). For the first time, Pt NPs appeared to be located inside the zeolite wall and/or cavity. The Pt@Hollow β presented the same crystal size and morphology as the hollow Beta presented before. ICP analysis reveals a final Pt content of 1wt. %, indicating that there was Pt loss during the hydrothermal synthesis (~60%).

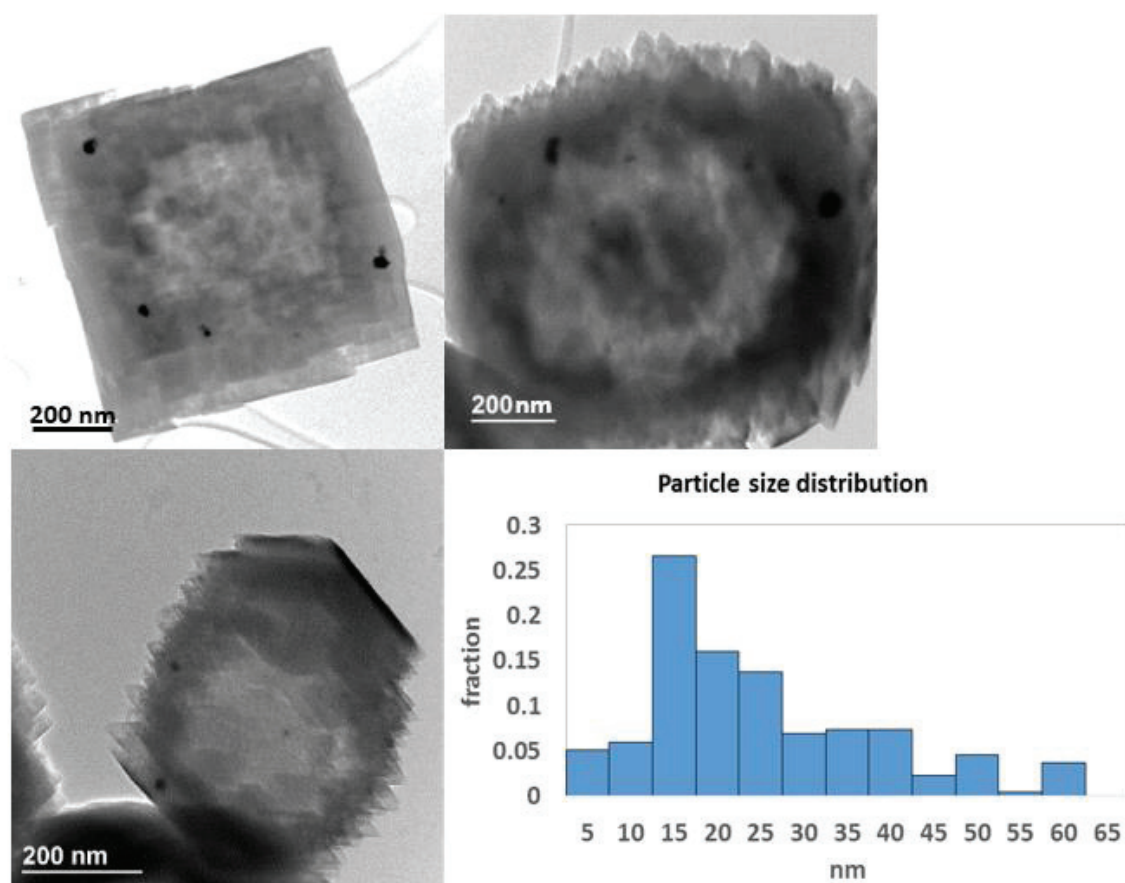


Figure 37 - TEM images of Pt@Hollow β prepared following pathway E.

Regarding all the synthesis methods presented so far, this one appears to be the one where Pt NPs are exclusively encapsulated in the zeolite shell and/or inside the inner cavity, as suggested by TEM images. However, as explained before, this is not enough evidence to prove the location of the Pt NPs.

Transmission electron tomography with corresponding 3D reconstruction was carried out on an isolated hollow crystal, confirming the absence of visible Pt nanoparticles on the external surface (Figure 38). On the other hand, the nanoparticles are clearly observed on the inner surface of the cavity, and inside the zeolite wall, in the mesoporous region, with an average diameter of 28 nm (Figure 39).

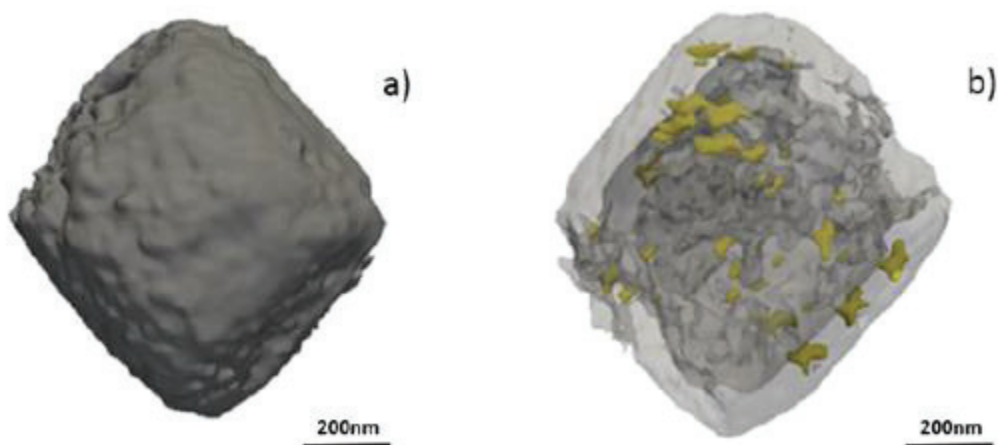


Figure 38 – 3D model of Pt@Hollow β zeolite crystal reconstructed from electron tomography. The zeolite is represented in grey and Pt NPs are represented in yellow. External view (left hand side), transparent view (right hand side).

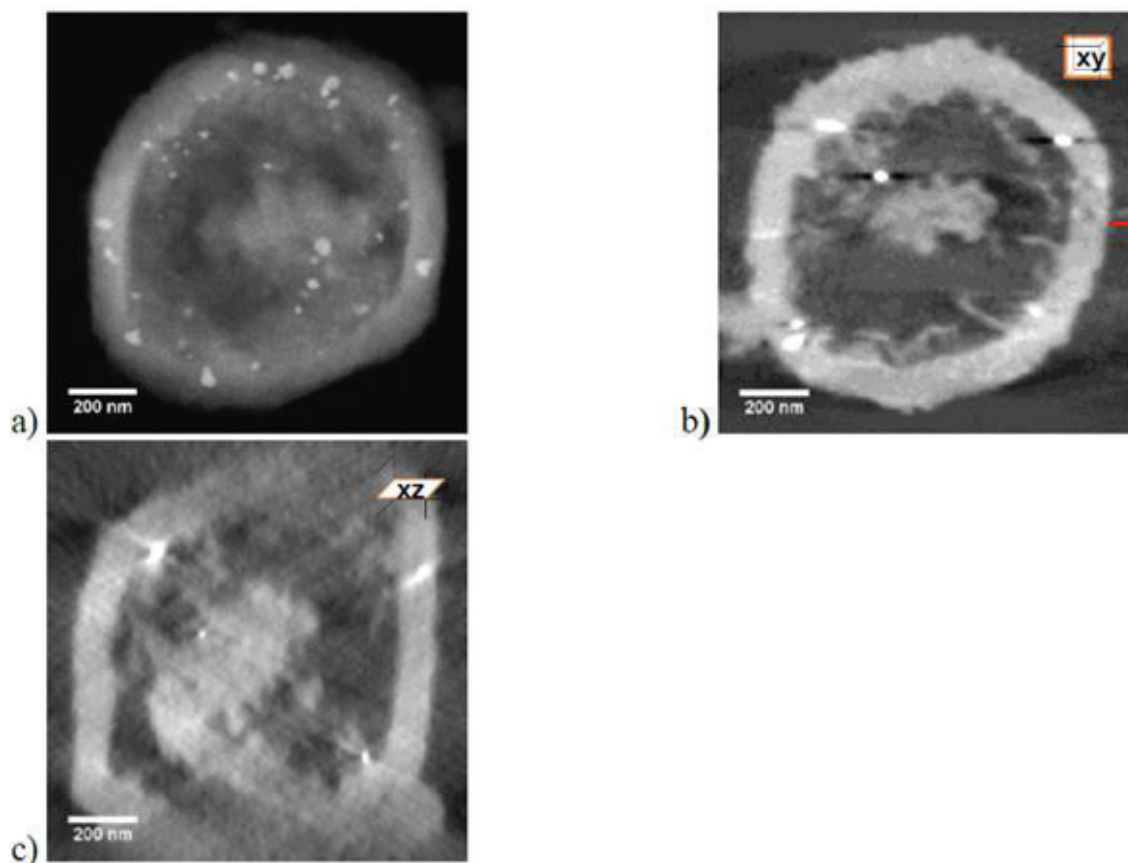


Figure 39 – a) HAADF-STEM image at 0° forming the tilt series used to reconstruct the volume. The white dots are the Pt NPs. b) and c) Orthogonal cross-sections from the volume of the object parallel to the XY and XZ planes, respectively. The red line in image b) shows the intersection line of the cross-sections.

Moreover, Pt@Hollow β crystals show to be resistant to calcination at 750°C for 10 hours. The particle size distribution and dispersion of the Pt NPs remains very similar regarding the as-made Pt@Hollow β (Figure 40). This indicates that indeed the Pt NPs are probably encapsulated “deep” in the zeolite framework and/or inside the cavity, and migration of these NPs is very limited.

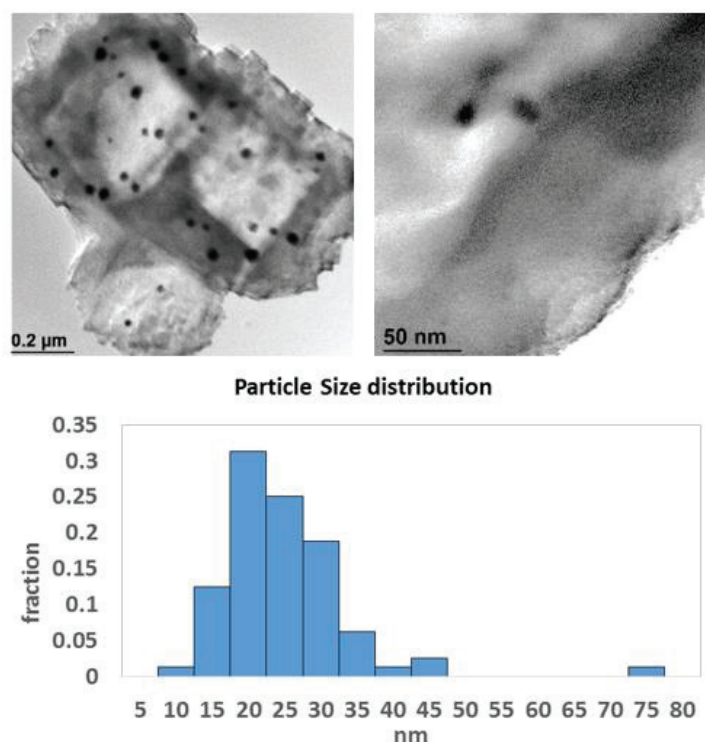


Figure 40 – TEM images of Pt@Hollow β after calcination at 750 °C, for 10h, and Pt particle size distribution determined from TEM images.

The N₂ physisorption isotherms (at 77K) show that Pt@Hollow β had similar porous structure than hollow Beta (check Annexes- Chapter III).

Chemical analysis of the Pt@Hollow β crystals gives Si/Al and Si/Zn molar ratios of 8 and 237, respectively. Zn content is smaller than the one from hollow Beta, suggesting that there may be loss of Zn during NaBH₄ reduction.

- Toluene and mesitylene hydrogenation reactions

The absence of Pt NPs on the external surface of the crystal was also confirmed by a model hydrogenation reaction using reactants with different diffusion rates. The catalytic hydrogenations of toluene and mesitylene were chosen as model reactions to demonstrate that there are no particles at the zeolite surface. The activity of Pt@Hollow β in the hydrogenation of these two substrates was compared with that obtained over a conventional Pt catalyst supported on silica (Pt/SiO₂), for which all Pt nanoparticles are accessible without any diffusion constraints (see Figure 41). The Pt/SiO₂ data were reported in an earlier paper²⁸ and are reused here for the sake of comparison.

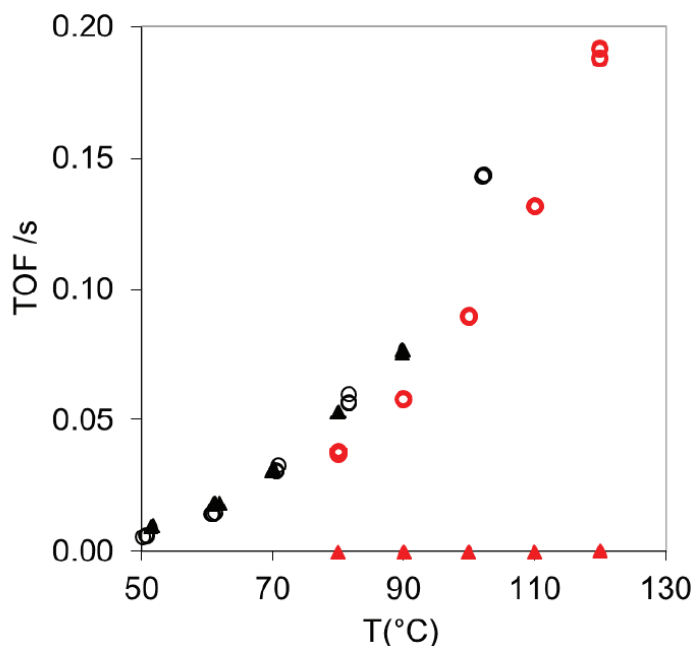


Figure 41 - Activity (turnover frequency) of Pt/SiO₂ catalyst (black symbols) and Pt@Hollowβ catalyst (red symbols), in the hydrogenation of toluene (circles) and mesitylene (triangles). Toluene pressure = 0.9 kPa, balance H₂. Mesitylene pressure = 0.06 kPa and 0.2 kPa, for Pt/SiO₂ and Pt@Hollowβ respectively, balance H₂.

The Pt/SiO₂ catalyst was active for the hydrogenation of both toluene and mesitylene, showing very similar turnover frequencies, see Figure 41. The turnover frequency and apparent activation energy values (e.g., $\text{TOF}_{\text{Pt/SiO}_2} = 6 \times 10^{-2} \text{ s}^{-1}$ at 80 °C and $55 \pm 3 \text{ kJ/mol}$ for toluene, see Annexes-Chapter III) are consistent with the literature data for both reactions.²⁸

Catalytic activity of Pt@Hollowβ for toluene hydrogenation shows similar TOF values to those observed in the case of Pt/SiO₂ (e.g., at 80 °C, $\text{TOF}_{\text{Pt@Hollow}\beta} = 4 \times 10^{-2} \text{ s}^{-1}$). Similarly, the value for the apparent reaction activation energy ($E_a = 47 \text{ kJ/mol}$) is consistent with those reported in the literature for Pt/SiO₂^{28,33} (more details in Annexes –Chapter III). On the other hand, mesitylene conversion was negligible (conversion in the error range of ca. 0.01%), and the corresponding TOF is therefore essentially nil over Pt@Hollowβ, in contrast to Pt/SiO₂. Even though the mesitylene pressure used was slightly different for the two catalysts, this should not affect the TOF values since the reaction order with respect to the aromatic on Pt-based catalysts is typically zero or close to zero.^{33,34}

The TOF values of Pt/SiO₂ and Pt@Hollowβ are similar. Based on our latest studies^{28,35} we can rationalize that no significant diffusional limitation occurs in the toluene hydrogenation thanks to the small shell thickness. In contrast, we can conclude that severe diffusional limitation occurs for the bulkier mesitylene for Pt@Hollowβ. Although mesitylene is able to enter into the *BEA pore system, its diffusion in the microporous framework is significantly slower than that of toluene due to its larger kinetic diameter, which is 0.86 nm compared to 0.61 nm for toluene (Annexes- Chapter III).

The fact that toluene (but not mesitylene) is readily hydrogenated **clearly demonstrates the absence of NPs on the external surface**. It also evidences the single crystal nature of this material, as well as **the absence of a mesopore network connecting the external surface and the inner cavity**. A mesopore system would allow the diffusion of mesitylene through the zeolite shell, and as consequence its hydrogenation.

This synthesis approach was the only one that guarantees the selective encapsulation of Pt NPs in the hollow Beta. It should be noted that on the other hand, NPs dispersion is very low, 3% considering NP size distribution measured by TEM images and below 5% according to H₂ chemisorption. Generally for catalytic tests, highly dispersed catalysts have higher active surface and therefore high dispersions of NPs are more suitable.

2.4.3. Selective removal of Pt NPs by Br₂ treatment

In the subchapter above, we have presented a method to obtain hollow Beta with encapsulated Pt NPs. However, dispersion was extremely low which would be not desirable for catalytic tests. In here, we present a method to encapsulate Pt NPs while obtaining very high dispersion values. Earlier in this chapter, we have shown how we can obtain highly dispersed Pt distributions in hollow Beta zeolites, with Pt NPs located within the micropores and on the external surface. The idea is to take this same type of Pt@Hollow β to selectively remove the Pt NPs from the external surface, while keeping the encapsulated Pt NPs with its initial dispersion.

Knapp *et al.*³⁶ presented a technique to selectively remove Pt NPs from the outer surface of ZSM-5 zeolite, based on a halogen-halide system for metal dissolution.^{37,38} In the case of Knapp's study, the treatment was performed in an organic solvent containing a halogen and a tetraalkylammonium (TAA) halide. The highest dispersion measured after the treatment was obtained with Br₂ and tetraethylammonium bromide (TEABr) in acetonitrile. According to the literature,³⁶ the halide (TEABr) stabilizes the halogen (Br₂) in the form of a complex [TEA⁺Br₃⁻] which is too large to enter the zeolite pores. As a consequence, the halogen cannot react with the Pt NPs supported within the micropores and dissolves only those which are fully accessible on the surface of the crystals.

Herein, we present a similar approach applied to a highly dispersed Pt@Hollow β sample, with encapsulated Pt NPs and Pt NPs supported on the external surface. We managed to remove the Pt NPs from the external surface of the samples, creating a more active and selective catalysts.

Calcined Hollow β crystals were impregnated with Pt(NH₃)₄(NO₃)₂ solution, 8.4 wt. % Pt, according to the procedure described in Chapter II. The resulting crystal had a dispersion of Pt NPs on the external surface and inside the porous framework. Selective Pt removal was performed in the presence of Br₂ as halogen compound and a series of tetraalkylammonium

bromides, from C1 to C4, (TMABr, TEABr, TPABr and TBABr), in acetonitrile. The resulting samples were named **TMA-Pt@Beta**, **TEA-Pt@Beta**, **TPA-Pt@Beta** & **TBA-Pt@Beta**, according to the type of halide used for the treatment. The influence of the chain length on the average size and location of Pt nanoparticles in the treated crystals was studied by TEM and by catalytic performance in the hydrogenation of mono- and tri-substituted arenes, toluene and mesitylene.

2.4.3.1. Characterization of Pt@Hollow β – sample before treatment

Firstly, Pt@Hollow β was characterized in what concerns Pt dispersion and wt. %. Figure 42 shows TEM pictures of Pt/Beta and the respective particle size distribution. There are mainly two types of dispersion groups: a “larger” NPs (6-40nm) seem to be placed mainly on the external surface of the crystal, and a highly dispersed group of NPs placed apparently inside the crystal (1-3nm). Even though the numerical proportion of large particles does not exceed a few percent their mass contribution is certainly far from negligible.

The overall dispersion calculated using the two distributions of Pt NPs is close to $13 \pm 2\%$.

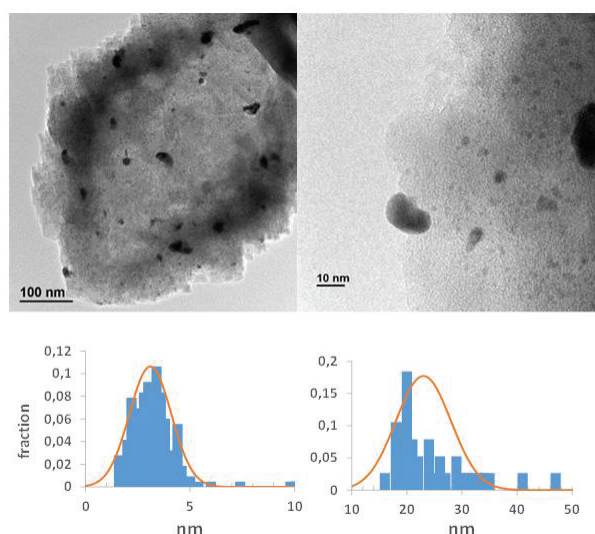


Figure 42 - TEM images of Pt@Hollow β at two different magnifications and corresponding particle size distributions for small (left) and large (right) Pt NPs.

The overall Pt wt. % is 7.5% and XPS analysis provides a Pt/Si atomic ratio of 0.016, corresponding to the Pt/Si of the surface of the sample (up to 10 nm deep), thus supporting the presence of Pt NPs on the external surface, see Table 8.

Table 8 - Metal content and dispersion in the different samples.

Sample name	Pt/Si (a)	Pt wt. % (b)	Dispersion (%)
Pt@Hollow β	0.016	7.5	13
TMA-Pt@Beta	0.009	5.0	60
TEA-Pt@Beta	0.005	4.9	65
TPA-Pt@Beta	0.006	5.2	60
TBA-Pt@Beta	0.007	5.1	50

(a) Surface Pt/Si ratio obtained by XPS

(b) Overall Pt content obtained by chemical analysis

2.4.3.2. Characterization of the samples after Br₂ treatment

Pt@Hollow β was then treated with four different halogen-halide-organic solvent systems, in which the halogen and organic solvent were always Br₂ and acetonitrile respectively (as described in chapter II). XRD patterns show that tetraalkylammonium-Br₂ treatments have no impact on the crystallinity of the zeolite, see Figure 43. However, peaks at $2\theta = 40^\circ$ and 46° visible on the diffractogramme of Pt@Hollow β , which correspond to (111) and (200) reflections of the fcc structure of metallic platinum,³⁹ are no longer observed after treatment with TMA, TEA and TPA cations. These results indicate that the metallic phase has been modified (see Figure 43). The intensity of XRD reflections of supported metal NPs strongly depends on the amount of metal and on the size and shape of the NPs. Besides concentrations that are too low to be observable under standard recording conditions, very small NPs with a diameter around 2 nm generally lead to broad XRD reflections difficult to distinguish from the background, particularly when the latter is a crystalline zeolite.⁴⁰ In contrast, Pt reflections do not totally disappear when the zeolite is treated with the bulky TBABr but their intensity is reduced by more than 75%.

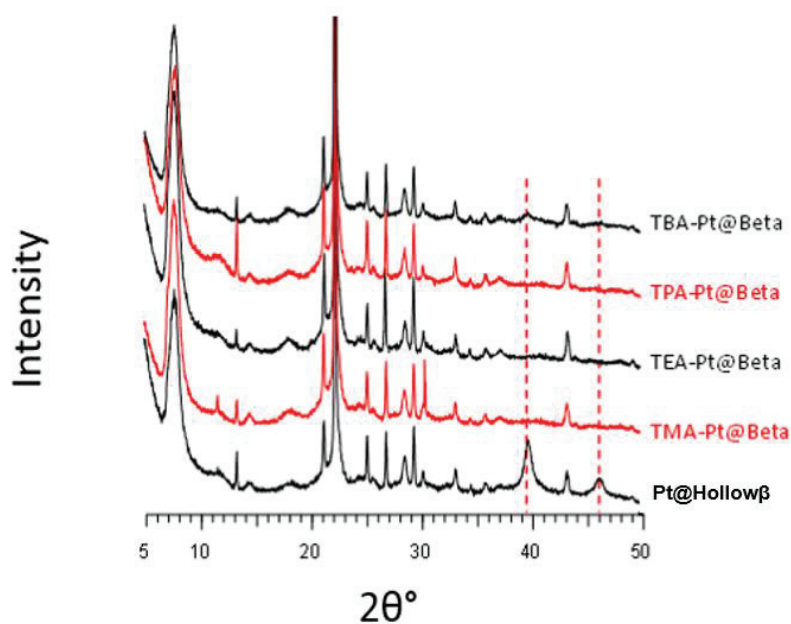


Figure 43 - XRD patterns of the original Pt@Hollow β and zeolites treated with the different tetraalkylammonium cations. Dashed lines show the position of two major reflections of metallic Pt.

Pt removal was studied by TEM observations compared with data regarding Pt wt. % and Pt/Si on the crystal surface. TEM images of TMA-, TEA- and TPA-Pt@Beta show that the large particles that were present on the surface of Pt@Hollow β disappeared (see Figure 44), indicating that those were certainly responsible for the XRD reflections at $2\theta = 40^\circ$ and 46° for the untreated Pt@Hollow β . In contrast, nanoparticles located inside the walls are still present, supporting the selective removal of external metal species by the Br₂-tetraalkylammonium bromide tandem. This was further supported by a significant decrease of the Pt/Si ratio measured by XPS (see Table 8).

The partial Pt removal was also confirmed by the decrease of the overall metal content in the different zeolites as compared to the untreated solid. Indeed, the Pt content, which was initially 7.5 wt. % in Pt@Hollow β decreases to 5.0 ± 0.2 wt. % in all treated samples, whatever the nature of the tetraalkylammonium cation (see Table 8). This suggests that all these three treatments very likely remove the particles located on the external surface of the crystals. Quantitatively, these external NPs represent approx. 33 % of the total mass of platinum initially present on Pt@Hollow β (if we take into account the wt. % Pt before and after treatment see Table 8). For the TMA⁻, TEA⁻ and TPA⁻ treated samples, the measurable particles were between 0.5 and 3 nm in size with metal dispersions in the 60–65 % range, similar to the value obtained on the family of internal NPs in Pt@Hollow β (see Figure 42).

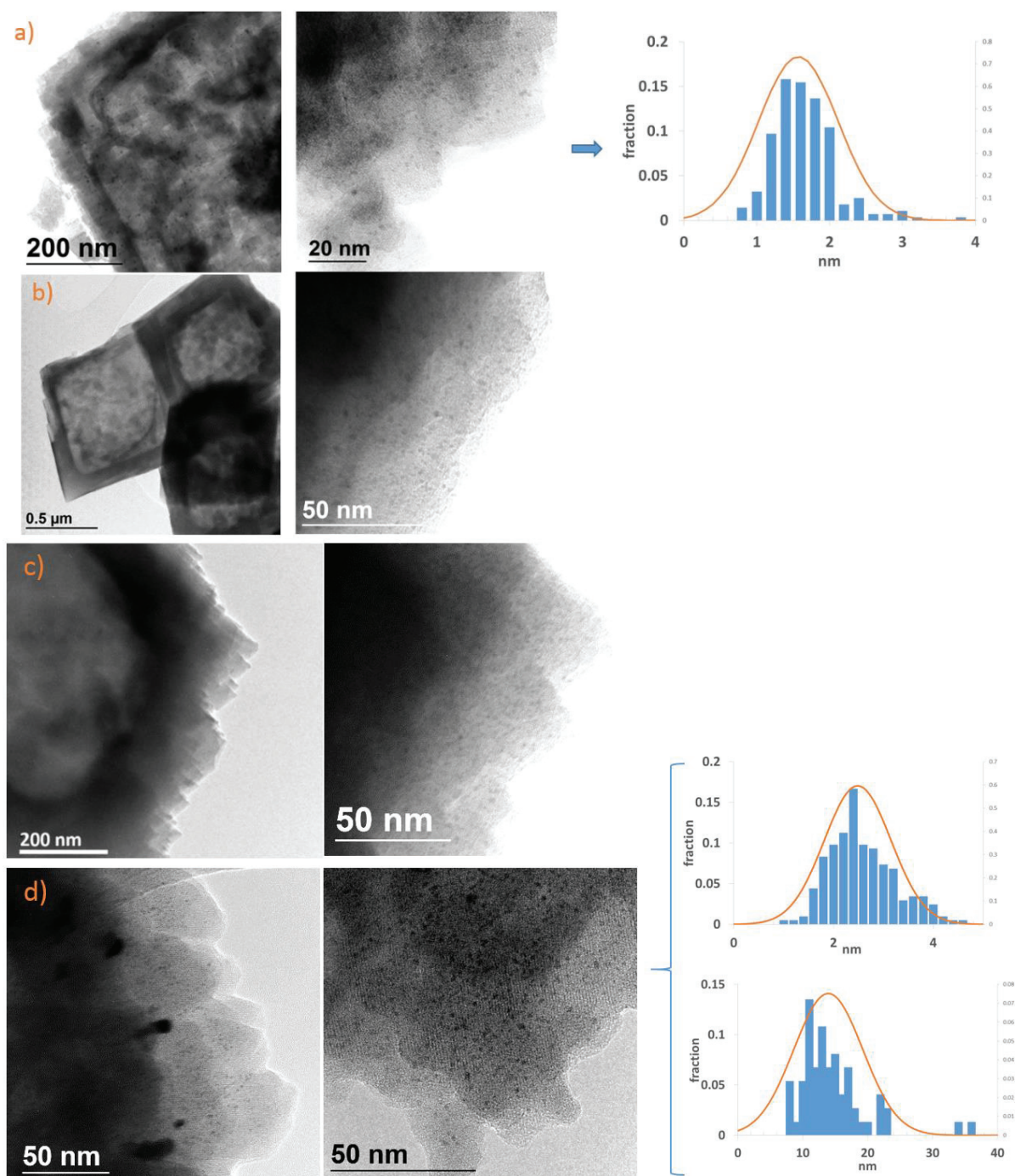
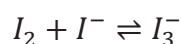


Figure 44 - TEM pictures of Pt/Beta zeolite treated with TMA⁺ (a), TEA⁺ (b), TPA⁺ (c) and TBA⁺ (d) cations and corresponding particle size distributions for TMA-Pt@Beta and TBA-Pt@Beta. For TBA-Pt@Beta the two distributions correspond to small internal (left) and large partially embedded (right) particles.

The solid treated with the large TBA⁺ cation differs from the others by the presence of two families of Pt nanoparticles, as observed on the original Pt@Hollowβ (see Figure 44d). Despite a significant decrease of both the overall and surface Pt concentrations, it seems that TBA⁺ is not able to remove completely the portion of large particles present on the external region of hollow crystals, which contrasts with TAA cations with smaller alkyl chains (see Table 8 and Figure 44, d). A clear examination of corresponding TEM pictures reveals that large Pt

NPs that remain after the treatment are not located on the extreme surface but in a particular region of the zeolite walls, typically 20 to 50 nm beneath the surface (see Figure 44d). This conclusion is also supported by the XPS results for this sample, showing a surface Pt content close to zero, similarly to the other treated samples. Hollow Beta crystals obtained from the dissolution of CIT-6 are not completely smooth and they generally show polysynthetic, multi-terminated faces with rough surfaces.⁴¹ Such surfaces can favor the confinement of some of the nanoparticles, making them less accessible to bulky ammonium cations in solution. Hence, the bulky reagent system can easily dissolve NPs that are on the external surface, but the dissolution of these “buried” big NPs in the intercrystalline voids is more problematic. Similar results were demonstrated during the dissolution of Pt NPs in ZSM-5 using TEABr as halide compound³⁶.

In the particular case of gold redispersion, it has been reported that iodine could react with I⁻ species of tetramethylammonium iodide to form I₃⁻ ions, stabilized by TMA⁺ cations as [TAA]⁺[I₃]⁻^{37,42}.



In the presence of I⁻, those I₃⁻ cations could react with gold nanoparticles to form the stable [AuI₂]⁻ complex and subsequently, the [TEA⁺][AuI₂]⁻ complex.



We can therefore assume that similar Br₃⁻ species are formed when Br₂ and a TAA⁺ bromide salt are mixed together in an organic solvent. The dissolution of Pt nanoparticles is thus conditioned to their accessibility to [TAA][Br₃] complex. Such cations are bulky, with a size that depends on the alkyl chain length, and only the smaller ones will be able to enter or diffuse through the zeolite pores.

Several reasons can be pointed out to explain the apparent absence of changes in the morphology of nanoparticles occluded inside the walls, after all of the four different treatments:

- Firstly, it is possible that none of the TAABr₃ compounds are small enough to penetrate the zeolite micropores. TMABr, TEABr and TPABr possess kinetic diameters of 0.40, 0.76 and 0.92 nm respectively, which is similar to the pore opening of the Beta zeolite framework (0.66 x 0.77 nm). However, the TAABr₃ compounds may be too bulky to easily diffuse through the zeolite channels. For the TBA⁺ cation, the kinetic diameter of TBABr (1.18 nm)⁴³ is way larger than the pore opening and even the diffusion of the TBA⁺ cation alone in the zeolite framework is highly limited.

- A second reason concerns the nature of the interaction between the metal nanoparticle and the support. In the case of Au, the CH₃I system was very effective to redisperse nanoparticles deposited on TiO₂ or alumina, but not on SiO₂.⁴⁴ Small occluded Pt NPs are in strong interaction with the zeolite framework, which could affect their dissolution as compared to large external particles.
- Finally, in the case of the Au/I₃⁻ system, it was also reported that metallic Au could be redeposited when the reaction solution was cooled down at room temperature.⁴² Internal Pt particles could thus be dissolved and subsequently reformed when the reaction is stopped. However, the absence of visible Pt nanoparticles on the external surface of the crystals definitely refutes this possibility. Moreover the fact that the Pt means particle size and dispersion on TMA-, TEA- and TPA-treated samples correspond to one of the two families observed on Pt@Hollowβ suggests that internal small NPs have not been affected by the treatment.

2.4.3.3. Toluene and mesitylene hydrogenation reactions

Once again, the location of the nanoparticles was also confirmed by a model hydrogenation reaction using reactants with different diffusion rates, toluene and mesitylene. As we mentioned before, although mesitylene is able to enter into the *BEA pore system, its diffusion in the microporous framework is significantly slower than that of toluene, due to its larger kinetic diameter, which is 0.86 nm compared to 0.61 nm for toluene.⁴¹ Data from the same reaction over Pt/SiO₂ (Pt NPs supported on silica support) were used as a reference. For the later catalyst we cannot expect molecular sieve type selectivity since the Pt NPs are located on the external surface of the support. Similarly, we can assume that no mass transport limitations occur on silica powder. The samples TEA-Pt@Beta and TPA-Pt@Beta were not tested, as we assume that they are very similar to TMA-Pt@Beta.

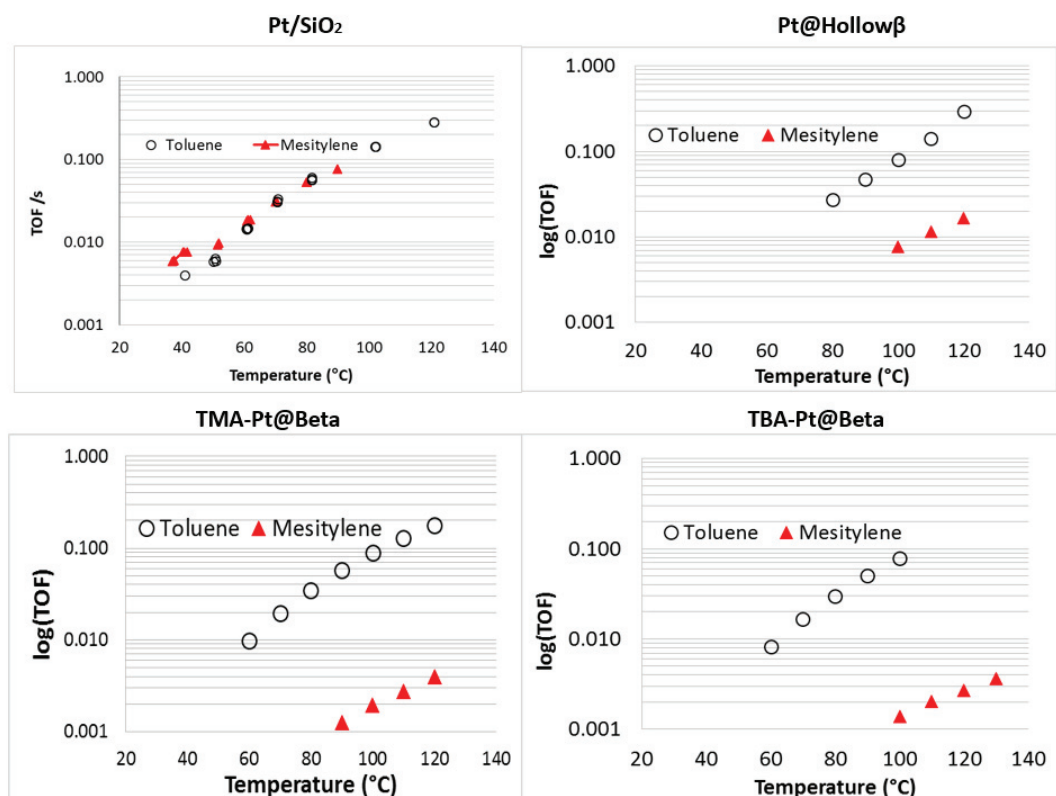


Figure 45 - Evolution of TOF values with temperature for the hydrogenation of toluene and mesitylene over Pt/SiO₂, Pt@Hollowβ, TMA-Pt@Beta and TBA-Pt@Beta.

Table 9 – Activity and apparent TOF at 100 °C for the hydrogenation of toluene and mesitylene over Pt@Hollowβ, TMA and TBA-Pt@Beta and Pt/SiO₂.

Sample	Pt@Hollowβ	TMA-Pt@Beta	TBA-Pt@Beta	Pt/SiO ₂
Dispersion (%)	13	60	50	20
Activity toluene (Mol/s/mgPt)	5.30x10 ⁻⁸	2.72x10 ⁻⁷	2.03x10 ⁻⁷	1.39x10 ⁻⁷
TOF Mes (s ⁻¹)	0.008	0.002	0.001	0.08
TOF Tol (s ⁻¹)	0.08	0.09	0.08	0.14
Mes/Tol TOF ratio	0.10	0.02	0.02	0.57
Wt. % Pt on the external surface ^{a)}	33	0	0	100

a) Determined by the different of Pt wt. % before and after the treatment.

When analyzing the catalytic activity per mass of Pt, regarding toluene hydrogenation, see Table 9, we observe that the activity increases as the dispersion of the Pt increases, as expected. Hence, the treated catalyst TMA-Pt@Beta and TBA-Pt@Beta present the highest catalytic activities, since they have the highest Pt surface available. Moreover, the treated catalyst also present higher activities regarding the Pt@Hollowβ with encapsulated Pt NPs

already presented in Chapter III. 2.4.2., “Pathway D”. The dispersion values for this sample are very low (~3%) and therefore catalytic activity is only 1.38×10^{-8} , and TOF values are negligible (~0), see Figure 41.

Considering the high selectivity of the model hydrogenation reaction of toluene and mesitylene depending on the Pt NPs location, the ratio between the TOF values for the two substrates (called here after Mes/Tol TOF ratio) is a good indication of the proportion of NPs located on the external surface. The Pt/SiO₂ catalyst in which Pt NPs are fully accessible on the external surface, showed a Mes/Tol TOF ratio of 0.57. This selectivity is therefore the reference value which can be expected for a Pt@zeolite for which all particles would be located at the external surface.

As expected, Pt@Hollow β catalyst was active for the hydrogenation of both toluene and mesitylene, but the mesitylene TOF value is lower than that observed over a standard Pt/SiO₂ catalyst (see Figure 45, Table 9). For this sample, even though there are Pt NPs on the external surface, most of the Pt wt. % is placed inside the zeolite micropores, which is hardly accessible to mesitylene. For the treated samples, the fraction of Pt on the external surface is almost zero, therefore, TOF for mesitylene hydrogenation is almost zero, see Table 9. In contrast, apparent TOF value for toluene were relatively similar for the three catalysts and comparable with the reference Pt/SiO₂, indicating any or very little transport limitations for toluene.

TMA-Pt@Beta, which did not contain Pt NPs on the external surface, was not totally inactive in mesitylene hydrogenation but the activity was quite low (see Figure 45). The low activity probably arose on internal small Pt NPs as we previously showed that mesitylene could enter the *BEA pore system⁴¹. Nonetheless, reaction is strongly limited by diffusion with a TOF value of 0.002 s^{-1} , see Table 9.

The zeolite treated with the large TBA⁺ cation shows quite similar TOF values and activation energies, suggesting that the large particles observed at grain boundaries inside the shell are not easily accessible and do not participate in mesitylene hydrogenation.

As we mentioned before, the ratio between mesitylene and toluene TOF values can be used as an indicator of the presence of Pt NPs on the surface of the crystals, since mesitylene hydrogenation is strongly affected by diffusion while that of toluene is only slightly. Indeed, at 100 °C Mes/Tol TOF ratio decreases to 0.10 on Pt@Hollow β to 0.02 on the two treated samples. In Pt@Hollow β , 33 wt. % of platinum are on the surface (Table 9) and possess an average dispersion of 13%, while the rest 67 wt. % of Pt is occluded in the porosity with a dispersion of ca. 50%. Assuming that internal NPs have not been modified by the treatment, **93 % of the total Pt surface sites** are in the porosity and catalyze the hydrogenation of mesitylene with a **TOF of 0.002 s^{-1}** (obtained from TMA-Pt@Beta), while the **remaining 7 %** located on the surface are characterized by a **TOF value of 0.08 s^{-1}** (obtained from Pt@Hollow β). Thus, the observed **TOF value for mesitylene** can be expressed as $X_{\text{ext}} \cdot \text{TOF}_{\text{ext}} + X_{\text{int}} \cdot \text{TOF}_{\text{int}}$, where X_{ext} and X_{int} are the proportions of surface Pt atoms on the external surface

and in the porosity of the zeolite, respectively, and TOF_{ext} and TOF_{int} the corresponding TOF values. For Pt@HollowB, the calculation gives 0.0082 s^{-1} , in excellent agreement with the value observed experimentally. As a consequence, the fraction of Pt NPs that remains on the surface of Beta zeolite crystals can be directly estimated by simply measuring the TOF value of the treated zeolite in the hydrogenation of mesitylene.

2.5. Summary on the “CIT-6 Dissolution-Recrystallization” approach

The “CIT-6 Dissolution - Recrystallization” approach yields hollow Beta crystals, with an average crystal size of 0.8-2.2 μm , and a wall thickness of about 100-200 nm, similarly to the crystals synthesized by Okubo.¹ The zeolite walls are mostly microporous, even though there is evidence of the presence of mesopores (namely ink-bottle type pores) which are mainly located in the inside surface. The crystal has a very low content of Zn, and $\text{Si}/\text{Al} \sim 8$. Okubo’s group obtained hollow Beta single crystals with different Si/Al (up to $\text{Si}/\text{Al} = 115$), but we were not able to obtain crystalline hollow Beta with different Si/Al . The synthesis of hollow Beta using different gel compositions was made, but the results led to a partial amorphous sample.

In the case of this PhD work, we were interested in hollow Beta with $\text{Si}/\text{Al} > 8$ for the transport and catalytic studies (Chap. IV and V). hollow Beta with $\text{Si}/\text{Al} = 20$ were obtained by dealumination treatment with HNO_3 , similarly to the procedure of Lami *et al.*⁴⁵

We have attempted to reduce the wall thickness using different amounts of wt. % CIT-6 per batch (25% instead of 10%), however, without success.

Pt@Hollow β can be obtained with different Pt dispersions and NPs location, depending on the synthesis method as we can see in Figure 46.

Hollow Beta crystals with encapsulated NPs were obtained by two different methods, namely by a) pre-impregnation of CIT-6 followed by NaBH_4 reduction (see Figure 46, green row) which lead to Pt NPs inside the cavity and inside the zeolite wall, and b) selective removal of Pt NPs from the external surface of the Pt@Hollow β (see Figure 46, rose row), which lead to a Pt dispersion encapsulated likely in the zeolite wall. The location of the NPs was evidenced not only by TEM pictures (and TOMO 3D reconstruction in the case of the pre-impregnation method), but also by the model hydrogenation reaction of toluene and mesitylene. In both cases, the catalyst has very low activity for mesitylene hydrogenation, probably due to high diffusion limitations. These model reactions indicate that: 1) the absence of NPs on the external surface of the crystal, 2) the hollow Beta crystals are indeed “closed” as in a hollow structure, and 3) the mesopores are likely not interconnected otherwise the activity would not be so strongly penalized.

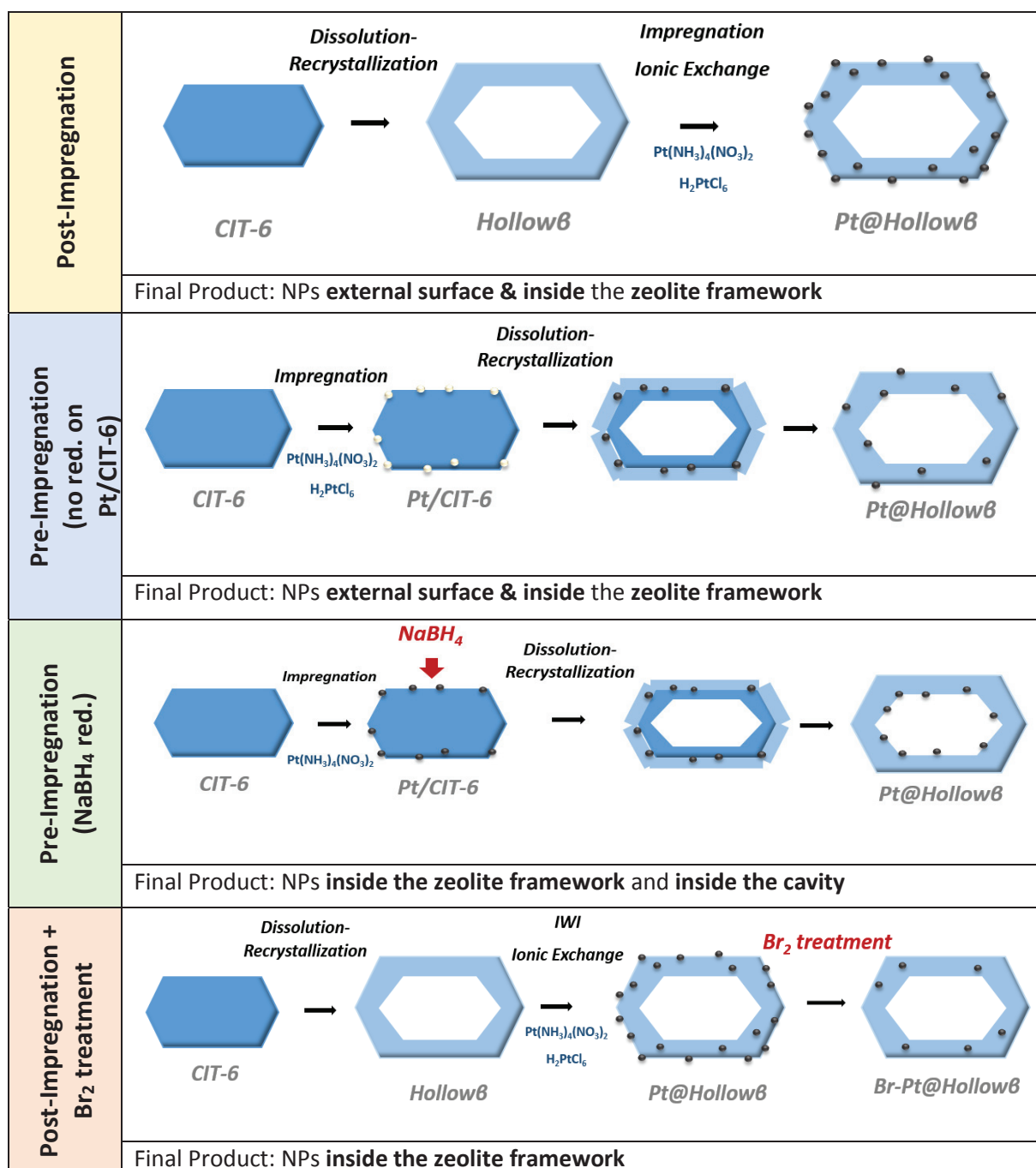


Figure 46 – Different methods for incorporation of Pt NPs in hollow Beta.

When Pt@Hollowβ is obtained by pre-impregnation method (see Figure 46, green row), Pt wt. % = 1 % and dispersion was very low (<5 %). Dispersion and Pt content are particularly difficult to control because of the reduction method, that is extremely sensitive and reactive, but also to the physical-chemical phenomena that happen during hydrothermal synthesis. We did not study how the influence of the hydrothermal synthesis parameters on Pt content and dispersion. The location of the Pt NPs is likely inside the zeolite wall and inside the inner cavity.

On the other hand, when Pt@Hollow β was obtained by Br₂ post-treatment (see Figure 46, rose row), high Pt contents and high dispersions were obtained. In fact, the final Pt % content and NPs dispersion, depend not on the treatment itself, but on the original sample before treatment. The final dispersion and Pt % content will correspond to the Pt % content and dispersion of the Pt NPs inside the framework. Regarding this method, the removal of external Pt NPs is clearly evidenced by a significant decrease of the overall Pt content after treatment and by TEM pictures of the surface of the crystals. Chemical analysis and particle size distributions in treated zeolites suggest that internal nanoparticles are not affected, even when the small TMA⁺ cation is used as halide compound. However, the largest TBA⁺ cation is less effective to remove Pt and the treated sample still contains large NPs, mainly located at crystal boundaries inside the shell.

3. Beta zeolite dissolution approach

A Chinese patent by Fan et al.² published in 2015 claimed a synthesis method of “nano” hollow Beta crystals. Unlike the “*CIT-6 Dissolution - Recrystallization*” approach, these hollow Beta crystals were 5 times smaller and with a quite different morphology, rather an egg-shaped form with a smooth surface. Consequently, the crystals also possessed a very thin wall (down to 30 nm). The synthesis method appeared to be based on a desilication process of calcined parent Beta zeolites. The respective parent Beta corresponded to a known synthesis of Beta zeolite, reported in the literature by Cambor *et al.*³⁹

This type of “nano” hollow Beta crystals would present complementary information regarding the hollow Beta by “*CIT-6 Dissolution - Recrystallization*” approach. Such smaller dimensions would allow to study the impact of hollow/bulk morphologies in a completely different size range (nm order). In addition, this “nano” hollow Beta could directly be compared with the bulk parent Beta, since both of them should have the same morphology, crystal size and external surface.

Herein, we present results concerning this “*Beta Zeolite Dissolution*” approach, based on example 1 of the patent (see below). The replication of example 1 resulted in an amorphous hollow structure. In order to obtain highly crystalline *BEA hollow crystals, several synthesis parameters were studied, such as alkalinity of the treatment and Al content. Attempts to favor crystallization were made by including TEA⁺ to the post treatment.

Finally, based on the results presented in this chapter, further studies were carried out at IRCELyon in order to achieve improved hollow Beta structures (with lower % of amorphous phase) and understand the parameters affecting this synthesis. These are described in the publication entitled “Hollow structures by controlled desilication of Beta zeolite nanocrystals”, that can be found in the section “Publications”.

It must also be noted that the description of the synthesis method claimed by Fan *et al.*² was extremely vague (each synthesis parameter had a wide range of possibilities), and no other publication was found later about this material or citing the patent.

3.1. Description of the synthesis as indicated in the patent

The synthesis is briefly described in the main following steps:

- preparation of an aqueous solution of NaOH (or KOH);
- addition of an aluminum source such as sodium aluminate, aluminum sulfate etc;
- dispersion of the parent zeolite (calcined) while stirring during 20 to 60 min.

The molar ratio of the previous solution should be preferably 5~15 NaOH: Al₂O₃: 1000~2000 H₂O, H₂O and the weight ratio of zeolite Beta 100 to 10, preferably 80 to 15;

- after stirring, the mixture should be charged into a sealed pressure vessel, under conditions of constant temperature at 50 - 150 °C for 1 – 8 h;
- washing with distilled water and drying.

As in any patent, the experimental conditions are given in a wide range, which makes the replication of the synthesis more difficult. Even though, there were given 4 examples with different synthesis approaches. The parent zeolite was the same for the 4 examples, and these differed from each other either by the sodium hydroxide concentration, the type of aluminum source (that would be sodium aluminate, aluminum nitrate, aluminum sulfate), or by the time and temperature of the heating step. We decided to start studying example 1 (more details in chapter II), which used sodium aluminate, a common aluminum source for Beta synthesis in general and for the parent Beta as well, and relatively mild dissolution conditions (5 h at 90 °C).

The synthesis scheme is represented bellow, see Figure 47, (more details in chapter II). Step 1 consists in making an aqueous solutions of NaOH and NaAlO₂, with pH~13.8. Step 2 consists in adding the zeolite into this solution and stir for 30 min. Subsequently, the dispersion should be placed in a sealed vessel at 90 °C for 5h, step 3.

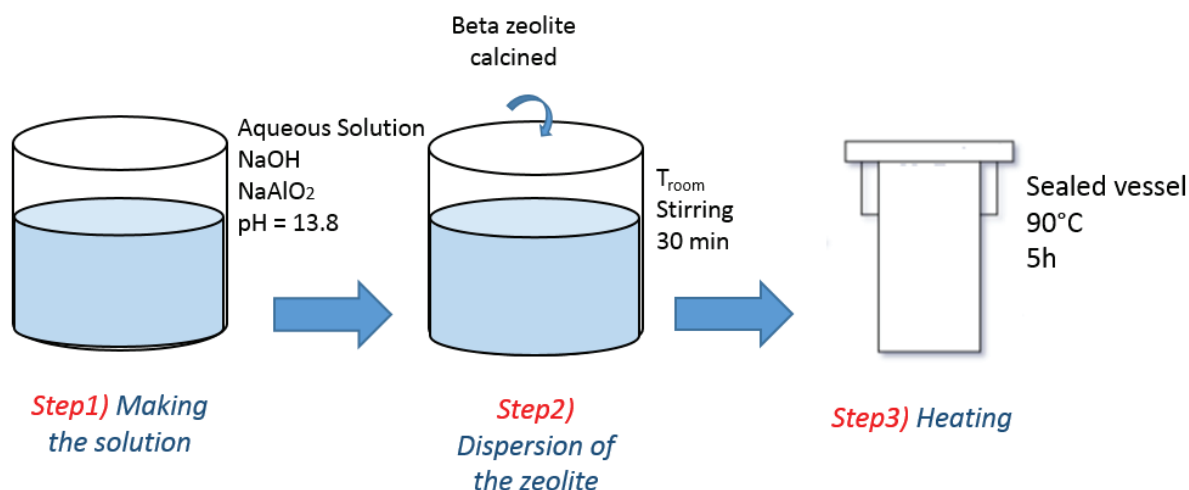


Figure 47 - Synthesis route correspondent to example 1 of the patent.²

The patent presented a very limited description/characterization of the final product hollow Beta, see Figure 48. The final product is described as a crystalline Beta zeolite, and the document presents a XRD pattern corresponding to *BEA framework type diffraction peaks. According to the reference, the crystal has a hollow morphology, with a crystal particle diameter of 100-1500 nm and a particle wall thickness of 30-500 nm. There are only two TEM images available, presenting what seems to be a homogeneous population of hollow particles (Figure 48), with a particle size of ~300 nm, a wall thickness of less than 100 nm and a “smooth” external surface (smooth compared to the pine shaped morphology of the hollow Beta obtained by CIT-6 dissolution recrystallization approach for example). The reference also claims that this crystal has a surface area of 100-500 m²/g and V_{total} of 0.08-0.35 cm³/g, but no further characterizations besides XRD and TEM images are available to support these affirmations. Note that these characterizations were not attributed to any particular example of the patent either.

Crystal Size: 100-1500 nm
 Wall thickness: 30-500 nm
 XRD available: ***BEA**
 framework type
 Texture:
 Surface area: 100-500 m²/g
 $V_{\text{total}} = 0.08-0.035 \text{ cm}^3/\text{g}$

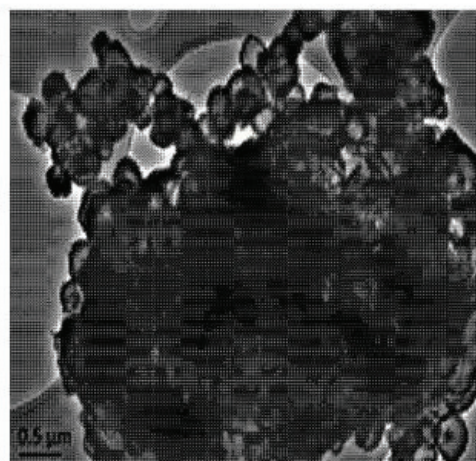
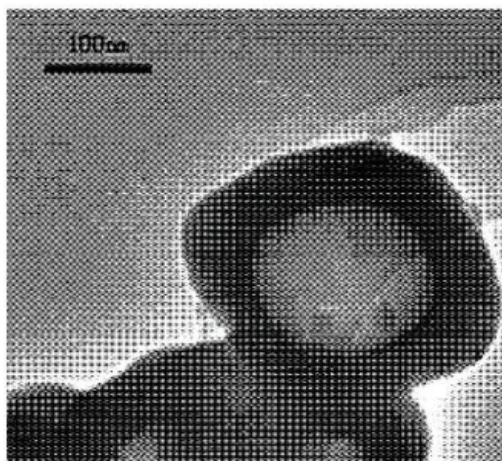
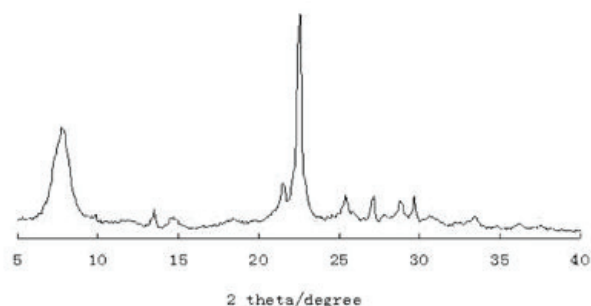


Figure 48 - Characterization of hollow Beta presented in the patent: XRD patterns, TEM images, and textural properties.²

3.2. Assumptions on synthesis mechanisms

In the case of **MFI** crystals, the selective dissolution of the core of the crystal is due to a natural higher concentration of defects²⁶ and/or lower content of Al.^{26,46} As recently reported⁴⁷ hollow Y zeolite can be obtained by artificial Al-zoning obtained by post-synthesis treatments of a NaY zeolite. However, to the best of our knowledge, there are no reports claiming any Al zoning in Beta zeolites, or any other physical/chemical property that would lead to a preferential dissolution of the core. Therefore, an artificial gradient should have been created.

Firstly, as-made Beta zeolite possesses natural structural vacancies or defects. At calcination step, there is partial dealumination (creating framework vacancies) and therefore creation of even more defects and EFAL.^{48,49} Depending on the characteristics of the Beta zeolite and on calcination conditions, a large number of aluminum atoms can be removed from the framework and generally, the more severe the calcination conditions, the more Al will be removed, creating more defects. Muller *et al.* report the case of two Beta zeolites, that

after calcination in zeolite bed at 550 °C, lose 75% of their Al framework into EFAL.⁵⁰ The group also reports that the degree of dealumination depends on the calcination procedure.

Secondly, according to the literature,^{48,49} Beta zeolite can be aluminated with an aqueous solution of NaAlO₂, between at least 50-90 °C. Alumination was evidenced by IR spectra of framework vibrations, chemical analysis⁴⁸ and also ²⁹Si and ²⁷Al NMR⁴⁹. Alumination can occur when a) extra-framework aluminum species fill the structural vacancies inherent to the structure and that are created during calcination, and b) by isomorphous substitution, where the aluminum species occupy the positions of silicon atoms into the framework.^{48,49} In the case of the synthesis of hollow Y, it is suggested that NaAlO₂ treatment is responsible for alumination of the external part of the crystals, and the core desilication occurs during alkaline treatment with NaAlO₂. This hypothesis is also supported by XPS analysis (Si/Al of the surface ~6 is much smaller than the overall Si/Al ~25).⁴⁷

In light with the above mentioned points, we can make assumptions on synthesis mechanism. We assume that there is dealumination during calcination, followed by realumination during NaAlO₂ treatment. Our hypothesis is that the realumination is more favorable on the surface of the crystal so that the core will have lower Al content, or/and will have more structural vacancies or defects. Due to the Si/Al composition or defect gradient, desilication can occur preferably in the core of the crystal.

Indeed, ²⁷Al NMR of the parent zeolite before and after calcination, shows that after calcination 25 % of the framework Al is removed and stays in the pores as EFAL (see Annexes). These results suggest that there is dealumination during the calcination step, leaving free vacancies through the crystal framework. XPS analysis before and after NaAlO₂ treatment would have given an indication about the eventual Al zoning (this analysis were not performed).

3.3. Reproducing the patent/first results

The synthesis of the parent zeolite corresponded to the synthesis of Beta zeolite already described by Cambior *et al.*⁵¹

The post-treatment procedure was carried out as described in chapter II. Essentially, the calcined parent zeolite was dispersed in a solution of sodium hydroxide and sodium aluminate. After stirring (step 2, see Figure 47), the dispersion went through heating treatment in a sealed autoclave at 90 °C for 5h static,(Step3, see Figure 47). The corresponding final product is referred as to **Hollowβ**.

Figure 49 shows the XRD patterns for the as-made parent zeolite, the solid before and after step 3) - Hollowβ. The as-made parent Beta presents a highly crystalline *BEA framework

type. After step 2) the intensity of the peaks decreases significantly and finally after step 3, the final solid is almost 100% amorphous, with the *BEA peaks with very low intensities. This is also evidenced by N₂ adsorption isotherms, with BET surface areas of a few m²/g (see Annexes Chapter III).

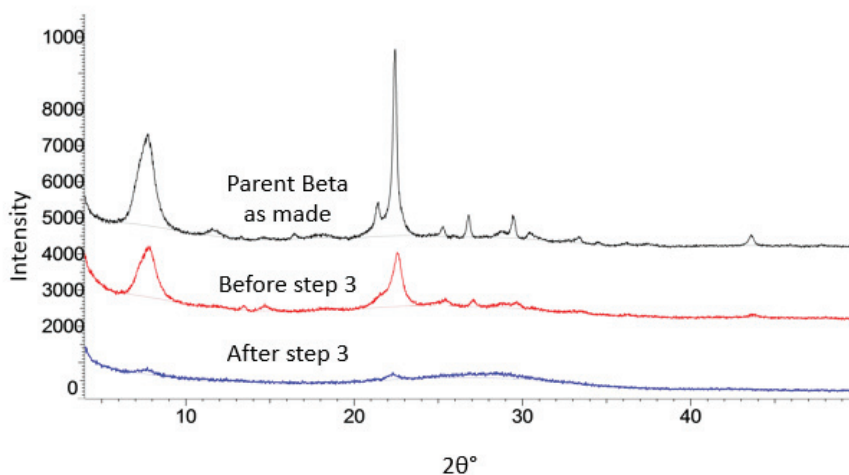


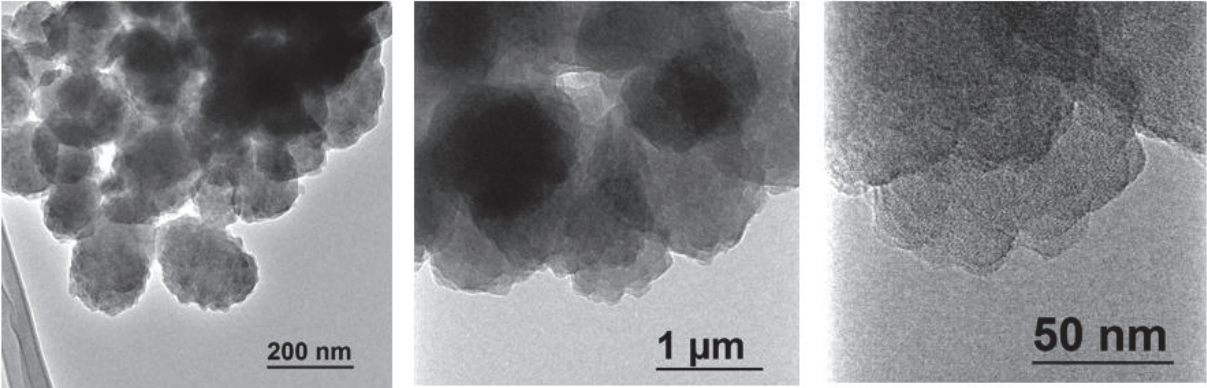
Figure 49 – XRD patterns of the as-made parent Beta, the solid right before step 3 and the final product.

TEM images show that the final product has a completely different morphology from the parent Beta, where most of the crystals appear to have an inner cavity, and some hollow structures are broken, Figure 50. The size of the Hollowβ is approximately the same as the parent Beta, suggesting that the hollow structures result from the selective dissolution of the crystal core, and not from a subsequent recrystallization of the species in solution (which also would be surprising at 90 °C). The wall size is approximately 25-30 nm, with a rather smoother surface than the parent Beta, which indicates a probable amorphization of the zeolite framework, as suggested by the XRD patterns (see Figure 49).

Clearly, the direct replication of example 1 of the patent did not give a crystalline Hollowβ, but an amorphous hollow structure. The treatment (pH = 13.8) was able to dissolve the core, but also destroyed the crystalline structure. Indeed, Yang *et al.* studied the effect of a similar treatment (NaAlO₂ and NaOH solution) on the realumination of zeolite Beta⁴⁸ and they conclude that at pH above 13 crystallinity decreases significantly.

The previous synthesis resulted in hollow structures, with approximately the same size as the respective parent Beta but amorphous. Using this synthesis as starting point, we studied the impact of several synthesis parameters, in order to obtain a highly crystalline Hollowβ and to understand the synthesis mechanism. The results are presented in the following subchapters.

Parent Beta:



Hollowβ:

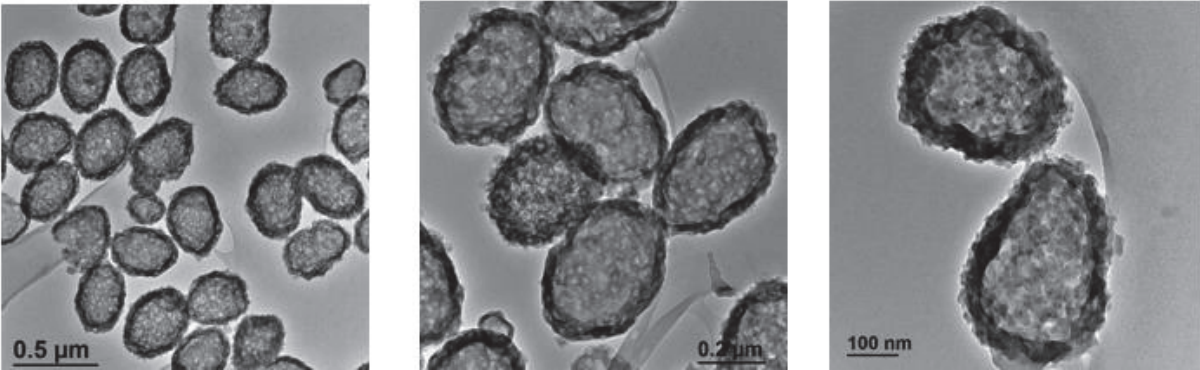


Figure 50 – TEM images of parent Beta and Hollowβ.

3.4. Effect of Al content

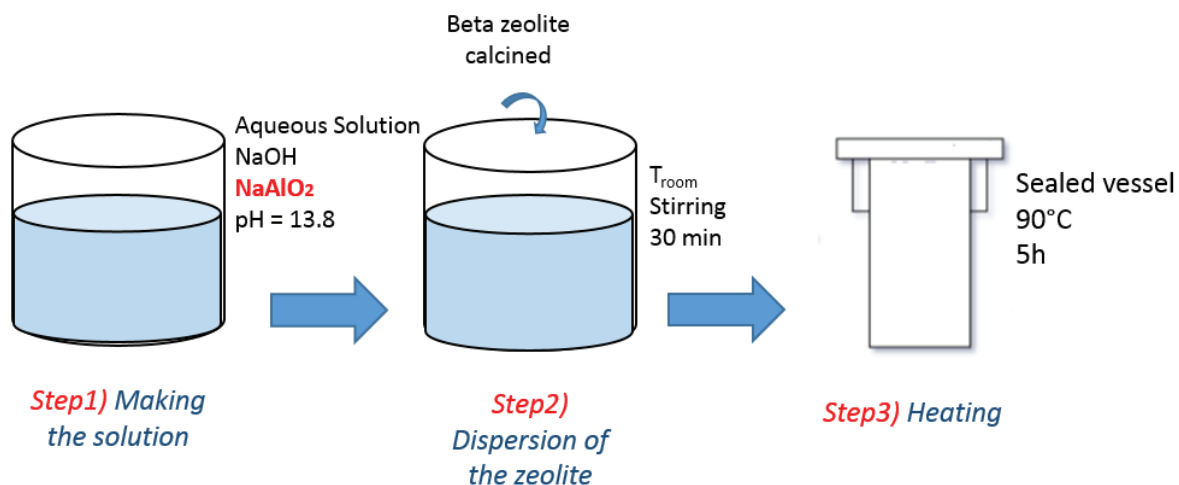


Figure 51 – Synthesis route of example 1 of the patent. This subchapter studies the effect of NaAlO₂ concentration (in red).

To understand the role of NaAlO₂ in this synthesis, the treatment was carried out using lower amounts of aluminum, see Figure 51, namely only 25 % mol of the total amount of aluminum and even 0 % mol, the samples are referred as **25%Al-Hollowβ** and **0%Al-Hollowβ**, respectively. The pH was kept constant adjusting with NaOH.

The XRD patterns show that for the samples that used 25% of NaAlO₂, there is an almost total amorphization of the Beta zeolite, see Figure 52, similarly to the sample replicated from example 1. In the absence of NaAlO₂, the zeolite was treated exclusively with sodium hydroxide solution, which lead to a completely amorphous sample, without any left reflections peaks of the *BEA framework type.

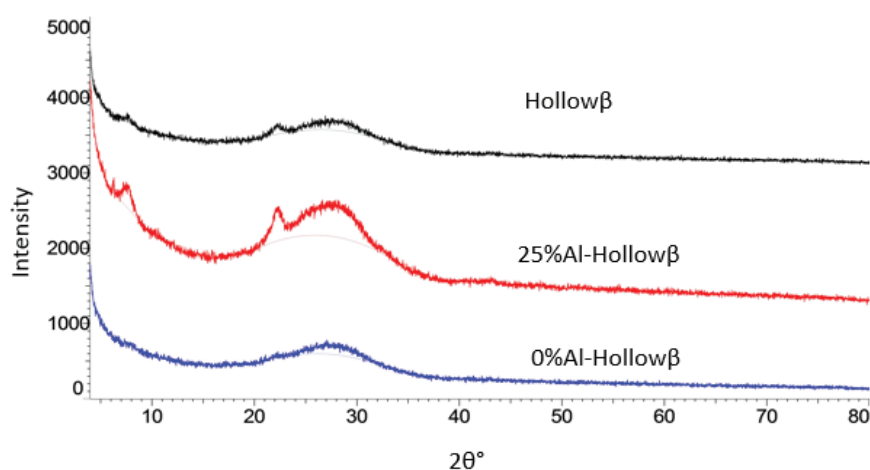
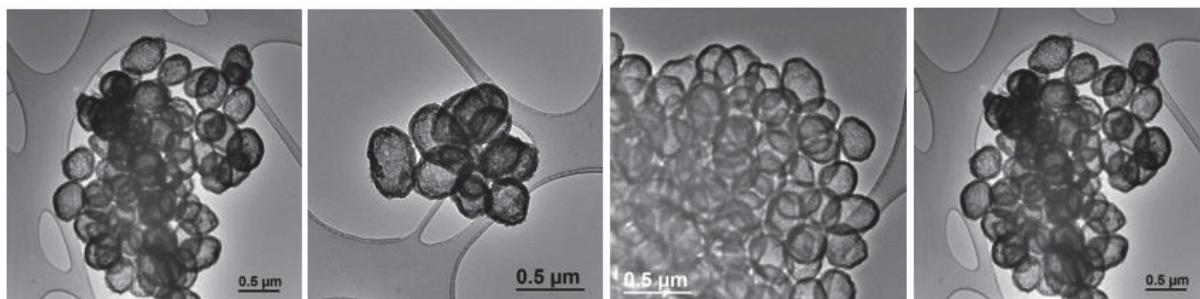


Figure 52 - XRD patterns of the Hollowβ, 25%Al-Hollowβ and 0%Al- Hollowβ.

TEM images show that 25%Al-Hollow β presents similar morphology than the standard Hollow β , see Figure 53, i.e. of hollow structures with a similar size to the parent zeolite. On the contrary, the sample 0%Al-Hollow β presents rather mesoporous crystals, quite different from the 25%Al-Hollow β and Hollow β , with some hollow structures, see Figure 53.

25%Al-HollowB



0%Al-HollowB

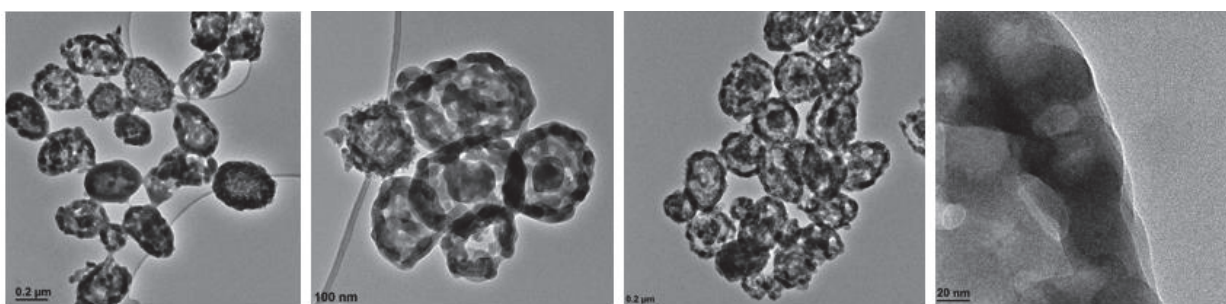


Figure 53 – TEM images of 25%Al-Hollow β and 0%Al- Hollow β .

These results indicate that the NaAlO₂ treatment has a big influence on the morphology of the corresponding final samples and therefore in the desilication process. Possibly, NaAlO₂ is indeed responsible for creating an Al zoning where the external part of the crystal is richer in Al, which not only leads to a selective desilication of the core, but also to a protection of the crystals against total amorphization (the two small diffraction peaks still present for Hollow β and 25%Al-Hollow β). The absence of sodium aluminate impedes the protective effect to Al species on the surface, and therefore creates several mesopores inside the crystal. The presence of some hollow structures in the sample 0%Al-Hollow β suggest that it might be a preferential dissolution of the core, eventually due to gradient of defects.

Nevertheless, both samples are totally or almost totally amorphous, which was expectable since the pH was kept constant at ~ 13.8 , (which was already reported to destroy the framework structure of a similar Beta zeolite).

3.5. Effect of pH

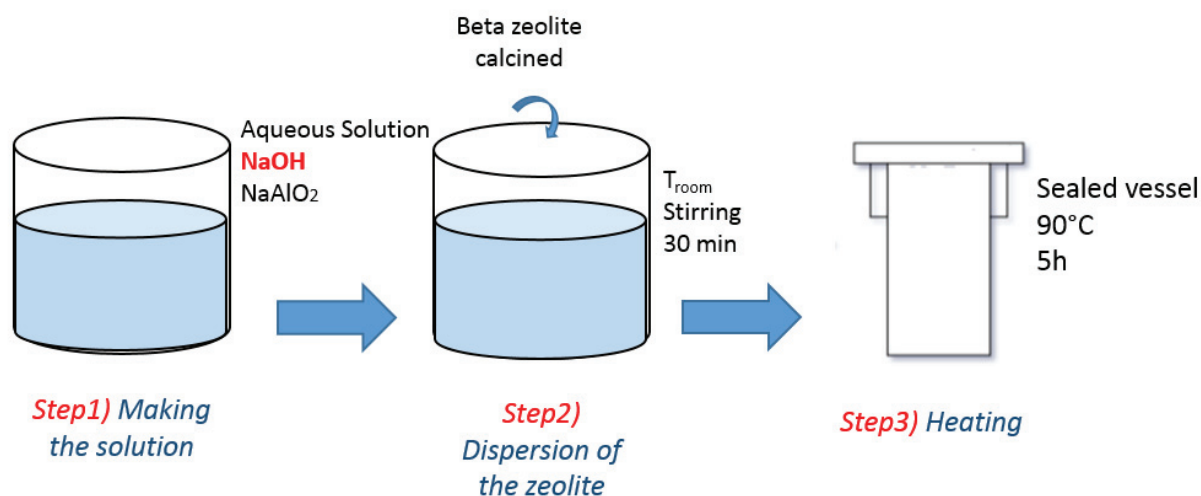


Figure 54 - Synthesis route of example 1 of the patent. This subchapter studies the effect of different $[OH]$, adjusting the NaOH concentration (in red).

Yang *et al.* studied the effect of a similar treatment (NaAlO₂ and NaOH solution) on the realumination of Beta zeolite crystals.⁴⁸ They concluded that at pH greater than 13, crystallinity starts decreasing considerably, and that aluminations treatments should be performed at pH < 13, adjusting pH with NaOH.

The treatment proposed in example 1 of the patent (the one we replicated), had a pH = 13.8, which might be responsible for the dissolution of the center of the crystal and eventually the amorphization of the hollow structure. Therefore, we decided to study the effect of the pH on crystallinity and on the morphology. The pH was adjusted by using different amounts of NaOH, namely pH = 13.5 and pH = 13, leaving the amount of sodium aluminate constant. The corresponding samples are referred to as **13,5Hollowβ** and **13Hollowβ** and are compared with Hollowβ (pH=13.8), respectively.

As we can observe in Figure 55, XRD patterns are more intense when decreasing pH. When performing the treatment at pH=13, the product presents a crystalline ***BEA** framework, and the treatment does not seem to have decreased significantly the crystallinity of the crystals. For the sample 13.5Hollowβ, the intensity of the reflection peaks decreased significantly regarding the calcined Parent Beta. Hollowβ (pH=13.8) presents the reflection peaks with even lower intensity, see Figure 55, showing how the crystalline phase % decreased as well.

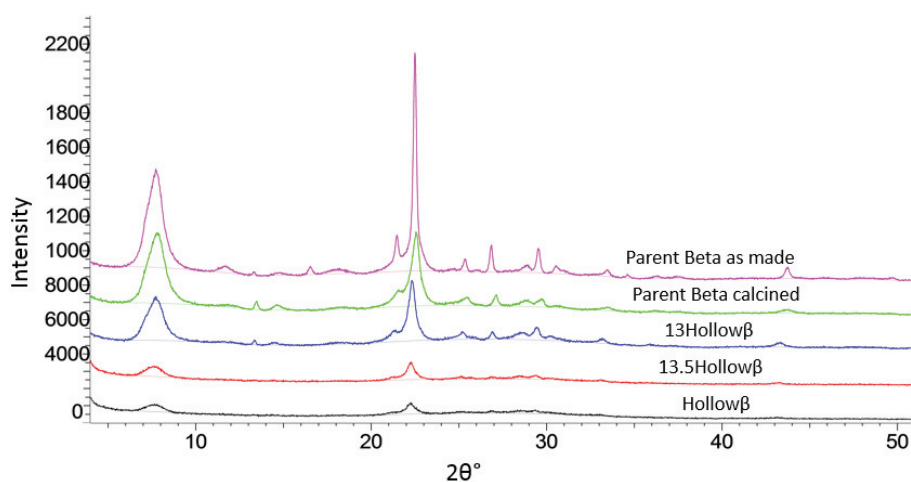


Figure 55 - XRD patterns of the Hollow β , 13.5Hollow β and 13Hollow β .

Regarding the morphology of the final crystals, see Figure 56, we can observe that for $\text{pH} \geq 13.5$ the morphology of the crystal is similar to the one obtained for Hollow β ($\text{pH} = 13.8$), the procedure according example 1. Indeed, the difference of pH is not very significant. On the other hand, for 13Hollow β , most of the crystals look intact or with no significant visible changes, regarding the parent zeolite. Even though, it is possible that there was formation of mesopores that are not noticeable on TEM images. No N_2 isotherms were made to support this hypothesis.

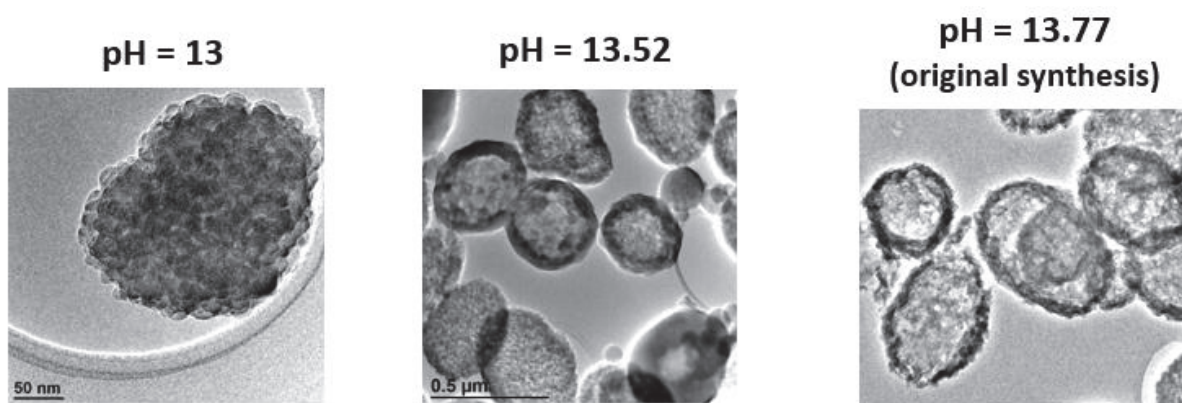


Figure 56 – TEM images of Hollow β , 13.5Hollow β and 13Hollow β .

This results suggest that crystallinity decreases with increasing pH , and that performing the treatment at $\text{pH} = 13$ manages to keep the crystallinity of the sample just like suggested by Yang *et al.*,⁴⁸ however, the treatment is not able to create an inner cavity, either because the solution is not alkaline enough to dissolve the core, or because no Al zoning was created.

Furthermore, according to Yang *et al.*, after treatment the Si/Al of the crystal decreases. In their case, the calcined parent zeolite had a Si/Al = 15.2, and after treatment it

decreased to $2.4 < \text{Si}/\text{Al} < 4.3$. In our case, the treatment conditions were very similar, so we might expect a lower Si/Al as well, especially on the external part of the crystal. To investigate the change in the Si/Al in the framework, chemical analysis and ^{29}Si NMR should be performed. Furthermore, XPS analysis would be an evidence of the creation of Al zoning.

It is clear that pH plays a big role in the zeolite crystallinity and morphology. It is seen that working at $\text{pH} < 13$ will maintain the crystallinity of the parent Beta, and that it is not enough to make dissolution of the zeolite core.

One possible approach would be to synthesize crystalline hollow Beta zeolites by a multi-step treatment. Firstly, creation of Al zoning by surface alumination, while keeping the crystalline structure, and, subsequently, perform alkaline desilication. The NaAlO_2 treatment at $\text{pH} = 13$ should be characterized in terms of Si/Al and Al zoning. The second step alkaline treatment should be mild enough to favor core desilication while keeping the crystallinity of the sample (NaCO_3 treatment for example like already seen in the literature for ZSM-5 nanoboxes).²⁶

3.6. Effect of TEA^+

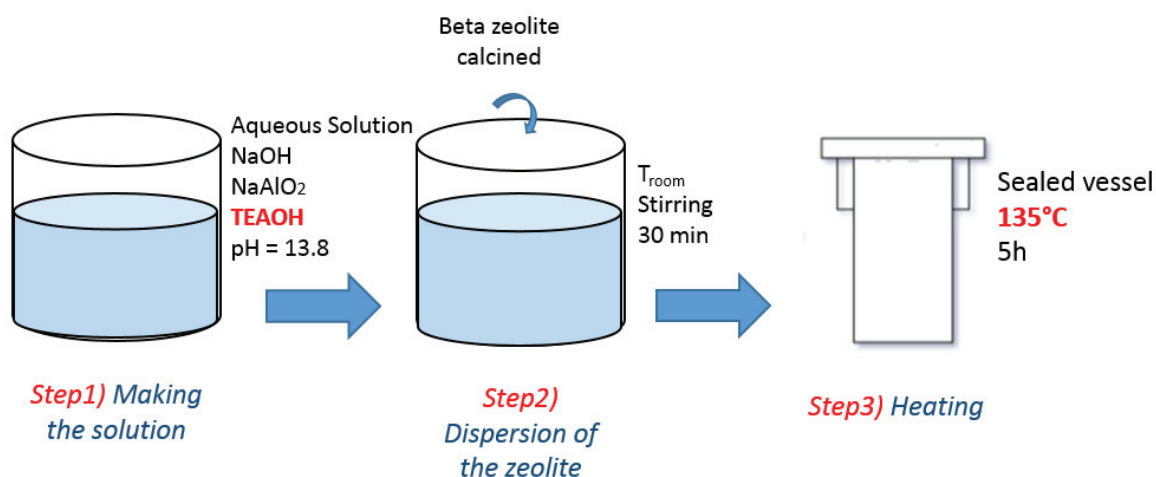


Figure 57 - Synthesis route of example 1 of the patent. This subchapter studies the effect of different TEA^+ , keeping the same OH/SiO_2 concentration by adjusting the NaOH, and increasing the temperature in step 3 (in red).

So far, all the samples presented a mainly amorphous hollow structure. The following synthesis was carried out in an attempt to keep not only the hollow morphology but also the crystallinity of the sample.

Regarding the synthesis of hollow **MFI** single crystals, when dissolution occurs in the presence of the structure-directing molecules (TPA⁺ for **MFI**), there is recrystallization of the dissolved species, which shows how the organic template is responsible for recrystallization.⁴¹ Guo *et al.*²² studied this dissolution-recrystallization process over silicalite-1, and claimed that TPA⁺ not only increases the yield of hollow silicalite-1, but also protects the parent crystal surface. The concentration and location of TPA⁺ on the zeolite surface are responsible for the formation of an intact shell²². Moreover, zeolites containing template are more resistant to desilication than calcined template-free zeolites.⁴

Taking into account these studies, TEAOH was added to the treatment in an attempt to favor recrystallization of the dissolved species, and/or protect the external surface of the parent zeolite, then avoiding destruction of the framework.

We decided to add TEAOH to step1 and the amount of NaOH was adjusted to keep the pH approximately constant (detailed description in chapter II and Figure 57). Step 3 was carried out at 135 °C to favor crystallization, considering that the crystallization temperature is the same than for the parent Beta. The sample was labelled as **TEA-Hollowβ**.

Contrary to the previous tests, TEA-Hollowβ show the characteristic XRD diffraction peaks of ***BEA** framework, presenting the same crystallinity of the calcined parent Beta, and a very small amount of amorphous phase (see Figure 58). Comparing to the standard Hollowβ, TEA-Hollowβ presents a much higher % of crystalline phase of ***BEA**.

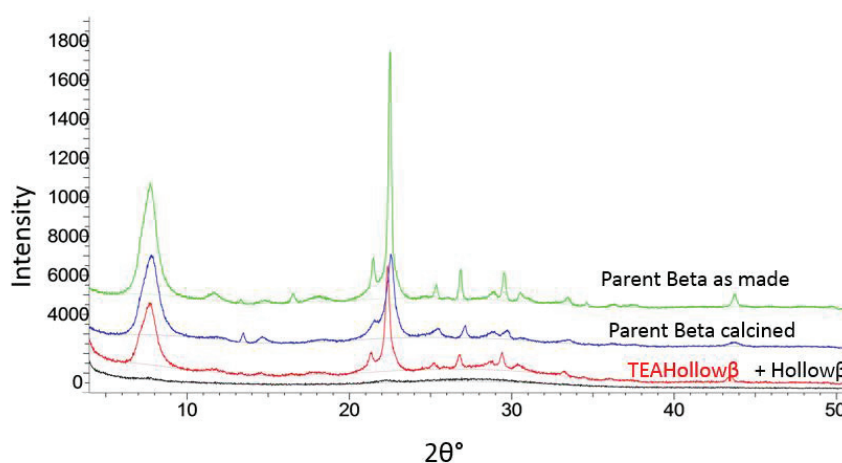


Figure 58 - XRD patterns of the Parent Beta as-made, TEA-Hollowβ as-made and the Hollowβ as-made.

TEM images of the final product TEA-Hollowβ show homogeneous hollow structures, a particle size similar to the parent zeolite, see Figure 59. This hollow structure presents a smooth external surface, and a thin shell of approx. 40-80nm. There is a small % of the sample that clearly presents a hollow structure with a mesoporous shell that seems to be constituted by several crystallites, as it is observable in Figure 59 by the structures pointed by the arrow.

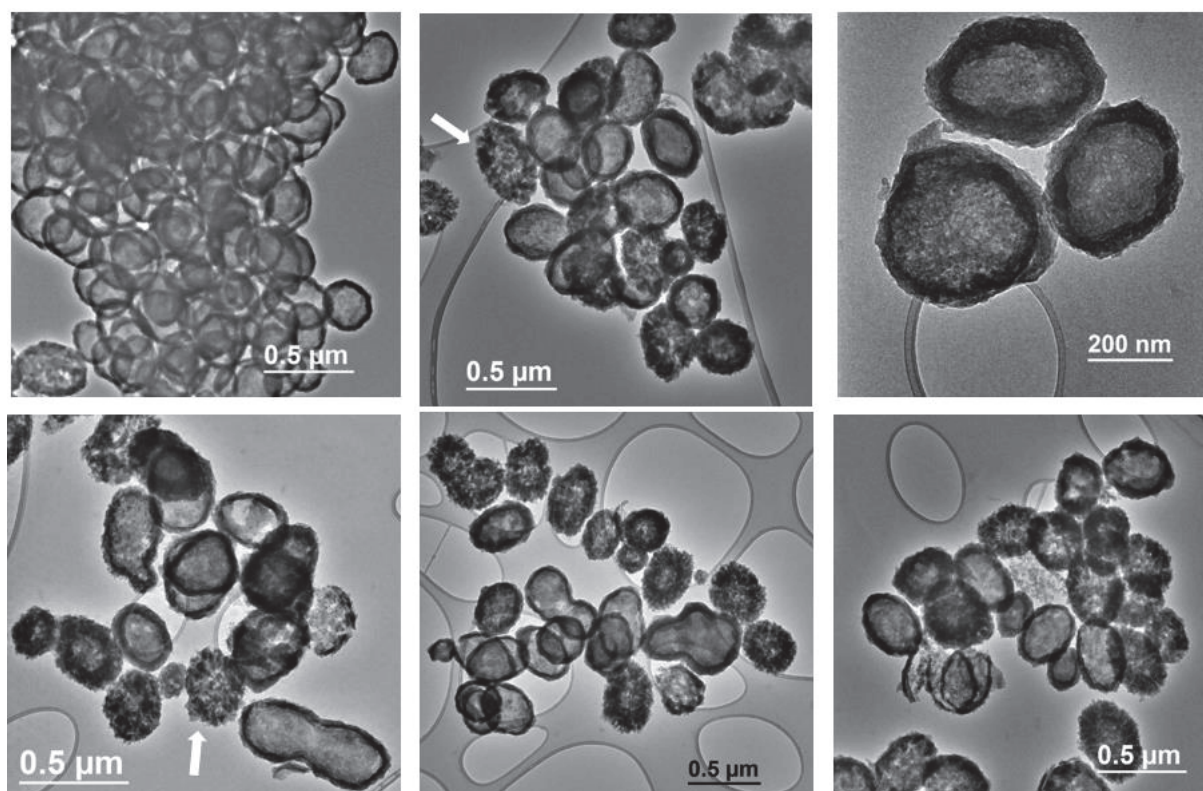


Figure 59 – TEM images of TEA-Hollow β . Arrow in picture indicate the presence of a hollow structure with a mesoporous shell.

At last, we had obtained crystallized hollow Beta structure. Based on XRD results, when using this treatment the crystalline yield appeared to be significantly higher than the standard Hollow β synthesis, see Figure 58, while keeping the hollow structure. It was not clear if the crystalline phase is part of the crystalline parent Beta that is still intact, or due to recrystallization of the dissolved species, or both.

However, once TEA-Hollow β was calcined at 550 °C, the sample became practically amorphous (no peaks present on the XRD, not shown) and the sample presented a dark grey/brown color.

The sample was calcined under different conditions: static in air at 550 °C and 600 °C, and under air flow conditions at 600 °C. Still, TEA-Hollow β presented the same grey/brown color. The origin of this brown/grey color is still a matter of debate. One of the possible explanations for the previous phenomena was that, if there was an amorphous phase around each crystal, the organic template would not be able to escape from the framework.

The presence of TEA⁺ in the crystalline part of the hollow structure could be an evidence of partial recrystallization of the dissolved species. TGA analysis should be performed in order to analyze the amount of organic molecules inside the final product (if any). ¹H-²⁹Si CP-MAS NMR spectrum of the TEA-Hollow β and the as-made parent zeolite presenting the

peaks characteristic of TEA⁺ cations in the porosity could be an evidence for the former assumption.

Assuming that some of the dissolved species recrystallize during step3), the presence of a small amount of amorphous phase indicates that recrystallization is not complete though. The synthesis of TEA-Hollow β was repeated, using higher crystallization times, but these resulted in the increasing yield of other crystalline phases rather than Beta (more details in the Annexes – Chapter III).

3.7. Summary on the “Beta Zeolite Dissolution” approach

In opposite to author’s claim, the synthesis of a crystalline hollow Beta zeolite by dissolution of a parent zeolite lead to mostly amorphous solids. However, the TEM images presented in the patent were very similar to the hollow structures obtained during this study. It is therefore questionable whether the XRD presented in the patent corresponds to the XRD reflections of the same samples presented in the TEM images. Also, no other publication was found studying this material or citing this patent.

In this work, we have obtained hollow structures by desilication of Beta zeolite nanocrystals, despite the absence of Al-zoning in the parent zeolite. These structures present approximately the same size as the parent zeolite, and are mostly amorphous. The crystallinity and morphology of these structures depended on several parameters, some of which have been studied herein:

- a) The presence of sodium aluminate appears to have a big impact in the morphology by protecting the surface of the parent zeolite from desilication and favoring dissolution of the center of the crystal.
- b) When performing the treatment at a pH value above pH=13.5, there is formation of hollow structures due to selective dissolution of the core of the crystal, but also amorphization of the crystalline structure. At pH=13, the crystalline structure is kept intact, but the crystal still has a bulky appearance, and no cavity inside.
- c) Crystal yield can be favored using TEA⁺ and performing the treatment at Beta crystallization temperatures. However, hollow structures were never 100 % crystalline and were always contaminated by some amorphous phase. Moreover, the crystal phase was not stable after calcination, and these samples became constantly brown/grey.

4. Conclusions

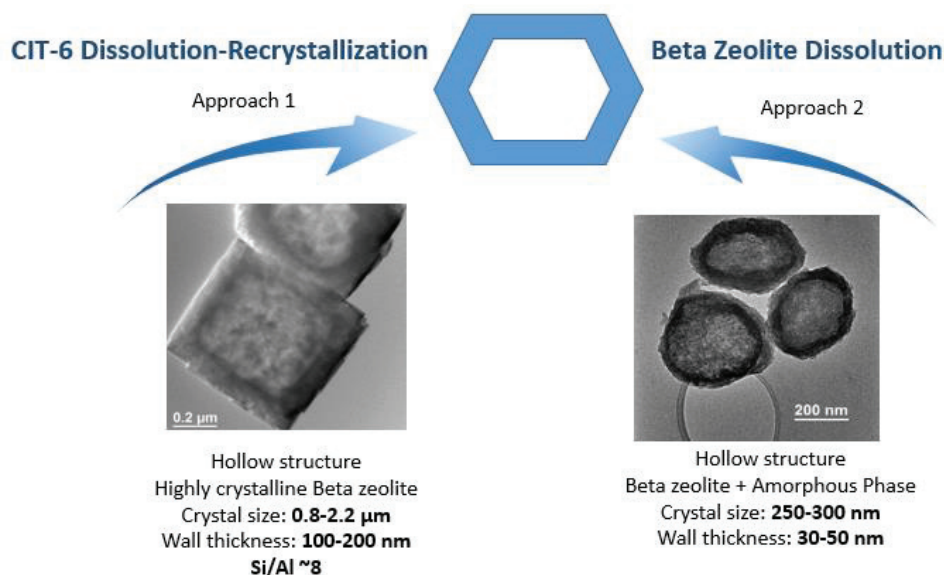


Figure 60 – Scheme of the two different approaches used for the synthesis of Hollowβ. Tem images of the results obtained and the main characterizations below.

In the case of the “CIT-6 Dissolution-Recrystallization” approach, an artificial gradient is obtained with the synthesis of a core-shell structure, where the core is a zincosilicate with the *BEA framework type. The core, having the same framework type, enables the crystallization of zeolite with the same framework type on its surface. The zincosilicate is less stable than aluminosilicate in alkaline media, leading to its preferential dissolution.

The main drawbacks of the hollow Beta obtained “CIT-6 Dissolution – Recrystallization” approach are:

- (i) There is still some residual presence of Zn^{2+} in the hollow Beta crystals ($Si/Zn = 138$ after ionic exchange with NH_4NO_3), which may impact catalytic activities. The evidence heterogeneous catalysis by framework Zn sites is still scarce. Davis *et al.*⁸ have shown the catalytic activity of CIT-6 with different Zn contents, even though this is not compared to an equivalent aluminosilicate. Zn sites in microporous zincosilicates behave as Lewis acid centers and CIT-6 was active for several Lewis acid mediated reactions. Nevertheless, CIT-6 crystals tested in Davis’ group had a high Zn content ($10 < Si/Zn < 20$), hence, we assumed that the low Zn content of the hollow Beta does not have a major impact in the catalytic tests performed in this thesis.
- (ii) The hollow Beta shell thickness is still relatively big, which may not be a significant improvement in terms of the transport and gain in catalytic activity

- (iii) Si/Al ratio is limited to a high Al content (Si/Al = 8) which might be too acidic for most of the acid catalyzed reactions. The synthesis of hollow Beta with higher Si/Al was not achieved and which would require more time of synthesis optimization. One alternative to obtain higher Si/Al was to use single step dealumination with HNO₃ similarly to.⁴⁵
- (iv) The scale-up of this synthesis may not be straightforward. CIT-6 synthesis can easily yield VPI-8, and the synthesis of hollow Beta can easily yield **MOR**. Also, several reproducibility problems were found during previous works at IFPEN by Maria Manko and during this thesis.

Regarding the “*Beta Zeolite Dissolution*” approach, hollow Beta single crystals were obtained. These crystals present a much smaller crystal size, and consequently a very thin wall thickness (30 – 50 nm), which can be an important advantage in terms of molecular transport and consequently a big gain in catalytic activity.

However, the hollow Beta crystals obtained by the “*Beta Zeolite Dissolution*” approach still have a small amount of amorphous phase. Furthermore, the crystals are not stable upon calcination (gaining also a brown/grey colour). Experimental procedures have to be optimized to totally remove amorphous material from the hollow structures. In any case, probably an artificial Al zoning was created by surface alumination, leading to a selective dissolution of the core of the crystal.

Experimental procedures should be optimized in order to completely remove the amorphous phase of these structures. Regarding the previous conclusions, the next step forward crystalline hollow structures should be pursued by keeping the sodium aluminate, TEA⁺, but eventually using a pH < 13.8 by adjusting the [NaOH/SiO₂] and or using TEABr instead of TEAOH.

Recently, some further studies were carried out in order to better understand this desilication process and try to achieve crystalline hollow Beta zeolites. Parameters such as Al content, pH, temperature, and parent Beta with different crystal sizes and compositions have been analyzed. Stirring during the desilication process appears to significantly increase the amorphous phase. Using TEA⁺ improves crystallinity, similarly to the results presented in this chapter. Homogeneous and smooth hollow structures were obtained, however, always contaminated with amorphous aluminosilicates. These results can be found in the article entitled “Hollow structures by controlled desilication of Beta zeolite nanocrystals”, listed in the section “Publications”.

5. References

- (1) Iyoki, K.; Itabashi, K.; Okubo, T. Seed-Assisted, One-Pot Synthesis of Hollow Zeolite Beta without Using Organic Structure-Directing Agents. *Chem. – Asian J.* **2013**, *8* (7), 1419–1427. <https://doi.org/10.1002/asia.201300365>.
- (2) Fan, F.; Ling, F.; Wang, S.; Zhang, H.; Chen, X.; Wang, C. One Kind of Hollow Beta Zeolite and Its Preparation Method. CN 104591220, 2013.
- (3) Kamimura, Y.; Chaikittisilp, W.; Itabashi, K.; Shimojima, A.; Okubo, T. Critical Factors in the Seed-Assisted Synthesis of Zeolite Beta and “Green Beta” from OSDA-Free Na⁺-Aluminosilicate Gels. *Chem.- Asian J.* **2010**, *5* (10), 2182–2191. <https://doi.org/10.1002/asia.201000234>.
- (4) Verboekend, D.; Perez-Ramirez, J. Design of Hierarchical Zeolite Catalysts by Desilication. *Catal. Sci. Technol.* **2011**, *1* (6), 879–890. <https://doi.org/10.1039/c1cy00150g>.
- (5) Takewaki, T.; Beck, L. W.; Davis, M. E. Zincosilicate CIT-6: A Precursor to a Family of *BEA-Type Molecular Sieves. *J. Phys. Chem. B* **1999**, *103* (14), 2674–2679. <https://doi.org/10.1021/jp9845726>.
- (6) Takewaki, T.; Beck, L. W.; Davis, M. E. Synthesis of CIT-6, a Zincosilicate with the (*)BEA Topology. *Top. Catal.* **1999**, *9* (1–2), 35–42. <https://doi.org/10.1023/A:1019150203436>.
- (7) Serrano, D. P.; van Grieken, R.; Davis, M. E.; Melero, J. A.; Garcia, A.; Morales, G. Mechanism of CIT-6 and VPI-8 Crystallization from Zincosilicate Gels. *Chem. Eur. J.* **2002**, *8* (22), 5153–5160. [https://doi.org/10.1002/1521-3765\(20021115\)8:22<5153::AID-CHEM5153>3.0.CO;2-E](https://doi.org/10.1002/1521-3765(20021115)8:22<5153::AID-CHEM5153>3.0.CO;2-E).
- (8) Orazov, M.; Davis, M. E. Catalysis by Framework Zinc in Silica-Based Molecular Sieves. *Chem. Sci.* **2016**, *7* (3), 2264–2274. <https://doi.org/10.1039/c5sc03889h>.
- (9) Yoshikawa, M.; Zones, S. I.; Davis, M. E. Synthesis of VPI-8: I. The Effects of Reaction Components. *Microporous Mater.* **1997**, *11* (3), 127–136. [https://doi.org/10.1016/S0927-6513\(97\)00031-X](https://doi.org/10.1016/S0927-6513(97)00031-X).
- (10) Koike, N.; Iyoki, K.; Chaikittisilp, W.; Okubo, T. Synthesis of Microporous Zincosilicate *BEA Molecular Sieves from Zincosilicate Gels Co-Precipitated in the Presence of an Organic Structure-Directing Agent. *Chem. Lett.* **2018**, *47* (7), 897–900. <https://doi.org/10.1246/cl.180264>.
- (11) Deimund, M. A.; Labinger, J.; Davis, M. E. Nickel-Exchanged Zincosilicate Catalysts for the Oligomerization of Propylene. *ACS Catal.* **2014**, *4* (11), 4189–4195. <https://doi.org/10.1021/cs501313z>.
- (12) Groen, J. C.; Abello, S.; Villaescusa, L. A.; Pérez-Ramirez, J. Mesoporous Beta Zeolite Obtained by Desilication. *Microporous Mesoporous Mater.* **2008**, *114* (1–3), 93–102. <https://doi.org/10.1016/j.micromeso.2007.12.025>.

- (13) Ding, L.; Zheng, Y.; Hong, Y.; Ring, Z. Effect of Particle Size on the Hydrothermal Stability of Zeolite Beta. *Microporous Mesoporous Mater.* **2007**, *101* (3), 432–439. <https://doi.org/10.1016/j.micromeso.2006.12.008>.
- (14) Hajjar, R.; Millot, Y.; Man, P. P.; Che, M.; Dzwigaj, S. Two Kinds of Framework Al Sites Studied in BEA Zeolite by X-Ray Diffraction, Fourier Transform Infrared Spectroscopy, NMR Techniques, and V Probe. *J. Phys. Chem.* **2008**, *112* (51), 20167–20175. <https://doi.org/10.1021/jp808356q>.
- (15) Thommes, M.; Kaneko, K.; Neimark, A. V.; Olivier, J. P.; Rodriguez-Reinoso, F.; Rouquerol, J.; Sing, K. S. W. Physisorption of Gases, with Special Reference to the Evaluation of Surface Area and Pore Size Distribution (IUPAC Technical Report). *Pure Appl. Chem.* **2015**, *87* (9–10), 1051–1069. <https://doi.org/10.1515/pac-2014-1117>.
- (16) Mitchell, S.; Pinar, A. B.; Kenvin, J.; Crivelli, P.; Karger, J.; Perez-Ramirez, J. Structural Analysis of Hierarchically Organized Zeolites. *Nature Commun.* **2015**, *6*, 8633. <https://doi.org/10.1038/ncomms9633>.
- (17) Morishige, K.; Tateishi, M.; Hirose, F.; Aramaki, K. Change in Desorption Mechanism from Pore Blocking to Cavitation with Temperature for Nitrogen in Ordered Silica with Cagelike Pores. *Langmuir* **2006**, *22* (22), 9220–9224. <https://doi.org/10.1021/la061360o>.
- (18) Thommes, M.; Cychosz, K. Physical Adsorption Characterization of Nanoporous Materials: Progress and Challenges. *Adsorption* **2014**, *20*, 233–250. <https://doi.org/10.1007/s10450-014-9606-z>.
- (19) Ravikovitch, P. I.; Neimark, A. V. Experimental Confirmation of Different Mechanisms of Evaporation from Ink-Bottle Type Pores: Equilibrium, Pore Blocking, and Cavitation. *Langmuir* **2002**, *18* (25), 9830–9837. <https://doi.org/10.1021/la026140z>.
- (20) Thommes, M.; Smarsly, B.; Groenewolt, M.; Ravikovitch, P. I.; Neimark, A. V. Adsorption Hysteresis of Nitrogen and Argon in Pore Networks and Characterization of Novel Micro- and Mesoporous Silicas. *Langmuir* **2006**, *22* (2), 756–764. <https://doi.org/10.1021/la051686h>.
- (21) Giesche, H. Mercury Porosimetry: A General (Practical) Overview. *Part. Part. Syst. Char.* **2006**, *23* (1), 9–19. <https://doi.org/10.1002/ppsc.200601009>.
- (22) Dai, C.; Zhang, A.; Li, L.; Hou, K.; Ding, F.; Li, J.; Mu, D.; Song, C.; Liu, M.; Guo, X. Synthesis of Hollow Nanocubes and Macroporous Monoliths of Silicalite-1 by Alkaline Treatment. *Chem. Mater.* **2013**, *25* (21), 4197–4205. <https://doi.org/10.1021/cm401739e>.
- (23) Gallezot, P.; Blanc, B.; Barthomeuf, D.; Dasilva, M. *Selective Hydrogenation of Cinnamaldehyde Controlled by Host-Guest Interactions in Beta-Zeolite*; Weitkamp, J., Karge, H. G., Pfeifer, H., Holderich, W., Eds.; Elsevier Science Publ B V: Amsterdam, 1994; Vol. 84.
- (24) Gates, B. Supported Metal-Clusters - Synthesis, Structure, and Catalysis. *Chem. Rev.* **1995**, *95* (3), 511–522. <https://doi.org/10.1021/cr00035a003>.
- (25) Thomas, J. M. *Handbook Of Heterogeneous Catalysis. 2., Completely Revised and Enlarged Edition. Vol. 1–8.*; G. Ertl, H. Knözinger, F. Schüth, J. Weitkamp; Vol. 48.

- (26) Pagis, C.; Morgado Prates, A. R.; Farrusseng, D.; Bats, N.; Tuel, A. Hollow Zeolite Structures: An Overview of Synthesis Methods. *Chem. Mater.* **2016**, *28* (15), 5205–5223. <https://doi.org/10.1021/acs.chemmater.6b02172>.
- (27) Tahri, Z.; Luchez, F.; Yordanov, I.; Poizat, O.; Moissette, A.; Valtchev, V.; Mintova, S.; Mostafavi, M.; Waele, V. D. Nanosecond Probing of the Early Nucleation Steps of Silver Atoms in Colloidal Zeolite by Pulse Radiolysis and Flash Photolysis Techniques. *Res. Chem. Intermed.* **2009**, *35* (4), 379–388. <https://doi.org/10.1007/s11164-009-0049-1>.
- (28) Li, S.; Boucheron, T.; Tuel, A.; Farrusseng, D.; Meunier, F. Size-Selective Hydrogenation at the Subnanometer Scale over Platinum Nanoparticles Encapsulated in Silicalite-1 Single Crystal Hollow Shells. *Chem. Commun.* **2014**, *50* (15), 1824. <https://doi.org/10.1039/c3cc48648f>.
- (29) Li, S.; Aquino, C.; Gueudr?, L.; Tuel, A.; Schuurman, Y.; Farrusseng, D. Diffusion-Driven Selectivity in Oxidation of CO in the Presence of Propylene Using Zeolite Nano Shell as Membrane. *ACS Catal.* **2014**, *4* (12), 4299–4303. <https://doi.org/10.1021/cs501349b>.
- (30) Dai, C.; Zhang, S.; Zhang, A.; Song, C.; Shi, C.; Guo, X. Hollow Zeolite Encapsulated Ni-Pt Bimetals for Sintering and Coking Resistant Dry Reforming of Methane. *J. Mater. Chem. A* **2015**, *3* (32), 16461–16468. <https://doi.org/10.1039/c5ta03565a>.
- (31) Bourgeat-Lami, E.; Drenzo, F.; Fajula, F.; Mutin, P.; Courieres, T. Mechanism of the Thermal-Decomposition of Tetraethylammonium in Zeolite-Beta. *J. Phys. Chem.* **1992**, *96* (9), 3807–3811. <https://doi.org/10.1021/j100188a044>.
- (32) Banfi, L.; Narisano, E.; Riva, R.; Stiasni, N.; Hiersemann, M.; Yamada, T.; Tsubo, T. Sodium Borohydride. In *Encyclopedia of Reagents for Organic Synthesis*; American Cancer Society, 2014; pp 1–13. <https://doi.org/10.1002/047084289X.rs052.pub3>.
- (33) Rousset, J. L.; Stievano, L.; Aires, F. J. C. S.; Geantet, C.; Renouprez, A. J.; Pellarin, M. Hydrogenation of Toluene over Gamma-Al₂O₃-Supported Pt, Pd, and Pd-Pt Model Catalysts Obtained by Laser Vaporization of Bulk Metals. *J. Catal.* **2001**, *197* (2), 335–343. <https://doi.org/10.1006/jcat.2000.3083>.
- (34) Bond; Geoffrey. *Metal-Catalysed Reactions of Hydrocarbons*; 2005.
- (35) Li, S.; Tuel, A.; Meunier, F.; Aouine, M.; Farrusseng, D. Platinum Nanoparticles Entrapped in Zeolite Nanoshells as Active and Sintering-Resistant Arene Hydrogenation Catalysts. *J. Catal.* **2015**, *332*, 25–30. <https://doi.org/10.1016/j.jcat.2015.09.006>.
- (36) Knapp, C.; Obuchi, A.; Uchisawa, J. O.; Kushiya, S.; Avila, P. Method for Selective Removal of Supported Platinum Particles from External Zeolite Surfaces: Characterisation of and Application to a Catalyst for the Selective Reduction of Nitrogen Oxide by Hydrocarbons. *Microporous Mesoporous Mater.* **1999**, *31* (1–2), 23–31. [https://doi.org/10.1016/S1387-1811\(99\)00054-2](https://doi.org/10.1016/S1387-1811(99)00054-2).
- (37) Nakao, Y. Dissolution of Noble-Metals in Halogen Halide Polar Organic-Solvent Systems. *J. Chem. Soc.-Chem. Commun.* **1992**, No. 5, 426–427. <https://doi.org/10.1039/c39920000426>.

- (38) Nakao, Y.; Sone, K. Reversible Dissolution/Deposition of Gold in Iodine-Iodide-Acetonitrile Systems. *Chem. Commun.* **1996**, No. 8, 897–898. <https://doi.org/10.1039/cc9960000897>.
- (39) Liu, H.; Lu, G.; Guo, Y.; Wang, Y.; Guo, Y. Synthesis of Spherical-like Pt–MCM-41 Mesoporous Materials with High Catalytic Performance for Hydrogenation of Nitrobenzene. *J. Colloid Interface Sci.* **2010**, *346* (2), 486–493. <https://doi.org/10.1016/j.jcis.2010.03.018>.
- (40) Yang, C.; Liu, P.; Ho, Y.; Chiu, C.; Chao, K. Highly Dispersed Metal Nanoparticles in Functionalized SBA-15. *Chem. Mater.* **2003**, *15* (1), 275–280. <https://doi.org/10.1021/cm020822q>.
- (41) Prates, A. R. M.; Pagis, C.; Meunier, F. C.; Burel, L.; Epicier, T.; Roiban, L.; Koneti, S.; Bats, N.; Farrusseng, D.; Tuel, A. Hollow Beta Zeolite Single Crystals for the Design of Selective Catalysts. *Cryst. Growth Des.* **2018**, *18* (2), 592–596. <https://doi.org/10.1021/acs.cgd.7b01635>.
- (42) Nakao, Y. Three Procedures of Reversible Dissolution/Deposition of Gold Using Halogen-Containing Organic Systems. *Chem. Commun.* **1997**, No. 18, 1765–1766. <https://doi.org/10.1039/a704171c>.
- (43) Takashima, Y.; Miras, H. N.; Glatzel, S.; Cronin, L. Shrink Wrapping Redox-Active Crystals of Polyoxometalate Open Frameworks with Organic Polymers via Crystal Induced Polymerisation. *Chem. Commun.* **2016**, *52* (50), 7794–7797. <https://doi.org/10.1039/c6cc03031a>.
- (44) Sá, J.; Taylor, S. F. R.; Daly, H.; Goguet, A.; Tiruvalam, R.; He, Q.; Kiely, C. J.; Hutchings, G. J.; Hardacre, C. Redisposition of Gold Supported on Oxides. *ACS Catal.* **2012**, *2* (4), 552–560. <https://doi.org/10.1021/cs300074g>.
- (45) Bourgeat-Lami, E.; Fajula, F.; Anglerot, D.; Courieres, T. Single-Step Dealumination of Zeolite-Beta Precursors for the Preparation. *Microporous Mater.* **1993**, *1* (4), 237–245.
- (46) Groen, J. C.; Brouwer, S.; Peffer, L. A. A.; Perez-Ramirez, J. Application of Mercury Intrusion Porosimetry for Characterization of Combined Micro- and Mesoporous Zeolites. *Part. Part. Syst. Char.* **2006**, *23* (1), 101–106. <https://doi.org/10.1002/ppsc.200601010>.
- (47) Pagis, C.; Prates, A. R. M.; Bats, N.; Tuel, A.; Farrusseng, D. High-Silica Hollow Y Zeolite by Selective Desilication of Dealuminated NaY Crystals in the Presence of Protective Al Species. *Cryst. Eng. Commun.* **2018**, *20* (11), 1564–1572. <https://doi.org/10.1039/c8ce00121a>.
- (48) Yang, C.; Xu, Q. H. Aluminated Zeolites Beta and Their Properties .1. Aluminated Zeolites Beta. *J. Chem. Soc.-Faraday Trans.* **1997**, *93* (8), 1675–1680. <https://doi.org/10.1039/a606807c>.
- (49) Xie, Z. K.; Bao, J. Q.; Yang, Y. Q.; Chen, Q. L.; Zhang, C. F. Effect of Treatment with NaAlO₂ Solution on the Surface Acid Properties of Zeolite Beta. *J. Catal.* **2002**, *205* (1), 58–66. <https://doi.org/10.1006/jcat.2001.3421>.
- (50) Muller, M.; Harvey, G.; Prins, R. Comparison of the Dealumination of Zeolites Beta, Mordenite, ZSM-5 and Ferrierite by Thermal Treatment, Leaching with Oxalic Acid and

- Treatment with SiCl₄ by H-1, Si-29 and Al-27 MAS NMR. *Microporous Mesoporous Mater.* **2000**, 34 (2), 135–147. [https://doi.org/10.1016/S1387-1811\(99\)00167-5](https://doi.org/10.1016/S1387-1811(99)00167-5).
- (51) *Verified Syntheses of Zeolitic Materials*, Elsevier.; Harry Robson, Karl Petter Lillerud, 2001. <https://doi.org/10.1016/B978-0-444-50703-7.X5094-7>.

Chapter IV – Study of the impact of the hollow morphology on diffusion

1. Introduction

There are strong motivations for the design of zeolites which can lead to smaller Thiele modulus (ϕ) for improved catalytic performances. Remember that Thiele modulus (ϕ) is function of the intrinsic reaction rate constant (k), the effective diffusivity (D_{eff}) and the mean diffusion length, (L):

$$\phi = L \sqrt{\frac{k}{D_{eff}}}$$

Hollow zeolites single crystals are unique examples of zeolite morphology with reduced mean diffusion length (L) while keeping the “same” external surface. Assuming that D_{eff} and k are equal for the bulk and hollow zeolites, one can study the direct effect of a reduced L on the effectiveness factor η , as the ratio of Thiele modulus should be equal to the ratio of the mean path lengths, which can be estimated from the size of the crystals (L_B and L_H), Figure 1.

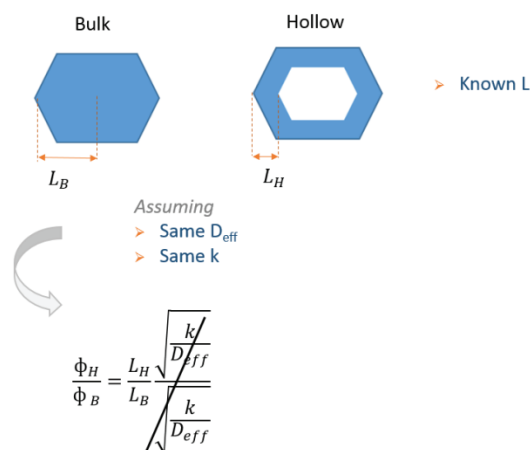


Figure 1 – Schematic diagram showing path length of bulk and hollow zeolites (L_B and L_H), the assumptions of similar D_{eff} and k and the respective impact on Thiele modulus, ϕ .

Colleagues at IRCELYON have recently reported the positive impact of hollow single zeolites in catalysis.¹ The study was executed by using the model reaction of cyclohexene

hydrogenation over Pt supported on bulk Y and hollow Y zeolites. Hollow Y presented higher activities than bulk Y, suggesting that mass transfer limitations could be affecting bulk Y catalytic performance. The Thiele modulus (ϕ) was determined assuming that D_{eff} was the same for hollow and bulk, and taking into account the different mean diffusion length (L) related to the particle size and wall thickness. Hollow Y showed lower values of ϕ , and an effectiveness factor of 97%, against 63% of the bulk sample.

Novruzova *et al.*² studied the sorption kinetic of isooctane in bulk and hollow silicalite-1 zeolites with different crystal sizes, by comparing the up-take curves obtained by in situ diffuse reflectance FT-IR spectroscopy. The small bulk and hollow crystals ($\sim 200\text{nm}$) showed faster up-takes than big crystals ($\sim 10\mu\text{m}$). When comparing a big bulk crystal with a big multi-hollow crystal (with several internal cavities) the multi-hollow crystal has a faster up-take than the bulk, as it has a smaller diffusion path length. However, when comparing a small hollow crystal with a small bulk crystal, these present the same up-take curve, showing that the different diffusional path length (or the inner cavity) did not have any impact in diffusion. The authors claimed that for small sized crystals, **external surface barriers are the dominant mechanism in diffusion**; hence, different crystal size (L) would not make a difference.

This conclusion is supported by other accounts in the literature.^{3,4} The depart in diffusion coefficients is generally accounted for surface barriers effects and/or inter-grain boundaries which can be hardly characterized. **Surface barriers** is a term generally attributed to any resistance to mass transfer at or near a surface, that can be: grain boundaries, intracrystalline defects, external surface of the crystal etc.⁴ but also surface coking, accumulation near the pore entry, collapse of the genuine pore structure close to the crystal boundary etc.⁵

It should be noted that the impact of surface barriers is often associated to crystal size as illustrated by Gueudré *et al.*³ who has carried out gravimetric uptake measurements with cyclohexane for silicalite-1 with different crystal sizes ($0.4\ \mu\text{m}$ up to $17\ \mu\text{m}$ of mean radius). For big crystals ($17\ \mu\text{m}$ & $10\ \mu\text{m}$) D_{eff} were the same, as it should be expected. However, for crystals smaller than $2\ \mu\text{m}$, D_{eff} were smaller by about one order of magnitude and quite different from each other. In the case of silicalite-1 crystals with $2\ \mu\text{m}$, surface resistance represented 60% of the total mass transfer resistance, leading to a smaller D_{eff} value than D_{eff} of bigger crystals. Note that “small” crystals have a bigger external surface/ m_{zeol} than “big” crystals.

A similar case was also illustrated by other studies concerning kinetics of cyclohexane in ZSM-5 crystals. Duncan *et al.*⁶ measured sorption kinetics of cyclohexane in ZSM-5 samples (**MFI**) using the ZLC method. The same values of D_{eff} and of diffusion energy, E_d , were found for all the samples. It should be noted the crystals had an average crystal diameter of $4\ \mu\text{m}$ up to $24\ \mu\text{m}$. Similarly, Teixeira *et al.*⁴ studied sorption kinetics of cyclohexane in silicalite-1 (**MFI**) samples, but this time the nominal crystal sizes were between $80\ \text{nm}$ to $3\ \mu\text{m}$. In all cases, D_{eff} values are inferior to those of Duncan *et al.*, and there is a reduction of D_{eff} as the crystal size

decreases. Li *et al.*⁷ also obtained completely different D_{eff} values for ZSM-5 crystals of 800 nm, 100 nm and multilamellar structures with 2 nm thick sheets.

It is obvious that the diffusion in zeolites is not fully understood yet and that additional transfer resistance may exist depending of the morphology of the crystals. Hence, considering the hollow Beta synthesized in chapter III ("*CIT-6 Dissolution-Recrystallization*" approach), we might wonder whether:

- the inner mesopores created in hollow Beta can have an impact on diffusion;
- if the inner cavity can be responsible for extra diffusion resistances – “inner surface barriers”;
- the highly rough external surface can have an impact on diffusion;

The aim of this chapter is to study the impact of the hollow morphology in molecular diffusion, regarding an equivalent bulk. Our hypothesis is that, if hollow and bulk zeolite present similar physical/chemical characteristics (crystal size, composition, V_{micro} , etc), then these have the same D_{eff} , allowing to quantify the decrease of L in molecular transport. For that, we put much attention to synthesize two bulk reference zeolites with morphologies and composition as close as possible to those of the hollow Beta zeolites synthesized in chapter III. These will be denoted here as ***Bulk1Beta*** and ***Bulk2Beta*** respectively. The hollow Beta sample will be denoted at ***HollowBeta***. Cyclohexane was chosen as probe molecule for the Beta samples.

Another set of samples, hollow silicalite-1 and bulk silicalite-1 crystals were also studied in order to compare the results to the hollow and bulk Beta samples. These are denoted here as ***HollowSil1*** and ***BulkSil1*** respectively, toluene was chosen as probe molecule, Figure 2.

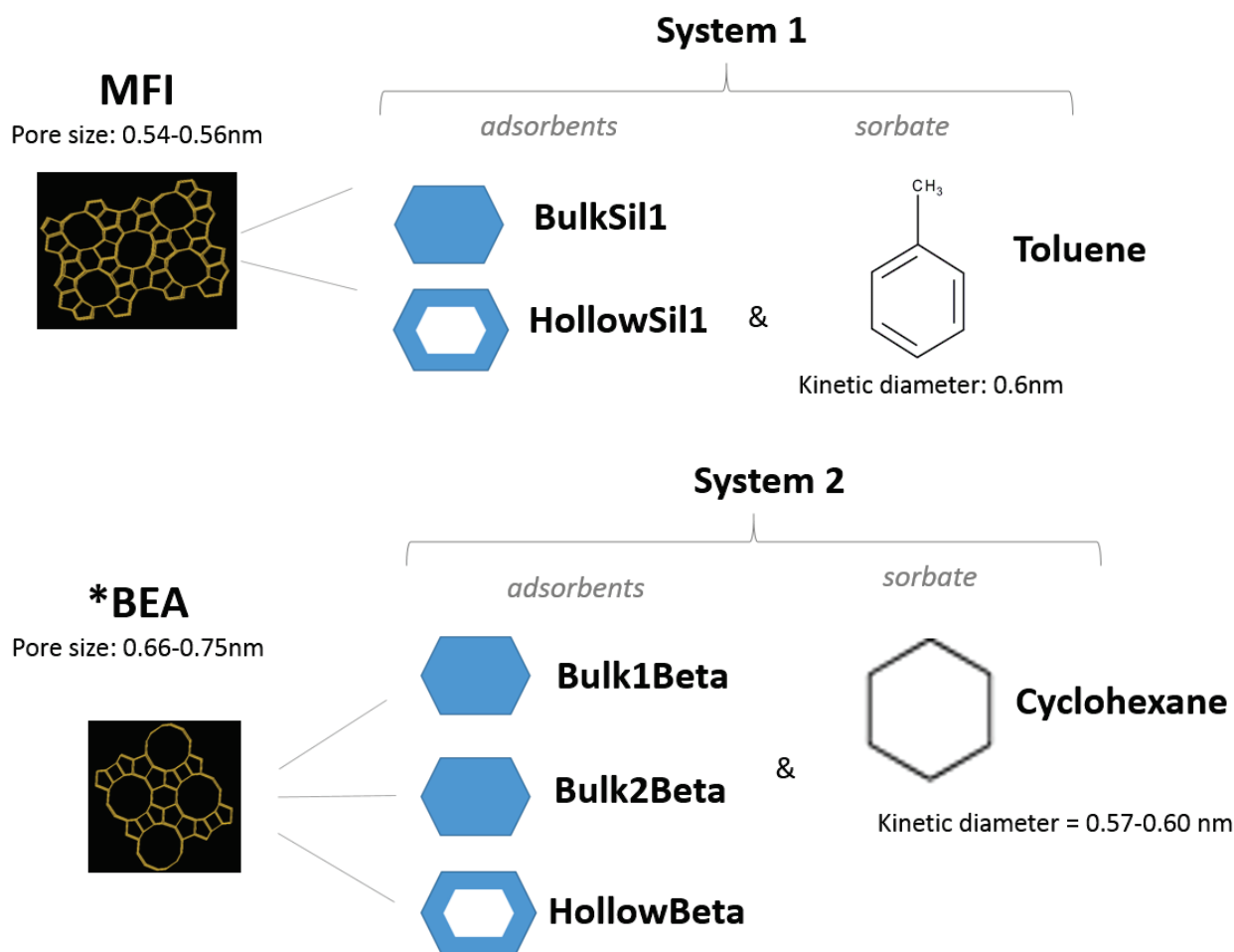


Figure 2 – Schematic diagram showing the adsorbents and sorbates chosen for the present study, presenting the pore size of the samples and kinetic diameter of the sorbates.

1.1. Choice of a technique for diffusion measurements

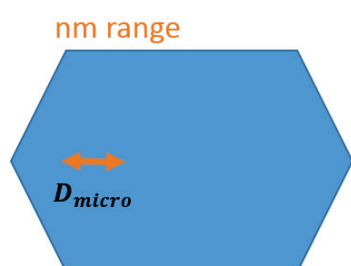
Several techniques can measure diffusion of molecules in porous materials.⁵ They vary regarding the time- and length scales at which the diffusion process is measured (which can be between nm to mm scale). Regarding the **length scale** at which diffusion measurements are made, the techniques of diffusion measurement may be classified into essentially three groups:^{8,7}

- For **microscopic techniques**, the diffusion path recorded during the experiment can be smaller than the particle size, see Figure 3, and the techniques provide information about the elementary steps of diffusion, including the mean time between molecular reorientation or diffusivities over a few nanometers of distance. Quasi elastic neutron scattering (sensitive to displacements over nanometers) and pulse field gradient NMR (nm- μ m resolution) are some of the examples. These are able to measure molecular

displacements exclusively in microporous regions even in hierarchical pore systems.⁸ ²⁹Xe NMR may provide molecular exchange rates between different pore spaces for example.⁹

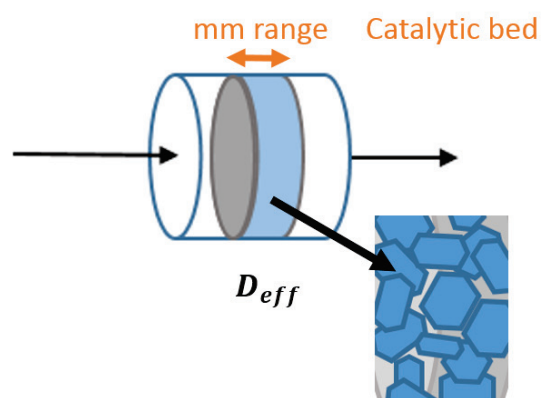
- **Micro-imaging techniques** such as interference microscopy and IR microscopy, provide the record of intracrystalline concentration profiles **of one single** crystal.⁸ Concentration profiles are obtained by the absorbance of a characteristic IR band. Absorbance can be recorded and defined spatially. Basically, this technique monitors the evolution of guest concentration profiles during transient up-take and release experiments, obtaining 2D and 3D representations.¹⁰
- **Macroscopic techniques** generally include a packed bed of zeolite crystals that suffers a change of the pressure of the surrounding atmosphere. Results are obtained by recording the overall uptake or release of the guest molecule from the whole packed bed of crystals/catalyst (Figure 3).⁹ Chromatographic method, zero length column, temporal analysis of products, diffuse reflectance FT-IR² etc. are common examples of macroscopic techniques.

Microscopic Techniques



$$D = D_{micro}$$

Macroscopic Techniques



$$D = D_{eff} = f(D_{micro}; D_{meso}; \text{surface barriers};)$$

Figure 3 – schematic representation of the different length scale of microscopic and macroscopic techniques for measuring molecular diffusion in zeolites. Below the respective diffusion coefficients are described.

Comparing the microscopic and macroscopic techniques, the measuring lengths scales are notably different. As a result, the measured **intracrystalline diffusion coefficients D** for a same system (sorbate and adsorbent) can be very different from one technique to another.⁵ Indeed, for a **microscopic technique** that is measuring diffusion within few nanometers of

highly crystalline defect free crystal, the intracrystalline diffusion coefficient will correspond to the micropore diffusion coefficient, D_{micro} . For **macroscopic techniques**, the measured intracrystalline diffusion coefficient D not only takes into account microporous diffusion D_{micro} , but all the other transport phenomena present within the whole crystals, such as mesoporous diffusion D_{meso} (in the case of presence of mesopores), surface barriers associated with the external surface, or the mesopores surface, diffusion barriers due to defects in the crystalline network etc, see Figure 3. Hence, for macroscopic techniques, the diffusion coefficient D is rather called effective or apparent diffusion coefficient D_{eff} , which represents the macroscopically observed diffusivity through the entire zeolite particle.⁴ This type of technique does only yield a true genuine microporous diffusion D_{micro} if the rate of mass transfer exclusively dominated by microporous diffusion (no mesopores and no significant diffusion barriers).⁸

In the case of this PhD project, we are interested in studying the eventual impact of hollow crystals in catalytic activity, hence, **in a catalytic packed bed scale**, rather than distinguish and qualify the different diffusion mechanism within a single crystal. Thus we found that macroscopic techniques are more suited to study our samples in this context.

Zero length column (ZLC) method was chosen as diffusion measuring technique for this study. This technique determines the effective diffusion coefficient (D_{eff}) of a given sorbate in a zeolite packed bed cell, analyzing the respective transient desorption curve. It is a common technique to measure diffusion of hydrocarbons over zeolite materials since it is sensitive to the typical characteristic diffusion times. Using a sufficiently high fluid velocity, the external resistances of heat and mass transfers can be negligible. ZLC has the particularity of using a very thin packed bed of zeolite (“zero length”), which eliminates the contribution of axial dispersion (which is an improvement regarding the chromatographic method for example), requiring only a very small amount of sample. As a result ZLC is known as an appropriate technique for measuring intracrystalline diffusion, which includes all type of transfer resistance within the zeolite crystals.

Herein, we introduce the ZLC theory and practical issues. We present a sensitivity analysis of the ZLC unit on certain experimental parameters (mass of sample, pressure drop, etc). Finally, results of ZLC measurements are presented on hollow and bulk zeolites and discussed.

2. Zero Length Column technique - ZLC

2.1. Choice of a probe molecule

The choice of the probe molecule shall take into account that 1) the probe molecule does not react at the temperature of the ZLC measurements (which could create coke depositions and change the diffusion results) 2) the characteristic diffusion time of the molecule through the crystal should be slow enough to be noticeable regarding the diffusion time of the system (at least 100-200 s) and finally 3) the probe molecule shall be small enough to “enter” and diffuse within the microporous zeolite.

Toluene was chosen as probe molecule for silicalite-1 samples. ZLC diffusion studies of toluene over mesostructured **MFI** zeolite can already be found in the literature.^{11,12} Diffusion of toluene is slow enough to show a difference between the desorption time between the microporous and the mesoporous samples.

Cyclohexane was chosen as probe molecule for Beta zeolite sample. Previous studies carried out at IRCELYON and recently published,¹ have shown an impact of the hollow morphology in catalysis (associated to the reduced diffusion path length L_H) for the model reaction of hydrogenation of cyclohexene to cyclohexane in **FAU** type zeolites. Note that **FAU** type zeolites possess has a pore entry of 0.74 nm, similar to those of ***BEA**.

2.2. ZLC theory

ZLC technique was introduced in 1987 by Eic and Ruthven,¹³ as a simple and rapid approach to study sorption kinetics.⁵ The principle of ZLC method is to equilibrate a small sample of zeolite crystals with a sorbate at a known partial pressure. Then, the desorption is induced by purging the sample by inert gas flow (He in this case) – purge flow rate - at high velocity. The desorption is monitored by measuring the concentration of sorbate as function of time. The column consists of a small amount of adsorbent (up to 10 mg as used in the literature), resulting in a very thin bed length (zero length column), avoiding any axial dispersion resistance and being considered as a well-mixed cell.^{5,13}

- **Mathematical model assuming spherical particles**

The model assumes that mass transport is controlled entirely by bulk diffusion (intracrystalline diffusion), and therefore with absence of any external resistance to mass

transfer. Starting with a 1-D, radial mass balance around a zeolite particle for a transient system, the system can be described by the following mathematical model:^{4,14}

Mass Balance (continuity equations):

$$V_s \frac{\partial q}{\partial t} + V_g \frac{\partial c}{\partial t} + Fc = 0 \quad 1$$

Mass balance through the solid phase, regarding Fick diffusion equation:

$$\frac{\partial q}{\partial t} = D_{eff} \left(\frac{\partial^2 q}{\partial r^2} + \frac{2}{r} \frac{\partial q}{\partial r} \right) \quad 2$$

Where q is the adsorbed phase concentration; c is the gas phase sorbate concentration; V_s is the adsorbent volume; V_g is the fluid phase volume; F is the volumetric flow rate; D_{eff} is the effective/apparent intracrystalline diffusivity; and r the radial coordinate.^{13,14}

Initial and Boundary conditions:

- At equilibrium, q is directly related to c by Henry's constant K_H , if adsorption takes place within Henry's region. c_0 is the sorbate initial steady state concentration in fluid phase; q_0 initial adsorbed phase concentration,¹⁴

$$t \leq 0, \quad q = q_0 = K_H c_0 \quad \text{for all } r$$

- There is a max or a min concentration of sorbate in the center of the spherical crystal,

$$t > 0, \quad \frac{\partial q}{\partial r} = 0, \quad r = 0$$

- Balancing the fluxes at the crystal surface, between the bulk gas phase and the equilibrium surface concentration.⁴ It is assumed here that external film mass transfer is fast enough to ensure that, under purging conditions, the sorbate concentration is very low, not only in the bulk gas but also on the crystal's surface.¹³ v stands for interstitial gas velocity, ϵ stands for voidage of the adsorbent bed, z for the bed depth.¹³

$$r = R, \quad -D_{eff} \frac{\partial q}{\partial r} = \frac{\epsilon v R}{3(1-\epsilon)z} \frac{q}{R}$$

The problem defined in this way is formally similar to the problem of diffusion in a sphere with surface evaporation that is discussed by Crank.^{13,15} Expressed in terms of the effluent concentration, the solution becomes:⁵

$$\frac{c}{c_0} = 2L \sum_{n=1}^{\infty} \frac{\exp\left(-\frac{\beta_n^2 D_{eff} t}{R^2}\right)}{\beta_n^2 + L_{ZLC}(L_{ZLC} - 1)} \quad 3$$

Where L_{ZLC} and β_n are ZLC model parameters defined as:

$$\beta_n \cot \beta_n + L_{ZLC} - 1 = 0 \quad 4$$

$$L_{ZLC} = \frac{\varepsilon v R^2}{3(1 - \varepsilon) K_H D_{eff} z} = \frac{F R^2}{3 V_{cat} K_H D_{eff}} = \frac{1 \text{ purge flow rate } R^2}{3 \text{ crystal volume } K_H D_{eff}} \quad 5$$

Under certain experimental conditions, this equation can be simplified and the diffusion coefficient D can easily be determined. When purge flow rate (F) is high, L_{ZLC} is large and $\beta = n\pi$ and the equation 3 is simplified to:

$$\frac{c}{c_0} = 2L \sum_{n=1}^{\infty} \frac{\exp\left(-\frac{n^2 \pi^2 D_{eff} t}{R^2}\right)}{(n\pi)^2 + L_{ZLC}(L_{ZLC} - 1)} \quad 6$$

On the “long time” region of the ZLC curve, only the first term of the summation ($n=1$) is significant, and the summation becomes an **asymptote**: in which the **slope** becomes independent of L_{ZLC} (therefore independent of flow rate) and equal to $\pi^2 * D_{eff} / R^2$.

$$\ln\left(\frac{c}{c_0}\right) = \ln\left[\frac{2L_{ZLC}}{\beta_1^2 + L_{ZLC}(L_{ZLC} - 1)}\right] - \frac{\beta_1^2 D_{eff}}{R^2} t \quad 7$$

Y = Intercept + Slope t

Under conditions of shallow bed and high purge flow rate (**high L_{ZLC}**), the **characteristic diffusion time $\tau = R^2/D_{eff}$** , can be estimated by equation 7.⁵ The **effective diffusion coefficient D_{eff}** can be calculated if R is known.

ZLC technique can be also applied for measuring adsorption equilibrium data. When the purge flow rate is low, $L_{ZLC} \rightarrow 0$, $\beta_1^2 \rightarrow 3L_{ZLC}$ and all higher order terms in equation 3 approach zero. Hence, the solution is given by equation 8:

$$\ln \frac{c(t)}{c_0} = \frac{F t}{K_H V_S + V_g} \quad 8$$

At low purge flow rate ($L_{ZLC} \rightarrow 0$), the contact time is large compared to the characteristic diffusion time, and the desorption rate is determined by convection under equilibrium conditions. Intracrystalline diffusion is fast enough so that a uniform concentration is always maintained through the crystal - equilibrium control regime⁵ - hence, it is the best regime to obtain Henry's constant K_H .

The desorption flow rate F, (that is proportionally related with L_{ZLC} by equation 5) used for the desorption curves dictates the desorption regime and what kind of parameters we can obtain from the ZLC model. Therefore, the L_{ZLC} value is an important criteria to check if the ZLC model is being applied under kinetic conditions, which will be discussed below.

For the present study, we are applying the **ZLC at high purge flow rates (high F, hence high L_{ZLC})**, as we mean to measure the **characteristic diffusion time τ and D_{eff}** .

2.3. Preliminary checks

There are several preliminary tests that shall be made to ensure that a ZLC system is generating reliable diffusivity data.

1) Measuring the blank response

It is important to measure the blank response of the system, i.e. run with no adsorbent, in order to correct the ZLC response. The difference between original curve and corrected curve by blank run obtained at the same conditions should be slight. It means there's no extraneous adsorption on tube walls, valves etc.⁵ In any case, the blank curve should be taken into account for the ZLC, for each temperature.

2) Check whether the system is (or not) within Henry's region

The original ZLC response model assumes that the adsorption occurs within Henry's law region, i.e., adsorption at sufficiently low concentrations so that the equilibrium relationship is linear, where the constant of proportionality between adsorbed phase and gas phase concentrations is the Henry's constant, K_H . Brandani *et al.*¹⁶ modified the ZLC model to take into account the non-linear region, working within conditions of non-linearity concentration. Brandani came to the conclusion that analyzing a ZLC experiment run under non-linear conditions and using a linear model had a major effect on the estimation of the apparent Henry's constant, but a little effect on diffusivity (if $L_{ZLC} > 8$).^{16,17}

The ZLC runs carried out for this study used very low concentrations of sorbate at adsorption step, which were limited by the temperature of the saturator and the volatility of sorbate. We cannot guarantee that, for all our studies, the concentrations of sorbate were low enough to be within Henry's region at the beginning of the ZLC measurements; however, the impact on the estimation of D_{eff} is minimal.

3) Equilibrium regime vs Kinetic regime

In order to obtain reliable diffusivity data, we must ensure that the run is made under kinetic regime. According to the literature, the value of the parameter L_{ZLC} is an indicator of the regime, where L_{ZLC} should be greater than 10 for assuring kinetic regime.⁴ To confirm the dominance of intracrystalline diffusion, one should vary the purge flow rates, and plot $\ln(c/c_0)$ versus t , the linear asymptote for the long time region. Under kinetic control conditions, the slope of the respective asymptotes should remain the same for the different flow rates. When the flow is high enough, (kinetic control regime), the slope should remain constant for increasing flow rates. In the equilibrium control regime, the desorption curve plotted as c/c_0 vs Ft should be the same for different F (flow rates).^{5,18}

2.4. Practical implementation

Herein, the general experimental issues related to the ZLC unit will be discussed, such as the experimental set-up, acquisition and data processing etc. The following subchapter "Sensitivity analysis" highlights configurational issues and criteria for the optimization of this unit.

2.4.1. Experimental set-up

Figure 4 shows a simplified schematic diagram of the ZLC set-up. The **adsorption line** carries a low concentration of sorbate diluted in He. This is prepared by dilution of a low flow saturated stream with a relatively large flow He bypass. The low flow saturated stream was prepared by passing a small He flow through a bubbler, maintained at low temperature by a Julabo ED (V.2) low temperature thermostat. The **desorption line** is a high flow He line. Both adsorption and desorption streams are feed by a mass flow controller. The “Switch valve” controls which of the two streams (adsorption or desorption) are delivered to the ZLC cell. Two pressure indicators are placed before the switching valve, one on the adsorption line – PI Ads – and the other on the desorption line – PI Des. These continuously control the pressure of each stream, and pressure drops during each run.

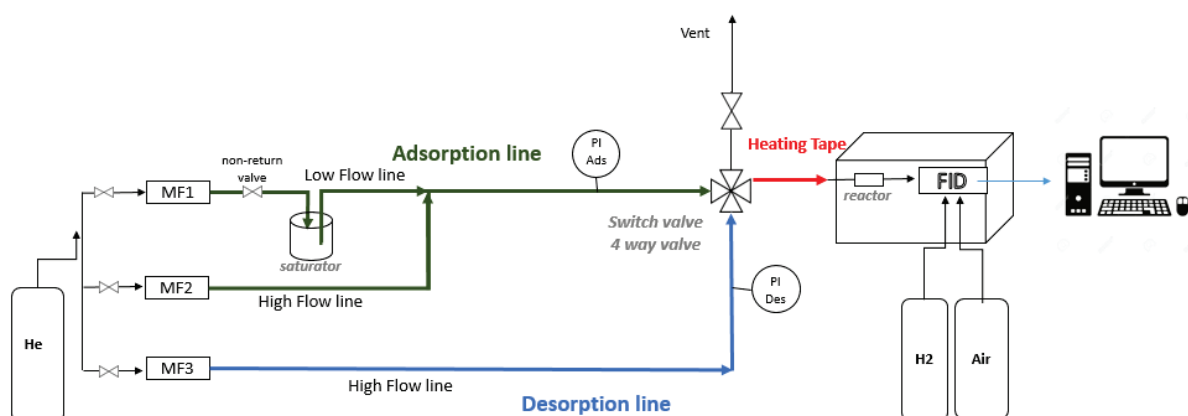


Figure 4 – Zero Length Column (ZLC) experimental set-up.

The ZLC cell, Figure 5, consists of a 1/8” Swagelok union. The sample of zeolite adsorbent is “sandwiched” between two porous nickel sintered disks with the same diameter, placed inside the Swagelok union. The sample is dispersed approximately as a monolayer to ensure good and homogenous contact with the purge gas stream, and a very thin disk is obtained. The cell is placed in a gas chromatograph oven (Agilent, 6850 Series GC system). The effluent stream is continuously monitored by a flame ionization detector (FID). The effluent concentration response is recorded after the valve switch to desorption.

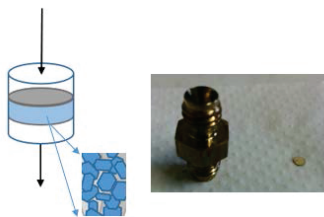


Figure 5 - ZLC cell and subsequent representation. The zeolite crystals are represented in blue.

2.4.2. Experimental procedures

When introducing a given sorbate into the unit, each stream must be previously flushed by high flow of He to eliminate any other sorbate traces or water adsorbed in the walls. Once the sorbate is placed in the bubbler, the lines must be flushed several hours, using already the flow parameters chosen for the experiments.

After introducing the zeolite sample into the reactor, and before starting the adsorption/desorption experiments, the zeolite sample must be activated by heating it in a pure He stream up to 300 °C, maintaining this temperature overnight. This procedure will guarantee that the zeolite porous network is practically free from adsorbed species. The procedure is generally called “**activation**”. Then, the sample is cooled to room temperature, always through He stream. The unit is ready to start the adsorption desorption runs.

Adsorption should start by leading the adsorption line into the ZLC cell. When adsorption reaches equilibrium the FID signal is constant for (~2h).

2.4.3. Data acquisition and processing

Following the equilibration step, desorption is started by switching the switch valve, so a pure He purge (desorption stream) feeds the ZLC cell. The concentration of sorbate species in the effluent stream is still followed continuously for a long period until complete desorption. The value of the FID signal (I) is proportional to the concentration of the sorbate in the effluent stream. The response curves were normalized to c/c_0 taking into account the offset signal of the FID (I_{inf}), equation 9.

$$\frac{c(t)}{c_0} = \frac{I - I_{inf}}{I_0 - I_{inf}} \quad 9$$

As shown in Figure 6, I_0 is the value of the FID signal at time zero (correspondent to the amount of sorbate of the adsorption line), I_{inf} is the offset signal of the FID. Also, for every run, data acquisition started approximately 0.10 min before the desorption step, i.e., 0.10 min before the switch in the valve (which gives time to the operator to start the FID data recording and get into position to press the switch valve). Therefore, the time scale had to be shifted each time in order to start at t_0 .

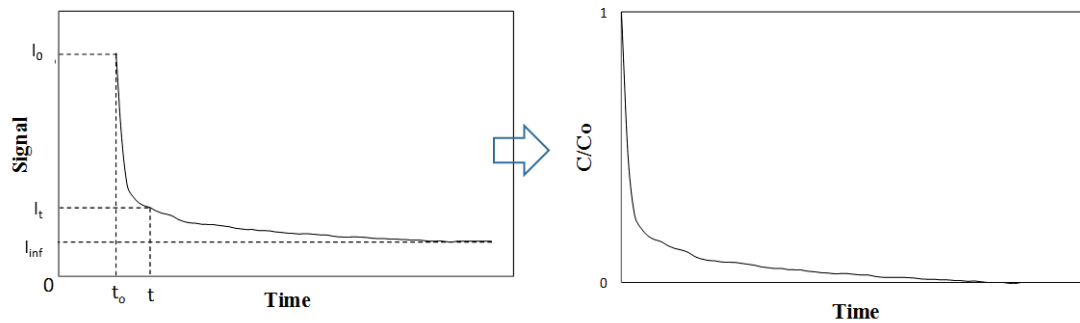


Figure 6 – Quantitative “raw” ZLC response (left side) and corresponding normalized response curve c/c_0 .

In the long time region, the desorption curve presents an asymptote. When applying the ZLC model for long time and high L_{ZLC} , the equation 7 describes this asymptote, from which we can obtain the “intercept” and “slope”, as shown in Figure 7. Knowing that L_{ZLC} and β are related by equations 4 and 5, we obtain D_{eff}/R^2 , the inverse of the **characteristic diffusion time $\tau = R^2 / D_{eff}$** .

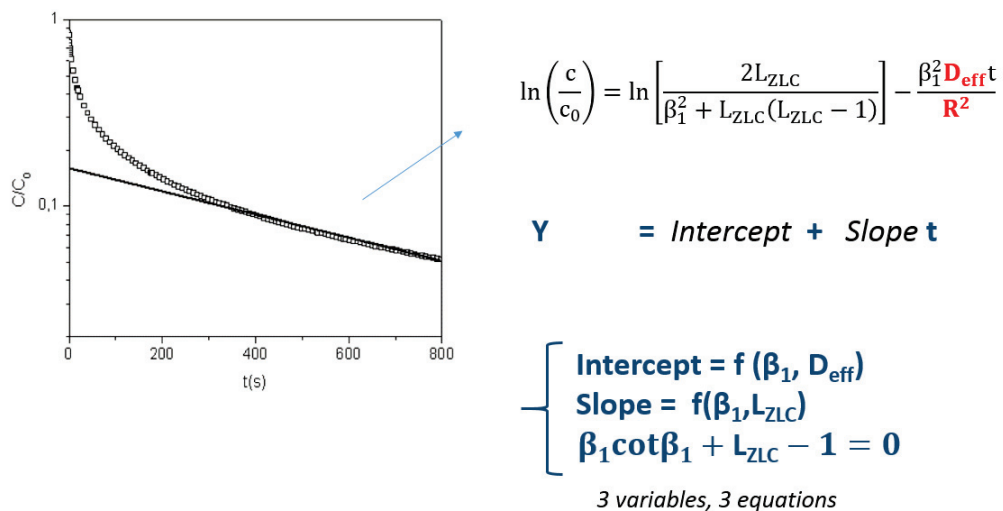


Figure 7 – Data treatment using ZLC model for long times and high flows.

As mentioned before, the **effective diffusion coefficient D_{eff}** can be calculated if R is known. In this case, **R is radius of the zeolite particle (if the particle has spherical shape).**

Generally, most zeolite crystals do not possess a spherical shape and **R can be estimated from the radius of the sphere with the same volume as the volume of the real zeolite particle**. For this, SEM or TEM images of the zeolite samples are required, to verify if the particle size distribution is homogeneous, and to measure the dimensions of the zeolite particles. The more different the zeolite particle is from a spherical shape, the bigger the error of R, hence, the bigger the error of D_{eff} coefficient. Generally, bulk zeolites with geometry close to a spherical particle, and a homogeneous particle size distribution are good candidates and the error on D_{eff} can be minimized.

For each system “sorbate – adsorbent”, the desorption curves are recorded at different temperatures. If the desorption is diffusion controlled, the diffusion coefficient is known to be temperature activated according to the Arrhenius relationship:⁴

$$D_{eff} = D_0 \exp\left(-\frac{E_d}{R_{gas}T}\right) \quad 10$$

Where E_d is the **effective diffusion energy**, D_0 accounts for the pre-exponential factor of the Arrhenius form, R_{gas} is the perfect gas constant and T is the temperature.⁴

2.4.4. Sensitivity analysis

A sensitivity analysis of the unit was carried out in order to make sure that the ZLC response was independent from the system (i.e. which unit parameters could have an effect of the D_{eff} parameter), and to determine the effects of process on the desorption response. In the “Annexes-Chapter IV” the sensitivity analysis is presented in detail, so the reader can analyze the effect of each parameter in the desorption signal.

One of the main issues studied, was the “switch” moment or t_0 moment. When the valve switches from adsorption stream to desorption stream, desorption starts, and therefore the signal should decrease as the concentration of probe molecule decreases, Figure 6. However, during the “switch” moment, the signal presented some wave shaped “fluctuations”, which intensity was found to be proportional to the pressure drop, see Figure 8 and Figure 9. This wave shaped fluctuation would last for at least 0.4 min with a very high wave amplitude “ ΔI ”. One of the main objectives was to decrease this fluctuation as much as possible and having a signal as close as possible to the “ideal” signal. The pressure drop was

varied by changing the amount of sample, the granulometry of the sample and its packing. The amount of sample was the parameter with the highest impact. An amount of 3 mg of sample was found to be a maximum to get a fluctuation of less than 0.01 min.

The t_0 was chosen as the maximum of the first peak. The sensitivity analysis also showed that the presence of the perturbation during the switch and the t_0 choice has little impact on t_0 the D_{eff} estimation.

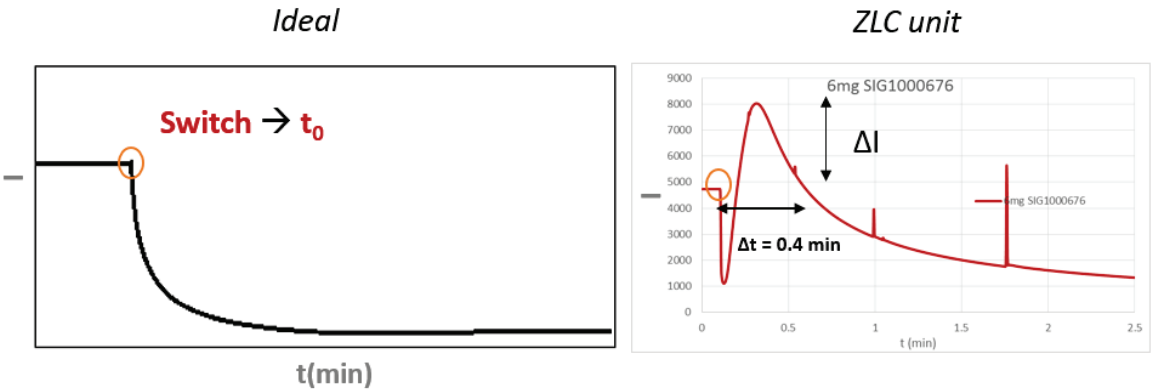


Figure 8 - Ideal ZLC response (left) and « raw » ZLC response before optimization, using 6mg of zeolite (right). The orange circle represents the “switch” moment, i.e., the t_0 : moment where the inlet feed is pure He and desorption starts. Black arrows point out the size of the perturbation of the signal.

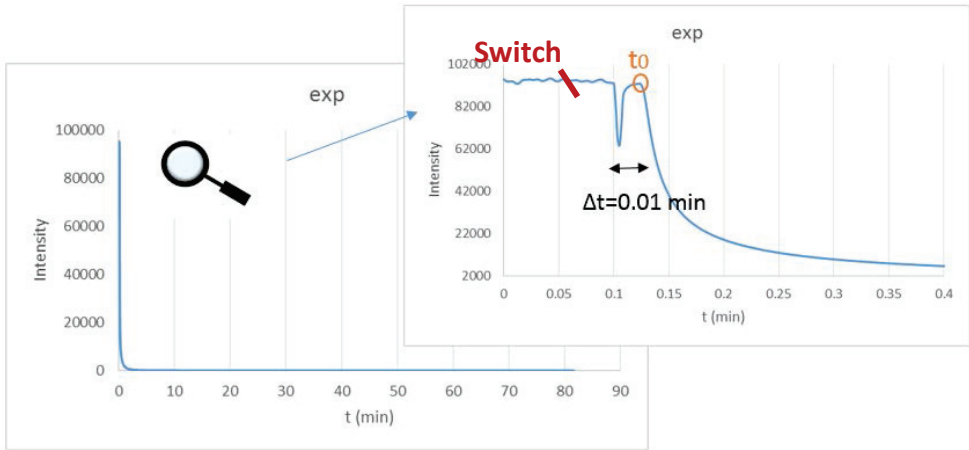


Figure 9 –“Raw” ZLC response after ZLC unit and process parameters optimization (left), zoom of the graphic during switch. The orange circle represents t_0 chosen for the data treatment, which is 0.01 min after the switch moment.

3. Characterization and comparison of reference bulk and hollow zeolites

Reference bulk and hollow zeolites were characterized in order to support the hypothesis that they have similar physico-chemical properties.

- XRD to check for any extra crystalline phases besides ***BEA** and **MFI**;
- N₂ isotherms for determination of V_{micro}, V_{meso}, BET surface;
- Chemical analysis to determine Si/Al and Na/Al;
- Adsorption isotherms of toluene and cyclohexane in order to compare the adsorption characteristics;
- SEM & TEM images: obtain the crystal size distributions, crystal shapes, and wall thickness, and determine the diffusion path length L, (which also corresponds to R parameter from the ZLC model, in the case of bulk crystals);

3.1. Silicalite-1 systems

HollowSil1 was synthesized according to previous works carried out at IRCELYON.^{19,20} The synthesis procedure essentially consists in the dissolution - recrystallization method already described in the literature and in the chapter I of this thesis, using a bulk silicalite-1 crystals as parent zeolite. The **BulkSil1** used for this study corresponds to the parent bulk crystal used to synthesize the hollow silicalite-1 crystals.

XRD data shows that both samples are highly crystalline with the **MFI** type structure with no extra crystalline phases (similarly to XRD presented in the references).

Similarly to BulkSil1, HollowSil1 is pure Si zeolite, as no Al sources were added during the synthesis.

TEM images of the synthesized BulkSil1 and HollowSil1 are shown in Figure 10 and Figure 11. Both samples are homogeneous in size, and they present an external morphology similar to a regular hexagon with a smooth surface. The crystal sizes for BulkSil1 and HollowSil1 are approximately 150 nm and 180 nm respectively. It must be noted that TEM images revealed that for the hollow samples, 20-30% of the crystals presented several inner cavities, denoted here as *multi-hollow crystals*, Figure 11 image b). Note that we do not know about the connectivity of these cavities, if they are isolated or connected.

The mean diffusion length, L_B for bulk and L_H for hollow, can be estimated from the TEM images. Assuming BulkSil1 as sphere, the diffusion path length can be admitted as the

radius of the sphere with the equivalent volume, in which $L_B \sim 70$ nm. For the Hollow samples, the mean diffusion length L_H is the zeolite wall that varies between 30 and 50 nm.

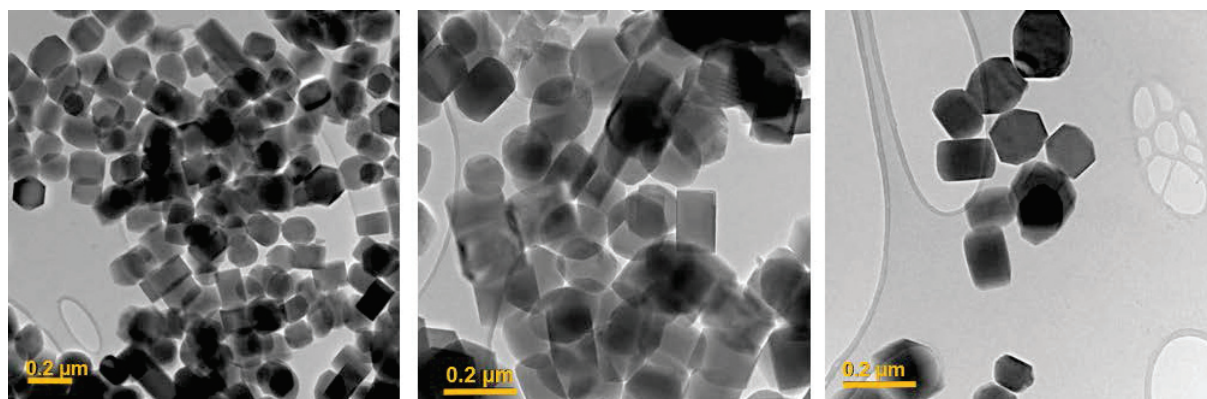


Figure 10 - TEM images of BulkSil1.

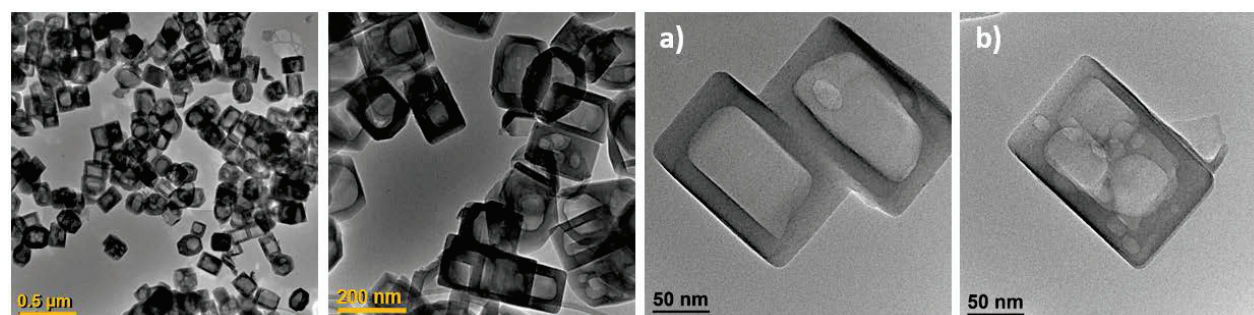
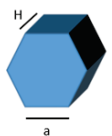
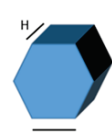


Figure 11 – TEM images of HollowSil1.

Table 1- BulkSil1 and HollowSil1 particle size, morphology characterization and mean diffusion length.

Sample name	BulkSil1	HollowSil1								
External morphology and dimensions	 <table border="1"> <tr> <td>H</td> <td>98 nm</td> </tr> <tr> <td>a</td> <td>75 nm</td> </tr> </table> <p>Regular hexagon</p>	H	98 nm	a	75 nm	 <p>Wall thickness: 30 nm – 50 nm (20-30% are multihollow)</p> <table border="1"> <tr> <td>H</td> <td>120 nm</td> </tr> <tr> <td>a</td> <td>92.5 nm</td> </tr> </table> <p>Regular hexagon</p>	H	120 nm	a	92.5 nm
H	98 nm									
a	75 nm									
H	120 nm									
a	92.5 nm									
L	Radius of the sphere with the same volume 70 nm	Wall thickness 30-50 nm								

Nitrogen adsorption/desorption isotherms of the considered samples are shown in Figure 12. BulkSil1 presents a type I adsorption branch at low pressure, which is typical of a microporous material. HollowSil1 also present a Type I adsorption branch, confirming the microporous nature of the zeolite walls and it presents a desorption branch with a hysteresis, which has been associated with condensation phenomena in the inner cavity. Adsorption data

of the samples are summarized in Table 2, showing that both samples present very similar textural properties, with high microporous volume and BET surface, and small mesoporous volume.

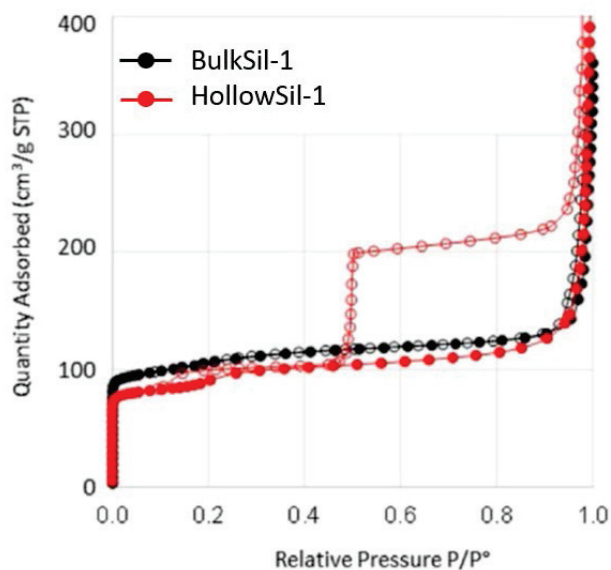


Figure 12 – N_2 adsorption isotherms of BulkSil1 and HollowSil1, according to Laprune et al.¹⁹

Table 2 – Textural properties of the samples BulkSil1 and HollowSil1, according to Laprune et al.¹⁹

Sample name	BulkSil1	HollowSil1
Isotherms type according to IUPAC	Type I	Type I + hysteresis
BET [m^2/g]	390	328
V_{micro} [cm^3/g]	0.13	0.12
V_{meso} [cm^3/g]	0.07	0.08

Toluene adsorption isotherms were measured for toluene for BulkSil1 and HollowSil1 to compare the physical interactions with hydrocarbon substrates. The adsorption isotherms exhibit similar adsorption tendency. HollowSil1 shows lower capacity as reflected by the lower microporous volume.

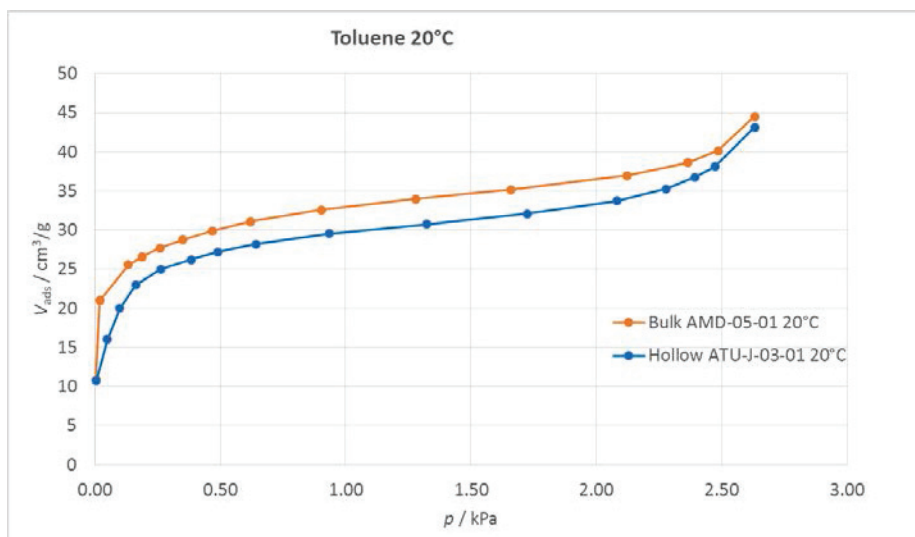


Figure 13 – Adsorption isotherms of toluene on BulkSil1 and HollowSil1 at 20°C.

The previous characterizations led to the conclusion that BulkSil1 and HollowSil1 have similar physical-chemical properties: same composition, similar crystal size, mainly microporous solids and similar adsorption behaviors. Therefore, it seems reasonable to assume that D_{eff} of HollowSil1 will be similar to D_{eff} of BulkSil1.

3.2. Beta systems

Regarding the Beta zeolite, three samples were synthesized for the ZLC studies, two bulk Beta crystals, **Bulk1Beta**, **Bulk2Beta**, and one hollow Beta crystal, **HollowBeta**.

The hollow sample was synthesized according to the synthesis presented in chapter III (“CIT-6 Dissolution – Recrystallization” approach). Contrarily to the silicalite-1 samples, we could not use the parent zeolite of the HollowBeta as the correspondent bulk Beta, once this is a zincosilicate CIT-6 and not an aluminosilicate. Instead, we have searched in the literature for bulk zeolite Beta with physical/chemical characteristics similar to those of HollowBeta: purely microporous crystal, similar Si/Al ratio, similar crystal size, similar external morphology, and similar synthesis (taking into account the same reactants). We have not found a Beta zeolite that could agree with all the criteria presented above. Instead, two other bulk Beta zeolites were synthesized, Bulk1Beta and Bulk2Beta, that could agree with some of the criteria presented above (synthesis details in chapter II).

It is important to note that the three samples were ion exchanged with NaCl twice. The issue was to avoid chemical reactions during diffusion tests, by exchanging the proton by

Na cation. Indeed, diffusivity studies over large molecules can be perturbed by the specter of catalytic activity. Ruthven and Kaul²¹ used NaX for the study of aromatics, to deactivate the Brønsted sites, and even in this case there was evidence of reaction for triethylbenzene, for example.¹⁷ Catalytic activity would jeopardize the ZLC measurements.

XRD data shows that the samples possess highly crystalline *BEA type structures, with no extra crystalline phases (see Annexes). TEM and SEM images of the three samples are shown in Figure 14. HollowBeta has a truncated octahedral morphology, pine tree shaped on each side, and a crystal size of 1.15 μm , Figure 14 and Table 3. It must be noted that approx.10% of the hollow crystals were found “broken” into pieces, probably due to the ion exchange with NaCl. Bulk1Beta seems to be composed by a compact aggregation of nanocrystals, egg shaped, and whose surface is rough. The average crystal size is 1.2 μm . Bulk2Beta has the same external morphology as HollowBeta, however the crystal are smaller, with an average crystal size of 0.6 μm . Chemical analysis shows that the Na content is similar for the 3 samples. HollowBeta and Bulk1Beta have approximately the same Si/Al (between 9 and 11), and Bulk2Bulk has fewer Al content, with Si/Al = 22.

Once again, the mean diffusion length, L , can be estimated from the SEM and TEM images. The diffusion path length for Bulk1Beta can be admitted as the radius of the sphere with the equivalent volume. Considering the Bulk1Beta with an ellipse shape with the average measurements listed in Table 3, then $L_B \sim 0.49 \mu\text{m}$. Assuming Bulk2Beta as sphere, the diffusion path length can be admitted as the average radius, in which $L_B \sim 0.33 \mu\text{m}$. For the Hollow sample, the mean diffusion length L_H is the zeolite wall, $\sim 150 \text{ nm}$.

Nitrogen adsorption/desorption isotherms of the considered samples are shown in Figure 15. Both bulk samples present a Type I adsorption branch, proving that the crystal is mainly microporous. HollowBeta also present a Type I adsorption branch, confirming the microporous nature of the zeolite walls, but it also presents a desorption branch with a hysteresis, which has been associated with condensation phenomena in bottle neck pores, as discussed in Chapter III. Some pore structure parameters are listed in Table 4, the three samples present high V_{micro} and S_{BET} , even though Bulk1Beta presents the smaller S_{BET} . V_{meso} are small and approximately the same for the three samples.

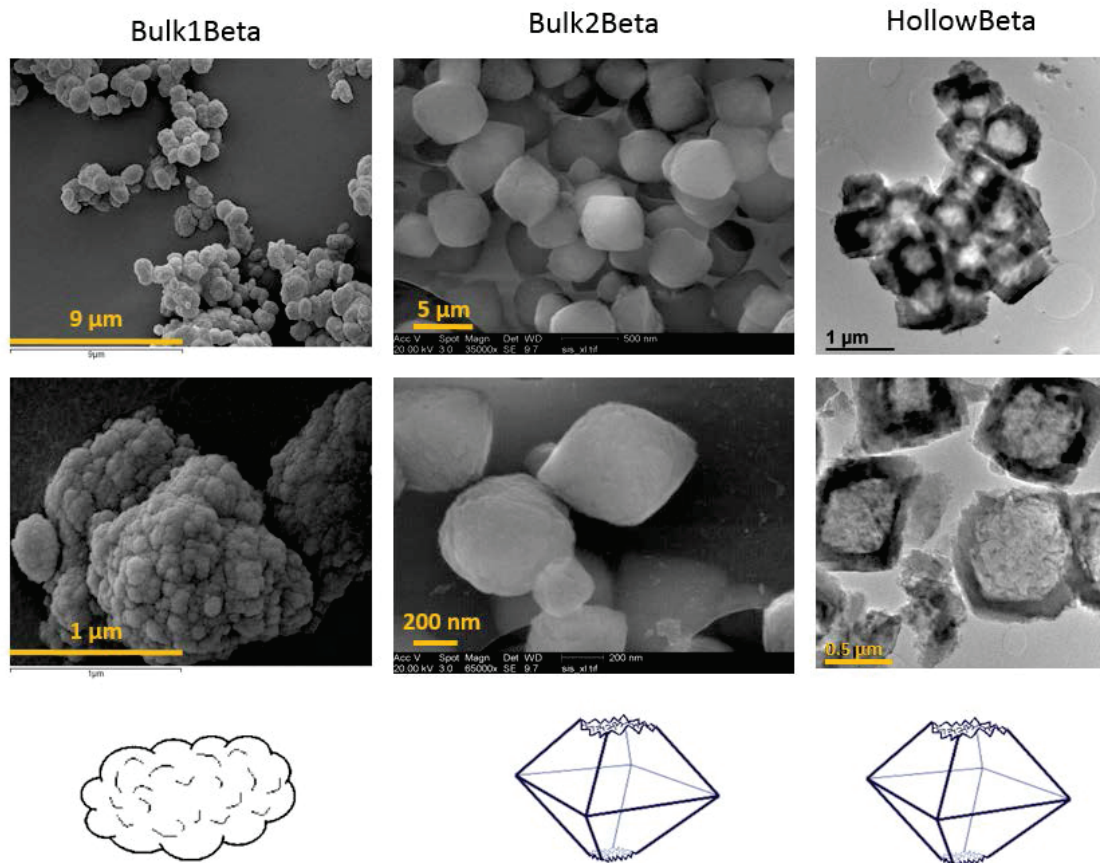


Figure 14 – Electronic microscopic images of the three Beta samples, Bulk1Beta, Bulk2Beta and HollowBeta, and the respective external morphology representations below.

Table 3 - Particle size and morphology characterization for Bulk1Beta, Bulk2Beta and HollowBeta. Si/Al and Na/Al values respectively.

	Bulk1Beta	Bulk2Beta	HollowBeta
External morphology and dimensions	Ellipse Shape R1: 0.443 μm R2: 0.606 μm  Average crystal size: 1.2 μm	Spherical Shape  Average crystal size: 0.6 μm	 Average crystal size: 1.15 μm Wall size: 150 nm
L	Radius of the sphere with the same volume 0.49 μm	Average radius 0.33 μm	Wall size 150 nm
Si/Al (ICP)	10.9	~22.1	8.7
Na/Al (ICP)	0.5	0.4	0.7

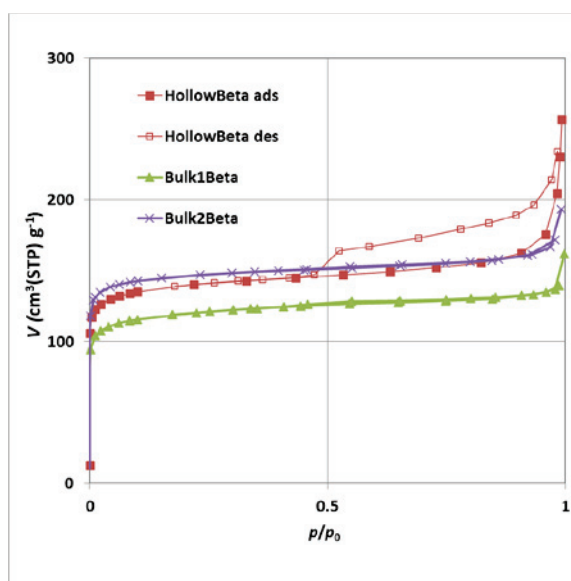


Figure 15 - N_2 adsorption isotherms of Bulk1Beta, Bulk2Beta and HollowBeta.

Table 4 - Textural properties of the samples Bulk1Beta, Bulk2Beta and HollowBeta.

Sample	Isotherm type	BET [m^2/g]	V_{micro} [cm^3/g]	V_{meso} [cm^3/g]
Bulk1Beta	Type I	500	0.15	0.06
Bulk2Beta	Type I	564	0.18	0.06
HollowBeta	Type I + hysteresis	542	0.16	0.09

Adsorption isotherms were measured for cyclohexane on the three Beta samples at 80 °C, Figure 16. The three samples present a type I adsorption isotherms, exhibiting similar adsorption tendencies. The values of Henry's constant were calculated and are presented in Figure 16. The Henry's constants of Beta samples are in the order Bulk2Beta < Bulk1Beta < HollowBeta, and increase with the Al content. Similar behavior was observed for NaX zeolites, where higher Henry constants were measured for zeolites with higher Al content, hence interaction is stronger.²²

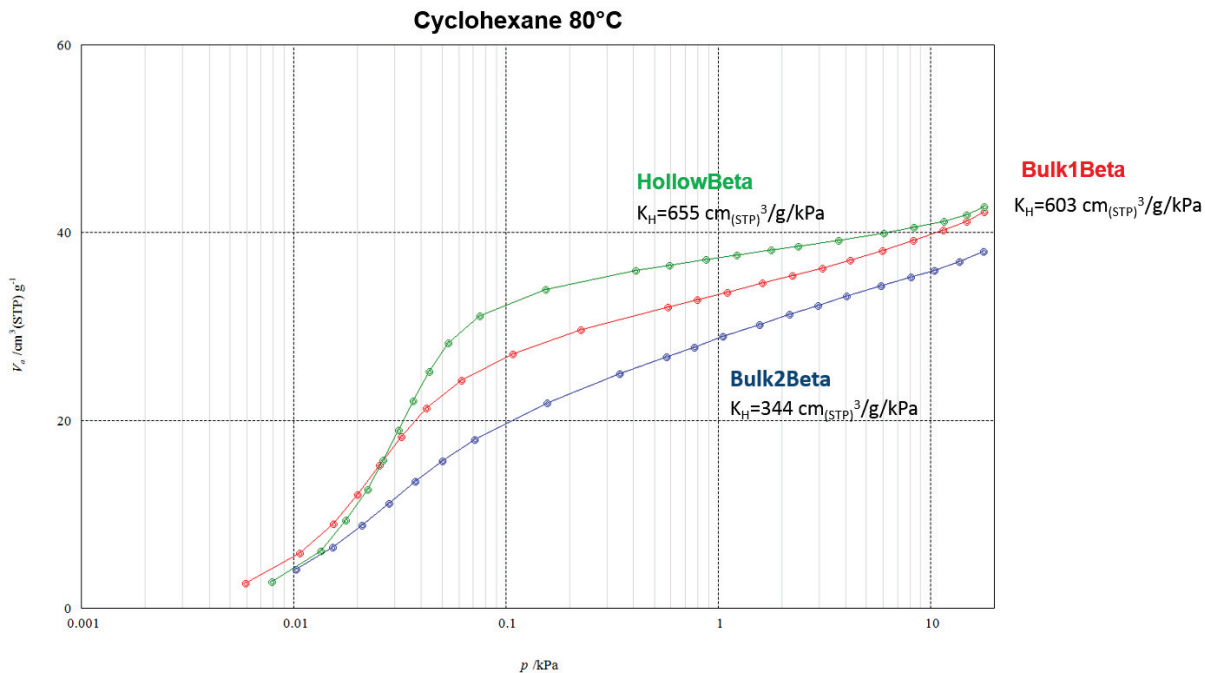


Figure 16 – Adsorption isotherms of cyclohexane on Bulk1Beta, Bulk2Beta and HollowBeta at 80 °C.

Considering the previous analysis, we can conclude that:

- HollowBeta and Bulk1Beta have similar crystal size, composition, adsorption behavior and they are both mainly microporous. However, the two samples have different external morphologies;
- HollowBeta and Bulk2Beta have the same external morphology, similar crystal size and they are mainly microporous. However Bulk2Beta has higher Si/Al and hence different adsorption properties.
- Bulk1Beta and Bulk2Beta are both bulk zeolites, with similar V_{meso} and V_{micro} , and similar crystal size, but they present different composition (Al content), and different external morphologies.

4. ZLC results

Figure 17 and Figure 18 display the ZLC response curves and fitting curves at different temperatures for silicalite-1/toluene and Beta samples/cyclohexane couples. For both systems, the fitting lines have an excellent agreement with the experimental data. The Arrhenius plots for for toluene and silicalite-1 sample and cyclohexane and Beta samples are presented in Figure 19 Figure 20 respectively.

System 1: silicalite-1 & toluene

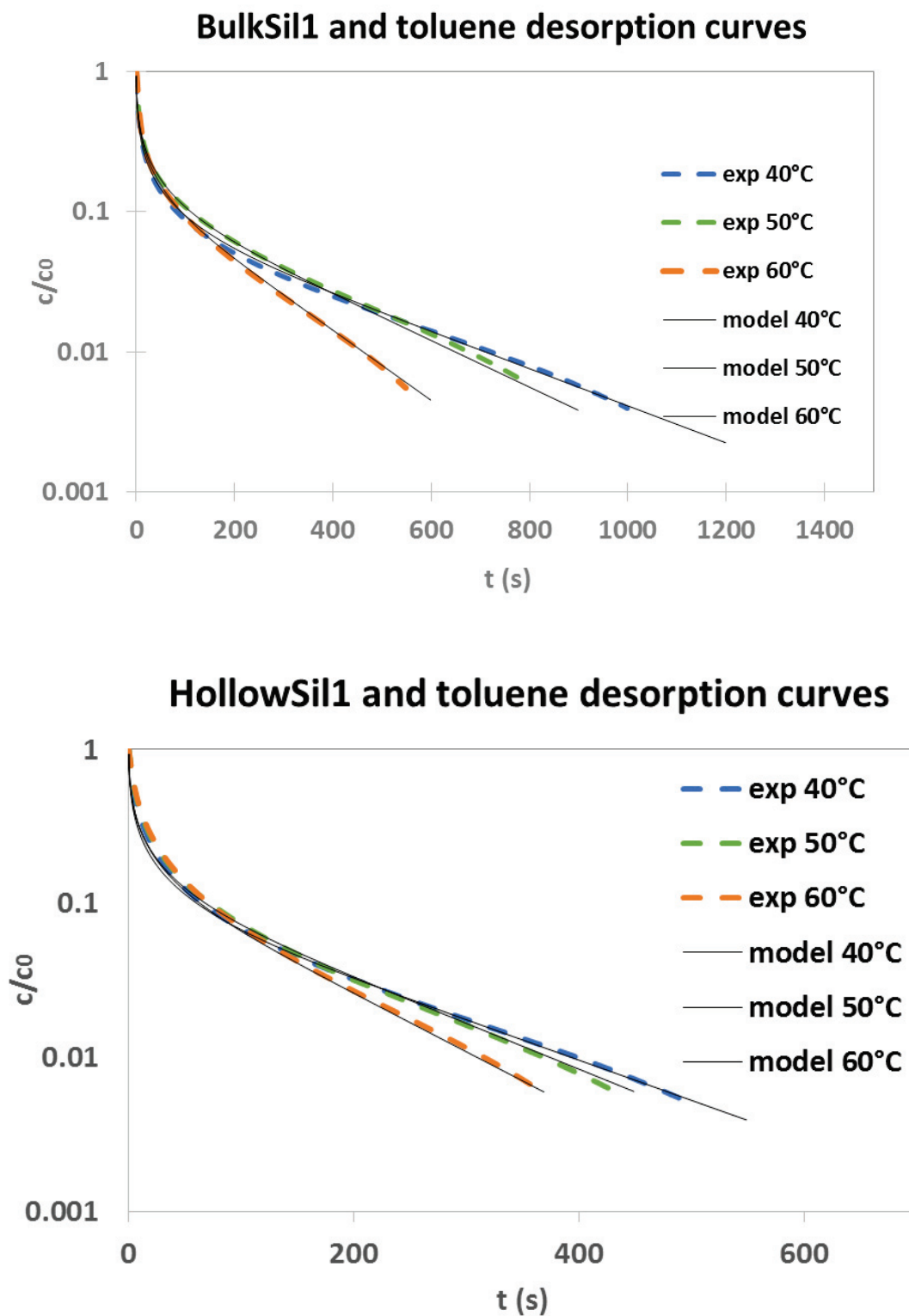
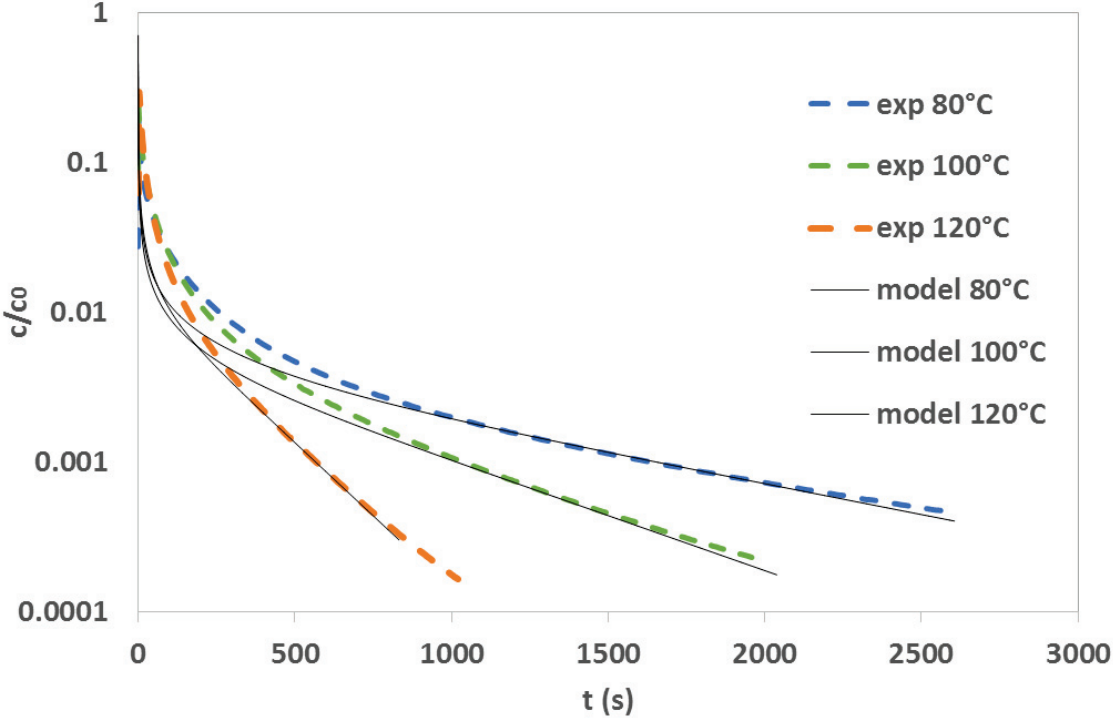
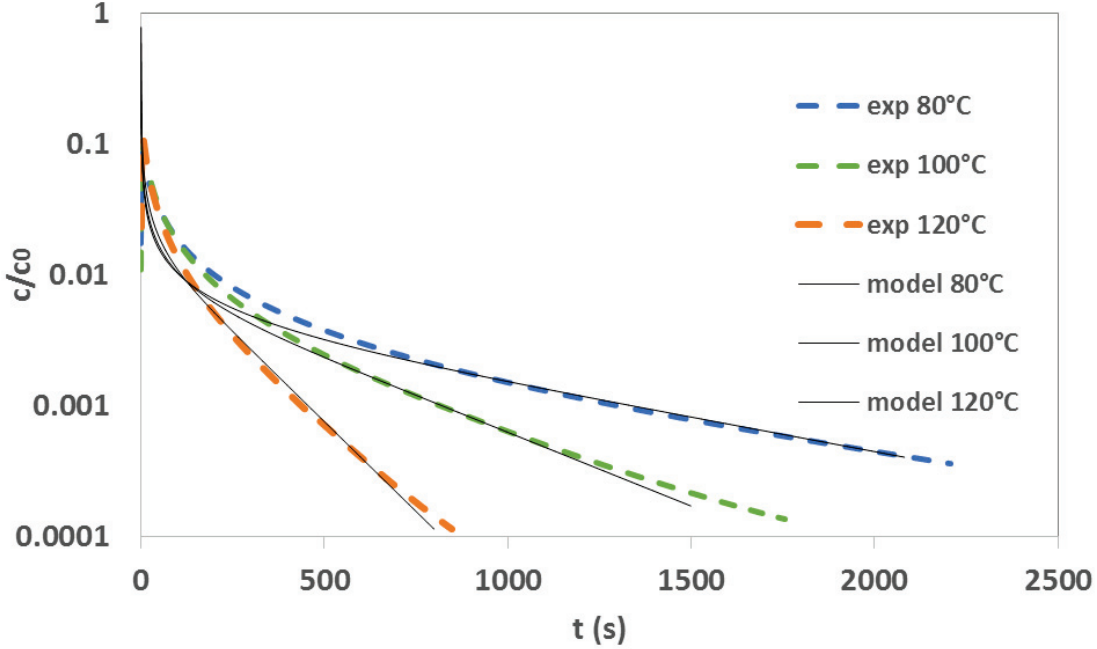


Figure 17 – Experimental data (dashed line) and theoretical ZLC curves (lines) for toluene in silicalite-1 samples at different temperatures.

Bulk1Beta and cyclohexane desorption curves



Bulk2Beta and cyclohexane desorption curves



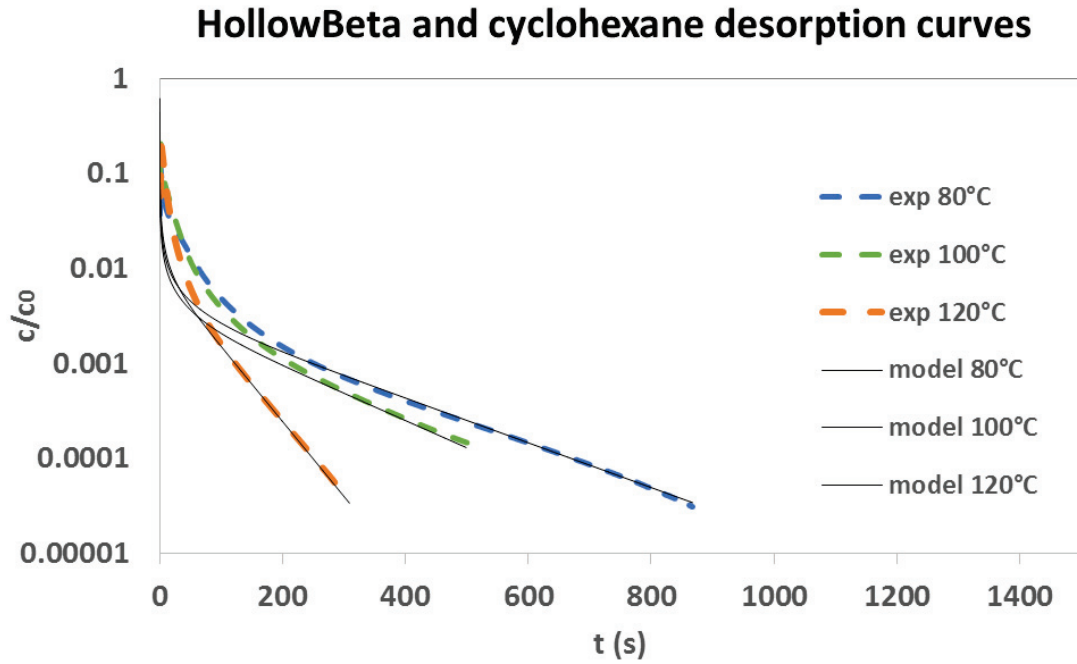


Figure 18 - Experimental data (dashed line) and theoretical ZLC curves (lines) for cyclohexane in Beta samples at different temperatures

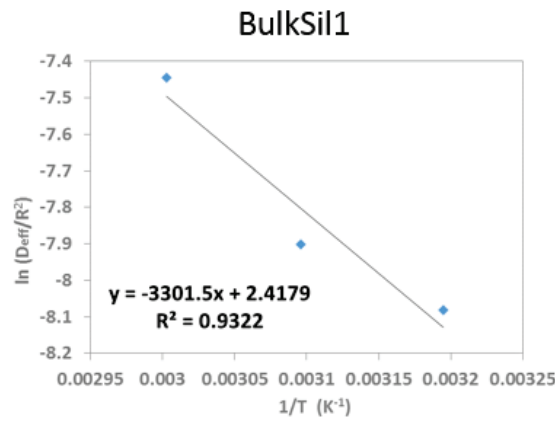


Figure 19 - Arrhenius plots for toluene and silicalite-1 sample.

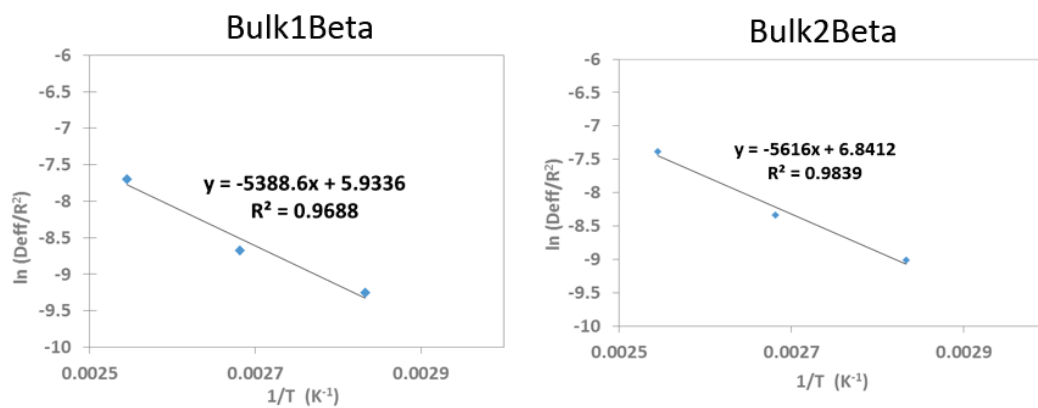


Figure 20 - Arrhenius plots for cyclohexane and Beta sample.

Table 5 and Table 6 present the diffusion parameters extracted from the theoretical fitting, such as L_{ZLC} values and the characteristic diffusion time ($\tau = R^2/D_{eff}$), as well as the energy of diffusion E_d . All L_{ZLC} values are greater than 10, showing that the processes are indeed in the diffusion controlled regime.⁴

Table 5 – Fitting data for toluene on silicalite-1 samples

Sample	T(°C)	L_{ZLC}	$\tau = R^2/D_{eff}$ (s)	E_d (kJ/mol)
BulkSil1	40	24	3236	27.4
	50	17	2703	
	60	14	1712	
HollowSil1	40	19	1645	-----
	50	16	1445	
	60	14	1134	

Table 6 - Fitting data for cyclohexane on Beta samples

Sample	T(°C)	L _{ZLC}	$\tau = R^2/D_{\text{eff}}$ (s)	E _d (kJ/mol)
Bulk1	80	427	10460	44.8
	100	365	5848	
	120	158	2193	
Bulk2	80	401	8197	46.7
	100	239	4167	
	120	113	1613	
Hollow	80	533	1822	-----
	100	570	1495	
	120	218	544	

4.1. Estimations of D_{eff} and R

Data analysis can be carried out by two different ways:

- 1) **Assuming that R is known, then D_{eff} can be estimated.** As mentioned before, this requires that the zeolite crystals in study have a homogeneous shape and size and a morphology as close as possible to the spherical morphology. In this case, an average crystal volume can be calculated and R will correspond to the radius of the sphere with an equivalent volume. In this case, we are assuming a spherical geometry, which is a proper assumption considering bulk zeolites with similar geometries. This is the general assumption found in the literature for **bulk zeolites**, and also on this thesis.
- 2) In the case of more complex geometries (as the **hollow** geometry), **the equivalent R** is unknown regarding a radius sphere, and therefore we cannot accurately determine D_{eff} , (that will be highly dependent of the chosen R value). When assuming that D_{eff} is the same for bulk and hollow zeolites, we can estimate the ratio of both R_{H} and R_{B} from the ratio of τ_{H} and τ_{B} . In order to pose that D_{eff} is the same for hollow and bulk crystals, the crystals shall show very similar physico-chemical properties: same zeolite structure, textural properties, adsorption properties etc.

4.1.1. Estimation of D_{eff} for bulk samples

The calculation of D_{eff} is highly dependent of the R value which can be modeled as the **radius of the sphere with the same volume as the particle volume, similarly to the L values already determined** in Table 1 and Table 3. For the case of the BulkSil1, the real average volume was determined admitting a regular hexagon, Table 1. Bulk1Beta was assumed to be an ellipse and real volume was determined measuring the two diameters, Table 3. Bulk2Beta real volume was determined assuming a spherical geometry, and measuring the average crystal radius. The respective R values were determined for the different average volumes.

Table 7 and Table 8 present the R , D_{eff} and E_d values for the bulk reference samples.

Table 7 – Diffusion constant D_{eff} and E_d for toluene and BulkSil1.

Sample	T(°C)	R (nm)	D_{eff} (m ² /s)	E_d (kJ/mol)
BulkSil-1	40	70	1.51×10^{-18}	27.4
	50		1.81×10^{-18}	
	60		2.86×10^{-18}	

Table 8 - Diffusion constant D_{eff} and E_d for cyclohexane and Bulk1Beta and Bulk2Beta.

Sample	R (nm)	T(°C)	D_{eff} (m ² /s)	E_d (kJ/mol)
Bulk1Beta	492	80	2.31×10^{-17}	44.8
		100	4.14×10^{-17}	
		120	1.10×10^{-16}	
Bulk2Beta	327	80	1.30×10^{-17}	46.7
		100	2.57×10^{-17}	
		120	6.63×10^{-17}	

The study of the sorption kinetics of toluene in **MFI** zeolites by ZLC technique has already been reported in the literature by Zhao *et al.*^{11,12} at higher temperature range, from 80 °C to 120 °C. In order to allow comparison, we estimated the values D_{eff} coefficients for 80 °C, 100 °C, and 120 °C, using our estimated E_d of BulkSil1, Table 9.

According to our data, D_{eff} are in the order of 10^{-18} for the temperatures of 80, 100 and 120 °C, which are about two orders of magnitude smaller than the values of Zhao *et al.* It must be noted that Zhao *et al.* used ZSM-5 crystals (**MFI** type) with Si/Al=18 and with an average diameter of 2 µm, whereas in this study we use silicalite-1 crystals (pure SiO₄ structure) of an average diameter of 0.15 µm. The difference may arise of the different composition and/or the difference in crystal size. However, the activation energy of diffusion E_d found in our system, 27 kJ/mol (see Table 7) is consistent with the E_d found by Zhao *et al.* (26-21 kJ/mol), which reassures the validity of our results in the case of silicalite-1 samples.

Table 9 – Diffusion coefficients measured in this study, and predicted for 80, 100 and 120 °C using the E_d . Diffusion coefficients found for Zhao *et al*¹¹

T°C	[Our study]	[Zhao <i>et al</i>]
	D_{eff} [m ² /s]	D_{eff} [m ² /s]
40	1.51×10^{-18}	-----
50	1.81×10^{-18}	-----
60	2.86×10^{-18}	-----
80	4.79×10^{-18}	1.51×10^{-16}
100	7.90×10^{-18}	2.42×10^{-16}
120	1.24×10^{-17}	3.75×10^{-16}

Regarding cyclohexane transport in Beta zeolite, there are no available ZLC studies over Beta zeolite in the literature. Instead there are several kinetic ZLC studies of cyclohexane in **MFI** type zeolite. As the pore size of **MFI** (0.54 - 0.56 nm) is slightly smaller than ***BEA** zeolite (0.66 - 0.75nm), one can expect that D_{eff} smaller for **MFI** type zeolite, but in same order of magnitude (or close). Indeed the E_d found in the literature for cyclohexane through **MFI** zeolite type by ZLC technique (38-56 kJ/mol)^{4,6,7,23,24} is comparable to the E_d found for bulk Beta zeolites, (45-47 kJ/mol).

The values of D_{eff} for cyclohexane in **MFI** available in the literature are compared with D_{eff} obtained in our study, Figure 21. We can observe major discrepancies of the D_{eff} values for cyclohexane in **MFI** zeolites in the literature, Figure 21. Although the effect of different Si/Al ratio cannot be ruled out, it appears that a correlation exists between D_{eff} values and the crystal size. For “small crystals” ($R < 0.1 \mu\text{m}$), D_{eff} are smaller whereas for “large crystals”, ($R > 2 \mu\text{m}$) D_{eff} are larger by orders of magnitude. In our study, Bulk1Beta and Bulk2Beta (that have a $R = 0.49 \mu\text{m}$ and $R = 0.33 \mu\text{m}$ respectively) present D_{eff} coefficients that fall into the range of **MFI** crystals of approximately the same size, (see Figure 21), namely the **MFI** zeolites of Teixeira *et al.* and Li *et al.* (triangles) which have a Si/Al of 18 and 30 respectively.

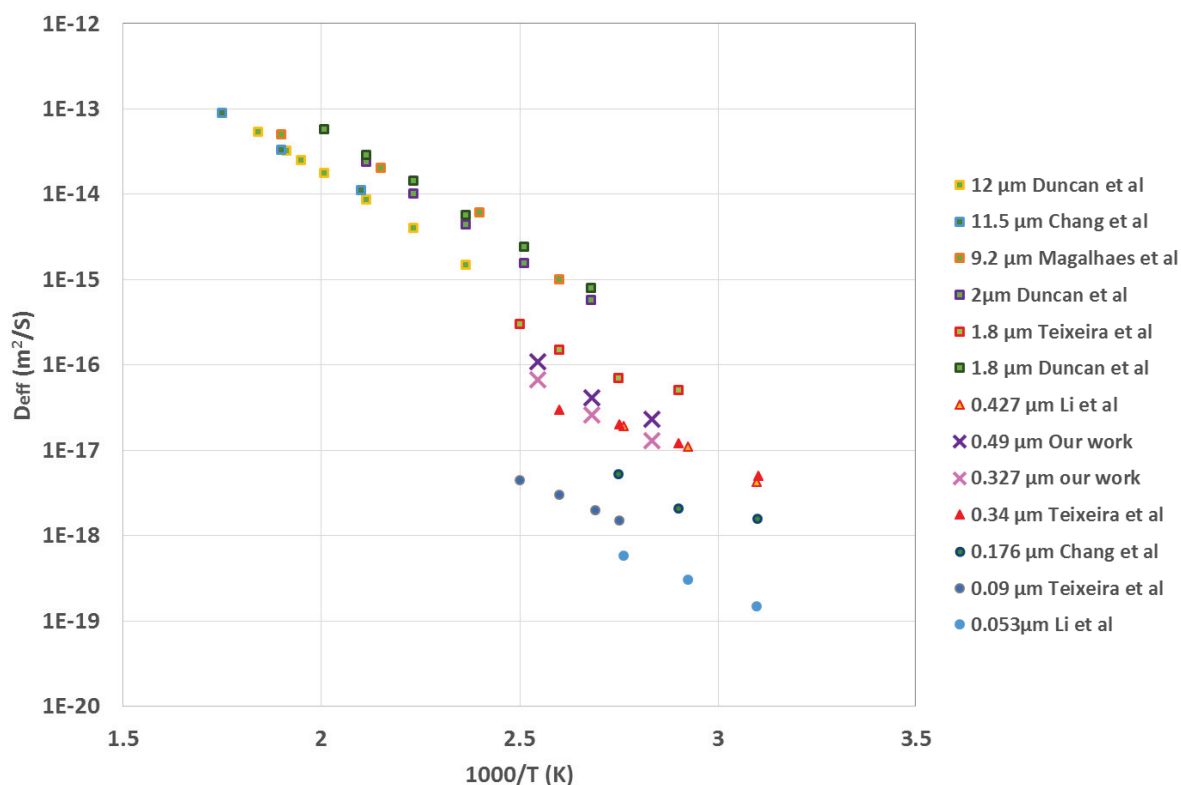


Figure 21 – Diffusion coefficients for cyclohexane in **MFI** found in the literature (circles, squares and triangles) and diffusion coefficients calculated in this study for cyclohexane in bulk Beta samples (“x” symbols). The legend presents the authors of each study but also the R assumed for each **MFI** sample.

4.1.2. Comparison of bulk vs hollow samples

The characteristic diffusion times (τ) for the hollow zeolites are always considerably inferior to the correspondent bulk zeolite, Table 5 and Table 6, where characteristic diffusion time was approximately 34-50% smaller for HollowSil1, and 64-78% smaller for HollowBeta. This is reflected in the faster desorption curves for hollow zeolites in the two cases silicalite-1 and Beta samples, for which hollow samples concentration of sorbate would reach approximately zero before than for the correspondent bulk zeolites, see Figure 22.

When comparing the diffusion parameters and desorption curves obtained for Bulk1Beta and Bulk2Beta, it is interesting to note that these two samples present similar D_{eff} coefficients and E_d (Table 8). These results indicate that the diffusion process is basically the same for the two bulk Beta samples, despite the slight differences in composition and external morphology. Hence, the observed much lower characteristic diffusion time τ for the hollow Beta cannot account for differences in the composition nor in the external morphology.

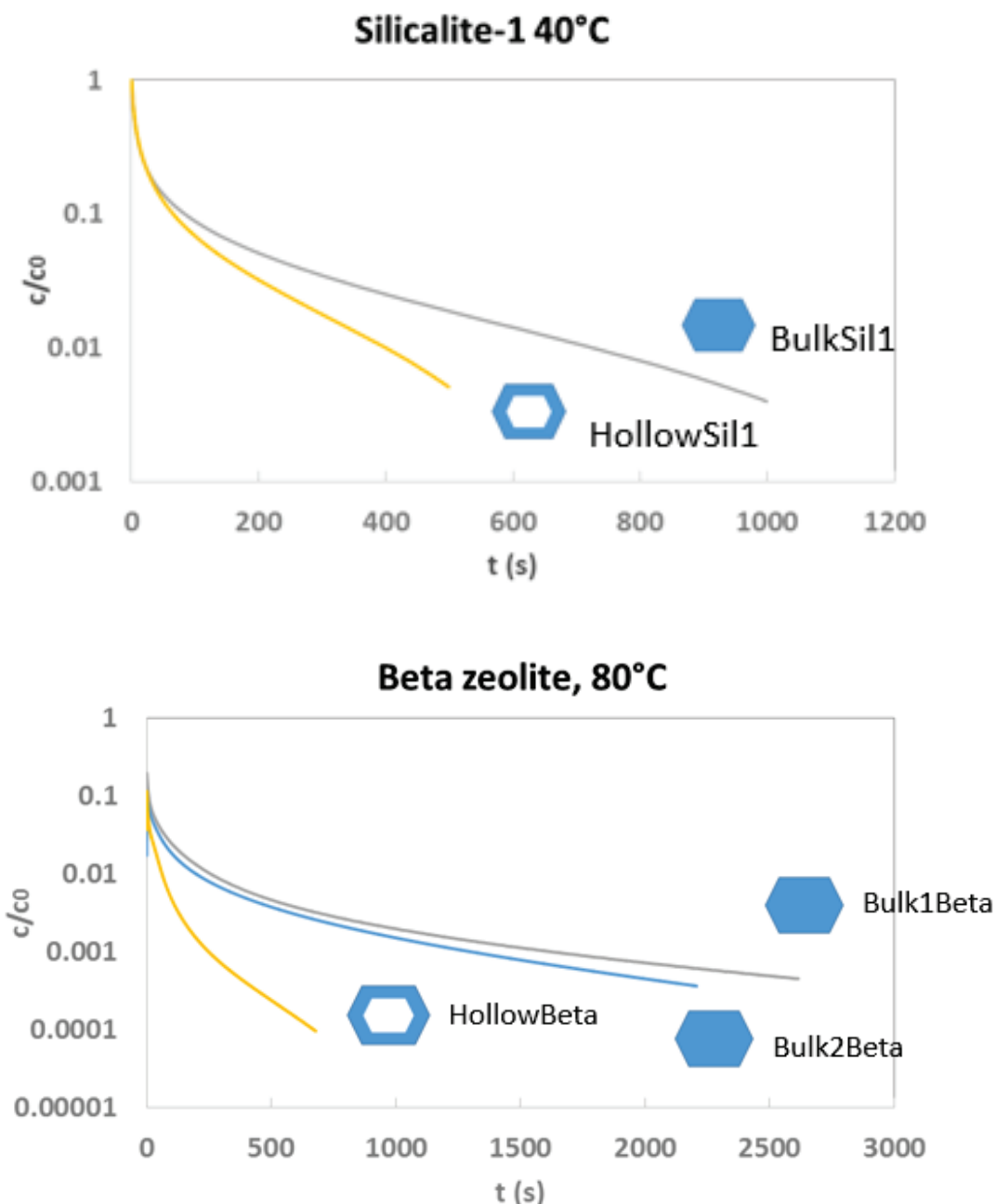


Figure 22 - Experimental data for toluene in silicalite-1 samples at 40 °C, and experimental data for cyclohexane in Beta samples at 80 °C.

Novruzova *et al.*² are the only example in the literature that studies the impact of a hollow structure in diffusion, using a different sorbate and a different technique from the one of the present thesis. The authors studied the sorption kinetic of isooctane in the exact same bulk and hollow silicalite-1 samples of this thesis and other bigger bulk and multi-hollow silicalite-1 crystals, by comparing the up-take curves obtained by in situ diffuse reflectance FT-IR spectroscopy. When comparing the big bulk silicalite-1 crystals and the big silicalite-1 multi-hollow crystal (with several internal cavities), the multi-hollow crystal presented a faster up-take than the bulk, (the multi-hollow presented an up-take slope of 100 while the

correspondent bulk presented an up-take slope of 70-80). However, when comparing the small hollow crystal and the small bulk crystals (equivalent to our HollowSil1 and BulkSil1), these present the same up-take curve, showing that the hollow structure has no impact on diffusion. The authors claim that for small sized crystals, such as the small hollow crystal and the small bulk crystals (corresponding to our BulkSil1 and HollowSil1), external surface barriers are the dominant mechanism in diffusion, and hence, different L does not make a difference. Contrary to Novruzova *et al.*, the present study shows that HollowSil1 has improved transport properties regarding BulkSil1, Figure 22. When comparing the studies of Novruzova and our study, it must be noted that: 1) the sorbates in study are different, whereas isooctane is used in the study of Novruzova *et al.* we have used here cyclohexane, and 2) Novruzova *et al.* estimated the D_{eff} at 150 °C, whereas we have studied the desorption at much lower temperature range 40-60 °C. We can conclude that the impact of the hollow morphology on small crystals is condition dependent. While the diffusion is controlled by thermodynamic or surface aspects for isooctane, the diffusion of cyclohexane is kinetically controlled.

4.1.3. Estimation of R of hollow crystals

In the case of the **silicalite-1 samples**, the characterization carried out over the samples showed that HollowSil1 and BulkSil1 have similar physical/chemical properties (crystal size, composition, adsorption behavior, etc.) supporting the hypothesis of similar D_{eff} .

For the **Beta samples**, we have showed that, even though Bulk1Beta and Bulk2Beta have different morphology, different composition and different adsorption behavior (different Henry Constant), still the D_{eff} are similar for the two bulk crystals. ZLC measurements strongly suggest that these differences have a very minor impact on the diffusion. If differences in composition, adsorption behavior and external morphology do not have a major impact in the diffusion process, we can support the hypothesis that D_{eff} is the same for bulk and hollow samples.

If the effective diffusion coefficient D_{eff} is approximately the same for bulk and hollow samples, then ratio $(\tau_H / \tau_B)^{1/2}$ shall be equal to R_H / R_B , and this value should be equivalent to the ratio of the corresponding mean diffusion length L_H / L_B , (the average radius for the bulk, and the wall thickness for the hollow, both obtained by electronic microscope images).

$$D_{effB} \approx D_{effH} \approx D_{eff}$$

$$\sqrt{\frac{\tau_H}{\tau_B}} = \frac{\sqrt{\frac{R_H^2}{D_{eff}}}}{\sqrt{\frac{R_B^2}{D_{eff}}}} = \frac{R_H}{R_B} \quad 11$$

For silicalite-1 samples, the ratio of τ_H and τ_B are between 0.7-0.8 for the three temperatures (Table 10). On the other hands, the characteristic length of the crystals are the equivalent radius of the crystals (70 nm) for BulkSil-1, and the wall thickness for HollowSil1 which we estimate between 45 nm, Table 1. The Hollow/Bulk ratio of characteristic length L_H/L_B is approximately 0.6, which is very close from the ratio of R_H/R_B estimated by ZLC measurements.

Table 10 - Ratio of HollowSil1 and BulkSil1 particle radius, (R_H/R_B), obtained from ZLC measurements. Ratio of HollowSil1 and BulkSil1 mean diffusion lengths (L_H/L_B), obtained from electronic microscope images.

Ratio of Particle Radius (by ZLC) If D_{eff} are equal:		Ratio of mean diffusion lengths L (Microscopy) $\frac{\text{wall size (45nm)}}{\text{radius (70nm)}}$
$\frac{\tau_H}{\tau_B} = \frac{\frac{R_H^2}{D_{eff}}}{\frac{R_B^2}{D_{eff}}} \leftrightarrow \frac{R_H}{R_B} = \sqrt{\frac{\tau_H}{\tau_B}}$		$\frac{L_H}{L_B}$
40°C	0.7	0.6
50°C	0.7	
60°C	0.8	

The same approach was taken for comparing the hollow and bulk morphologies of the Beta crystals. In this case, the HollowBeta was compared with respect to Bulk1Beta and Bulk2Beta. Similarly to silicalite-1 samples, the ratio of R_H/R_B obtained from τ_H/τ_B have been found to be very similar for all the temperatures, Table 11 and Table 12.

Table 11 - Ratio of HollowBeta and Bulk1Beta particle radius, (R_H/R_B), obtained from ZLC measurements. Ratio of HollowBeta and Bulk1Beta mean diffusion lengths (L_H/L_B), obtained from electronic microscope images.

Ratio of R – particle radius (by ZLC) If D_{eff} are equal: $\frac{\tau_H}{\tau_B} = \frac{\frac{R_H^2}{D_{eff}}}{\frac{R_B^2}{D_{eff}}} \leftrightarrow \frac{R_H}{R_B} = \sqrt{\frac{\tau_H}{\tau_B}}$		Ratio of mean diffusion lengths (Microscopy) $\frac{\text{wall size}}{\text{radius}} = \frac{L_H}{L_B}$
80°C	0.4	0.3
100°C	0.5	
120°C	0.5	

With Bulk1Beta

Table 12 – Ratio of HollowBeta and Bulk2Beta particle radius, (R_H/R_B), obtained from ZLC measurements. Ratio of HollowBeta and Bulk2Beta mean diffusion lengths (L_H/L_B), obtained from electronic microscope images.

Ratio of R – particle radius (by ZLC) If D_{eff} are equal: $\frac{\tau_H}{\tau_B} = \frac{\frac{R_H^2}{D_{eff}}}{\frac{R_B^2}{D_{eff}}} \leftrightarrow \frac{R_H}{R_B} = \sqrt{\frac{\tau_H}{\tau_B}}$		Ratio of mean diffusion lengths (Microscopy) $\frac{\text{wall size}}{\text{radius}} = \frac{L_H}{L_B}$
80°C	0.5	0.5
100°C	0.6	
120°C	0.6	

With Bulk2Beta

In both cases, there is a very good matching between the ratio of the characteristics lengths estimated by the ZLC (R values) and the ratio of the mean diffusion lengths L measured by SEM (the L values). It must be noted that the mean diffusion lengths, L, measured from electron microscopy images, might have a significant experimental error associated to the measurement itself, which can justify the differences between both ratios. The measurements obtained by SEM and or TEM images correspond to an average of a small population of 200-300 crystals. Moreover, in the case of the hollow silicalite-1 sample, HollowSil1, 20-30 % of the population is not a fully hollow structures, but rather multi-hollow structures for which L values can be hardly estimated. Possibly, the real average L_H is higher, which would originate

a higher L_H/L_B ratio. Also, hollow Beta presented around of 10 % of broken hollow crystals, which also might induce some error in the L_H/L_B value.

Despite experimental errors, R_H/R_B obtained from ZLC is very close from the ratio of the characteristic length obtained by SEM/TEM for the two zeolites. It definitely confirms our hypothesis that the effective diffusion **D_{eff} for hollow and bulk zeolite are equivalent** despite the difference in composition and external morphologies. As a result, the **hollow morphology allows shortening the characteristic diffusion time thanks to the inner cavity.**

In this study, we have clearly confirmed that the characteristic diffusion time is proportional to the square of the characteristic length. Although this conclusion may appear to be trivial, it is rarely reported in the zeolite literature as the change of crystals size usually results in modifications of other parameters (different Si/Al, higher external surface area) which does not allow discriminating kinetic from thermodynamic aspects.

5. Summary and conclusions

In the last decade, substantial efforts have been made in order to create more effective zeolite catalysts, i.e. with greater effective utilization, η . One approach consists in decreasing the characteristic length, L , facilitating the access to the active sites in the core of the crystals, increasing catalytic effectiveness. Hierarchical zeolites or nanosized zeolites are an example of zeolite morphologies with smaller L . In the case of hierarchical zeolites, L is smaller but unknown, and the creation of an extra mesoporous network implies that other properties will change as well, such as D_{eff} , external surface etc. For nanosized zeolites, even if L is smaller and known, the external surface is also larger, which also shall have an impact on catalytic activity. For both cases, it can be hardly stated that the decrease of the characteristic length is at the sole origin of enhanced catalytic activity as Thiele modulus may predict it.

Taking advantages of the hollow zeolite morphology, the **objective of this thesis was to investigate the impact of the reduction of the mean diffusion length L on the diffusion and the characteristic diffusion time. Our hypothesis was that, if hollow and bulk zeolite present similar physical/chemical characteristics (crystal size, composition, V_{micro} , etc), then these have the same D_{eff} .**

The synthesis of hollow zeolite single crystals targeted the synthesis of a zeolite morphology with reduced L , while keeping the same external morphologies and composition, with respect to the correspondent bulk zeolites. The reference bulk samples were synthesized so that their physical and chemical properties are as similar as the hollow zeolites. In order to validate the appropriateness of the bulk reference zeolites, extensive characterization of the samples was carried out by TEM and SEM images, Chemical Analysis, N_2 adsorption isotherms

and hydrocarbon adsorption isotherms. Hollow and bulk silicalite-1 zeolites were tested, presenting the same physical and chemical properties. Two bulk Beta samples and hollow Beta samples were studied, denoted as Bulk1Beta, Bulk2Beta and HollowBeta. Bulk1Beta and Bulk2Beta were both microporous but differed in terms of crystal sizes, different external morphologies, different Al content and different Henry's constant for cyclohexane adsorption. HollowBeta and Bulk1Beta presented approximately the same physical and chemical properties, to the exception of the external morphology. While HollowBeta and Bulk2Beta had in common the same type of external morphology, but presented slightly different crystal sizes, Al contents etc.

Characteristic diffusion times were measured by ZLC in a set-up that was validated against literature data on silicalite-1 sample. Bulk1Beta and Bulk2Beta presented very similar D_{eff} , even though these two samples had different composition, external morphologies etc.

The characteristic diffusion time (τ) was always shorter for hollow samples regarding the correspondent bulk samples, for both silicalite-1 and Beta zeolites. In the case of silicalite-1 samples, where characteristic diffusion time was approximately 34-50 % smaller for hollow silicalite-1 regarding bulk silicalite-1. For Beta samples, hollow samples presented 64-78 % smaller characteristic diffusion times regarding the correspondent bulk crystals.

Despite experimental errors of particle measurements from SEM/TEM images, the obtained the ratios of the mean diffusion length, L_H/L_B , are very similar to the ratios R_H/R_B obtained from ZLC model, for the two zeolite systems studied here. It definitely confirms the hypothesis that the effective diffusion coefficient **D_{eff} for hollow and bulk zeolite are equivalent**, despite the minor differences in composition and external morphologies. These results support that the inner cavity shortens the mean diffusion length L , and that the **hollow morphology is a good candidate to study the effect of smaller mean diffusion length L** , while others factors can be neglected, such as surface barriers due to the cavity itself. It is important to note that this is rarely reported in the zeolite literature, as the change of crystals size usually results in modifications of other parameters (different composition, external surface area etc) which results in different D_{eff} for the same zeolite type.

Considering the previous results, we wanted then to investigate whether the catalytic activity of hollow Beta would be increased following a Thiele modulus approach. In the next chapter, the impact of the hollow Beta morphology is studied in Catalysis using two model reactions.

6. References

- (1) Pagis, C.; Meunier, F.; Schuurman, Y.; Tuel, A.; Dodin, M.; Martinez-Franco, R.; Farrusseng, D. Demonstration of Improved Effectiveness Factor of Catalysts Based on Hollow Single Crystal Zeolites. *ChemCatChem* **2018**, *10* (10), 4525–4529.
- (2) Novruzova, N.; Tuel, A.; Farrusseng, D.; Meunier, F. C. Influence of Crystal Size on the Uptake Rate of Isooctane in Plain and Hollow Silicalite-1 Crystals. *Microporous Mesoporous Mater.* **2016**, *228*, 147–152. <https://doi.org/10.1016/j.micromeso.2016.03.039>.
- (3) Gueudre, L.; Jolimaite, E.; Bats, N.; Dong, W. Diffusion in Zeolites: Is Surface Resistance a Critical Parameter? *Adsorpt.-J. Int. Adsorpt. Soc.* **2010**, *16* (1–2), 17–27. <https://doi.org/10.1007/s10450-010-9213-6>.
- (4) Teixeira, A. R.; Chang, C.-C.; Coogan, T.; Kendall, R.; Fan, W.; Dauenhauer, P. J. Dominance of Surface Barriers in Molecular Transport through Silicalite-1. *J. Phys. Chem. C* **2013**, *117* (48), 25545–25555. <https://doi.org/10.1021/jp4089595>.
- (5) Karger, J.; Ruthven, D.; Theodorou, D. *Diffusion in Nanoporous Materials*; Wiley-VCH: Weinheim: Germany, 2012.
- (6) Duncan, W. L.; Möller, K. P. On the Diffusion of Cyclohexane in ZSM-5 Measured by Zero-Length-Column Chromatography. *Ind. Eng. Chem. Res.* **2000**, *39* (6), 2105–2113. <https://doi.org/10.1021/ie9907573>.
- (7) Li, C.; Ren, Y.; Gou, J.; Liu, B.; Xi, H. Facile Synthesis of Mesostructured ZSM-5 Zeolite with Enhanced Mass Transport and Catalytic Performances. *Appl. Surf. Sci.* **2017**, *392*, 785–794. <https://doi.org/10.1016/j.apsusc.2016.09.054>.
- (8) Karger, J.; Valiullin, R. Mass Transfer in Mesoporous Materials: The Benefit of Microscopic Diffusion Measurement. *Chem. Soc. Rev.* **2013**, *42* (9), 4172–4197. <https://doi.org/10.1039/c3cs35326e>.
- (9) Mitchell, S.; Pinar, A. B.; Kevin, J.; Crivelli, P.; Kaerger, J.; Perez-Ramirez, J. Structural Analysis of Hierarchically Organized Zeolites. *Nature Commun.* **2015**, *6*, 8633. <https://doi.org/10.1038/ncomms9633>.
- (10) Karger, J. Transport Phenomena in Nanoporous Materials. *ChemPhysChem* **2015**, *16* (1), 24–51. <https://doi.org/10.1002/cphc.201402340>.
- (11) Zhao, H.; Ma, J.; Zhang, Q.; Liu, Z.; Li, R. Adsorption and Diffusion of N-Heptane and Toluene over Mesoporous ZSM-5 Zeolites. *Ind. Eng. Chem. Res.* **2014**, *53* (35), 13810–13819. <https://doi.org/10.1021/ie502496v>.
- (12) Xu, D.; Ma, J.; Zhao, H.; Liu, Z.; Li, R. Adsorption and Diffusion of N-Heptane and Toluene over Mesostructured ZSM-5 Zeolitic Materials with Acidic Sites. *Fluid Phase Equilibria* **2016**, *423*, 8–16. <https://doi.org/10.1016/j.fluid.2016.04.013>.
- (13) Eic, M.; Ruthven, D. A New Experimental-Technique for Measurement of Intracrystalline Diffusivity. *Zeolites* **1988**, *8* (1), 40–45. [https://doi.org/10.1016/S0144-2449\(88\)80028-9](https://doi.org/10.1016/S0144-2449(88)80028-9).
- (14) Brandani, F. Development and Application of the Zero Length Column (ZLC) Technique for Measuring Adsorption Equilibria, University of Maine, 2002.
- (15) Crank, J. *The Mathematics of Diffusion*, 2 edition.; Oxford University Press: Oxford, 1980.

- (16) Brandani, S.; Jama, M. A.; Ruthven, D. M. ZLC Measurements under Non-Linear Conditions. *Chem. Eng. Sci.* **2000**, *55* (7), 1205–1212. [https://doi.org/10.1016/S0009-2509\(99\)00411-X](https://doi.org/10.1016/S0009-2509(99)00411-X).
- (17) Zaman, S. F.; Loughlin, K. F.; Al-Khattaf, S. S. Kinetics of Desorption of 1,3-Diisopropylbenzene and 1,3,5-Triisopropylbenzene. 1. Diffusion in Y-Zeolite Crystals by the Zero-Length-Column Method. *Ind. Eng. Chem. Res.* **2005**, *44* (7), 2027–2035. <https://doi.org/10.1021/ie049095u>.
- (18) Mangano, E.; Brandani, S.; Ruthven, D. M. Analysis and Interpretation of Zero Length Column Response Curves. *Chem. Ing. Tech.* **2013**, *85* (11), 1714–1718. <https://doi.org/10.1002/cite.201300083>.
- (19) Laprune, D.; Tuel, A.; Farrusseng, D.; Meunier, F. C. Highly Dispersed Nickel Particles Encapsulated in Multi-Hollow Silicalite-1 Single Crystal Nanoboxes: Effects of Siliceous Deposits and Phosphorous Species on the Catalytic Performances. *ChemCatChem* **2017**, *9* (12), 2297–2307. <https://doi.org/10.1002/cctc.201700233>.
- (20) Li, S.; Boucheron, T.; Tuel, A.; Farrusseng, D.; Meunier, F. Size-Selective Hydrogenation at the Subnanometer Scale over Platinum Nanoparticles Encapsulated in Silicalite-1 Single Crystal Hollow Shells. *Chem. Commun.* **2014**, *50* (15), 1824. <https://doi.org/10.1039/c3cc48648f>.
- (21) Ruthven, D. M.; Kaul, B. K. Adsorption of Aromatic Hydrocarbons in NaX Zeolite. 2. Kinetics. *Ind. Eng. Chem. Res.* **1993**, *32* (9), 2053–2057. <https://doi.org/10.1021/ie00021a029>.
- (22) Daems, I.; Leflaive, P.; Methivier, A.; Baron, G. V.; Denayer, J. F. M. Influence of Si : Al-Ratio of Faujasites on the Adsorption of Alkanes, Alkenes and Aromatics. *Microporous Mesoporous Mater.* **2006**, *96* (1–3), 149–156. <https://doi.org/10.1016/j.micromeso.2006.06.029>.
- (23) Chang, C.-C.; Teixeira, A. R.; Li, C.; Dauenhauer, P. J.; Fan, W. Enhanced Molecular Transport in Hierarchical Silicalite-1. *Langmuir* **2013**, *29* (45), 13943–13950. <https://doi.org/10.1021/la403706r>.
- (24) Magalhaes, F. D.; Laurence, R. L.; Conner, W. C. Diffusion of Cyclohexane and Alkylcyclohexanes in Silicalite. *J. Phys. Chem. B* **1998**, *102* (13), 2317–2324. <https://doi.org/10.1021/jp972036s>.

Chapter V – Impact of the hollow morphology in catalysis

1. Introduction

By ZLC measurements (chapter IV), we have demonstrated that the characteristic diffusion time ($\tau=R^2/D_{\text{eff}}$) of hollow Beta crystals is 64-78% shorter than the equivalent bulk Beta. Based on Thiele modulus (ϕ) - effectiveness factor (η) approach, we have made the assumption that the hollow structure may result in higher catalyst effectiveness, i.e. higher portion of the zeolite volume used.

The **objective** of this chapter is **to study the impact of the hollow Beta in catalytic reactions**. Hollow Beta crystals were synthesized according to the “*CIT-6 Dissolution-Recrystallization*” approach presented in chapter III. Bulk Beta crystals were synthesized in order to have the similar physical and chemical properties as the correspondent hollow: similar crystal size, and similar number of acid sites (Si/Al) of the same strength etc. Our hypothesis is that if physical and chemical characteristics are similar for both samples, hollow beta will allow us to study the impact of different diffusional path length L in catalysis.

This set of bulk and hollow zeolites will be tested for two model reactions: the hydroisomerization of n -hexadecane ($n\text{-C}_{16}$) and cracking of cyclohexane. The hydroisomerization of n -paraffin's such as $n\text{-C}_{16}$ are very important in the petroleum refining industry.¹ The use of a bulky molecule such as $n\text{-C}_{16}$ should put in evidence the impact of the diffusion differences between the hollow and bulk Beta, as already demonstrated by colleagues at IRCELYON for hollow and bulk **FAU** zeolites.² Cyclohexane cracking reaction was chosen as a second model reaction taking into account the results obtained in chapter IV for the diffusion of cyclohexane.

2. Impact of diffusion in catalysis

The molecular sized pore network of zeolite catalysts is responsible for highly selective reactions. However, even if the molecules are small enough to enter the pore system, its diffusion may be highly limited due to the narrow pore size, which greatly affects reaction rates. If the diffusion of a given reactant is too slow, this might not even reach the center of the crystal in useful time, and therefore the active centers present inside the crystal are not even used. Also, one must take into account that the reactant must reach the active site, but

the respective product must also diffuse back to the surface. **Internal diffusion limitations** are responsible for reducing the “useful” fraction of the crystal, i.e. the part of catalyst that is actually active in the catalytic process. This represents a loss of efficiency for many industrial processes catalyzed by zeolites, such as cracking, oxidation, (hydro)isomerization, alkylation and esterification, because the catalyst does not work at its full potential.^{3,4} Also, diffusion limitations might favor conversion of reactants and products into unwanted side products (“overcracking” for example), which may also serve as coke precursors, leading eventually to catalyst deactivation.⁵

One way to study the impact of diffusion limitations is to determine the degree of catalyst utilization, classically described by the effectiveness factor, η , which is linked to the Thiele modulus ϕ , Figure 1. The effectiveness factor is given by the ratio of the observed reaction rate and the intrinsic reaction rate, equation 1. When $\eta \rightarrow 1$, there is a full utilization of the catalyst volume, and therefore the observed reactions rates correspond to the intrinsic reaction rate. In this case, the reaction is limited by the reaction kinetics, the concentration of reactant is constant within the crystal and Thiele modulus ϕ is small. On the opposite scenario where the reaction is diffusion limited, there is a concentration profile within the crystal, thus part of the catalyst volume is not being used for the chemical reaction and therefore, the observed reaction rate decreases $\eta \rightarrow 0$, and Thiele modulus ϕ is larger.

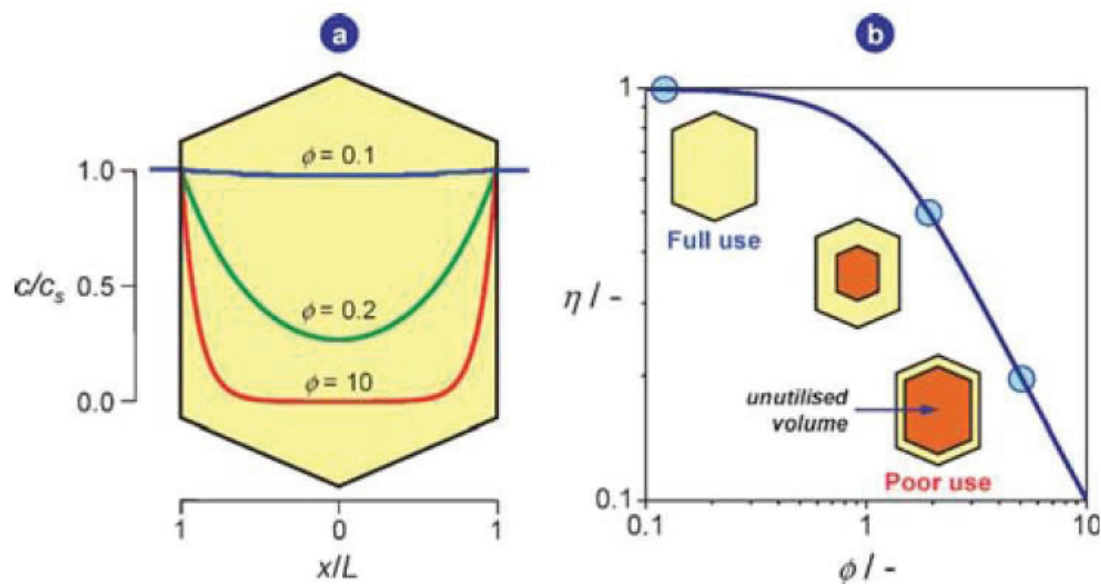


Figure 1 – Concentration profiles across a zeolite crystal (slab geometry) at different values of Thiele modulus, ϕ , (a). The relation between the effectiveness factor and Thiele modulus, (b). Reproduced from.⁴

The effectiveness factor is given by:⁵

$$\eta = \frac{\tanh(\phi)}{\phi} = \frac{r_{obs}}{r_{intrinsic}} \quad 1$$

Where

r_{obs} – is the experimentally observed reaction rate (mol/g_{zeol}/s);

$r_{intrinsic}$ – is the intrinsic reaction rate without diffusion limitations (mol/g_{zeol}/s);

ϕ – Thiele modulus (dimensionless);

We shall point out that for acid catalysis in zeolites, the intrinsic activity ($r_{intrinsic}$) of the site can hardly be measured experimentally which makes difficult to estimate the effectiveness. Indeed for metal supported catalysis on meso-macroporous support, the intrinsic rate of a catalytic reaction can be measured on powders (very low L) because it is assumed that there is no diffusional limitation in powder form. In the case of acid catalysis, this assumption cannot be made as the catalytic sites are in the zeolite micropore network which may impose diffusional limitation.

Remember that, for a 1st order irreversible reaction, Thiele modulus is given by:^{6,7}

$$\phi = L \sqrt{\frac{k}{D_{eff}}} \quad 2$$

Where:

k – intrinsic constant rate, i.e. reaction without diffusion limitations (s⁻¹)

Note that:

$$k = \frac{r_{intrinsic} \rho}{C_A}$$

And, from equation 1:

$$r_{intrinsic} = \frac{r_{obs}}{\eta}$$

Then:

$$\phi = L \sqrt{\frac{r_{obs} \rho}{\eta D_{eff} C_A}} \quad 3$$

Where:

r_{obs} – is the experimentally observed reaction rate (mol/g_{zeol}/s)
 ρ – zeolite density (g_{zeol}/m_{zeol}³)
 C_A – concentration of reactant A adsorbed at catalyst surface (mol/ m_{zeol}³)
 L – diffusion path length (m_{zeol})
 D_{eff} – effective diffusion coefficient (m_{zeol}²/s)

According to the equation 2, low Thiele modules (i.e. no diffusion limitations) can be achieved increasing D_{eff} or decreasing L . Zeolite synthesis has been focused on creating zeolite morphologies with more efficient catalyst utilization. While nanozeolites enable to decrease the diffusion length (L) zeolites with hierarchical pore structure (ie. an extra interconnected network of macro-,mesopores) enable to increase the effective diffusion (D_{eff}) at grain scale.⁸

Several works indicated that hierarchical zeolites showed enhanced catalytic performances, however the establishment of structure-property-function is not often clear.^{5,9,10} Indeed, it must be noted that post-treatments to create hierarchical zeolites (desilication, dealumination etc.) can modify the acidity of the zeolite in terms of amount and nature of acid sites and well as its surface properties (hydrophobicity).^{4,11} Also, it increases the external surface. Nanozeolites possess a smaller diffusion path length L but also possess a much larger external surface that can also have an impact in catalytic activity as acid sites at the external surface are likely of different kind than in the zeolite crystal. In either cases, it is difficult to attribute the origin of the higher catalytic activity when many parameters change at a time and therefore it makes hard the establishment of a direct relation between the diffusion length and catalytic activity.

Hollow zeolites single crystals is an unique example of zeolite morphology with reduced the mean diffusion length (L) while keeping the “same” external surface. As hollow and bulk zeolite have similar chemical/physical characteristics, they can be used as a model material to understand the impact of the diffusional path length in catalysis.

3. Hydroisomerization n-C₁₆ – Bifunctional catalysis

Bifunctional catalysis is very important in the hydrocracking and hydroisomerization of hydrocarbon sources to provide high-quality diesel fuel. Hydroisomerization of n-paraffins is an important process in the petroleum industry, as converting n-paraffins to iso-paraffins improves the properties of oil products for example. Paraffins heavier than C₁₅ constitute more than 80% of wax that is used to produce jet fuel and lubricant oil. In order to achieve low freezing and pour points, n-paraffins should be transformed iso-paraffins, which can be done by hydroisomerization reactions.^{1,12}

Hydroisomerization reaction takes place over bifunctional catalysts, typically consisting of a noble metal finely dispersed over a zeolite (generally mixed with alumina). The reaction mechanism includes dehydrogenation of the alkane to alkene in the metallic sites, then isomerization (or cracking) in the Brønsted acid sites of the zeolite with formation of the corresponding alkylcarbenium, and finally hydrogenation of alkene in the metallic sites, see Figure 2.^{1,13}

The reaction is always accompanied by cracking in the Brønsted acid sites, as represented in Figure 2. Cracking reaction lowers the isomerization yield, and it is favored for multibranched alkanes.^{1,13} Cracking products are undesirable because they produce less valuable lighter products, which increase the volatility of the final products. Also, over cracking might lead to coke formation.

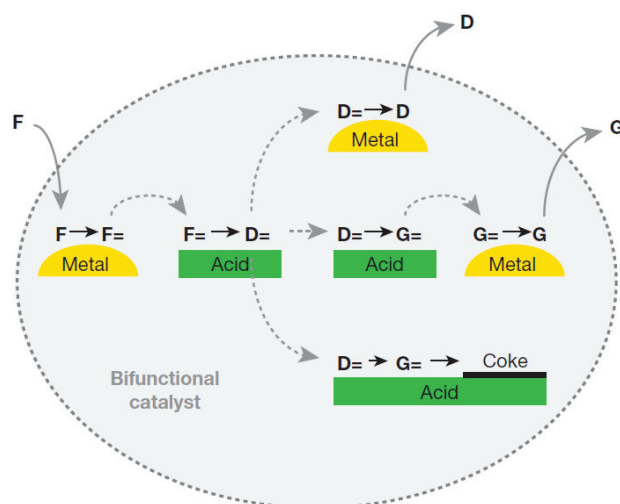


Figure 2 - **Scheme of hydrocracking reactions that use a bifunctional catalyst.** Feed normal alkane molecules (F) are dehydrogenated on a metal surface, producing alkene intermediates (F=). The alkenes diffuse to zeolite Brønsted acid sites, on which they undergo acid-catalysed skeletal isomerization, which can be followed by one (D=) or more (G=) cracking events, sometimes leading to coke formation. Isomerized (D=) and/or cracked (D=, G=) alkene intermediates diffuse to the metal site and are hydrogenated to form isomerized or cracked products D (diesel) and G (gas). Reproduced from.¹²

In this work, it is not an objective to develop a better catalyst for hydroisomerization reactions.^{12,13} It is clear that for an optimum bifunctional catalysis several parameters shall be optimized, such as the amount or and dispersion of the metallic phase, the acid strength, the distance between the acid and metallic phase, etc. Here we want to investigate whether the hollow morphology may increase the rate of acid driven catalytic reactions. For this purpose, the metal loading was carried out in large excess on the binder in order to make sure the catalytic activity is limited by the acidity, as explained in chapter II.

3.1. Synthesis and characterization of the zeolite phase

This study was carried out by comparing catalytic results of a hollow Beta (**20Hollow**) obtained from “CIT-6” with two three Beta benchmarks. Among them, two bulk Beta samples, **17Bulk** and **22Bulk**, and a commercial Beta zeolite, denoted by **REF**. Note that each sample is composed by a mix of the zeolite and γ -alumina as binder. The **metallic phase** is supported on γ -alumina (binder) for every sample. While the zeolite provides the acid phase (binder does not participate as acid catalyst).

The synthesis of the zeolite crystals for the samples 20Hollow, 17Bulk and 22Bulk are represented in the scheme below, Figure 3. More details are provided in chapter II. The numbers “20”, “17” and “22” included in the samples’ names stand for the value of Si/Al obtained from ICP analysis, as discussed below.

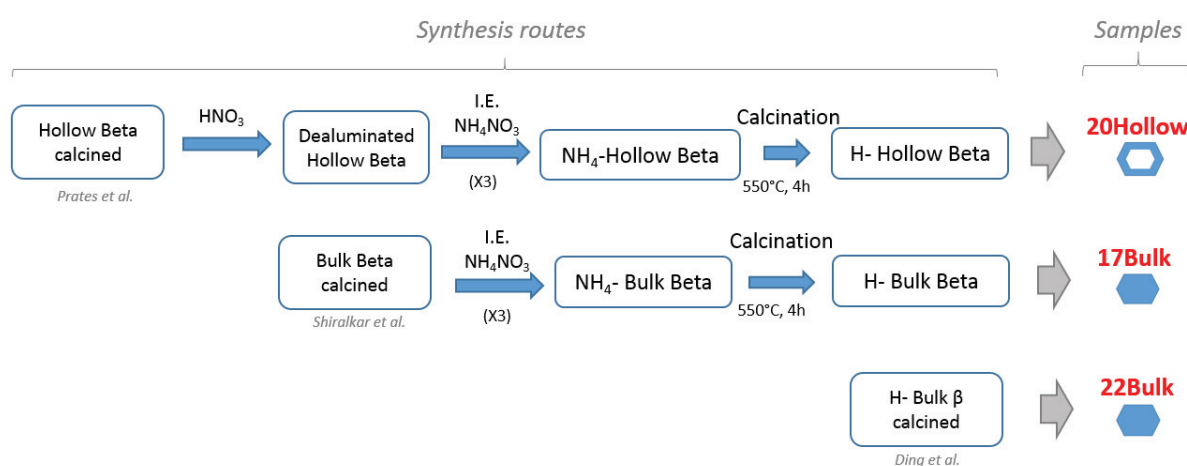


Figure 3 – Scheme of the synthesis route of the three samples 20Hollow, 17Bulk and 22Bulk.

Hollow Beta sample was synthesized according to the synthesis method presented in chapter III, “CIT-6 Dissolution - Recrystallization”. Then, the sample was dealuminated by a HNO_3 treatment, to increase the Si/Al, see Figure 3. Finally, the zeolite crystals were converted to their acid form by ion-exchange with NH_4NO_3 solution and further calcination. This sample was denoted as **20Hollow**.

The choice of the reference zeolite had to fulfill many criteria. In order to study the impact of the bulk vs hollow morphology, the hollow Beta should be compared to an “equivalent bulk Beta”, preferably having the same chemical/physical properties: the same textural properties (similar V_{micro} and V_{meso}) same crystal size, same Al and Na content (and

therefore similar acidic properties), same external morphology (bipyramidal morphology), ideally the same synthesis method, reactants, etc. Sample **17Bulk** was synthesized based on Shiralkar et al,¹⁴ and then being converted to its acidic form, Figure 3. Sample **22Bulk** was synthesized based on Ding *et al.*,¹⁵ which after direct calcination is already at its protonic form, Figure 3.

The main characterizations of **20Hollow**, **17Bulk**, **22Bulk** and **REF** are described in Table 1, namely Si/Al and Na/Al, the crystal size, morphology, V_{micro} , V_{meso} . XRD patterns, SEM images and N_2 adsorption isotherms are provided in the Annexes –Chapter V. In particular, SEM images of 20Hollow Beta showed that the crystals are intact regarding SEM images of the hollow Beta crystals synthesized as "CIT-6 Dissolution – Recrystallization" method (not shown).

Table 1 - Main characterizations of the zeolite crystals of the samples 20Hollow, 17Bulk, 22Bulk and REF.

Sample name	Si/Al ^{a)} Global composition	Na/Al ^{a)}	Average Crystal Size ^{b)}	External Morphologie ^{b)}	V_{micro} ; V_{meso} [cm ³ /g]
20Hollow 	19.6	0.05	Average: 1.15 μm 0.8 – 2 μm		0.19; 0.09
17Bulk 	17.0	0.06	Average: 0.7 μm 0,4 – 1,2 μm		0.15; 0.08
22Bulk 	22.1	0	Average: 0.6 μm 0,4 – 0,8 μm		0.20; 0.08
REF 	12.9	0	1-5 μm	Agglomerate	0.17; 0.79

- a) ICP analysis
- b) Obtained from electronic microscopy images
- c) Obtained from N_2 adsorption isotherms

Acid sites of zeolites were characterized by infrared spectra of the pyridine region, obtained for 150 °C, 250 °C, 350 °C and 450 °C in the range 1400-1700cm⁻¹, (see Annexes). The concentration of Brønsted and Lewis sites was determined as described in chapter II and listed in Table 2.

Table 2 – Concentration of Brønsted sites and Lewis/Brønsted ratio for samples 20Hollow, 17Bulk, 22Bulk and REF.

Sample name	20Hollow	17Bulk	22Bulk	REF
n° Bronsted (150°C) [μmol/g]	158	170	126	322
Lewis/Bronsted (150°C)	0.87	0.88	1.39	0.77

The number of Brønsted sites increase as the Al content increases. The REF sample show greater number of Brønsted sites which can be expected from its higher Al content regarding the other samples.

As we can see from Table 1 and Table 2, the zeolite **20Hollow**, **17Bulk**, **22Bulk** possess quite similar physical and chemical characteristics, in terms of crystal size, micro-mesoporous volumes, but also in number and strenght of Brønsted acid type. Hence, we can consider that 17Bulk and 22Bulk are equivalent to 20Hollow, except for the different diffusional path length, L, and the presence of the inner cavity. In contrast, the commercial Beta zeolite from *Zeolyst*, departs from the other 3 samples, by its morphology, high V_{meso} and high Al content.

3.2. Catalytic results

Considering global reaction order 1, the observed reaction rate r_{obs} (mol_{n-C16}/g/s) and average Turnover Frequency (TOF) (mol_{n-C16}/ mol_{Brønsted}/s) are calculated as:¹⁶

$$r_{obs} = \ln \frac{1}{(1-X)} \frac{F}{m_{zeol}} \quad 4$$

$$TOF = \frac{r_{obs}}{N_S} = \ln \frac{1}{(1-X)} \frac{F}{N_S m_{zeol}} \quad 5$$

Where:

F – inlet flow rate of $n\text{-C}_{16}$ (mol/s)

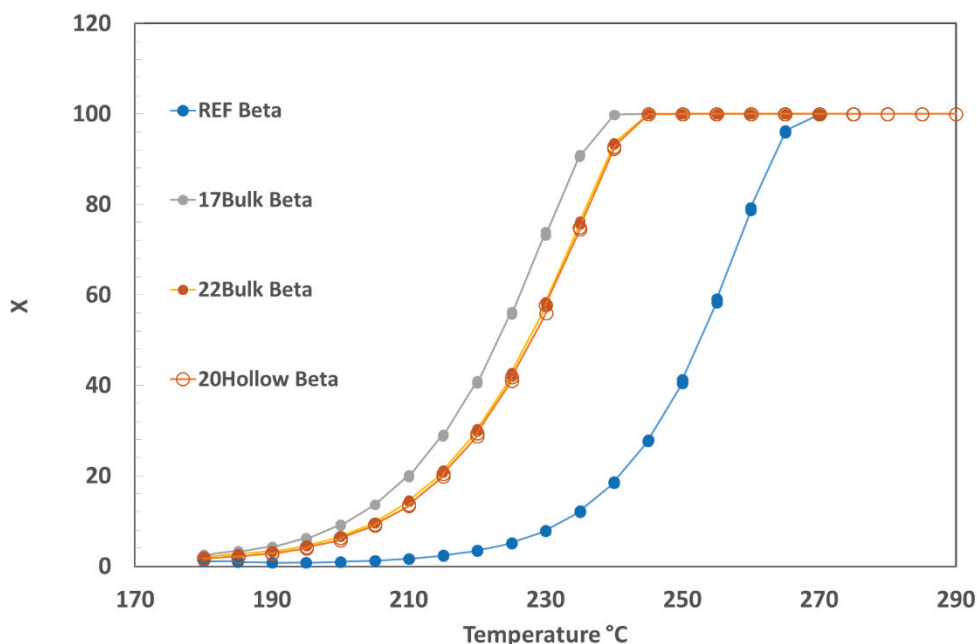
X – the fraction of converted $n\text{-C}_{16}$

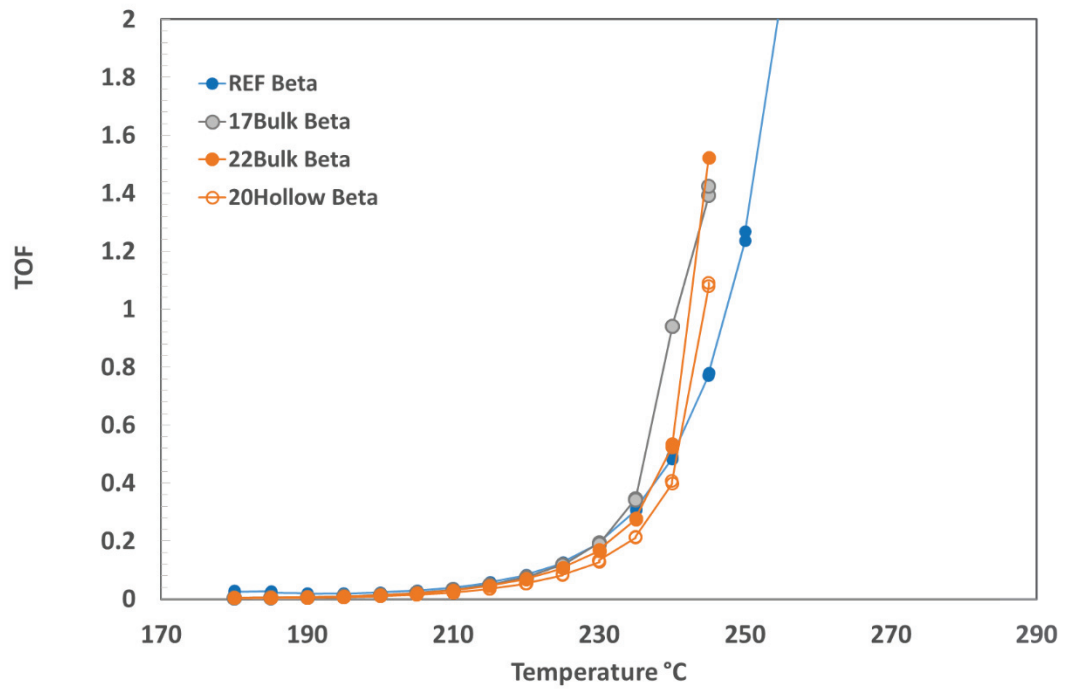
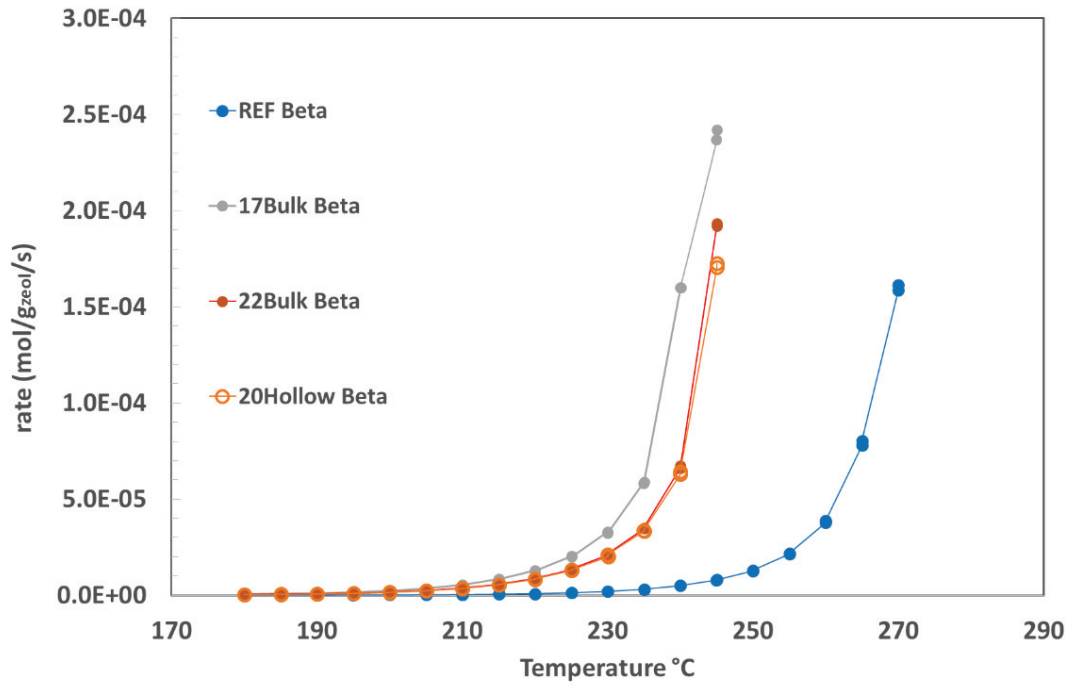
N_s – number of acid sites (Brønsted) per gram of zeolite (mol/ g_{zeolite})

m_{zeolite} – mass of zeolite (g_{zeolite})

The conversion, observed reaction rates (r_{obs}) and TOF values for the four Beta samples are presented below, as well as the yield of skeletal isomers, Figure 4.

The three samples 22Bulk, 17Bulk and 20Hollow show very similar behavior, in terms of reaction rates, TOF and yield% $i\text{C}_{16}$, suggesting that neither hollow morphology, neither the physical/chemical differences between the samples had an important impact on the catalytic behavior. The commercial REF presents similar TOF values but higher yield% $i\text{C}_{16}$, Figure 4. It can be expected that the REF show different catalytic profile because of the difference in morphology and mesoporous volume. The study and understanding of the particular behavior of REF sample is out of scope of this thesis. However, we note that the higher yield% $i\text{C}_{16}$ might be correlated to the high V_{meso} , which may allow an easy access of the reaction intermediates between the acid and metallic site, limiting cracking reactions.





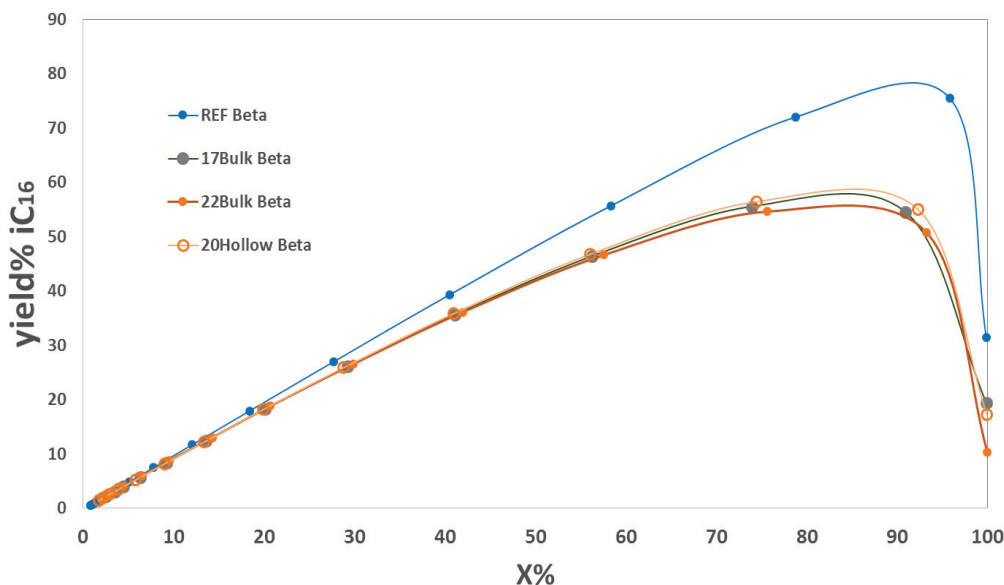


Figure 4 – The experimental reaction rate, TOF and yield% $i\text{-C}_{16}$ for samples 20Hollow, 17Bulk, 22Bulk and REF.

In any case, these results stress out that even for samples with the same framework structure *BEA, different catalytic profiles are obtained for different crystal morphology and that the interpretation has to be carried out very carefully when one try to quantify the origins in catalytic performances.^{17,18}

3.3. Discussion

These results suggest that the different bulk/hollow morphologies do not impact the catalytic activity for these particular reaction conditions. We can propose two opposite hypothesis which are discussed below:

- The reaction rate is strongly diffusion limited and the conversion occurs at the very surface of the crystals (or close to the surface). As a consequence, the small L of the hollow morphology should not show an effect on catalytic activity.
- The reaction rate is NOT diffusion limited and the both crystals have an effectiveness factor of 100%, i.e. the whole zeolite volume is used for the catalytic reaction. As consequence same catalytic activity per mass is expected for the hollow and bulk Beta (the same mass of zeolite is used for each sample).

In catalysis, the reduction of grain size is a standard method for the identification whether a reaction is under catalytic or diffusion controlled regime. For a reaction limited regime the catalytic activities are the same whatever the grain size for a particular catalyst in given

conditions. This is apparently what we can observe for the hollow and bulk Beta (Figure 4) which have diffusion length L of 150 nm and 300-400 nm respectively. At first glance, it supports the absence of diffusion limitation.

Let's consider the hypothesis of **strong diffusion limitations**. This hypothesis of strong diffusion limitation was already proposed by Zecevic *et al.*¹² when studying the hydroisomerization of *n*-alkanes (*n*-C₁₀ and *n*-C₁₉) on Pt-Binder/Y. The authors claimed that alkenes intermediates reacted mainly **near the crystal surface**, from where they could rapidly diffuse back to the metal sites present on the binder, a so-called pore mouth catalysis. The ***BEA** framework type has pore diameters of 0.56 and 0.75 nm, which are smaller than for the Y zeolite. We can anticipate that the energy of diffusion is significantly higher than for HY, and $D_{\text{eff}}(\text{Beta}) > D_{\text{eff}}(\text{Y})$, so diffusion limitations would be even more prominent in beta zeolite. Unfortunately, there are no data of diffusion constant of long alkanes at these temperatures which would enable the estimation of Thiele Modulus. In addition, the intrinsic TOF of the catalytic site cannot be experimentally measured in zeolites as diffusion phenomenon occurs.

Regardless the mechanism of the reaction, let's assume that the reaction occurs only at the very **surface of the crystals**. In this case, the reaction rate is proportional to the amount of crystal surface available, which is proportional to the number of crystals in the reactor. The catalytic tests were carried out with the same mass of zeolites, which means that for the same mass of zeolite, **there were more crystals of hollow beta than bulk zeolite**. Note that, assuming a hollow crystal with crystal size of 1 μm and a shell thickness of 0,15 μm , the apparent density of hollow Beta would be 50% smaller than the crystal density an equivalent bulk Beta. As consequence, at equal mass of zeolites, there are **1.5 more crystals of hollow Beta than of bulk Beta**. Hence, the external surface available for the hollow sample is 1.5 bigger than of the bulk test, which would mean that **TOF_{Hollow} would be equally 1.5 times bigger than TOF_{Bulk}**. Obviously, the results do not support the hypothesis of "surface reaction" as the apparent TOF_{Hollow} is not x1.5 higher than the TOF of the other bulk samples, Figure 4.

Colleagues at IRCELYON have recently reported the *n*-C₁₆ hydroisomerization over hollow and bulk Y (**FAU**) samples² in which the reaction conditions correspond to the very same reaction conditions of the present study. Similarly to the present work, hollow and bulk Y crystals present the same physical/chemical characteristics, and approximately the same density of acid sites. However, contrarily to our results, **hollow Y present higher apparent TOF than bulk Y** in a factor of approximately 2.2, see Figure 5. For the same reasons cited above, authors have proposed that the **reaction is certainly limited by diffusion** as the reduction of the diffusional path length allows increasing the reaction rate. It was hypothesized that the effectiveness of bulk Y was 45% against 100% for hollow Y.

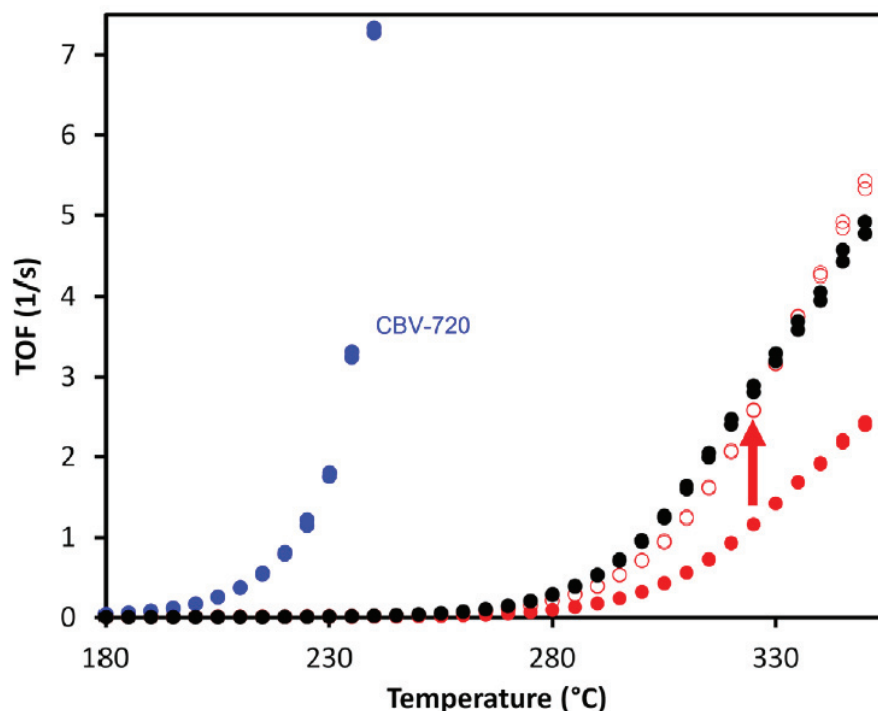


Figure 5 - Activity of the different Y catalysts with temperature. Bulk Y crystals in black circles and hollow Y crystals as red circles. Open symbols correspond to the activity of 2.2 times the amount of bulk crystals. Reported from Pagis et al.²

At this point of the discussion, the hypothesis that the n-C₁₆ hydroisomerisation reaction is **diffusion limited on Y** crystals and **NOT diffusion limited in *BEA** crystals appear contradictory. In particular, this hypothesis does not hold when considering the respective diffusion coefficient in Beta and Y. As mentioned above, the pore size of *BEA being smaller (absence of beta cage) than Y, the diffusion shall be slower in *BEA than in Y zeolite, imposing even stronger diffusional limitations.

Looking at the Thiele modulus equation 2, and comparing Beta and Y, we cannot explain the observed catalytic results of *BEA and Y zeolites by inferring different crystal sizes (L) nor diffusion coefficient (D_{eff}). Indeed, concerning these two zeolites, L is approximately the same (both Y and Beta zeolites had an average crystal size of 1 μm). Concerning D_{eff} , even if *BEA pores are smaller than FAU framework type pores, the difference between $D_{eff}(\text{Beta})$ $D_{eff}(\text{Y})$ shouldn't be high enough to justify the different results.¹⁹

The only parameter which has not been discussed yet is the concentration of reactant adsorbed at surface site (C_A), in the Henry regime defined by:

$$C_A = K_H P$$

Where:

C_A - concentration of reactant adsorbed at surface site ($\text{mol}/\text{m}^3_{\text{zeol}}$)

K_H - Henry's Constant ($\text{mol}/\text{m}^3_{\text{zeol}}/\text{atm}$)

P – pressure of reactant A (atm)

On a qualitative point of view, the pore size of *BEA being smaller than Y, the larger shall be the concentration of adsorbed n-C₁₆ in *BEA by confinement effect. A much larger concentration of adsorbed n-C₁₆ in Beta with respect to Y would decrease the Thiele modulus for Beta samples. As consequence, a greater adsorption in Beta zeolite could explain in theory the absence of diffusional limitation in Beta samples and the presence of diffusional limitation in Y zeolite. Nevertheless, the increase of concentration in Beta shall be at least one to two order of magnitudes larger to impact significantly the Thiele modulus and thus catalyst effectiveness.

In lack of experimental values, we have estimated Henry's constant K_H from the literature and empirical data as explained below:

The concentration of adsorbed n-C₁₆ in Beta and Y zeolites can estimated from the study of Denayer²⁰ who have measured entropy and enthalpy values for linear alkanes on different (acid) zeolites.

According to Atkinson and Curthoys,²¹ the relationship between localized adsorption entropy, ΔS , enthalpy, $-\Delta H$, temperature, and the Henry's constant K_H ($\text{mol}/\text{kg}_{\text{zeol}}/\text{atm}$) is given by:

$$\ln(K_H) = \frac{-\Delta H}{R_{gas}T} + \left(\frac{\Delta S}{R_{gas}} + \ln\left(\frac{n_T}{2p^\theta}\right) \right) \quad 7$$

Where:

$-\Delta H$ – adsorption enthalpy (J/mol)

ΔS – adsorption entropy (J/mol/K)

R_{gas} – perfect gas constant

n_T – total number of adsorption sites ($\text{mol}/\text{kg}_{\text{zeol}}$)

p^θ - standard state of the gas phase (chosen as 1 atm)

Denayer *et al.* have established linear relationships between carbon number of linear alkanes and adsorption enthalpy and entropy up to n-C₉ and n-C₁₂, Figure 6.

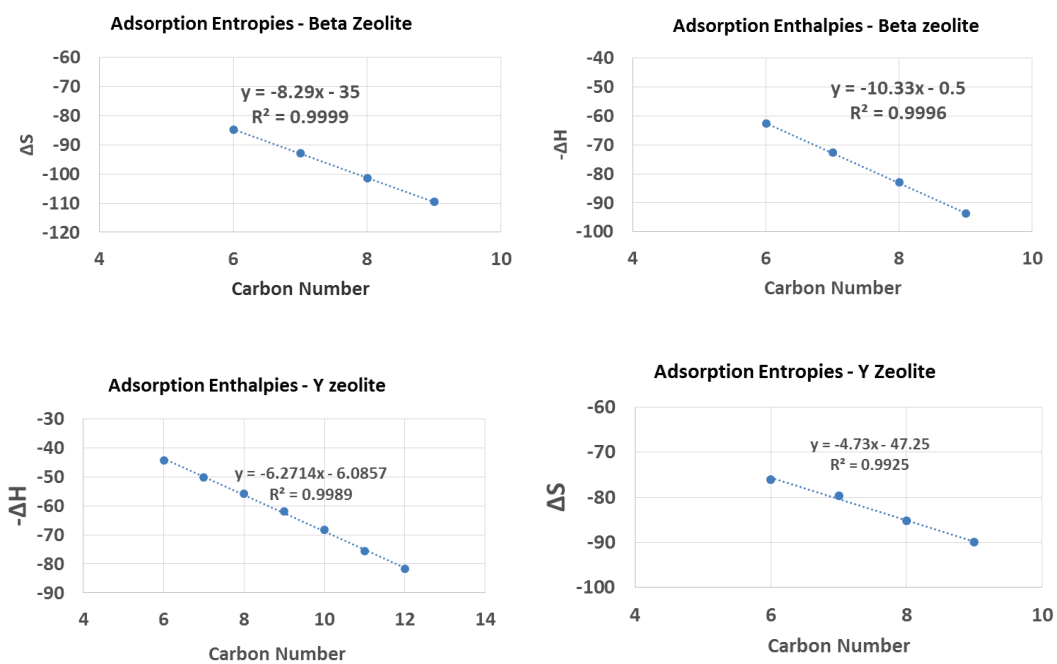


Figure 6 – Adsorption enthalpies and entropies for Beta and Y zeolite, for different *n*-alkanes.

By extrapolating the carbon number to $n=16$, we have estimated the adsorption enthalpy and adsorption entropy of $n\text{-C}_{16}$ for Beta and Y zeolites, Table 3.

Table 3 – Adsorption enthalpies and entropies for Beta and Y zeolite for alkane with number of carbons = 16.

	Beta	Y
$-\Delta H$ (kJ/mol)	-165.8	-106.3
ΔS (J/mol/K)	-167.6	-122.4

Finally, we have estimated the Henry constants at temperatures of 225 °C and 310 °C, for $n\text{-C}_9$, Table 4 and $n\text{-C}_{16}$, Table 5, according to Atkinson and Curhoys relationship, equation 7.

Table 4 - Henry's constant for Beta and Y zeolites at 225 °C and 310 °C, n-C₉.

T (°C)	Beta & n-C ₉ K _H (mol/kg/Pa)	Y & n-C ₉ K _H (mol/kg/Pa)
225	9.4 x 10 ⁻³	1.2 x 10 ⁻⁵
310	3.5 x 10 ⁻⁴	1.4 x 10 ⁻⁶

Henry's coefficients obtained by Atkinson and Curhoys relationship, equation 7, admitting:

- Brønsted sites density of n_T(Beta) ~ 150 μmol/g and n_T(Y) ~ 40 μmol/g
- Experimental values of -ΔH and ΔS for n-C₉ obtained by Denayer et al.²⁰

Table 5 – Henry's constant for Beta and Y zeolites at 225 °C and 310 °C, n-C₁₆.

T (°C)	Beta & n-C ₁₆ K _H (mol/kg/Pa)	Y & n-C ₁₆ K _H (mol/kg/Pa)
225	3.2 x 10 ²	1.1 x 10 ⁻²
310	9.3 x 10 ⁻¹	2.7 x 10 ⁻⁴

Henry's coefficients obtained by Atkinson and Curhoys relationship, equation 7, admitting:

- Brønsted sites density of n_T(Beta) ~ 150 μmol/g and n_T(Y) ~ 40 μmol/g
- Experimental values of -ΔH and ΔS for n-C₁₆ obtained by extrapolation of experimental data, Table 3.

As expected we observe larger Henry's constants for Beta with respect to Y. The difference is greater as the carbon chain is longer (from n-C₉ to n-C₁₆).

The temperature of 225 °C for Beta and 310 °C for Y have been chosen as a temperature of comparison of the Thiele Modulus because they provide the same observed reaction rate r_{obs}=20 μmol/g_{zeol}/s) at relative low conversion (56% for 17Bulk (Beta) and 57% for bulkY), Figure 7.

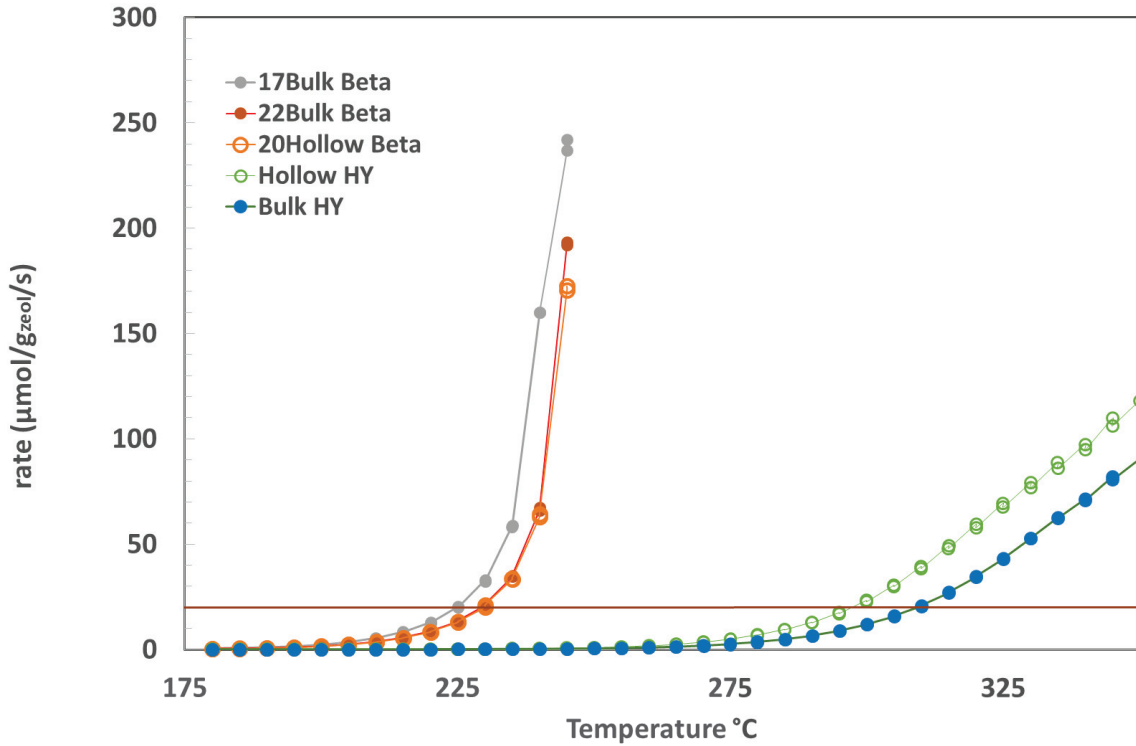


Figure 7 Reaction rate of $n\text{-C}_{16}$ conversion for Beta and Y zeolites as function temperature. Brown line points out for which temperatures $r_{obs}=20 \mu\text{mol}/g_{zeol}/s$.

We can estimate the effect of the Henry constants on the Thiele modulus assuming that:

- The observed reaction rate is nearly equal for Bulk Y at 310 °C and 17Beta (bulk) at 225 °C;
- the characteristic diffusion length (L) are nearly equal for Y and Beta (crystal size of approximately an average size of 1 μm for BulkY and 17Bulk (Beta)).
- $D_{eff}(Y, 310 \text{ }^\circ\text{C}) \sim 10D_{eff}(\text{Beta}, 225 \text{ }^\circ\text{C})$; ¹⁹
- Beta and Y possess approximately the same density value ρ ;
- The pressure of reactant $n\text{-C}_{16}$, P is the same for both tests;

It comes:

$$\left(\frac{\Phi_{Beta}}{\Phi_Y}\right)^2 = \left(\frac{L_{Beta}}{L_Y}\right)^2 \frac{\frac{r_{obs.Beta} \cdot \rho}{\eta_{Beta} D_{eff Beta} C_{ABeta}}}{\frac{r_{obsY} \cdot \rho}{\eta_Y D_{eff Y} C_{AY}}} \quad 8$$

If :

$$\begin{aligned} L_{Beta} &\sim L_Y \\ r_{obsBeta} &\sim r_{obsY} \end{aligned}$$

Then :

$$\left(\frac{\Phi_{Beta}}{\Phi_Y}\right)^2 = \frac{\eta_Y D_{eff Y} K_{HY}}{\eta_{Beta} D_{eff Beta} K_{HBeta}} \quad 9$$

If we assume that $D_{eff}(Y, 310^\circ\text{C}) \sim 10D_{eff}(Beta, 225^\circ\text{C})$, $\eta_Y \sim 0.5$ and $\eta_{Beta} \sim 1$, the equation above simplifies to:

$$\Phi_{Beta} = 2.2 \sqrt{\frac{K_{HY}}{K_{HBeta}}} \Phi_Y \quad 10$$

With the above assumptions and estimated Henry constants, the **Thiele modulus would be 100 to 10,000 smaller for Beta than for Y**, considering different temperatures or at the same temperature, and for different n-alkanes, see Table 6.

Table 6 – Square root of the ratio of Henry’s constant at different temperatures and different sorbates.

n-alkane	$\sqrt{\frac{K_Y(310^\circ\text{C})}{K_{Beta}(225^\circ\text{C})}}$	$\sqrt{\frac{K_Y(225^\circ\text{C})}{K_{Beta}(225^\circ\text{C})}}$	$\sqrt{\frac{K_Y(310^\circ\text{C})}{K_{Beta}(310^\circ\text{C})}}$
n-C ₉	1.2×10^{-2}	3.7×10^{-2}	6.4×10^{-2}
n-C ₁₆	9.2×10^{-4}	1.0×10^{-4}	1.7×10^{-2}

There are several assumptions which may appear “doubtful”, such as posing the same rate constant at different temperature, or the extrapolation of adsorption constants K_H to n-C₁₆. In order to estimate the effect of such assumptions, we have estimated the ratio of Thiele modulus with different hypothesis, (namely using the same temperatures and different n-alkanes).

The estimations of the effect of Henry constants of Beta and Y zeolites presented here on the Thiele modulus are very significant, most likely between two to four orders of magnitudes. Hence, the hypothesis of no diffusion limitations for n-C₁₆ hydroisomerization reaction on Beta zeolite holds.

4. Cyclohexane cracking – Acid catalysis

Herein, we wanted to investigate the **effect of the hollow morphology in the cyclohexane cracking reaction**. As for the n-C₁₆ reaction, the cracking reaction occurs on acid sites. The reaction of cyclohexane has been specifically chosen in order to estimate the diffusion coefficient at reaction temperature and thus to calculate an estimate of Thiele Modulus. The estimation of D_{eff} has been carried out in chapter IV (ZLC).

4.1. Samples synthesis and characterization

The samples used for the present reaction correspond to the samples HollowBeta and Bulk1Beta used in chapter IV for the ZLC tests. However, In order to increase catalytic activity, these samples were not exchanged with NaCl, resulting in smaller Na content, and therefore, more Brønsted sites should be available. The samples are denoted and **HollowBeta'** and **Bulk1Beta'** respectively. The Si/Al and Na/Al for both samples are presented in Table 7. The number of available protonic Brønsted sites was calculated considering the Al and Na content (and assuming that the EFAL amount are not significant). Bulk1Beta' appears to present higher concentration of Brønsted sites than HollowBeta'.

Table 7 – Catalyst Si/Al and Na/Al

	HollowBeta'	Bulk1Beta'
Si/Al ^{a)}	7.2	9.2
Na/Al ^{a)}	0.5	0.2
Si/Al Brønsted ^{b)}	14.4	11.9

a) Obtained from ICP analysis

b) Calculated from the difference of Si/Al global and the amount of Na

The synthesis and characterization of these samples can be found in detail in chapter IV, and is summarized in Table 8.

Table 8 – Morphology and crystal size characteristics of HollowBeta' and Bulk1Beta'

Sample	HollowBeta' 	Bulk1Beta' 
Characteristic length (L)	Wall size: 150 nm	0.5 μm
Crystal size	Average diameter: 1.15 μm Diameter: 0.8-2.2 μm	Average diameter: 1.2 μm Diameter: 0.6-1.90 μm
External Morphology		

As already mentioned in chapter IV, in general, these two samples present very similar physico/chemical properties and the same D_{eff} . In this case, it is plausible to assume that HollowBeta is a good candidate to study the effect of different L size in catalytic activity.

4.2. Catalytic results

The details about the catalytic tests can be found in chapter II. The outfeed composition is analysed by a gas chromatograph (GC). The operation conditions were based on the literature of cyclohexane cracking over zeolites.

The catalytic tests were performed at 400, 450, 500, 550, 600 and 650 °C. For all temperatures tested, both catalysts present a peak of catalytic activity as reaction starts, and start losing catalytic activity immediately after, as illustrated in Figure 8. After 10-20 min, both catalysts are deactivated.

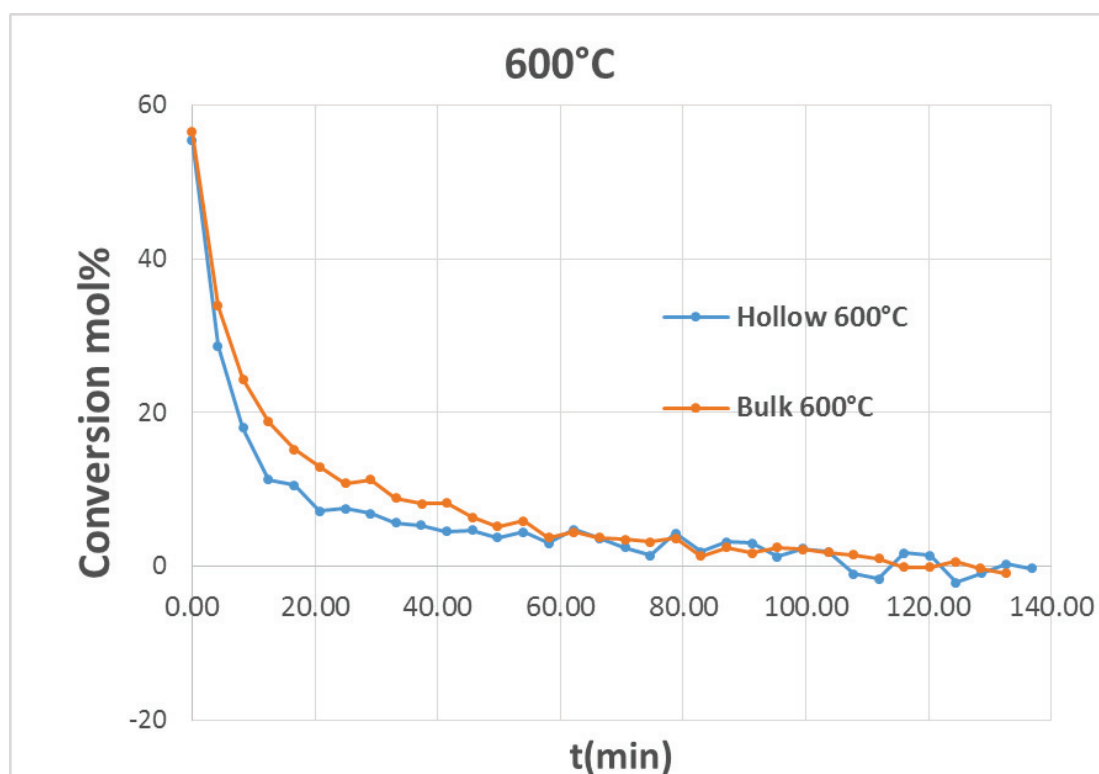


Figure 8 – Conversion of cyclohexane on Bulk1Beta' and HollowBeta' at 600 °C.

This rapid deactivation can be associated to coke formation. Cracking reactions occurs rapidly, creating coke depositions that will poison the acid sites, leading to deactivation of the catalyst.²² Low conversions and rapid deactivation for model reaction cyclohexane cracking has already been reported in the literature.^{22–24} The conversion profiles obtained for Bulk1Beta' and HollowBeta' are similar, with similar initial conversions of approximately 55%. Deactivation is immediate for both catalyst.

The results presented in Figure 8 suggest that the hollow morphology did not have any impact on the catalytic activity. Similarly to the n-C₁₆ hydroisomerization reaction, there are two situations that can explain these results:

- 1) either most of the catalytic activity occurs on the external part of both crystals. Coke formation on the external part of the crystals can result in pore blockage, leading to catalyst deactivation.
- 2) Either there are no diffusion limitations hence, most of the zeolite volume participates in the reaction do activity is the same for both catalysts.

4.3. Effectiveness factor

The influence of the hollow structure on reaction kinetics at was discussed in terms of Thiele modulus and effectiveness factor (equations 1 and 3). Like elsewhere in the

literature,^{23,25} it is assumed that cracking of cyclohexane is a first order reaction. D_{eff} of cyclohexane in each of these samples can be estimated from the results obtained from the ZLC model, chapter IV, using the Arrhenius relation and the E_d parameter, see Annexes-Chapter IV. The diffusion path length L is related with the crystal size and it is determined by electronic microscope images, Table 8. Henry's constant can be estimated according to Atkinson and Curthoys,²¹ and P of cyclohexane is 1 atm. However, the intrinsic reaction rate constant, k , as well as the intrinsic reaction rate are unknown, so we cannot determine ϕ . However, from the previous catalytic results we have obtained an "observable" reaction rate, which is definitely affected by diffusion limitations and/or coke deposition, and it is undoubtedly smaller than the intrinsic reaction rate.

Therefore, we have defined a *modified Thiele modulus* ϕ' , equation 1, **obtained with the observed reaction rate, r_{obs}** , instead of the intrinsic reaction rate, and the respective modified effectiveness factor, η' , equation 12 (see more details in Annexes).

$$\phi' = L \sqrt{\frac{r_{obs} \rho}{D_{eff} K_H P}} \quad 11$$

$$\eta' = \frac{\tanh(\phi')}{\phi'} = \frac{r_{obs}}{r_{intrinsic}} \quad 12$$

The observed reaction rate value was estimated from the catalytic results obtained previously, Figure 8, using the initial activity values obtained for each sample. It must be noted that these observed reaction rates are lower than intrinsic ones, due to deactivation phenomena. ($r_{obs} \leq r_{intrinsic}$), hence $\phi' \leq \phi$, which can be an indicator of the real reaction limiting conditions. This modified Thiele modulus ϕ' will give an idea of the real value of ϕ .

For Bulk1Beta', the modified Thiele modulus ϕ' was estimated between 0.3 and 0.9 with η' of 98-80 %, therefore, the real ϕ is at least bigger than 0.3 and η at least smaller than 98%. For HollowBeta', the modified Thiele modulus ϕ' was estimated between 0.1 and 0.3 with η' of 100 – 98 %, therefore, the real ϕ is at least bigger than 0.1 and η smaller than 100%.

Table 9 – Estimated values of modified Thiele modulus and modified effectiveness factor at 600 °C

Sample	$r_{\text{obs}}^{\text{a}}$ (600 °C) (mol/g _{zeol} /s)	$D_{\text{eff}}^{\text{b}}$ (600 °C) (m ² /s)	K_{H}^{c} (mol/kg/Pa)	Modified Thiele Modulus Φ' ^{d)}	Modified Effectiveness η' (x100%) ^{e)}
Bulk1Beta'	4.2×10^{-5}	6.2×10^{-14}	2.1×10^{-7}	0.3 <-> 0.9	80 <-> 98
HollowBeta'	4.1×10^{-5}	7.4×10^{-13}		0.1 <-> 0.3	98 <-> 100

a) – determined from the maximum conversion ever obtained during reaction

b) – determined from the E_d obtained in chapter IV, admitting an error of 20%, see Annexes

c) – estimated from Atkinson and Curthoys equation,²¹

d) – defined by equation 11

e) – defined by equation 12

5. Conclusions

In this chapter, we tested the **impact of the hollow morphology for two catalytic model reactions**: n-C₁₆ hydroisomerization and cyclohexane cracking.

In the previous chapters the synthesis of hollow Beta single crystal was obtained. When comparing to a bulk crystal, hollow Beta presents a smaller diffusion path length, L, while keeping the same external surface. Previous diffusion studies carried on bulk and hollow zeolites showed that hollow zeolites have enhanced transport properties proportional to the decrease diffusion path length L.

Pagis *et al.* studied the n-C₁₆ hydroisomerization over hollow and bulk Y (**FAU**) samples.² **Hollow Y presented higher activity than bulk Y, due to the higher catalyst utilization.** However, in the present study, **hollow Beta and bulk Beta presented the same catalytic activity** suggesting that the hollow morphology had no impact on the catalytic reactions. This results show how different zeolite types can have a major impact in catalysis. ***BEA** presents a smaller pore size and does not possess the 1.25 nm cages of **FAU** zeolite types, hence,

diffusion might be more limited than in Y samples. In the case where n-C₁₆ diffusion is severely limited, catalytic reaction will occur mainly on the external surface of the crystals. This hypothesis has already been claimed in the literature by Zecevic *et al.*,¹² for the hydroisomerization of long chain n-alkanes, suggesting that the alkene intermediates react mainly in the outer zeolite layers near the surface, to rapidly diffuse back to the metal sites on alumina. On the other hand, the estimation of the ratio of Y and Beta Thiele modulus shows that $\phi_{\text{Beta}} \ll \phi_{\text{Y}}$, suggesting that unlike Y zeolite, the reaction on Beta zeolite is not diffusion limited (or much less) than Y zeolites. This difference is explained by strongest adsorption (namely higher Henry's constant) and hence higher concentration of reactant on active site in Beta samples.

A set of hollow and bulk Beta samples was also tested for the cyclohexane cracking reaction. These samples were the same used for the diffusion tests in chapter IV, showing similar physical-chemical characteristics and similar D_{eff} . For the cyclohexane cracking reaction bulk and hollow samples **presented approximately the same catalytic activities, however, deactivation was almost instantaneous**. Deactivation might be due to coke deposition on the external part of the crystal, which will block the access to the internal active sites of the crystals. A modified Thiele modulus ϕ' was estimated using: L obtained by electron Microscopy images; D_{eff} estimated in the previous chapters for similar samples; K_{H} estimated from the literature; and the maximum reaction rate observed r_{obs} instead of intrinsic reaction rate $r_{\text{intrinsic}}$. The observed reaction rate is surely inferior to the intrinsic reaction rate, and therefore $\phi' < \phi$. The values estimated for ϕ' for BulkBeta' were between 0.3-0.9, which guarantees that the real ϕ is superior to 0.3 and the respective η inferior to 98. For HollowBeta' ϕ' values were between 0.1-0.3, which guarantees that real ϕ is superior to 0.1, and the respective η inferior to 100. These results show that there is the possibility the reaction is not diffusion limited, which explains the same catalytic activity for both samples.

6. References

- (1) Deldari, H. Suitable Catalysts for Hydroisomerization of Long-Chain Normal Paraffins. *Applied Catalysis A: General* **2005**, *293*, 1–10. <https://doi.org/10.1016/j.apcata.2005.07.008>.
- (2) Pagis, C.; Bouchy, C.; Dodin, M.; Franco, R. M.; Farrusseng, D.; Tuel, A. Hollow Y Zeolite Single Crystals: Synthesis, Characterization and Activity in the Hydroisomerization of n-Hexadecane. *Oil Gas Sci. Technol. – Rev. IFP Energies nouvelles* **2019**, *74*, 38. <https://doi.org/10.2516/ogst/2019015>.
- (3) Pagis, C.; Morgado Prates, A. R.; Farrusseng, D.; Bats, N.; Tuel, A. Hollow Zeolite Structures: An Overview of Synthesis Methods. *Chemistry of Materials* **2016**, *28* (15), 5205–5223. <https://doi.org/10.1021/acs.chemmater.6b02172>.

- (4) Perez-Ramirez, J.; Christensen, C. H.; Egeblad, K.; Christensen, C. H.; Groen, J. C. Hierarchical Zeolites: Enhanced Utilisation of Microporous Crystals in Catalysis by Advances in Materials Design. *Chem. Soc. Rev.* **2008**, *37* (11), 2530–2542. <https://doi.org/10.1039/b809030k>.
- (5) Hartmann, M.; Machoke, A. G.; Schwioger, W. Catalytic Test Reactions for the Evaluation of Hierarchical Zeolites. *Chem. Soc. Rev.* **2016**, *45* (12), 3313–3330. <https://doi.org/10.1039/C5CS00935A>.
- (6) Gilbert, F.; Bischoff, K.; De Wilde, J. *Chemical Reactor Analysis and Design*, 3rd edition.; 2010.
- (7) Pagis, C.; Meunier, F.; Schuurman, Y.; Tuel, A.; Dodin, M.; Martinez-Franco, R.; Farrusseng, D. Demonstration of Improved Effectiveness Factor of Catalysts Based on Hollow Single Crystal Zeolites. *ChemCatChem* **2018**, *10* (10), 4525–4529.
- (8) Mitchell, S.; Pinar, A. B.; Kenvin, J.; Crivelli, P.; Kaerger, J.; Perez-Ramirez, J. Structural Analysis of Hierarchically Organized Zeolites. *Nat. Commun.* **2015**, *6*, 8633. <https://doi.org/10.1038/ncomms9633>.
- (9) Verboekend, D.; Perez-Ramirez, J. Design of Hierarchical Zeolite Catalysts by Desilication. *Catal. Sci. Technol.* **2011**, *1* (6), 879–890. <https://doi.org/10.1039/c1cy00150g>.
- (10) Holm, M. S.; Taarning, E.; Egeblad, K.; Christensen, C. H. Catalysis with Hierarchical Zeolites. *Catalysis Today* **2011**, *168* (1), 3–16. <https://doi.org/10.1016/j.cattod.2011.01.007>.
- (11) Wilde, N.; Pelz, M.; Gebhardt, S. G.; Gläser, R. Highly Efficient Nano-Sized TS-1 with Micro-/Mesoporosity from Desilication and Recrystallization for the Epoxidation of Biodiesel with H₂O₂. *Green Chem.* **2015**, *17* (6), 3378–3389. <https://doi.org/10.1039/C5GC00406C>.
- (12) Zecevic, J.; Vanbutsele, G.; de Jong, K. P.; Martens, J. A. Nanoscale Intimacy in Bifunctional Catalysts for Selective Conversion of Hydrocarbons. *Nature* **2015**, *528* (7581), 245+. <https://doi.org/10.1038/nature16173>.
- (13) Jacobs, P. A.; Flanigen, E. M.; Jansen, J. C.; Herman van Bekkum. *Introduction to Zeolite Science and Practice*, 2nd edition.; Vol. 137.
- (14) Eapen, M.; Reddy, K.; Shiralkar, V. Hydrothermal Crystallization of Zeolite-Beta Using Tetraethylammonium Bromide. *Zeolites* **1994**, *14* (4), 295–302. [https://doi.org/10.1016/0144-2449\(94\)90099-X](https://doi.org/10.1016/0144-2449(94)90099-X).
- (15) Ding, L.; Zheng, Y. Effect of Template Concentration and Gel Dilution on Crystallization and Particle Size of Zeolite Beta in the Absence of Alkali Cations. *Microporous Mesoporous Mat.* **2007**, *103* (1–3), 94–101. <https://doi.org/10.1016/j.micromeso.2007.01.034>.
- (16) Mendes, P. S. F.; Silva, J. M.; Filipa Ribeiro, M.; Duchene, P.; Daudin, A.; Bouchy, C. Quantification of Metal-Acid Balance in Hydroisomerization Catalysts: A Step Further toward Catalyst Design. *AIChE J.* **2017**, *63* (7), 2864–2875. <https://doi.org/10.1002/aic.15613>.
- (17) Christensen, C. H.; Schmidt, I.; Christensen, C. H. Improved Performance of Mesoporous Zeolite Single Crystals in Catalytic Cracking and Isomerization of N-Hexadecane. *Catalysis Communications* **2004**, *5* (9), 543–546. <https://doi.org/10.1016/j.catcom.2004.07.003>.
- (18) Lanzafame, P.; Perathoner, S.; Centi, G.; Heracleous, E.; Iliopoulou, E. F.; Triantafyllidis, K. S.; Lappas, A. A. Effect of the Structure and Mesoporosity in Ni/Zeolite Catalysts for n-Hexadecane Hydroisomerisation and Hydrocracking. *ChemCatChem* **2017**, *9* (9), 1632–1640. <https://doi.org/10.1002/cctc.201601670>.
- (19) Zaman, S. F.; Loughlin, K. F.; Al-Khattaf, S. S. Kinetics of Desorption of 1,3-Diisopropylbenzene and 1,3,5-Triisopropylbenzene. 1. Diffusion in Y-Zeolite Crystals by the Zero-Length-Column Method. *Ind. Eng. Chem. Res.* **2005**, *44* (7), 2027–2035. <https://doi.org/10.1021/ie049095u>.
- (20) Denayer, J. F.; Baron, G. V.; Martens, J. A.; Jacobs, P. A. Chromatographic Study of Adsorption of N-Alkanes on Zeolites at High Temperatures. *J. Phys. Chem. B* **1998**, *102* (17), 3077–3081. <https://doi.org/10.1021/jp972328t>.
- (21) Atkinson, D.; Curthoys, G. Heats and Entropies of Adsorption of Saturated-Hydrocarbons by Zeolites-X and Zeolite-Y. *Journal of the Chemical Society-Faraday Transactions I* **1981**, *77*, 897–907. <https://doi.org/10.1039/f19817700897>.

- (22) Oliveira, H. M. T.; Herbst, M. H.; Cerqueira, H. S.; Pereira, M. M. Vanadium Effect on HUSY Zeolite Deactivation during Hydrothermal Treatment and Cyclohexane Model Reaction. *Appl. Catal. A-Gen.* **2005**, *292*, 82–89. <https://doi.org/10.1016/j.apcata.2005.05.043>.
- (23) Slagtern, A.; Dahl, I. M.; Jens, K. J.; Myrstad, T. Cracking of Cyclohexane by High Si HZSM-5. *Appl. Catal. A-Gen.* **2010**, *375* (2), 213–221. <https://doi.org/10.1016/j.apcata.2009.12.032>.
- (24) Abbot, J. Active-Sites and Intermediates for Isomerization and Cracking of Cyclohexane on Hy. *J. Catal.* **1990**, *123* (2), 383–395. [https://doi.org/10.1016/0021-9517\(90\)90137-9](https://doi.org/10.1016/0021-9517(90)90137-9).
- (25) Konno, H.; Ohnaka, R.; Nishimura, J.; Tago, T.; Nakasaka, Y.; Masuda, T. Kinetics of the Catalytic Cracking of Naphtha over ZSM-5 Zeolite: Effect of Reduced Crystal Size on the Reaction of Naphthenes. *Catal. Sci. Technol.* **2014**, *4* (12), 4265–4273. <https://doi.org/10.1039/c4cy00733f>.

Conclusions and Perspectives

Hollow zeolite single crystals are particularly attractive in catalysis. The presence of a large cavity in these model zeolites enables the study of diffusional limitation. The cavity also enables the encapsulation of metal nanoparticles. However, their synthesis requires specific structural characteristics and it has been limited for long to zeolites with the **MFI** structure.

In this thesis the synthesis of hollow Beta zeolite single crystals has been explored following two different synthesis approaches, referred to here as 1) "*CIT-6 Dissolution-Recrystallization*" based on Okubo *et al.*¹ and 2) "*Beta Zeolite Dissolution*".

The "*CIT-6 Dissolution - Recrystallization*" approach can be described as a seed-assisted synthesis of Beta zeolite, using zincosilicate CIT-6 as crystals seeds. After crystallization of Beta zeolite on the CIT-6 surface, the zincosilicate dissolves leaving a hollow structure of Beta zeolite. This synthesis method yielded hollow Beta crystals, with an average crystal size of 0.6-1.8 μm , and a wall thickness of about 100-200 nm. The zeolite walls are mostly microporous, even though there is evidence of the presence of mesopores (namely ink-bottle type pores) which are mainly located in the inside surface and do not seem to be interconnected. The crystal has a very low content of Zn and Si/Al ~ 8 , suggesting an almost total dissolution of the zincosilicate.

Pt nanoparticles were encapsulated in the cavity of hollow Beta using a pre-impregnation method on CIT-6. These Pt encapsulated hollow Beta crystals showed remarkable size-selectivity in the hydrogenation of aromatics and are extremely resistant to sintering phenomena.

Regarding the "*Beta Zeolite Dissolution*" approach, it is assumed an artificial Al zoning is created by surface alumination, followed by a selective dissolution of the core of a parent Beta zeolite. Hollow Beta single crystals were obtained with a crystal size of 250-300 nm, and a very thin wall thickness (30 – 50 nm). These crystals present a much smaller crystal size regarding the hollow Beta obtained by the first approach, which can be an important advantage in terms of molecular transport and consequently a big gain in catalytic activity. However, the hollow Beta crystals obtained by the "*Beta Zeolite Dissolution*" approach still have a small amount of amorphous phase. Furthermore, the crystals are not stable upon calcination. Hence, this hollow crystals were not used diffusion and catalytic tests. Whenever possible experimental procedures have to be optimized in order to totally remove amorphous material from the hollow structures and obtain a stable crystal.

The effect of the hollow morphology in molecular diffusion and catalysis was studied, using the hollow Beta sample obtained by "*CIT-6 Dissolution - Recrystallization*" approach. For

each test, hollow Beta was compared to an “equivalent” bulk Beta zeolite, i.e. bulk sample with similar physical/chemical properties, crystal size, external morphology etc. It is assumed that if the hollow and bulk samples are “equivalent”, one can measure the sole impact of different diffusion path length L as all other structural parameters are the same for both samples.

-The impact of the hollow morphology on molecular **diffusion** and transport was studied using the Zero Length Column (ZLC) technique. The technique was set-up and optimized in order to compare the diffusion of cyclohexane in hollow and bulk Beta crystal. The characteristic diffusion time ($\tau=R^2/D_{\text{eff}}$) of the hollow Beta was reduced by 64-78% compared to the corresponding bulk zeolite. This reduction was proportional to the square of the ratio of the diffusion path length between hollow and bulk samples, showing that the effective diffusion constant D_{eff} was the same for hollow and bulk Beta. These results indicate that the hollow morphology is a good candidate to study the effect of smaller mean diffusion length, for equivalent hollow and bulk samples.

- The impact of the hollow morphology was studied in acid catalysis through the model reactions of hydroisomerization of $n\text{-C}_{16}$ and cyclohexane cracking. Despite the impact of the hollow morphology in the previous diffusion studies, the hollow morphology did not show any impact for the previous catalytic tests, where hollow and bulk Beta presented similar catalytic activities per mass unit for both. One hypothesis to explain these results is that the reaction is highly limited by diffusion, hence reaction occurs on the external surface of the crystals. However, if this is the case, hollow beta should present higher activities, at its Sext is superior than the Sext of bulk samples. Hence, this hypothesis does not seem fit to explain the results. Another possible explanation is the opposite situation, where there are no diffusion limitations and the effectiveness factor is equivalent to 100%. In this case, the catalytic activity per mass of zeolite should be the same, which is actually the case. Interestingly, when the same reaction was performed over Hollow Y and Bulk Y, these were found to be diffusion limited, hence, hollow Y presented higher activity than BulkY. The Thiele Modulus has been estimated for both reactions and samples taking into account adsorbed concentration through Henry's constants. For Beta samples, ϕ values are low and consequently η are close to 1, for both hollow and bulk samples. However, Henry's constant for Y zeolites are up to 3 orders inferior to Beta zeolite, hence, $\phi_Y \gg \phi_{\text{Beta}}$. Beta has a greater affinity with the respective reactants, which can explain why the reaction is not diffusion limited as for Y zeolites.

This thesis presents two distinct methods to synthesize hollow Beta zeolites. Not that long ago, this type of morphology was limited to zeolites with a natural spatial gradient, namely **MFI** type zeolites. It is clear that hollow structures can be obtained either by using a similar parent

zeolite (such is the case of CIT-6 to Beta), either by creating an artificial Al gradient such as in the “Beta zeolite dissolution” approach (not yet found in the literature), and such for **FAU** zeolites (as recently published by colleagues in our group). Hence, these works open the possibility of synthesizing hollow structures of other zeolite structures.

Again, we have succeeded to synthesize hollow beta zeolites by the “*CIT-6 Dissolution - Recrystallization*” approach, which opened several possibilities of applications and studies. It must be noted that scale-up of this material may not be straightforward due to reproducibility problems already verified during this thesis, and the tendency of yielding other crystalline phases such as VPI-8 or MOR. Hence, this type of material would be more interesting as a model material to study parameters such as diffusional path length in diffusion and catalysis, as presented in this thesis.

Regarding the diffusion studies, it would be interesting to test hollow Beta samples in a broader range of temperatures, ideally with temperatures closer to the catalytic conditions. The major inconvenient of performing this type of tests at high temperatures is that reactions occur on the acid sites of the zeolite, even if the zeolite is in the Na form, which can jeopardize the results. One possibility would be to use dealuminated hollow Beta samples with high Si/Al. Moreover, diffusion tests should be also performed over “equivalent” nanozeolites and hierarchical zeolites, i.e. with the same composition as hollow and bulk Beta zeolites. This type of tests would help to understand the impact of different diffusion path length L , external surface, etc.

Finally, the catalytic tests have shown that there is no impact of the hollow morphology beta samples, as the Henry’s constant is high enough to guarantee that the sorbate is rapidly adsorbed. This is not the case for Y zeolites, for which Henry’s constants are significantly smaller, hence, the reaction is diffusion limited and hollow Y presents higher catalytic activities than bulk Y. So far, the lack of catalytic efficiency has been related to diffusion limitations and there has been a big effort into synthesizing zeolites with reduced L and improved $Deff$. However, our results show that the adsorption affinity (i.e. confinement) has an important impact in zeolite efficiency, and is usually underestimated with regards to diffusion concern. The impact of Henry’s constant should be considered in catalyst efficiency by testing zeolites with different affinities to the reactant, while keeping the same L and external surface. For example, testing a set of bulk and hollow Beta, but with different Si/Al.

Publications and Patents

- Prates, Tuel, Farrusseng, Bats, **PROCEDE DE PREPARATION DE CRISTAUX DE ZEOLITHE BETA SE PRESENTANT SOUS FORME DE BOITE CREUSE CONTENANT UN METAL SUR SA SURFACE INTERNE ET DANS SES PAROIS**, FR Patent 3059916, 2019
- Prates, Tuel, Farrusseng, Bats, **PROCEDE DE PREPARATION DE CRISTAUX DE ZEOLITHE BETA SE PRESENTANT SOUS FORME DE BOITE CREUSE CONTENANT UN METAL DANS SA PAROI ZEOLITHIQUE ET SUR SA SURFACE EXTERNE**, Fr Patent 3059915, 2019
- Pagis, Prates, Farrusseng, Bats, Tuel, **Hollow Zeolite Structures: An Overview of Synthesis Methods**, Chem. Mater. 2016, 28
<https://doi.org/10.1021/acs.chemmater.6b02172>
- Prates, Pagis, Meunier, Burel, Epicier, Roiban, Koneti, Bats, Farrusseng, Tuel, **Hollow Beta Zeolite Single Crystals for the Design of Selective Catalysts**, Crys. Growth Des, 2018, 18
<https://doi.org/10.1021/acs.cgd.7b01635>
- Pagis, Vennerie, Prates, Bats, Tuel, Farrusseng, **Hollow Polycrystalline Y zeolite shells obtained from selective desilication of Beta-Y core-shell composites**, Microporous and Mesoporous Materials, 2018, 265
<https://doi.org/10.1016/j.micromeso.2018.02.012>
- Pagis, Prates, Bats, Tuel, Farrusseng, **High-silica hollow Y zeolite by selective desilication of dealuminated NaY crystals in the presence of protective Al species**, CrystEngComm, 2018, 20
<https://doi.org/10.1039/c8ce00121a>
- Prates, Meunier, Dodin, Franco, Farrusseng, Tuel, **Hydrogenation Size-Selective Pt/Hollow Beta Catalysts**, Chemistry – A European Journal 2019, 15
<https://doi.org/10.1002/chem.201805041>

- Prates, Chetot, Burel, Pagis, Martinez-Franco, Dodin, Farrusseng, Tuel, Journal of Solid State Chemistry, **Hollow structures by controlled desilication of Beta zeolite nanocrystals** (in preparation)

Annexes - Chapter III

III.1. “CIT-6 Dissolution-Recrystallization” approach

In here we present some other studies and characterizations carried out for this synthesis approach.

III.1.1. CIT-6 crystals -effect of the “quality” of the reactant in CIT-6 synthesis

This type of parameter can be easily neglected and omitted, but in this case it accentuates how “sensitive” the synthesis of CIT-6 crystals might be. In the case of this study, we realized that the amorphous phase that was present not only in the XRD patterns but also in the SEM images, drastically decreased after using new Ludox HS-40, while keeping all the other synthesis parameters, see Figure 1. Indeed, it is known that after some months, silica in Ludox precipitates, which changes completely the quality of this reactant.

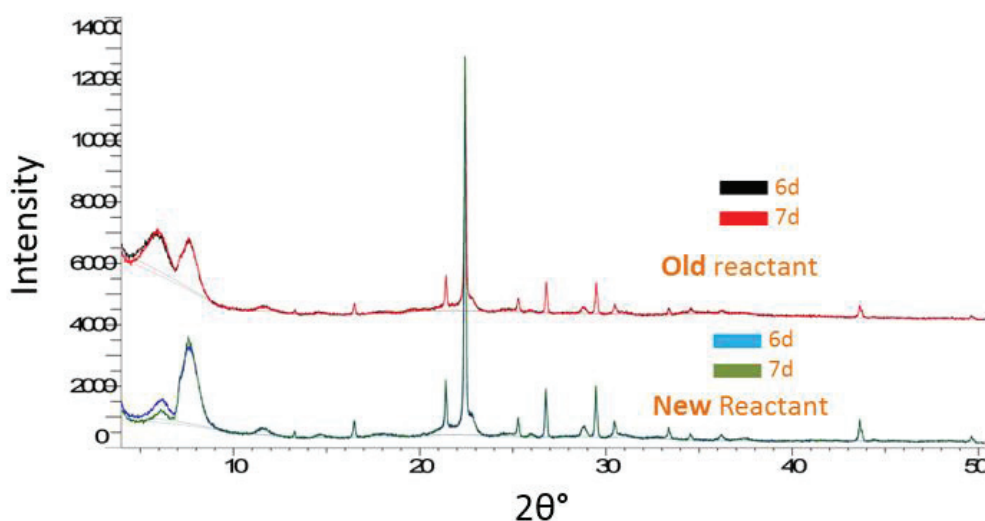
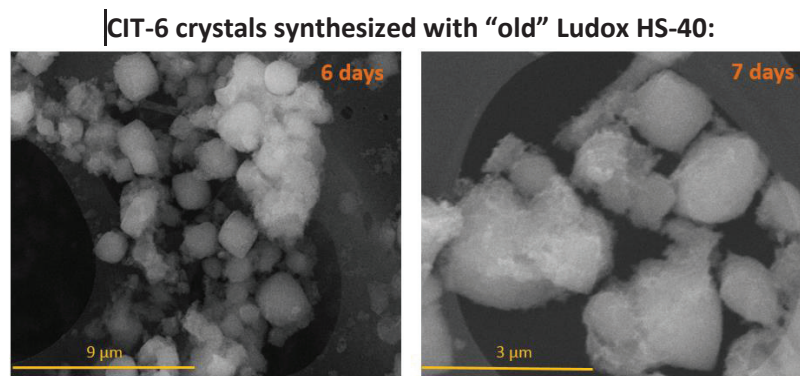


Figure 1 – XRD patterns of the same CIT-6 synthesis, using new and old reactants. Hydrothermal synthesis carried out at 140 °C, for 6 and 7 days.

Figure 1 shows the XRD patterns of the samples of the same synthesis using “old” and “new”/fresh bottles of Ludox HS-40, and how the initial “hump” decreased when using the fresh Ludox HS-40. Also, using the brand new reactants the intensity of the *BEA peaks increased, suggesting a higher crystallinity. Yield wt. % SiO₂ also increases from 24% for t_c=6 days and 27% for t_c=7 days, to 50% and 58% respectively. Moreover, the respective SEM images, see Figure 2, also show a population of CIT-6 crystals with no VPI-8 and no apparent amorphous phase, unlike the same synthesis products that were obtained with the old bottle of Ludox.



CIT-6 crystals synthesized with “new”(fresh) Ludox HS-40:

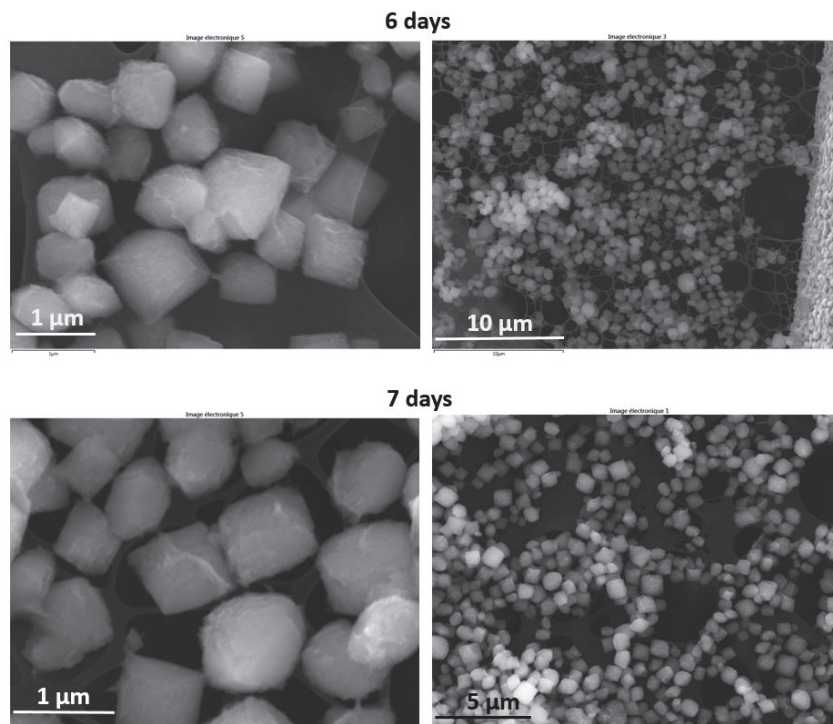


Figure 2 – SEM images of CIT-6 synthesized with new reactants. Hydrothermal synthesis performed at 140°C, for 6 days (above) and 7 days (bellow).

III.1.2. CIT-6 crystals – effect of crystallization and temperature

Figure 3, Figure 5 and Figure 6 show the XRD patterns and respective SEM images of the synthesized samples, at different crystallization temperatures and different crystallization times. As already mentioned in chapter III, as crystallization goes on, the amorphous phase decreases and CIT-6 yield increases, until eventually, there's no amorphous phase left, and VPI-8 yield starts increasing. VPI-8 is a needle shaped crystal phase that can be found on Figure 6 for the synthesis carried out at 150 °C. As the crystallization temperature increases, CIT-6 crystallization is faster, however, the yield of VPI-8 is higher as well, as there is faster transformation of CIT-6 into VPI-8, which is in accordance to our results.

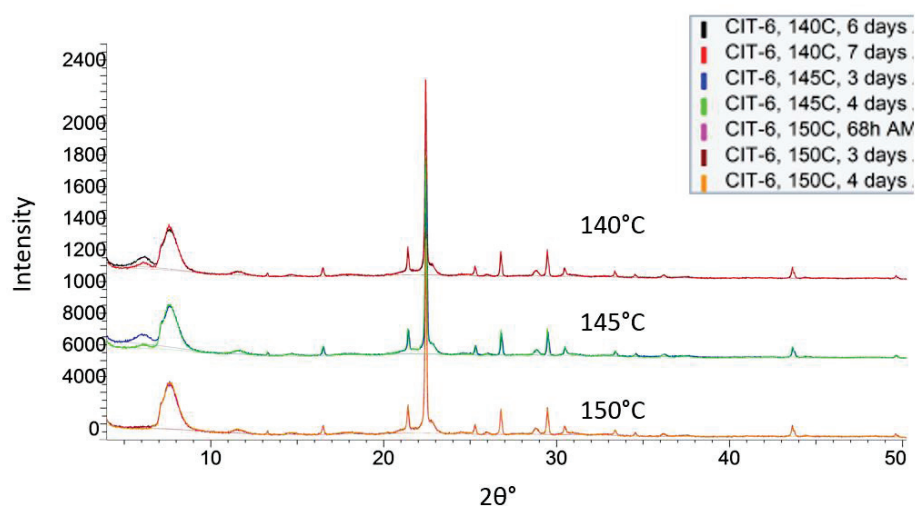


Figure 3 - XRD Patterns of the synthesized samples. Hydrothermal synthesis carried out at 140 °C for 6 and 7 days, 145 °C for 3 and 4 days and at 150 °C for 68h, 3 days and 4 days.

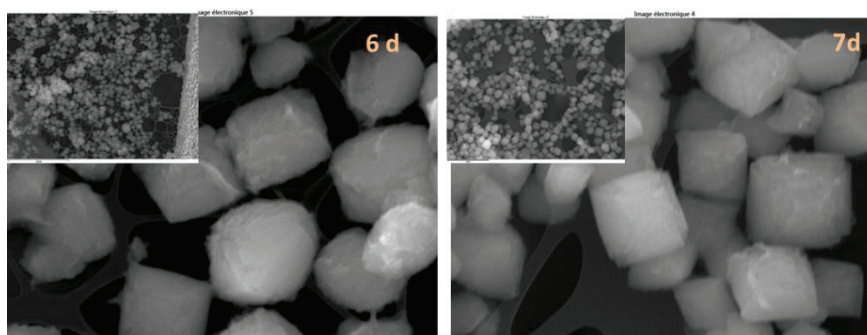


Figure 4 - SEM images of the synthesized samples. Hydrothermal synthesis carried out at 140 °C for 6 and 7 days. The yellow circles point out the VPI-8 crystals that can be found in some of the samples.

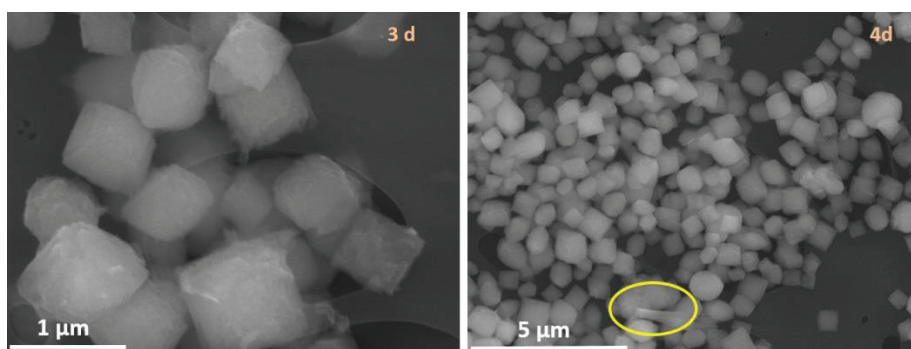


Figure 5 - SEM images of the synthesized samples. Hydrothermal synthesis carried out at 145 °C for 3 and 4 days. The yellow circles point out the VPI-8 crystals that can be found in some of the samples.

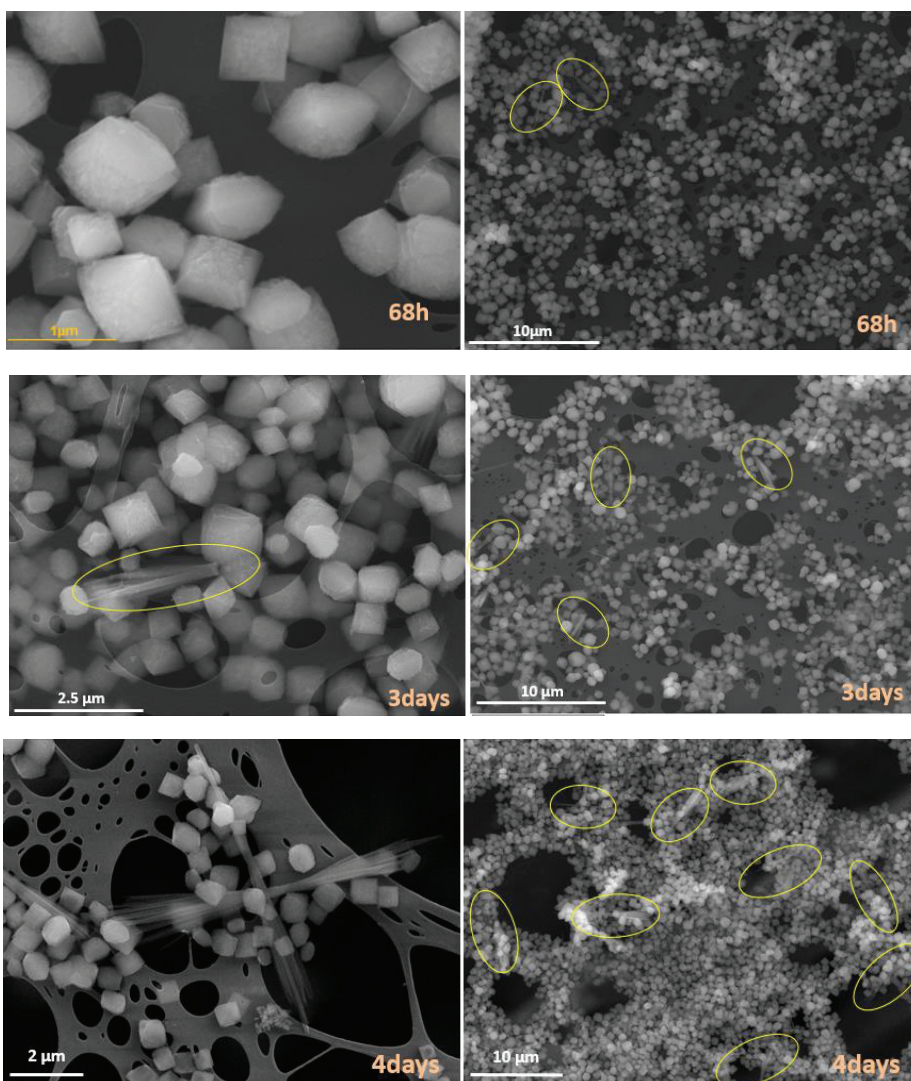


Figure 6 – SEM images of the synthesized samples. Hydrothermal synthesis carried out at 150 °C for 68h, 3 days and 4 days. The yellow circles point out the VPI-8 crystals that can be found in some of the samples.

III.1.3. CIT-6 crystals - TGA analysis of as-made CIT-6 crystals

TGA analysis has been carried out over as-made CIT-6, see Figure 7, to check the amount of organic template present in the crystal. According to Figure 7, the thermal decomposition of TEA⁺ starts before 300 °C (increasing heat flow), until approx. 600 °C. The weight loss beyond ~270 °C-300 °C corresponds to the organic template, which is around 14 wt. %.

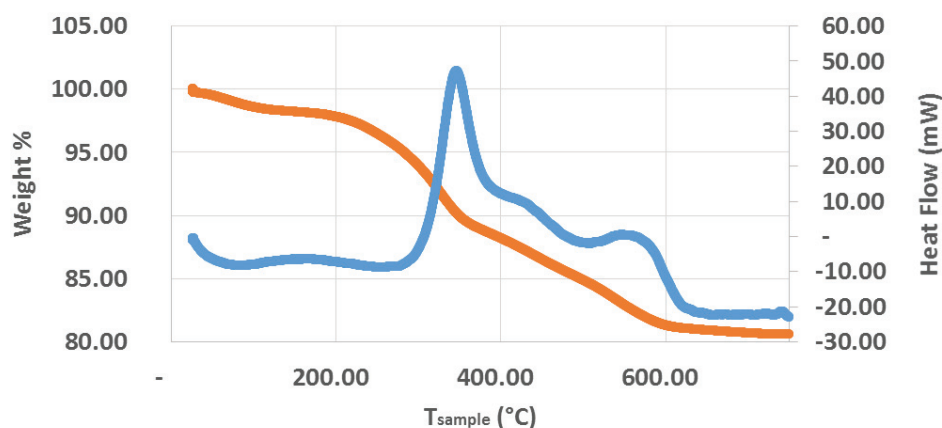


Figure 7 – TGA patterns for as made CIT-6 (orange) and corresponding heat flow (blue).

III.1.4. Hollow Beta crystals - mercury intrusion over hollow Beta

MIP experiments were performed over hollow Beta and an equivalent bulk Beta zeolite, with the same morphology and approx. the same crystal size, for the sake of comparison.

One should expect that Hg penetrates for the first time into the zeolite when pressure is high enough to penetrate into the mesopores in contact with the external surface (if any). Hg will fill up firstly the mesopores and then the inner cavity, if the mesopore system is branched from the external surface into the cavity. Following this logic, one should obtain high values of injected volume in the mesopore and micropore range.

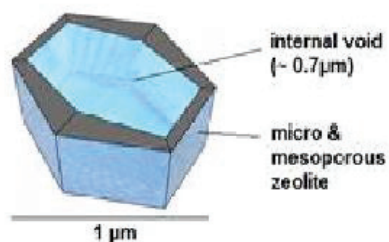


Figure 8 – Model of an “open” hollow Beta.

Nonetheless, one should take into account that:

- 1) the Washburn model assumes cylindrical pores, which is probably not the case.¹
- 2) a given mesopore probably doesn't have the same diameter throughout its length. In this case, when Hg travels through the pore, if the diameter increases, intrusion stops. Intrusion will continue when pressure is high enough. In this case, the correspondent pore size will be underestimated.

Figure 9 shows the pore size distribution derived from mercury intrusion porosimetry (MIP), for bulk Beta zeolite and hollow Beta respectively. Below, there are the N₂ isotherms and crystal size distribution for both samples, see Figure 10. Note that the contribution between 100-500 nm (Bulk) et 200-10000 nm (Hollow), see Figure 9, should be assigned to intercrystalline porosity/voids, according to Groen *et al.*² The diameter range is different, because the crystal size is different as well. Bulk Beta has smaller crystal size, so intercrystalline voids should be "smaller", which means that the diameter of the correspondent mesopore is smaller (100-500nm instead of 200-10000 nm for hollow sample).

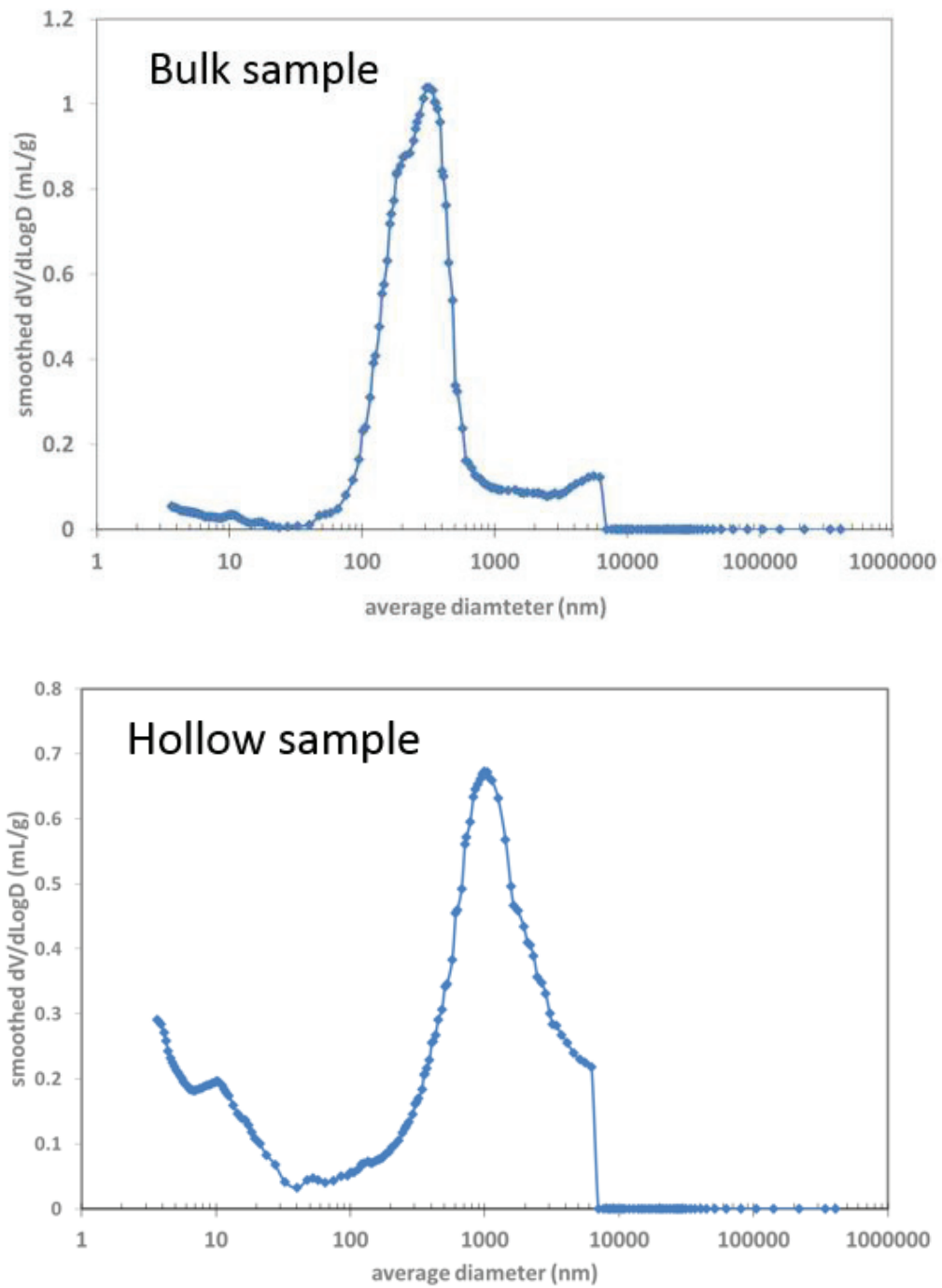


Figure 9 – Pore size distribution for bulk Beta and hollow Beta.

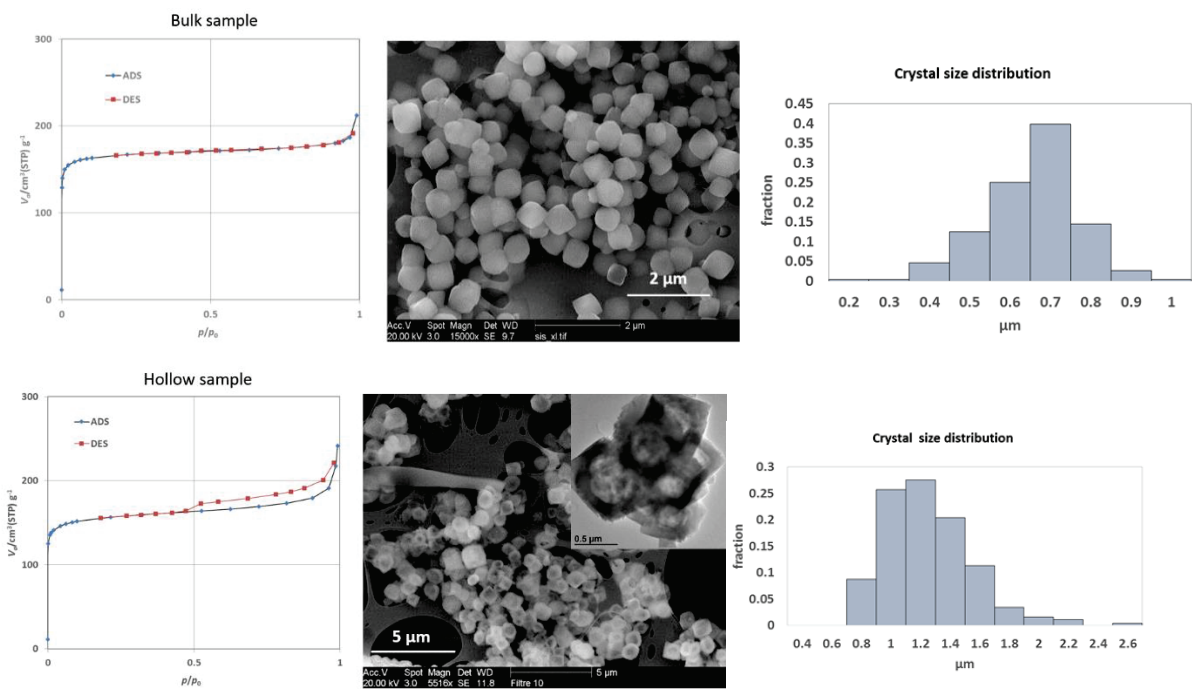


Figure 10 – SEM, crystal size distribution and N_2 isotherms of bulk Beta (above) and hollow Beta (bellow).

III.1.5. Hollow Beta crystals – effect of temperature and crystallization time

The hydrothermal synthesis of hollow Beta was carried out at different crystallization times and temperatures: at 140 °C for 12h, 24h, 46h, and 68h, and at 150 °C for 22h and 48h. SEM images are shown in Figure 11 and Figure 12. The crystals have the same crystal size and morphology as the hollow Beta reported previously, a truncated tetragonal pyramidal morphology, pine tree shaped on each sides.

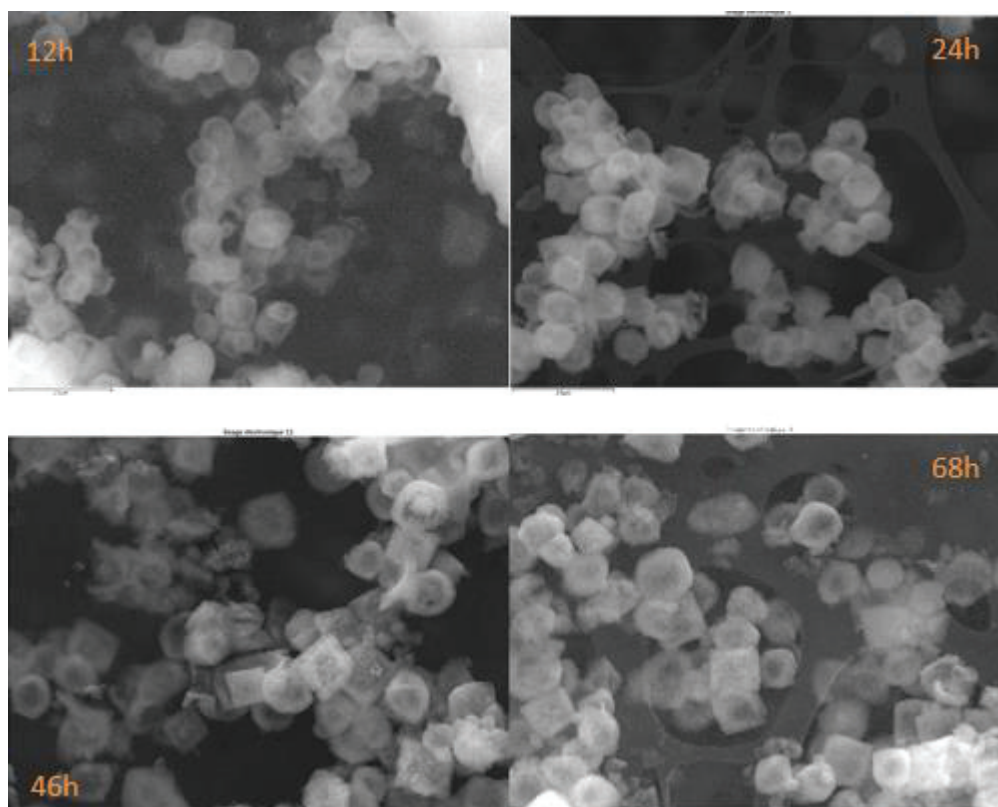


Figure 11 - SEM images of hollow Beta, hydrothermal treatment at 140 °C for 12h, 24h, 46h and 68h.

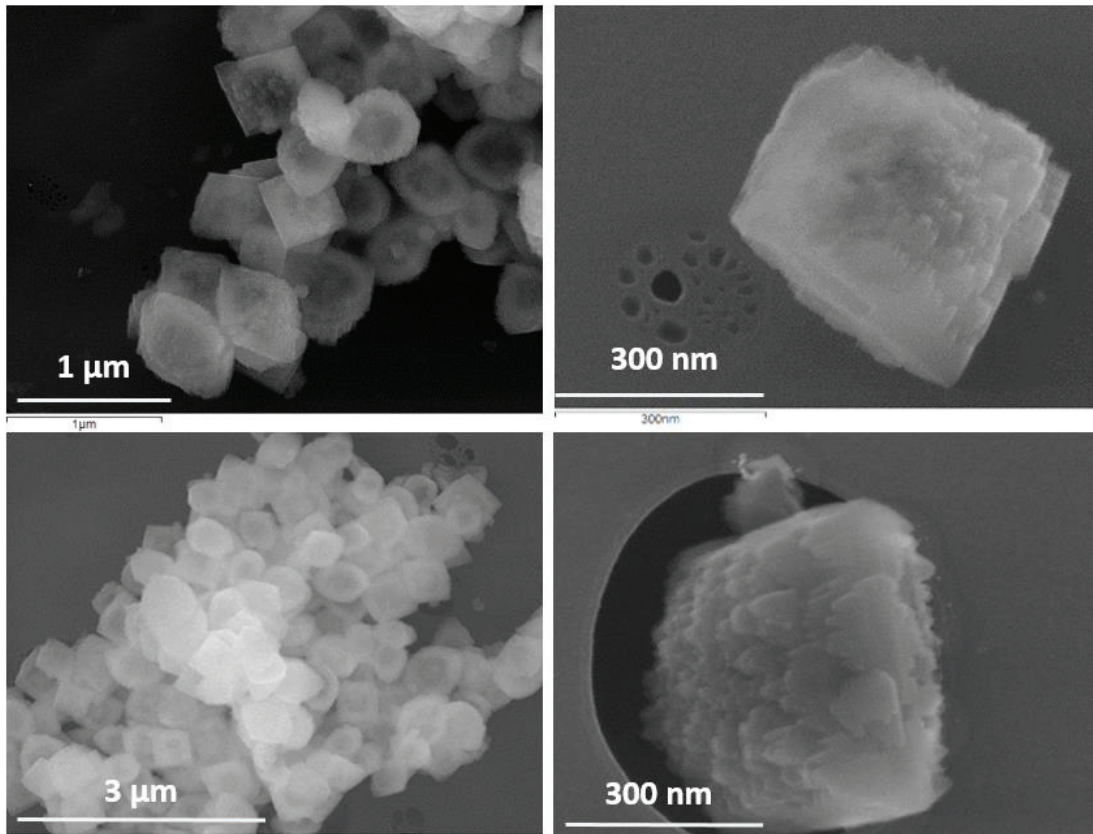


Figure 12 - SEM images of hollow Beta, hydrothermal treatment at 150 °C for 22h (above) and 48h (bellow).

III.1.6. Hollow Beta crystals - XRD of samples TEAHollow β and ++TEAHollow β

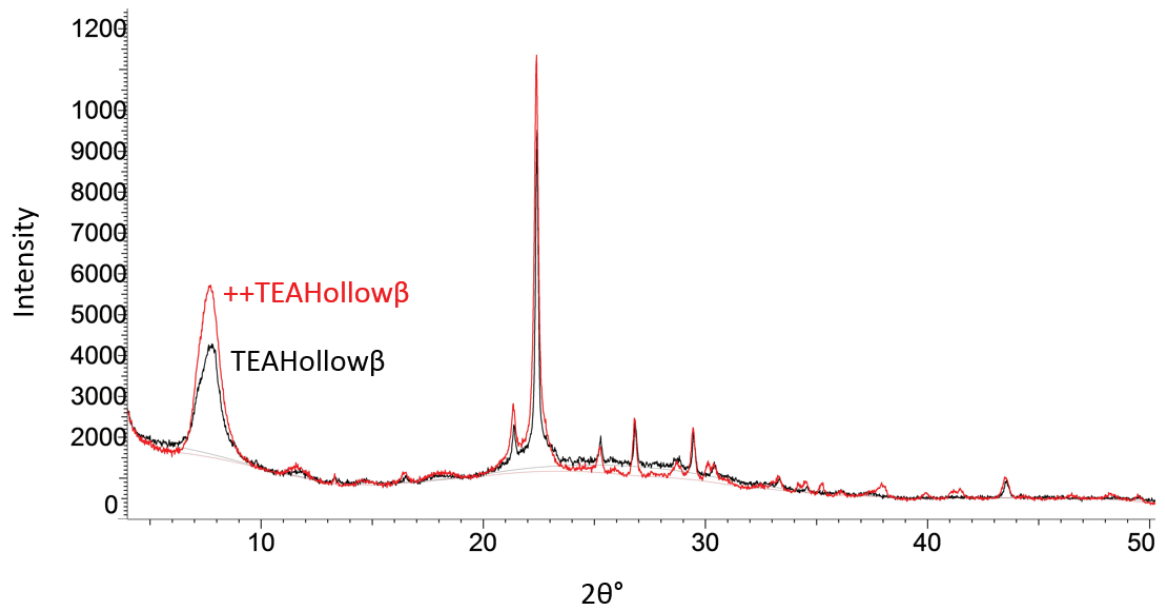


Figure 13 – XRD patterns for TEAHollow β (black line) and ++TEAHollow β (red line).

III.1.7. XRD patterns

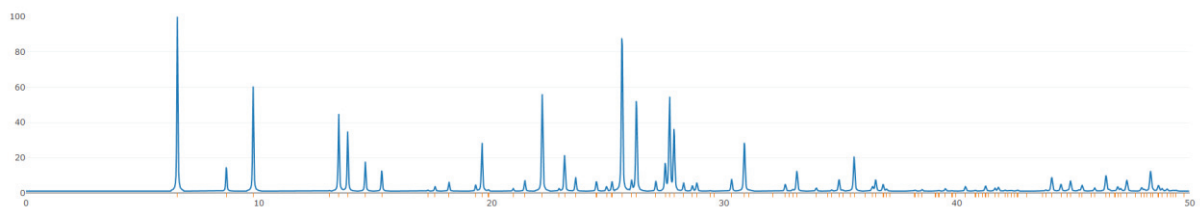


Figure 14 - XRD pattern of **MOR** by IZA.

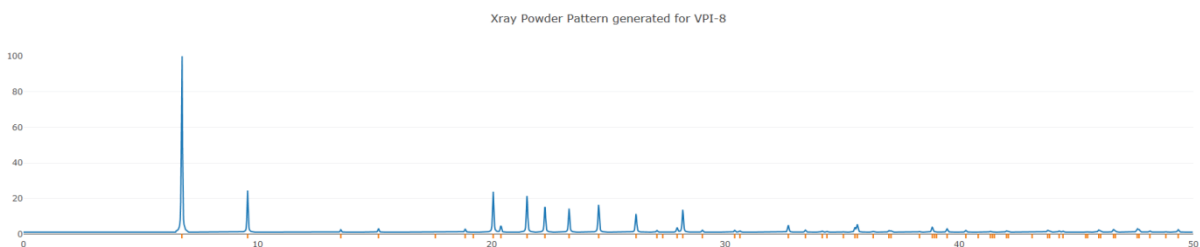


Figure 15 - XRD pattern of VPI-8 (**VET**) by IZA.

III.2. Encapsulation of Pt NP's in hollow Beta single crystals

III.2.1. Optimization of NaBH₄ reduction over Pt/CIT-6

NaBH₄ reduction reaction was studied over Pt/CIT-6. This sample was prepared by impregnation using H₂PtCl₆ solution, 2 wt. % Pt, as described in chapter II.

Figure 16 presents the TEM images of Pt/CIT-6 reduced, using a NaBH₄ aqueous (aq) solution at different life times, and by direct adding of NaBH₄ salt (s) into dispersion containing the Pt/CIT-6 as made. Indeed, if the NaBH₄ solution is prepared 1h before the adding the Pt/CIT-6, most of the NaBH₄ will be already reacted with water, leaving no NaBH₄ left to reduce the Pt ions present on the zeolite. On the other hand, if NaBH₄ salt is added directly to the zeolite containing solution, reduction results in bigger Pt NPs and also agglomerations of Pt NPs.

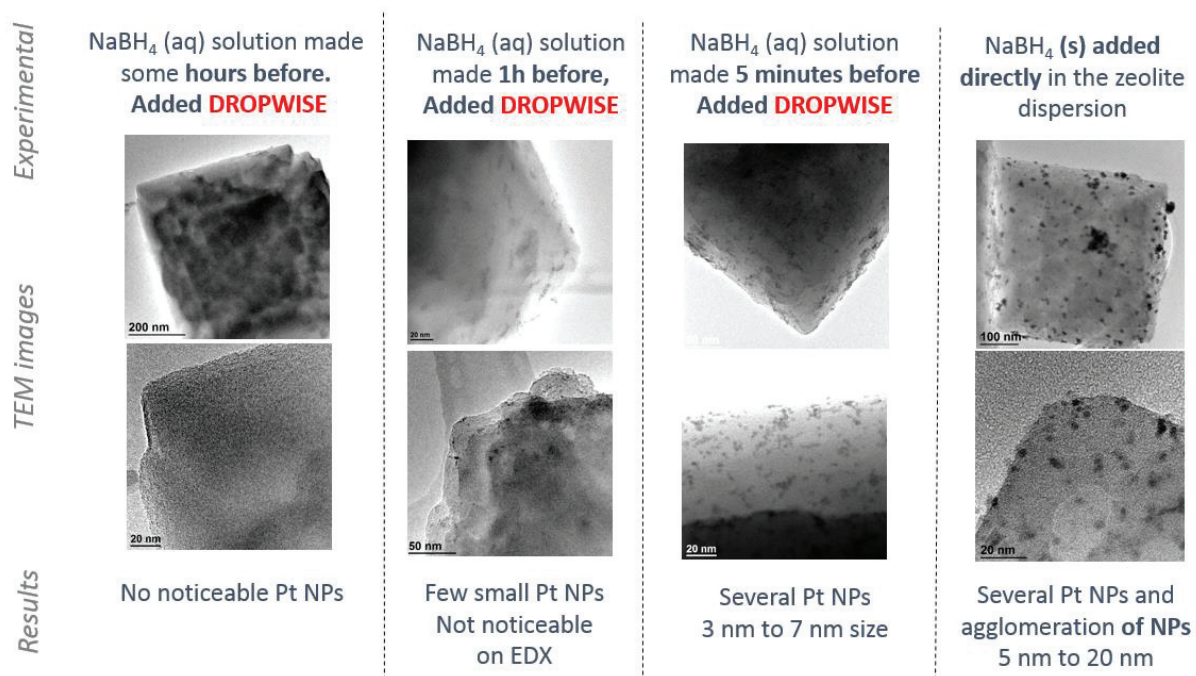


Figure 16 – the effect of the life time of NaBH₄ aqueous solution (5 mM, 0.05 g_{zeol}/ml) over reduction and Pt NPs size. TEM images of the resulting Pt/CIT-6.

Moreover, we have studied the effect of NaBH₄ concentration on amount of Pt reduced and Pt NP distribution. The same Pt/CIT-6 was reduced by two different NaBH₄ solutions: NaBH₄/Pt = 1 and NaBH₄/Pt = 20, Figure 17.

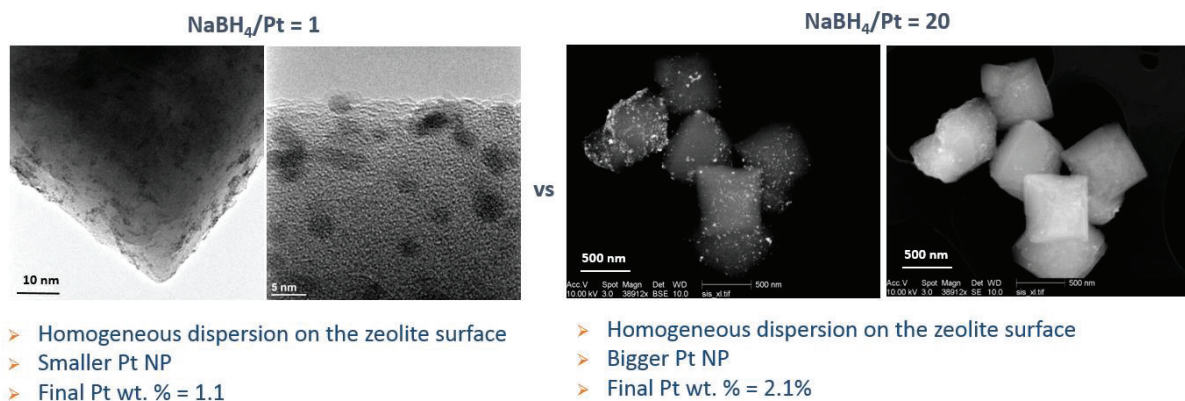


Figure 17 – Diagram representing the differences between the Pt dispersion and wt. % over CIT-6, after chemical reduction with two different concentrations of NaBH₄ solutions; the effect of NaBH₄ concentration on reduction.

As expected, for higher amounts of NaBH₄, reduction is more effective. Therefore, the amount of reduced Pt is higher for NaBH₄/Pt=20 with a final Pt wt. % of 2 % which actually corresponds approximately to the total amount of Pt introduced during the impregnation. Also, when NaBH₄/Pt=20 the Pt NPs size is bigger. As for NaBH₄/Pt = 1, the reduction is not complete as the wt. % Pt of the final product is only 1 wt. %. On the other hand, dispersion is higher. These results suggest that part of the NaBH₄ molecules react with water and therefore, a significant excess of NaBH₄ is needed in order to obtain a complete reduction.

XRD patterns of the previous samples show that the zeolite structure is unchanged after NaBH₄ reduction, even for the highest concentration NaBH₄/Pt, Figure 18. The two small peaks at 40° and 46° for Pt/CIT-6 are attributable to platinum nanoparticles.

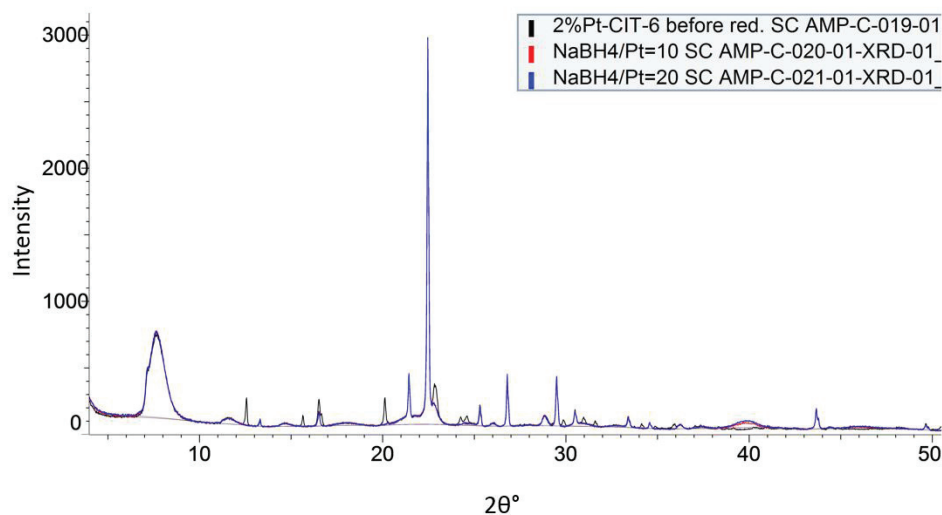


Figure 18 – XRD patterns of Pt/CIT-6 before reduction (black), and after NaBH₄ reduction, NaBH₄/Pt=10 (red) and NaBH₄/Pt=20 (blue).

These two studies allowed us to find the optimal reduction conditions for Pt/CIT-6, in order to have a complete reduction of the whole amount of Pt, and a relatively high and

homogeneous dispersion. The same tests were repeated for Pt/CIT-6 prepared by $\text{Pt}(\text{NH}_3)_4(\text{NO}_3)_2$ impregnation and the results were in accordance with the previous results. Finally, the best experimental conditions found for high dispersion and high amount of Pt, consisted in preparing a fresh NaBH_4 solution at each reduction procedure, $\text{NaBH}_4/\text{Pt} = 20$ concentration, and add it to the zeolite after 1 min. Reduction details in chapter II.

III.2.2. Pathway E – characterizations and catalytic data treatment

III.2.2.1. N_2 isotherms

Figure 19 shows the N_2 physisorption isotherm (at 77K) of Pt@Hollow β (prepared by pathway E) and the standard Hollow Beta. Results show that both samples have a similar porous structure. The hysteresis type appears to be the same, but with bigger volume for Pt@Hollow β , indicating that this sample might have a bigger mesopore pore volume. One must take into account that hollow Beta synthesis does not account for impregnation over CIT-6.

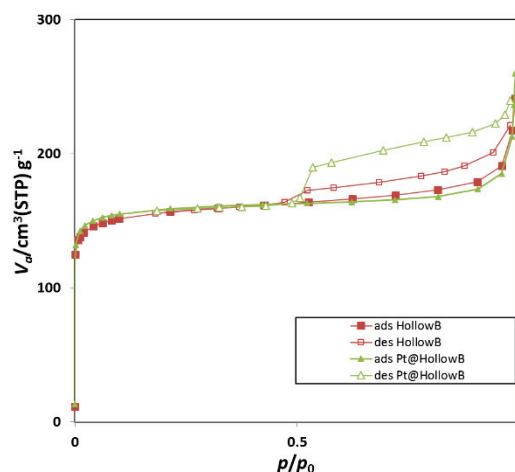


Figure 19 - N_2 adsorption/desorption isotherms of hollow Beta and Pt@Hollow β .

III.2.2.2. Determination of E_a

Value for the apparent reaction activation energy for toluene hydrogenation over Pt@Hollow β ($E_a = 47$ kJ/mol) and over Pt/SiO $_2$. The apparent activation energy for both catalysts was calculated using the turnover frequencies (TOFs, expressed as molecules of substrate converted per second per surface Pt atom) given as an Arrhenius plot, see Figure 20 and Figure 21. The TOFs reported corresponded to less than 5% conversion.

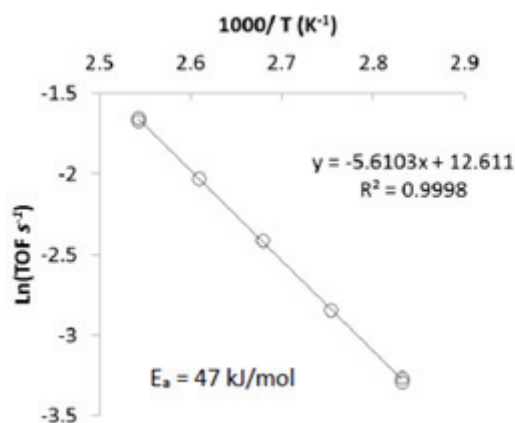


Figure 20 - Arrhenius-type plot relating the natural logarithm of the turnover frequency (TOF) to the reciprocal temperature for toluene hydrogenation over 1% Pt@Hollow β . The corresponding apparent activation energy is 47 kJ/mol/s.

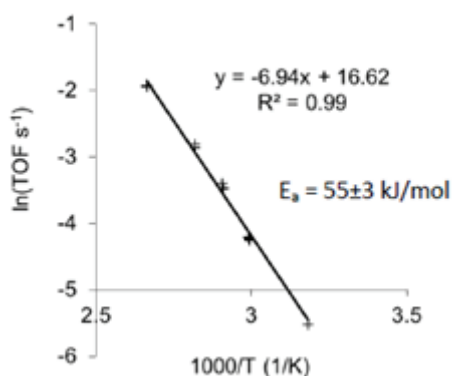


Figure 21 - Arrhenius-type plot relating the natural logarithm of the turnover frequency (TOF) to the reciprocal temperature for toluene hydrogenation over 1% Pt/SiO $_2$. The corresponding apparent activation energy is 55 kJ/mol/s.

III.2.2.3. Mesitylene and toluene adsorption isotherm

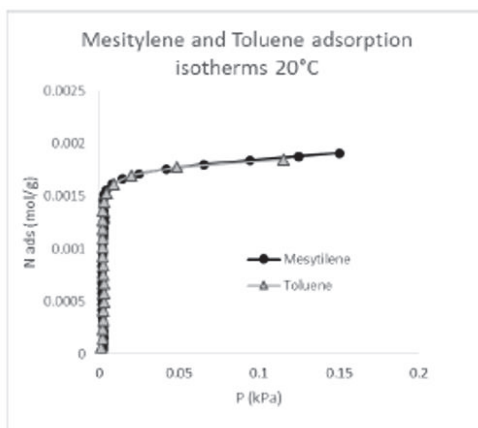


Figure 22 - Mesitylene adsorption isotherm at 20 °C (black circles) and toluene adsorption isotherm at 20 °C (grey triangles) for Pt@Hollow β .

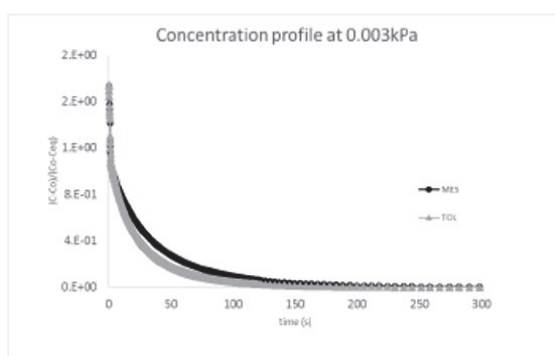


Figure 23 - Mesitylene (black circles) and toluene (grey triangles) concentration profiles: uptake kinetics at 3 Pa.

III.3. “Beta Zeolite Dissolution” approach

III.3.1. N₂ isotherms of Hollowβ

N₂ adsorption isotherms of Hollowβ, presenting very low values of porous surface ($S_{\text{BET}} = 9.3 \text{ m}^2/\text{g}$), see Figure 24.

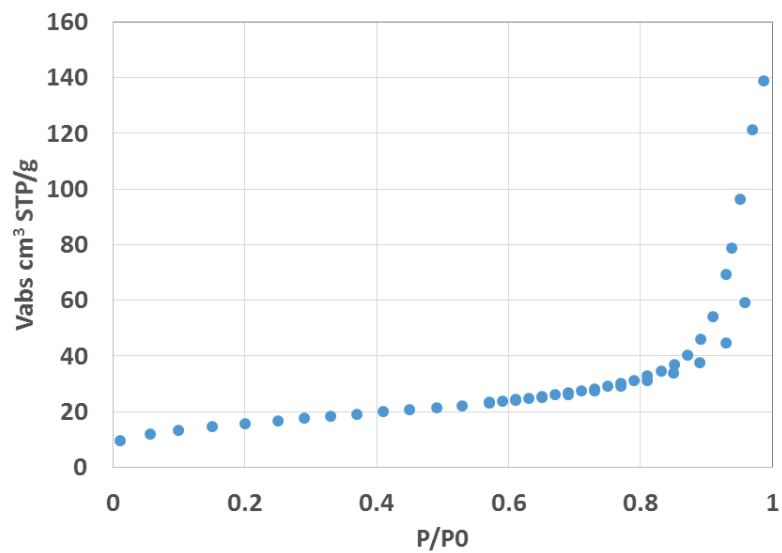


Figure 24 - N₂ adsorption/desorption isotherms of Hollowβ.

III.3.2. ^{27}Al NMR of as-made and calcined parent Beta zeolite

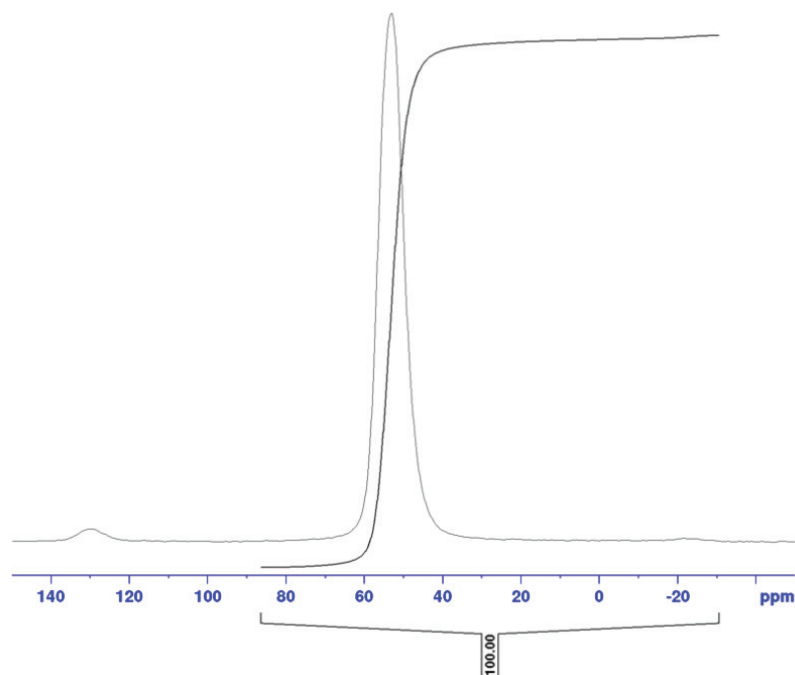


Figure 25 – ^{27}Al NMR of as-made parent Beta zeolite.

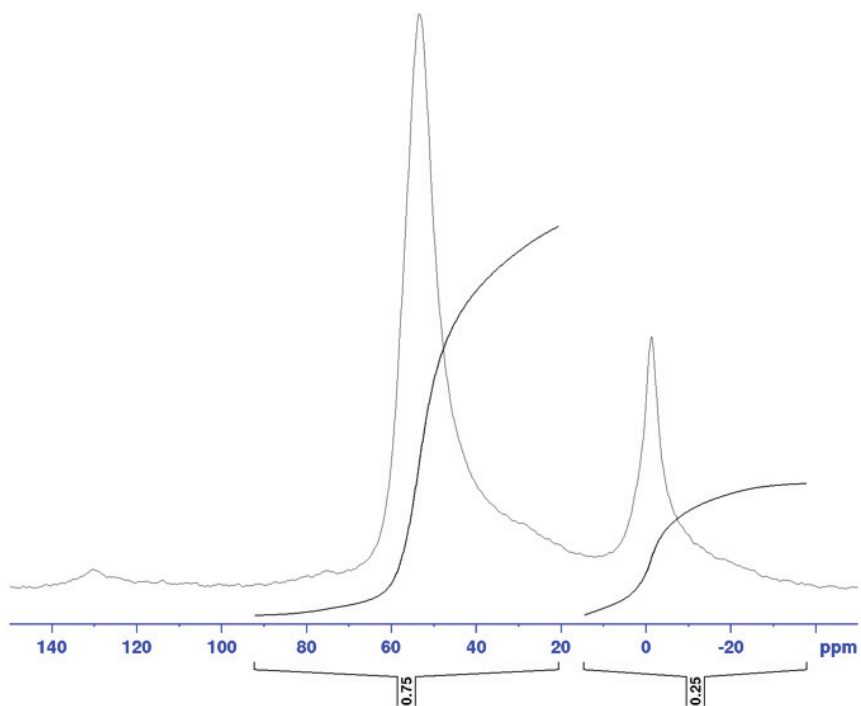


Figure 26 – ^{27}Al NMR of calcined parent Beta zeolite.

III.3.3. Effect of TEA⁺ - Increasing “crystallization time” – step3)

The literature reports hydrothermal transformations of amorphous silica supports to Beta zeolite in the presence of TEAOH^{3,4} which suggest a possible transformation of the amorphous phase into Beta zeolite. Also, assuming that the amorphous phase is due to an incomplete recrystallization, increasing crystallization time should increase the yield of crystalline zeolite.

The synthesis of TEA-Hollow β was repeated but with longer crystallization times: 14h, 21h30 and 84h. XRD results show that other crystalline phases start to appear and amorphous phase, see Figure 27.

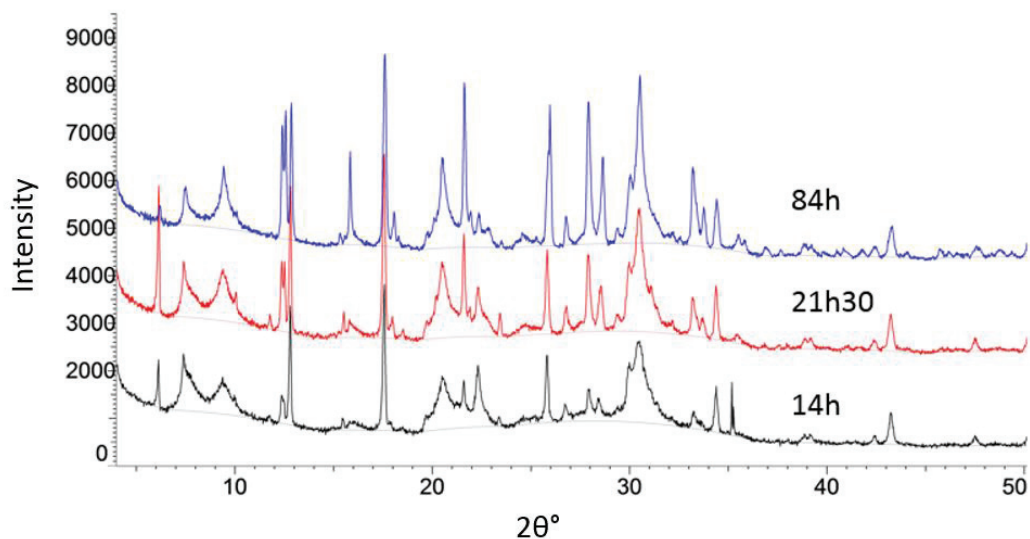


Figure 27 - XRD patterns for TEAHollow β , crystallization time of 14h (black pattern), 21h30 (red pattern) and 84h (blue pattern).

Annexes – Chapter IV

IV.3. ZLC unit - sensitivity analysis

Herein we present the parameters studied for the ZLC unit. These parameters were analyzed based on the FID signal during adsorption and desorption, and also based on the data obtained by the long time ZLC approach.

As mentioned before, while performing a run, there was a perturbation during the “switch” moment. This perturbation was always proportional to the pressure drop in the stream feeding the reactor: the bigger pressure drop, the bigger the perturbation was. These were the parameters studied in order to decrease pressure drop: granulometry, the amount of sample, etc. Other parameters were studied in order to understand the impact on the diffusion coefficient. For these tests, **MFI** adsorbent was tested with toluene as sorbate.

- Effect of the amount of sample

The ZLC technique requires testing a very small amount of sample, and one of the reasons is the need of very thin or “zero” length zeolitic bed. In the literature different runs are performed with 1 to 20 mg of sample. To decrease pressure drop as much as possible, minimum amounts of sample were tested, namely 3 and 6 mg. Figure 28 shows the impact of the different amounts of sample in the pressure drop, and therefore, in the size of the fluctuation right after switch moment.

As expected, the smaller amount of sample, the smaller the pressure drop is and thus the perturbation is minimal as well. When comparing the experimental data with the ZLC model generated, for 6 mg the model couldn't fit the experimental data, see Figure 29.

After several tests, we concluded that 3 mg should be the maximum amount of sample in order to obtain proper ZLC response curves.

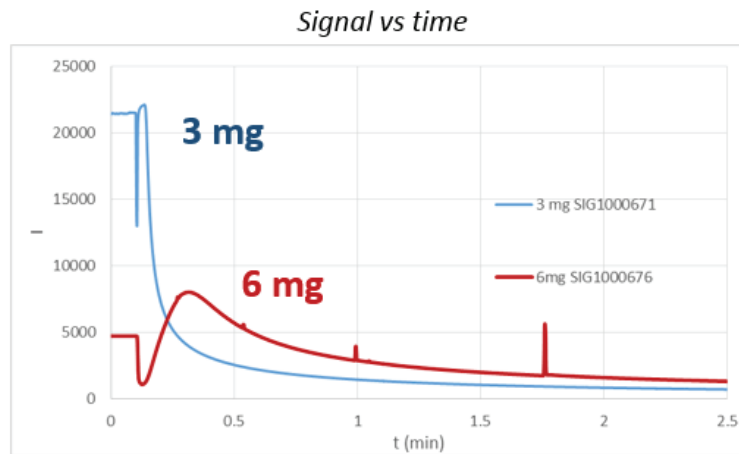


Figure 28 – FID signal for two different amounts of zeolite sample. Zoomed on the right side.

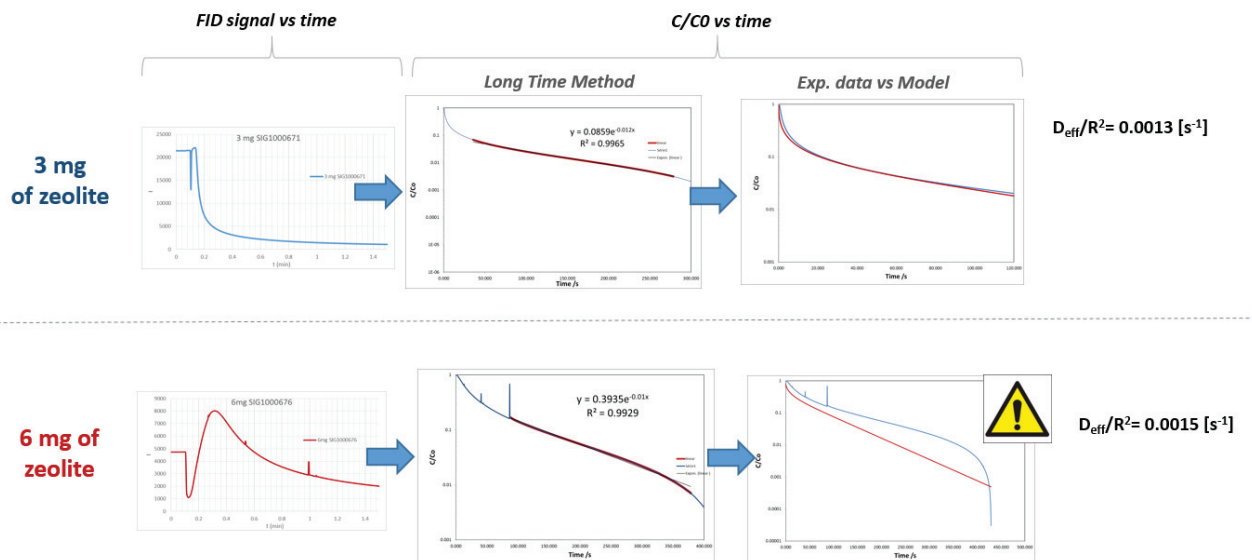


Figure 29 – FID signal (left), followed by fitting the long time part with the respective linear function, followed by the respective model compared with experimental data, and D_{eff}/R^2 value on the right. The graphics on the top correspond to the run for the 3 mg sample, and below for the 6 mg sample.

- Effect of granulometry

Zeolite pellets of 150-200 μm were made. The ZLC test was carried out using zeolite powder and zeolite pellets, in order to check if there was any change in the desorption curve, i.e. changes in pressure drop, “switch” response, and eventually the final D_{eff} .

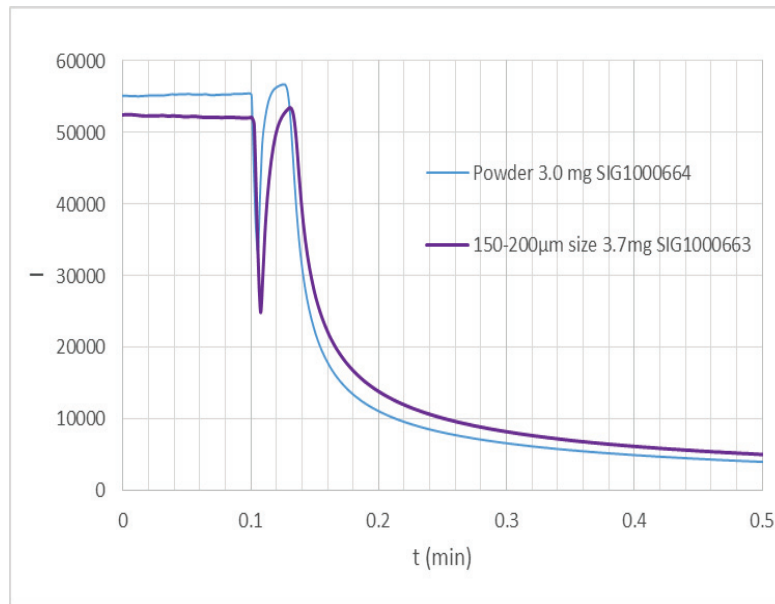
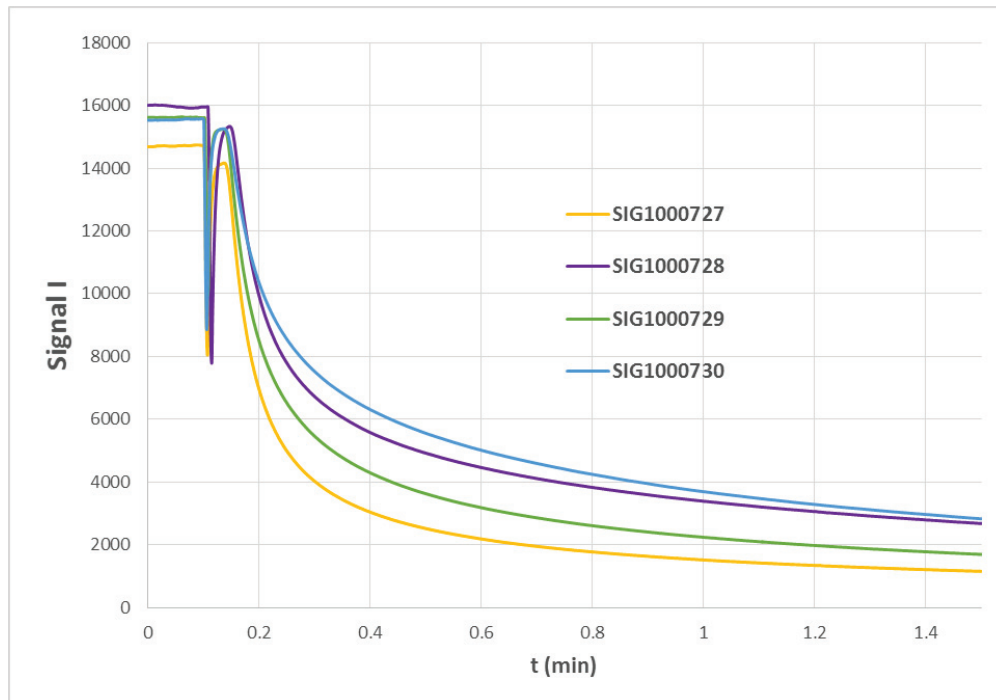


Figure 30 – FID signal using zeolite powder and zeolite pellets 150-200 μm .

Figure 30 shows that using pellets did not have a major impact on the perturbation, neither in the D_{eff} coefficient (not shown). Therefore, for the studies presented in this thesis all the tests were carried out using zeolite as fine powder.

- **Effect of sample preparation**

The texture of zeolite powder can be very different function of the amount of humidity for example. We tested zeolite powders with different “preparations” to check if those would have an immediate impact on the pressure drop, and therefore on the switch moment. The same zeolite sample was prepared by four different ways: 1) sample just left at room conditions, 2) sample has been dried overnight at 80 °C, 3) sample has been placed in closed humid atmosphere, d) sample has been placed through ultrasounds for at least 1 min.



Caption

- **SIG1000727 – Dry Sample**

Sample has been dried overnight at 80 °C

- **SIG1000728 – Humid Sample**

Sample has been placed in closed humid atmosphere (30 °C, with some water evaporating nearby)

- **SIG1000729 – Ultrasound for 1 min**

Sample has been placed in ultrasound (without water) for 1 minute

- **SIG1000730– Normal sample (powder at room conditions)**

Figure 31 – FID signals for different zeolite preparations.

The different zeolite preparations did not have an impact on pressure drop, even though the desorption curves were different, probably because of the different amount of water present in the zeolite. Note that the desorption curve of the “humid sample” (purple curve) is relatively different from the others, pointing out that the presence of water in the zeolite might have an impact on diffusion, hence, the importance of the activation step before every set of tests.

• Influence of t_0

As mentioned before, “ t_0 ” is supposed to be the moment when desorption starts, and therefore the moment of the switch between the adsorption stream and the desorption stream. t_0 was placed on the peak of the perturbation, once the concentration of the probe molecule starts decreasing immediately after. Visually, this maximum is difficult to recognize, it was important to understand the effect of the placement of t_0 on the peak.

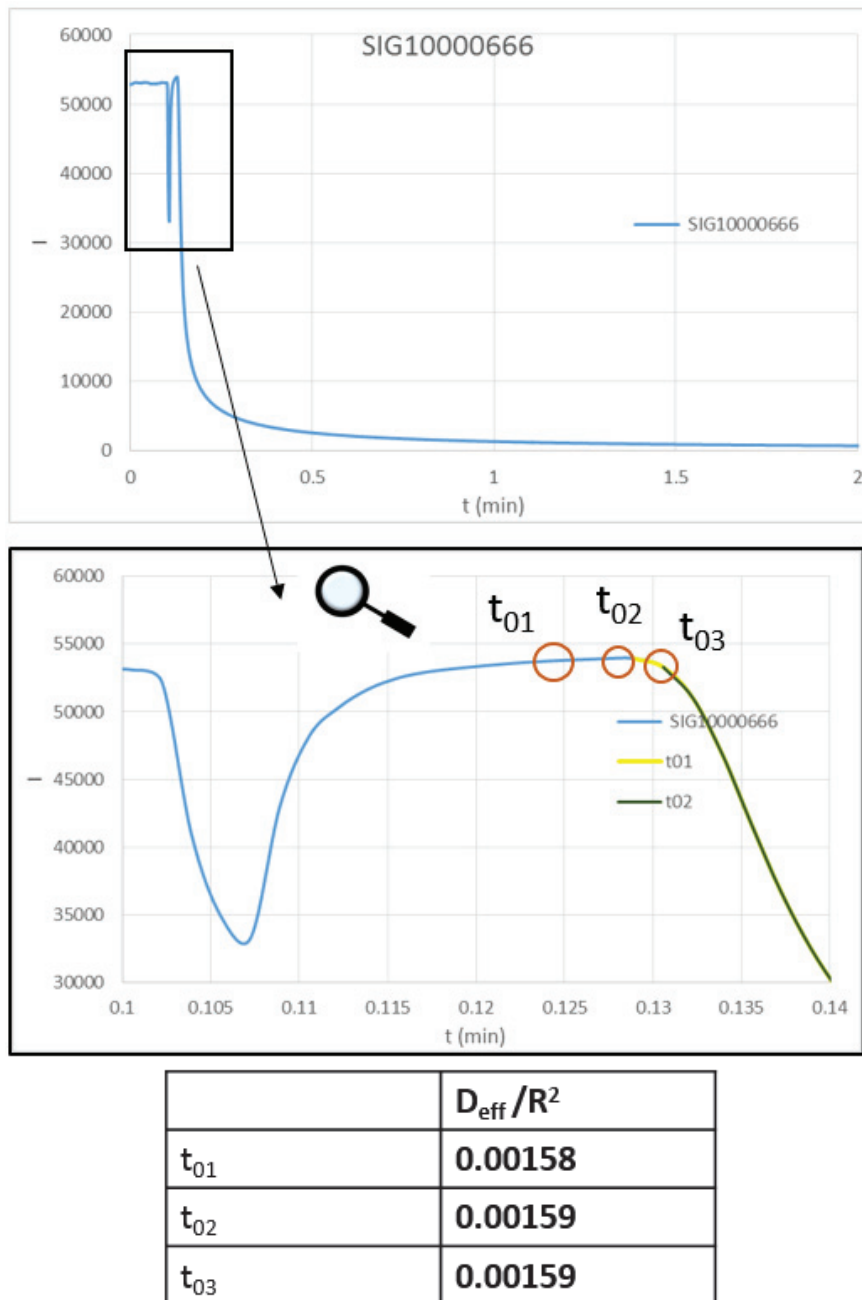
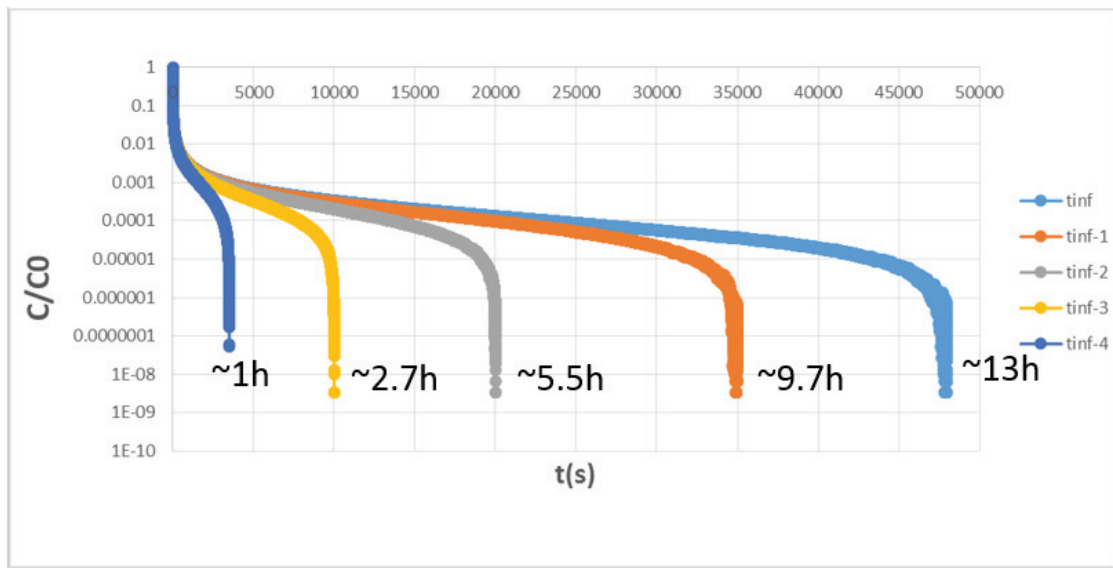


Figure 32 - Showing 3 different t_0 placed on different parts of the peak. Table below shows the values obtained for D_{eff}/R^2 using the three different t_0 .

Figure 32 shows that the precision of the t_0 over the peak does not have great impact over the ZLC long time model or the D_{eff}/R^2 obtained.

- **Baselining**

As mentioned before, the curve has to be baselined before further calculations can be made. If done incorrectly, this can have consequences in the long time method. It can significantly change the slope of the long time “tail” and, thus, the D_{eff}/R^2 value.^{5,6} Some studies⁷ showed the impact of baselining over the D_{eff}/R^2 given by the long time methods. Baselining errors of 0,1 % led to variations of D_{eff}/R^2 up to 50 %-70 %. Herein, we present the impact of different baselining on D_{eff}/R^2 . The system used was **MFI** and toluene as sorbate. For a single test, the l_{inf} of different desorption times was taken into account, resulting in different c/c_0 curves and D_{eff}/R^2 , Figure 33.



$$\frac{c^0}{c} = \frac{1^0 - I^{1/l_{inf}}}{1 - I^{1/l_{inf}}}$$

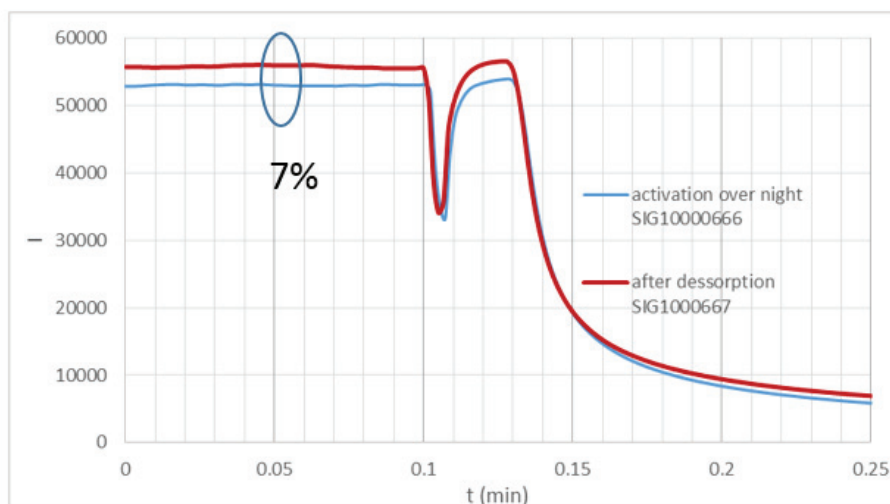
13μ	18	0'0000003
9.7μ	22	0'000013
5.5μ	25	0'000051
2.7μ	35	0'000044
1μ	55	0'00013
time Desorption	l_{inf}	$D_{eff}/R^2 [s^{-1}]$

Figure 33 – c/c_0 of a single test carried out using different desorption times: 1h, 2.7h, 5.5h, 9.7h and 13h. Table below shows the value of l for each desorption time, and the correspondent D_{eff}/R^2 value.

Figure 33 shows that different l_{inf} (55 to 18) have a big impact on the final D_{eff}/R^2 and therefore, it must be carefully chosen.

- Effect of zeolite activation

An experiment was performed right after the zeolite activation (inert flow at 300 °C over night). Once desorption of the first experiment was over, the same run was repeated but without zeolite (activation) regeneration.



	$D_{eff}/R^2 [s^{-1}]$
Run1: After zeolite activation over night	0.00127
Run2: after desorption of run1	0.00127

Figure 34 – FID signal for run1 and run2 during the switch between adsorption and desorption. Run1 was carried out after zeolite activation (blue) and run2 was carried out after the desorption step of run1, without zeolite regeneration (red line). The table below presents the D_{eff}/R^2 values for each run.

The desorption curve and D_{eff}/R^2 obtained from the ZLC model were the same, showing that zeolite activation is not needed before every test, but only before starting a set of tests, see Figure 34. The 7% of difference of intensity are within the sensibility of the FID.

Annexes – Chapter V

V.1. Characterization of the samples used for n-C₁₆ hydroisomerization reaction

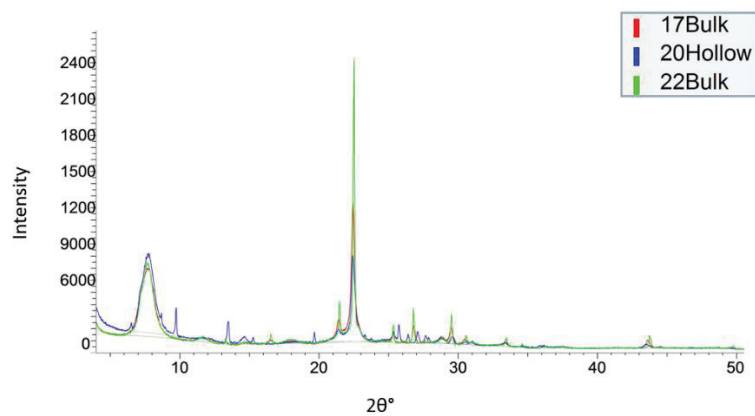


Figure 35 – XRD patterns for 17Bulk, 20Hollow and 22Bulk.

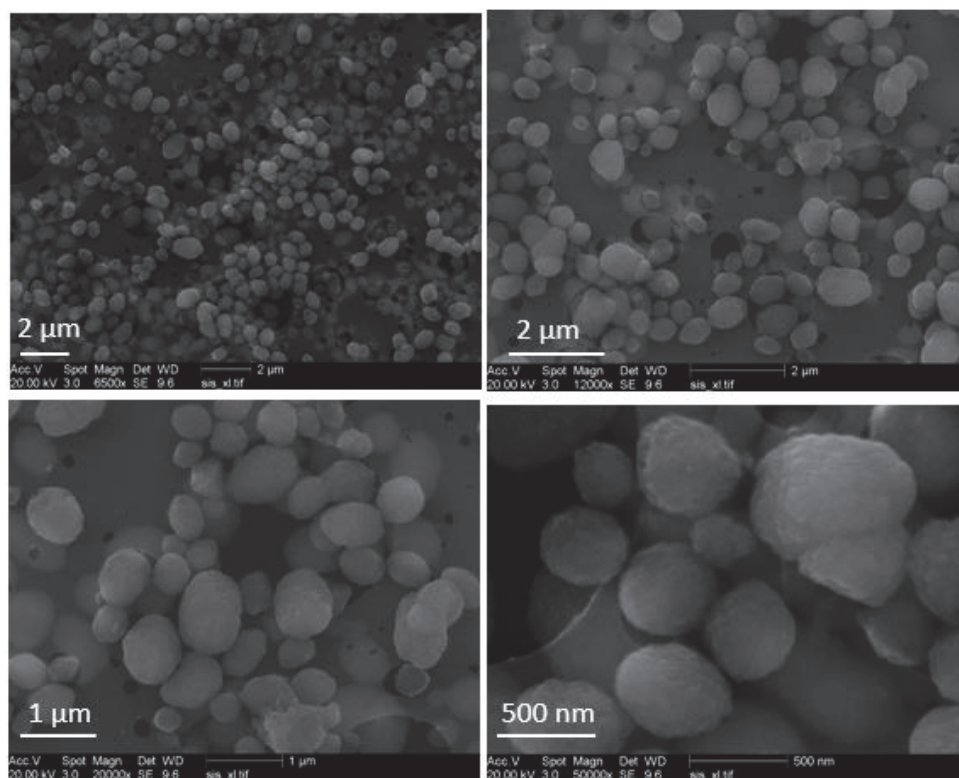


Figure 36 – SEM images of the zeolite crystals of sample 17Bulk.

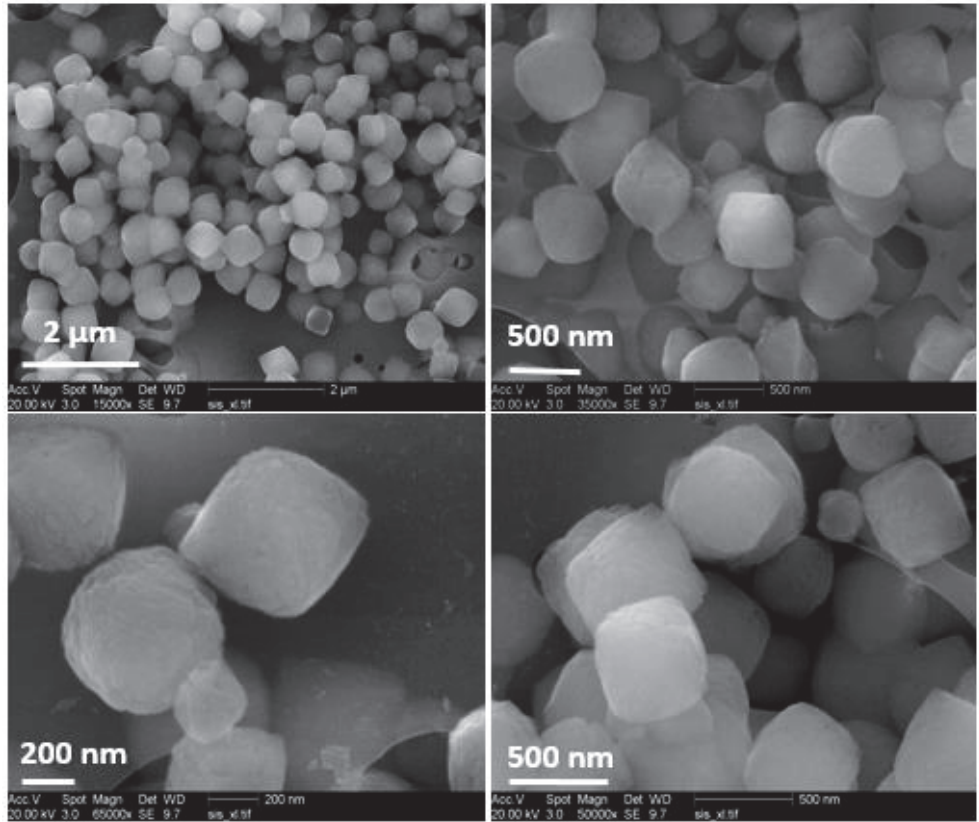


Figure 37 – SEM images of the zeolite crystals of the sample 22Bulk.

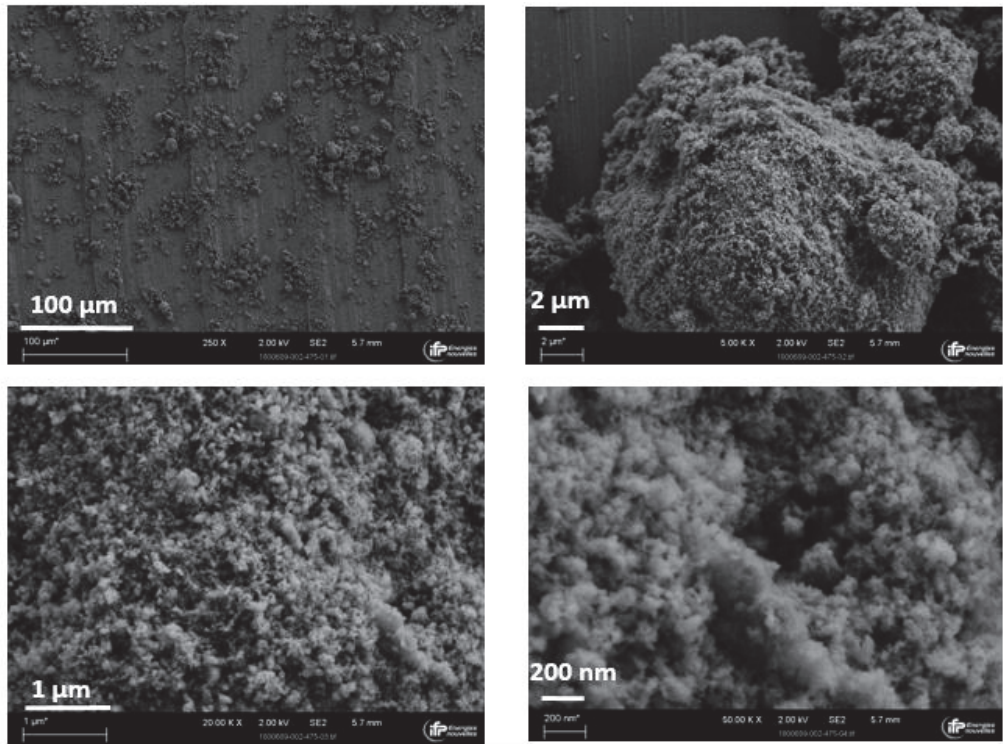


Figure 38 – SEM Images of zeolite crystals of sample REF.

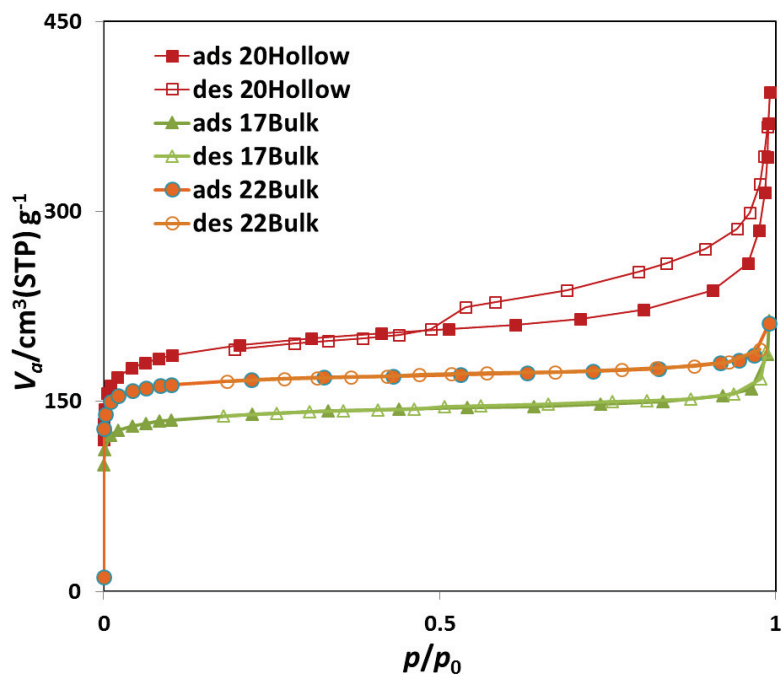


Figure 39 – N_2 isotherms of 17Bulk, 22Bulk, 20Hollow.

V.2. Pyridine adsorption

Table 1 - The main interactions that pyridine may have with Brønsted and Lewis sites and the corresponding bands, according to Marques et al.⁸

Type of interaction	Frequency (cm^{-1})
Pyridium ion – Brønsted site PyH ⁺	1545 + 1637
Lewis site type 1 PyL1	1456/1455 + 1622
Lewis site type 2 PyL2	1603 + 1446
Superposition of Lewis and Brønsted	1490 / 1491

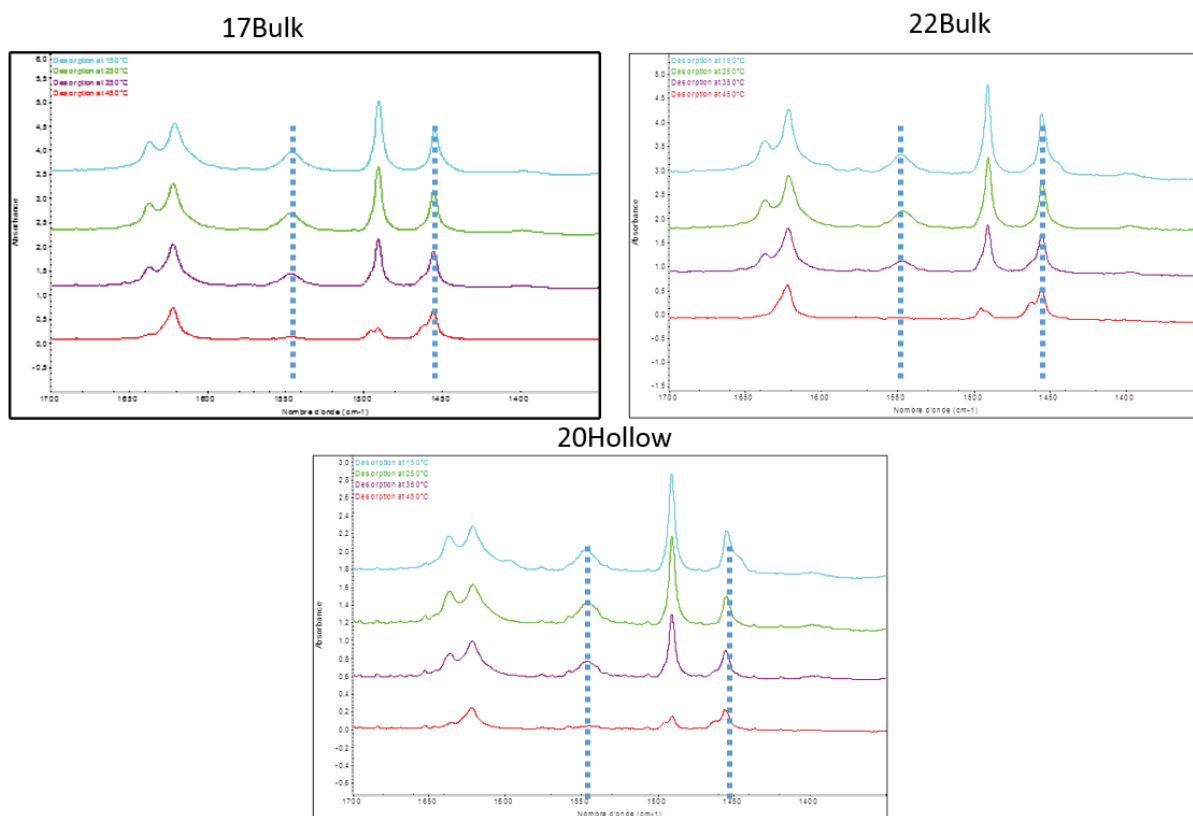


Figure 40 - Infrared spectra of the pyridine region of activated samples 17Bulk, 22Bulk and 20Hollow at 150, 250, 350 and 450 °C. The dashed lines indicate the interaction with Brønsted sites (left) and the interaction with Lewis sites (right).

Figure 40 shows the intensities of the bands corresponding to pyridine adsorbed on Lewis and/or Brønsted sites, at different temperatures, in bulk and hollow Beta samples. The concentrations of the Brønsted and Lewis acid sites were calculated from the integrated area of the PyH^+ and PyL bands (1545 and 1456 cm^{-1} , respectively) using the values of the molar extinction coefficients of these bands ($\epsilon_B=1.67$ $\text{cm}/\mu\text{mol}$ et $\epsilon_L=2.22$ $\text{cm}/\mu\text{mol}$).⁹

V.3. Cyclohexane cracking reaction

V.3.1. Determination of K_H at 600 °C

According to Atkinson and Curthoys,¹⁰ the relationship between localized adsorption entropy, ΔS , enthalpy, $-\Delta H$, temperature, and the Henry's constant K_H (mol/kg_{zeol}/atm) is given by:

$$\ln(K_H) = \frac{-\Delta H}{R_{gas}T} + \left(\frac{\Delta S}{R_{gas}} + \ln\left(\frac{n_T}{2p^\theta}\right) \right) \quad 1$$

Where:

$-\Delta H$ – adsorption enthalpy (J/mol)

ΔS – adsorption entropy (J/mol/K)

R_{gas} – perfect gas constant

n_T – total number of adsorption sites (mol/kg_{zeol})

p^θ - standard state of the gas phase (chosen as 1 atm)

In our case, using data for n-C₆

$T = 600$ °C

$-\Delta H$ (n-C₆ alkane) = -62,7 kJ/mol

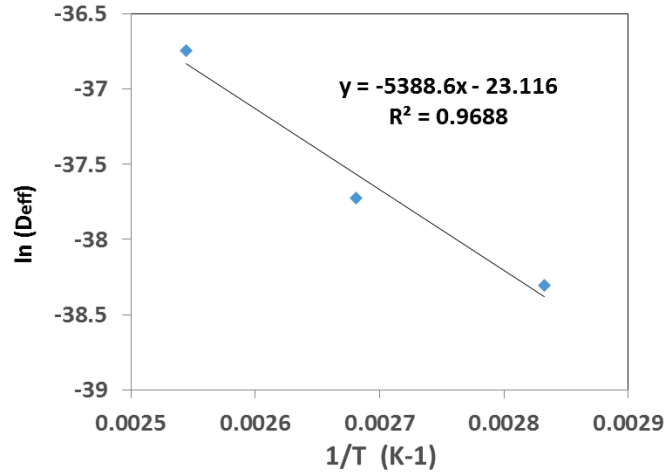
ΔS (n-C₆ alkane) = - 84.8 J/mol/K

$n_T \sim 0.2$ mol/kg_{zeol}

Then, K_H (Beta, n-C₆, 600 °C) = 2×10^{-2} (mol/kg/atm) = 2×10^{-7} (mol/kg/Pa).

V.3.2. Determination of D_{eff} at 600 °C

D_{eff} for HollowBeta' and Bulk1beta was estimated using the D_{eff} values found for Bulk1Beta in chapter IV. D_{eff} was calculated from the Arrhenius relation between D_{eff} and temperature. The D_{eff} values obtained in chapter IV were in a temperature range significantly below the reaction temperature range. Therefore, we have assumed an error of +- 20% on E_d .



	Ed (kJ/mol)	Slope	D _{eff} (600°C)
raw value	44.8	5389	2.1 x 10 ⁻¹³
20%	53.8	6466	6.2 x 10 ⁻¹⁴
-20%	35.8	4311	7.4 x 10 ⁻¹³

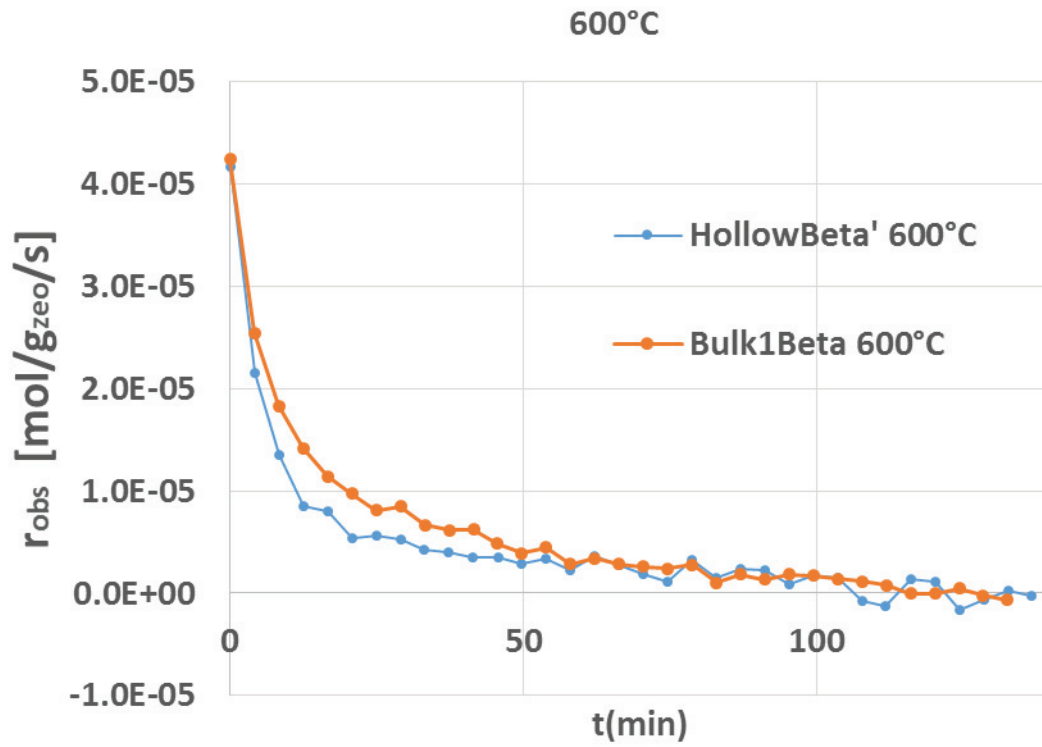
Therefore, $6.2 \times 10^{-14} < D_{\text{eff}} (\text{Beta}, 600^\circ\text{C}) < 7.4 \times 10^{-13}$

V.3.3. Observed reaction rate

Knowing that

$$r_{\text{obs}} = \frac{X F}{m_{\text{zeol}}}$$

Where, X is the cyclohexane conversion, F = 0.0273 mol/h and $m_{\text{zeol}} = 0.101$ g, then:



V.3.4. Observed reaction rate

$$\phi' = L \sqrt{\frac{r_{obs} \rho}{D_{eff} K_{HP}}}$$

And

$$\eta' = \frac{\tanh(\phi')}{\phi'}$$

Parameters:

	Bulk1Beta'	HollowBeta'
P (atm)	1	
k_H (mol/kg/atm)	2.1×10^{-2}	
k_H (mol/kg/Pa)	2.1×10^{-7}	
r_{obs} (mol/g _{zeol} /s)	4.2×10^{-5}	4.1×10^{-5}
ρ (kg/m ³ _{zeol})	1000	
L (m)	4.92E-07	1.5E-07
$D_{\text{eff min}}$ (m ² /s)	6.2E-14	
$D_{\text{eff max}}$ (m ² /s)	7.4E-13	

References

- (1) Giesche, H. Mercury Porosimetry: A General (Practical) Overview. *Part. Part. Syst. Char.* **2006**, *23* (1), 9–19. <https://doi.org/10.1002/ppsc.200601009>.
- (2) Groen, J. C.; Brouwer, S.; Peffer, L. A. A.; Perez-Ramirez, J. Application of Mercury Intrusion Porosimetry for Characterization of Combined Micro- and Mesoporous Zeolites. *Part. Part. Syst. Char.* **2006**, *23* (1), 101–106. <https://doi.org/10.1002/ppsc.200601010>.
- (3) Selvam, T.; Bandarapu, B.; Mabande, G. T. P.; Toufar, H.; Schwioger, W. Hydrothermal Transformation of a Layered Sodium Silicate, Kanemite, into Zeolite Beta (BEA). *Microporous Mesoporous Mater.* **2003**, *64* (1–3), 41–50. [https://doi.org/10.1016/S1387-1811\(03\)00508-0](https://doi.org/10.1016/S1387-1811(03)00508-0).
- (4) Mihalyi, R. M.; Pal-Borbely, G.; Beyer, H. K.; Szegedi, A.; Koranyi, T. I. Characterization of Aluminum and Boron Containing Beta Zeolites Prepared by Solid-State Recrystallization of Magadlite. *Microporous Mesoporous Mater.* **2007**, *98* (1–3), 132–142. <https://doi.org/10.1016/j.micromeso.2006.09.001>.
- (5) Han, M. H.; Yin, X. Y.; Jin, Y.; Chen, S. Diffusion of Aromatic Hydrocarbon in ZSM-5 Studied by the Improved Zero Length Column Method. *Ind. Eng. Chem. Res.* **1999**, *38* (8), 3172–3175. <https://doi.org/10.1021/ie9807856>.
- (6) Hufton, J.; Ruthven, D. Diffusion of Light Alkanes in Silicalite Studied by the Zero Length Column Method. *Ind. Eng. Chem. Res.* **1993**, *32* (10), 2379–2386. <https://doi.org/10.1021/ie00022a022>.
- (7) Karger, J. Transport Phenomena in Nanoporous Materials. *ChemPhysChem* **2015**, *16* (1), 24–51. <https://doi.org/10.1002/cphc.201402340>.
- (8) Marques, J. P.; Gener, I.; Ayrault, P.; Bordado, J. C.; Lopes, J. M.; Ribeiro, F. R.; Guisnet, M. Infrared Spectroscopic Study of the Acid Properties of Dealuminated BEA Zeolites. *Microporous Mesoporous Mater.* **2003**, *60* (1–3), 251–262. [https://doi.org/10.1016/S1387-1811\(03\)00382-2](https://doi.org/10.1016/S1387-1811(03)00382-2).
- (9) Emeis, C. Determination of Integrated Molar Extinction Coefficients for Infrared-Absorption Bands of Pyridine Adsorbed on Solid Acid Catalysts. *J. Catal.* **1993**, *141* (2), 347–354. <https://doi.org/10.1006/jcat.1993.1145>.

- (10) Atkinson, D.; Curthoys, G. Heats and Entropies of Adsorption of Saturated-Hydrocarbons by Zeolites-X and Zeolite-Y. *Journal of the Chemical Society-Faraday Transactions I* **1981**, 77, 897–907. <https://doi.org/10.1039/f19817700897>.